

5-2014

# Development and evaluation of a calibration free exhaustive coulometric detection system for remote sensing.

Thomas James Roussel  
*University of Louisville*

Follow this and additional works at: <https://ir.library.louisville.edu/etd>

 Part of the [Mechanical Engineering Commons](#)

---

## Recommended Citation

Roussel, Thomas James, "Development and evaluation of a calibration free exhaustive coulometric detection system for remote sensing." (2014). *Electronic Theses and Dissertations*. Paper 1238.  
<https://doi.org/10.18297/etd/1238>

This Doctoral Dissertation is brought to you for free and open access by ThinkIR: The University of Louisville's Institutional Repository. It has been accepted for inclusion in Electronic Theses and Dissertations by an authorized administrator of ThinkIR: The University of Louisville's Institutional Repository. This title appears here courtesy of the author, who has retained all other copyrights. For more information, please contact [thinkir@louisville.edu](mailto:thinkir@louisville.edu).

DEVELOPMENT AND EVALUATION OF A  
CALIBRATION FREE EXHAUSTIVE COULOMETRIC  
DETECTION SYSTEM FOR REMOTE SENSING

by

Thomas James Roussel, Jr.

B.A., University of New Orleans, 1993  
B.S., Louisiana Tech University, 1997  
M.S., Louisiana Tech University, 2001

A Dissertation  
Submitted to the Faculty of the  
J. B. Speed School of Engineering of the University of Louisville  
in Partial Fulfillment of the Requirements  
for the Degree of

Doctor of Philosophy

Department of Mechanical Engineering  
University of Louisville  
Louisville, Kentucky

May 2014

Copyright 2014 by Thomas James Roussel, Jr.

All rights reserved



DEVELOPMENT AND EVALUATION OF A  
CALIBRATION FREE EXHAUSTIVE COULOMETRIC  
DETECTION SYSTEM FOR REMOTE SENSING

By

Thomas James Roussel, Jr.  
B.A., University of New Orleans, 1993  
B.S., Louisiana Tech University, 1997  
M.S., Louisiana Tech University, 2001

A Dissertation Approved on

April 21, 2014

by the following Dissertation Committee:

---

Dissertation Director  
Robert Keynton, Ph.D.

---

Richard Baldwin, Ph.D.

---

John Naber, Ph.D.

---

Balaji Panchapakesan, Ph.D.

---

Stuart Williams, Ph.D.

## DEDICATION

This dissertation is dedicated to the memory of my mother

Cherry Hall Roussel

who always believed in me.

Promised you I'd finish, mom.

And I did.

Toxey's Favorite

Mama Z's Azaleas

and Deep Purple Falls

## ACKNOWLEDGMENTS

I would like to thank my mentor and friend, Dr. Robert Keynton, for his guidance over the many years we have collaborated. Who knows where I would be and what I would be doing had he not knocked on my door and sat me down for a chat in the spring of 1997. Not that I ever contemplate those possibilities; pursuing research as a career was a great decision, and next to marrying my wife, probably the best one I've ever made. Many thanks to Dr. Richard Baldwin for getting this all started by introducing me to the field of electrochemistry. Additionally, I want to thank my other committee members, Dr. John Naber, Dr. Balaji Panchapakesan, and Dr. Stuart J. Williams for their support and words of encouragement. Special thanks to Doug Jackson and Scott Cambron, two of the most talented engineers I know. Those guys might not know it, but both have the patience and hearts of teachers. To my lab mates, Dr. Susan Carroll and Mohamed Marei, thanks for their hard work and dedication to the project, and also for tolerating my odd schedule. Finally, to my wife, Melissa Ann Becker: Thank you for rewarding me with Emily Claire and for keeping everything together through all the late nights and long weekends while I worked towards this goal.

## ABSTRACT

### DEVELOPMENT AND EVALUATION OF A CALIBRATION FREE EXHAUSTIVE COULOMETRIC DETECTION SYSTEM FOR REMOTE SENSING

Thomas J. Roussel, Jr.

April 21, 2014

Most quantitative analytical measurement techniques require calibration to correlate signal with the quantity of analyte. The purpose of this study was to employ *exhaustive coulometry*, an implementation of coulometric analysis in a stopped-flow, fixed-volume, thin-layer cell, to attain calibration-free measurements that would directly benefit intervention-free analysis systems designed for remote deployment. This technique capitalizes on the short diffusion lengths ( $<100\ \mu\text{m}$ ) to dramatically reduce the time for analysis ( $<30\ \text{sec}$ ). For this work, a thin-layer fluidic cell was designed in software, fabricated via CNC machining, and evaluated using Ferri/Ferrocyanide  $\{\text{Fe}(\text{CN})_6^{3-/4-}\}$  as a model analyte. The  $2\ \mu\text{L}$  fixed volume incorporated an oval, 8mm by 4 mm, thin-film gold electrode sensor with an integrated Ag|AgCl pseudo-reference electrode. The flow cell area matched the shape of the sensor, with a volume set by the thickness of a laser-cut silicone rubber gasket ( $\sim 80\ \mu\text{m}$ ). A semi-permeable membrane isolated the working electrode and counter electrode chambers to prevent analyte diffusion. A miniaturized custom potentiostat was designed and built to measure reaction currents ranging from 10 mA to 0.1 nA. Software was developed to perform step



voltammetry as well as cyclic voltammetry analysis for verifying electrode condition and optimal redox potential levels. Experimentally determined oxidation/reduction potentials of -100 mV and 400 mV, respectively, were applied to the working electrode for sample concentrations ranging from 50  $\mu\text{M}$  to 10,000  $\mu\text{M}$ . The current generated during the reactions was recorded and the total charge captured at each concentration was obtained by integrating the amperograms. When compared to the expected charge for a 2  $\mu\text{L}$  sample, the total charge vs. concentration plots displayed a near perfect linearity over the full concentration range, and the expected charge (100 % converted) was reached within 20 seconds. The reaction currents ideally should have decayed to background levels, but exhibited constant offset values slightly larger than the background signal, a phenomenon assumed to be lingering residual flow from sample injection. After adding rigid tubing and external valves, the thin-layer cell was shown to remain within 6% of the theoretical charge after 200 seconds. Continued development of this system will offer the possibility of remote, calibration-free determinations of real-world analytes such mercury and lead.

## TABLE OF CONTENTS

	PAGE
ACKNOWLEDGMENTS .....	iv
ABSTRACT .....	v
LIST OF TABLES .....	xii
LIST OF FIGURES .....	xiii
LIST OF EQUATIONS.....	xix
CHAPTER I. INTRODUCTION .....	1
1.1 Purpose of Study .....	5
1.2 Specific Aims.....	5
1.3 Significance of the Study.....	7
CHAPTER II. BACKGROUND.....	8
2.1 Microtechnology and Microfluidics .....	8
2.1.1 Microtechnology .....	9
2.1.2 Microfluidics.....	10
2.2 Modern Analytical Chemistry.....	11
2.3 Analytical Instrumental Methods of Detection.....	13
2.4 Electrochemical Detection.....	15
2.4.1 Principles of Electrochemistry.....	16
2.4.1.1 Redox Reactions .....	17
2.4.1.2 The Electrochemical Cell.....	19
2.4.1.2.1 Electrochemical Electrodes.....	19
2.4.1.2.2 Electrode Materials .....	23
2.4.1.2.3 The Reference Electrode.....	25

2.4.1.2.4	The Electrode-Electrolyte Interface.....	27
2.4.1.2.5	Electrode Fabrication.....	30
2.4.2	ECD Electronics.....	31
2.4.2.1	The Potentiostat.....	31
2.4.3	Volumetric Configurations and Flow Considerations.....	33
2.4.3.1	Bulk Electrolysis.....	35
2.4.3.2	Wall Jet Configuration.....	37
2.4.3.3	Flow Over/By Configuration.....	38
2.4.3.4	Stopped Flow Thin-Layer Cell.....	40
2.4.4	Quantitative Electrochemistry.....	41
2.4.4.1	Types of Electrochemical Detection.....	41
2.4.4.1.1	Voltammetric Techniques.....	42
2.4.4.1.2	Amperometric Techniques.....	44
2.4.4.2	Applied Electrochemistry.....	47
2.5	Literature Review.....	49
2.5.1	Coulometry/Micro-Bulk Electrolysis.....	50
2.5.2	Remote Field/Deployable Sensing.....	57
2.5.3	Custom Instrumentation.....	58
2.6	Summary.....	63
CHAPTER III. MATERIALS AND METHODS.....		65
3.1	Electrochemical Sensor Platform.....	65
3.1.1	Sensor Electrode Design.....	66
3.1.2	Thin-film Sensor Fabrication:.....	67
3.1.3	Estimated Sensor Yield.....	69
3.1.4	Wafer Dicing.....	70
3.1.5	Sensor Gasket Mask Design.....	71
3.1.6	Ag/AgCl Pseudo-Reference Electrode.....	72
3.2	Flow Cell Design and Fabrication.....	76

3.2.1	Flow Cell Considerations and Specifications .....	76
3.2.2	Computational Fluid Dynamics .....	78
3.2.3	Custom Flow Cell Design .....	80
3.2.4	Flow Manifold Materials .....	83
3.2.5	Fabrication .....	83
3.2.6	Assembly.....	84
3.2.7	Fluidic Connections .....	86
3.2.8	Pressure Testing.....	86
3.3	Instrumentation.....	87
3.3.1	Electrochemical Cell Equivalent Circuit .....	87
3.3.2	Potentiostat Circuit.....	89
3.3.2.1	Trans-Impedance Amplifier Circuit.....	89
3.3.2.2	Applied Potential Location .....	92
3.3.2.3	Feedback Circuit .....	93
3.3.3	Analog-to-Digital Conversion .....	95
3.3.4	Physical Connections .....	97
3.3.5	Power Regulation.....	98
3.3.6	Custom Printed Circuit Boards .....	99
3.3.7	Electrical Testing .....	100
3.3.7.1	Ripple and Offset Voltage .....	100
3.3.7.2	Potentiostat Electrical Performance.....	101
3.4	Software.....	103
3.4.1	Electroplating Software .....	104
3.4.2	Electrochemical and Coulometric Analysis Software .....	105
3.4.3	Data Processing and Interpretation .....	106
3.5	Analytical Technique, Experimental Methods and Conditions .....	106
3.5.1	Model Analytes.....	106

3.5.2	Analytical Chemistry Experiments .....	108
3.5.3	Exhaustive Coulometry.....	109
3.5.3.1	Chronoamperometry .....	112
3.5.3.2	Comparison to Commercial Electrochemical System .....	112
3.6	Summary.....	113
CHAPTER IV. RESULTS AND DISCUSSION .....		114
4.1	Final Flow Cell Design .....	114
4.1.1	Solid Model and Design Features .....	115
4.2	Computational Fluid Dynamics .....	119
4.2.1	Model Details.....	120
4.2.2	Numerical Analysis.....	122
4.2.3	Mesh Convergence Test.....	126
4.3	Final Flow Cell Prototype .....	128
4.3.1	Rubber Gasket Fabrication .....	132
4.3.2	Membrane Fabrication .....	134
4.3.3	Assembly Issues.....	135
4.3.4	Pressure and Leak Testing .....	136
4.4	Sensor Fabrication .....	140
4.4.1	Pseudo Electrode Fabrication Results.....	142
4.5	Electronics.....	144
4.5.1	Final Schematic and Board Layout.....	145
4.5.2	Final Printed Circuit Board .....	147
4.5.3	Electrical Testing and Performance Evaluation.....	148
4.5.3.1	Reference Electrode/Feedback Circuit Testing .....	149
4.5.3.2	Power Regulator Output Stage Evaluation .....	151
4.5.3.3	Transimpedance Stage vs. Differential Input Evaluation .....	153
4.5.3.4	Transimpedance Amplifier Gain Stage Analysis.....	154

4.5.3.5	Dummy Cell Testing.....	161
4.6	Software.....	162
4.6.1	Web Interface Control.....	164
4.6.2	Ag/AgCl Conversion Interface .....	165
4.6.3	Data Processing.....	167
4.7	Electrochemical Analysis.....	170
4.7.1	Chronocoulometry Experimental Results .....	171
4.7.2	Coulometric Experimental Results .....	173
4.7.3	Linear response of concentration range .....	176
4.7.4	Coulometric Determination over Time.....	177
4.7.5	Flow Cell Comparison to Thin Layer Theory.....	180
4.7.6	Comparison of Commercial Detector and Custom Potentiostat Data	181
4.8	Thin Layer Cell Redesign .....	184
4.8.1	Particle Image Velocimetry .....	186
4.8.2	Electrochemical Analysis.....	190
4.9	Future Work.....	192
CHAPTER V. CONCLUSIONS .....		195
REFERENCES .....		197
Appendix A Potentiostat Bill of Materials .....		204
Appendix B TLC2202 Datasheet (First Ten Pages).....		206
Appendix C DAQCard-6062E Specifications.....		216
Appendix D Flow Cell Designs.....		226
Appendix E Printed Circuit Board Layout .....		230
CURRICULUM VITA .....		231

## LIST OF TABLES

TABLE	PAGE
Table 2.1 - Abbreviated list of metallic electrode materials and half-cell potentials .....	24
Table 3.1 – Trans-Impedance Amplifier Feedback Resistor Gain Settings.....	91
Table 3.2 – Electrical Connection Breakout Board Connection.....	98
Table 3.3 – Theoretical Total Charge Generated by Oxidation of Ferrocyanide .....	108
Table 4.1 – Measurement Data for Rubber Gaskets .....	132
Table 4.2 – Measurement Data on Feedback Control.....	150
Table 4.3 – Measurement Data for +5V and -5V Supply Voltages.....	152
Table 4.4 – Comparison of Current Measuring Techniques.....	153
Table 4.5 – Theoretical vs. Experimental Cutoff Frequencies .....	160
Table 4.6 – Chronocoulometry Results .....	173
Table 4.7 – Coulometric Analysis Results.....	177
Table 4.8 – Calculation of Total Charge Over Time for Increasing Concentrations.....	179
Table 4.9 – Comparison of Commercial vs. Custom Potentiostat.....	181

## LIST OF FIGURES

FIGURES	PAGE
Figure 1.1 – Sample Reaction Current vs. Time Chronoamperogram .....	3
Figure 2.1 – Benchtop Gas Chromatograph .....	12
Figure 2.2 – Micro GC 3000 from Inficon Petrochemical .....	13
Figure 2.3 – Schematic of a basic redox process .....	17
Figure 2.4 – Simple two electrode galvanic cell.....	20
Figure 2.5 – Simplified three electrode configuration .....	22
Figure 2.6 – Commercial Reference Electrode.....	26
Figure 2.7 – Electrode-Electrolyte Interface.....	29
Figure 2.8 – Simple Electrical Equivalent Circuit for Cell.....	30
Figure 2.9 – Potentiostat Schematic.....	32
Figure 2.10 – Basic Bulk Electrolysis Experiment Configuration .....	36
Figure 2.11 – Wall-jet configuration. ....	38
Figure 2.12 – Flow-over configuration.....	40
Figure 2.13 – Stopped-flow thin-layer schematic.....	41
Figure 2.14 – Example of linear sweep voltammetry .....	43
Figure 2.15 – Cyclic voltammogram voltage scan and Voltage vs. Current Plot.....	44
Figure 2.16 – Sample amperogram for a flowing sample.....	45
Figure 2.17 – OneTouch Glucose Home Diagnostic Kit.....	49



Figure 2.18 – Thin-layer cell created from Cu plate and PTFE spacers.....	51
Figure 2.19 – Schematic diagram of the electrochemical cell described by Lee et al.....	52
Figure 2.20 – Coulometric analysis of three reductases .....	53
Figure 2.21 – Macro thin-layer cell .....	54
Figure 2.22 – Diagrammatic exploded view of Tubular Thin-Layer Cell.....	55
Figure 2.23 – Oxidation current versus flow rate and total analyte conversion (%) .....	56
Figure 2.24 – Remote system for measuring phosphate in the field.....	57
Figure 2.25 – System schematic for remote sensing system .....	60
Figure 2.26 – Sample Cadmium and Lead data.....	61
Figure 2.27 – Microcontroller-based instrumentation configuration.....	61
Figure 2.28 – Microcontroller-based instrumentation .....	62
Figure 3.1 – Primary sensor layout.....	67
Figure 3.2 – Alternate Sensor designs .....	68
Figure 3.3 – Microfabrication process flow steps.....	69
Figure 3.4 – Full Si wafer photolithography mask .....	70
Figure 3.5 - Photolithography fiducial alignment markers and dicing streets.....	71
Figure 3.6 - Sensor Gasket Mask Design.....	73
Figure 3.7 – Schematic outlining Step 1 in the Pseudo-Reference Electrode conversion	74
Figure 3.8 – Schematic outlining Step 2 in the Pseudo-Reference Electrode conversion	75
Figure 3.9 - Simplified coulometric flow cell schematic.....	76
Figure 3.10 - Simplified flow cell schematic to account for reversible reactions .....	78
Figure 3.11 - Flow cell three-dimensional model/schematic diagram.....	81
Figure 3.12 - Bottom half of the thin-layer flow cell .....	82

Figure 3.13 – 3D model of the assembled Flow Cell. ....	85
Figure 3.14 – 3D visualization of the chip gasket compression prior to full assembly....	86
Figure 3.15 – Flow cell equivalent circuit. ....	88
Figure 3.16 – Simplified trans-impedance amplifier circuit.....	90
Figure 3.17 – Expanded Potentiostat Schematic showing feedback path.....	93
Figure 3.18 – Voltage regulation schematic .....	99
Figure 3.19 – Potentiostat schematic highlighting the <i>dummy cell</i> .....	102
Figure 3.20 – Exponential decay of oxidation/reduction current .....	110
Figure 4.1 – Flow cell solid model .....	116
Figure 4.2 – Front projected view of the top section of the flow cell.....	117
Figure 4.3 – Side projected view of the top section of the flow cell .....	118
Figure 4.4 – Top view of the bottom flow cell and thin membranes.....	119
Figure 4.5 – Isometric side view of the CFD model.....	120
Figure 4.6 – Zoomed in view of the interface between the inlet and the thin-layer cell	121
Figure 4.7 – CFD results - decreasing thin-layer cell height .....	122
Figure 4.8 – CFD results - increasing flow rate.....	124
Figure 4.9 – CFD results for increase in velocity .....	125
Figure 4.10 – Mesh convergence simulation .....	127
Figure 4.11 – CFD results for simulating the increase in back pressure .....	128
Figure 4.12 – Final flow cell used in this study .....	129
Figure 4.13 – Bottom of the top of the third generation flow cell .....	130
Figure 4.14 – Manually tapping inlet/outlet ports and screw holes.....	131
Figure 4.16 – Extremely thin (~ 100 um) chip gasket layer .....	133

Figure 4.15 – Upper gasket layer created using a laser cutter. ....	133
Figure 4.17 – Paper-based chemi-selective membrane.....	134
Figure 4.18 – Fully assembled prototype flow cell.....	136
Figure 4.19 – Pressure data over three weeks in an assembled flow cell .....	137
Figure 4.20 – Pressure data separated into different days .....	139
Figure 4.21 – Two versions of the microfabricated sensor electrode .....	140
Figure 4.22 – Full wafer of sensors showing liftoff of metal .....	141
Figure 4.23 – Large surface area electrode profilometry test results.....	142
Figure 4.24 – Post processing photographs of the Ag AgCl pseudo-electrodes.....	143
Figure 4.25 – Magnified view (4x) of a Ag AgCl pseudo-reference .....	144
Figure 4.26 – Final schematic of the custom potentiostat .....	146
Figure 4.27 – Silkscreen image of the final printed circuit board design layout. ....	147
Figure 4.28 – Final populated board containing the potentiostat circuit .....	148
Figure 4.29 – Custom potentiostat with leads.....	149
Figure 4.30 – Data showing the stability of the system to a pulse input .....	151
Figure 4.31 – Image showing the repair of enable pin connection.....	152
Figure 4.32 – Percent error between current measuring techniques .....	154
Figure 4.33 – Plot of 10kOhm gain stage setting.....	155
Figure 4.34 – Plot of 1MOhm gain stage setting .....	156
Figure 4.35 – Plot of 1MOhm gain stage setting (picoamps).....	157
Figure 4.36 – Plot of 100MOhm gain stage setting .....	158
Figure 4.37 – Frequency response plot of the transimpedance amplifier circuit.....	160
Figure 4.38 – Fast scan of a resistor/capacitor parallel pair .....	162

Figure 4.39 – Software user interface for controlling the coulometry experiments .....	163
Figure 4.40 – 100 mV/sec CV scan with dummy cell .....	164
Figure 4.41 – Web interface to allow remote control of the software .....	165
Figure 4.42 – Pseudo Reference Electrode Current Monitoring Program .....	166
Figure 4.43 – First major coulometric data processing program .....	168
Figure 4.44 – Data interrogation software .....	169
Figure 4.45 – Cyclic voltammetry experiment .....	171
Figure 4.46 – Repeated reduction/oxidation experiment .....	172
Figure 4.17 – Amperogram displaying 80 seconds of current .....	174
Figure 4.48 – Coulometric analysis long after electrolysis is done .....	175
Figure 4.49 – Plot showing linear response of system .....	176
Figure 4.50 – Integrated coulometric signals for four concentrations .....	178
Figure 4.51 – Plots comparing the performance to theoretical equations .....	180
Figure 4.52 – Plots comparing the performance of the custom potentiostat and commercial electrochemical system. ....	182
Figure 4.53 – Head to head coulometric data for the custom potentiostat and commercial detector .....	183
Figure 4.54 – The first ten seconds of a coulometric analysis .....	184
Figure 4.55 – Second generation flow cell solid model .....	185
Figure 4.56 – Second generation electrochemical sensor .....	185
Figure 4.57 – Second flow cell prior to assembly .....	187
Figure 4.58 – All parts needed for assembly of the second generation flow cell .....	187
Figure 4.59 – Glass spacer installed in the flow cell (viewed from the bottom) .....	188
Figure 4.60 – Flow visualization of particles still moving after injection of sample .....	189
Figure 4.61 – Valves added to inlet and outlet of all channels .....	191

Figure 4.62 –Plot with valves open.....	192
Figure 4.63 –Plot with valves closed .....	193

## LIST OF EQUATIONS

EQUATIONS	PAGE
Equation 1.1 – Faraday’s First Law of Electrolysis.....	4
Equation 1.2 – Concentration Relationship for Faraday’s First Law .....	4
Equation 1.3 – Redox Equation for Ferri/FerroCyanide.....	6
Equation 2.1 – Hydrogen Oxidation .....	18
Equation 2.2 – Hydrogen Reduction to form Water .....	18
Equation 2.3 – Determination of Half-Cell Potential .....	20
Equation 2.4 – Theoretical Exponential Decay of Current.....	30
Equation 2.5 – Nernst-Planck Equation.....	34
Equation 2.6 – Theoretical Analyte Concentration Profile.....	35
Equation 2.7 – Diffusion Length Equation .....	35
Equation 2.8 – Poisson’s Momentum Equation Criterion .....	37
Equation 2.9 – Poisson’s Momentum Equation.....	37
Equation 2.10 – Theoretical Coulometric Current Decay .....	46
Equation 2.11 – Theoretical Concentration Gradient .....	46
Equation 2.12 – Theoretical Charge Transfer With Respect to Time.....	46
Equation 2.13 – Cottrell Equation .....	47
Equation 2.14 – Anson Equation .....	47
Equation 3.1 – Calculation of Theoretical Die per Wafter .....	70

Equation 3.2 – Volume of Cell .....	72
Equation 3.3 – Silver Reduction .....	73
Equation 3.4 – Chloridization Process .....	73
Equation 3.5 – Hagen-Poiseuille Relationship .....	79
Equation 3.6 – Reynolds Number Calculation for Channels of Circular Cross Section ..	79
Equation 3.7 – Simplified Momentum Balance Equation .....	80
Equation 3.8 – Transimpedance Amplifier Output Relationship.....	90
Equation 3.9 – Differential Amplifier Current Conversion .....	95
Equation 3.10 – Thin-Layer Critical Dimension Equation.....	109
Equation 4.1 – Low-Pass Filter Cutoff Equation.....	159

# CHAPTER I

## INTRODUCTION

Electroanalytical chemistry, more specifically electrochemical detection (ECD), has become a popular quantitative detection technique primarily due to the lower costs associated with its implementation [1], particularly when directly compared to other popular detection methodologies such as atomic absorption spectroscopy (AAS) and inductively-coupled plasma mass spectrometry (ICP-MS). Also, the detection limits associated with ECD are as good, if not better than, AAS and ICP-MS [2-4]. The specificity of ECD is limited to electroactive analytes (oxidizable or reducible), and while this is a notable limitation when compared to other analytical techniques, the physical footprint of the instrumentation required to implement an ECD system is drastically smaller, and therefore adaptable to unique and custom deployments [5]. Comparatively, the equipment required to perform optical detection techniques such as laser induced fluorescence (LIF) makes miniaturization of these alternative analytical systems impractical. The reduction in size provided by miniaturization of the associated ECD components including the accompanying flow components also generally reduces the consumption of both the analyte and reagents and decreases analysis time. Additionally, the electronics required to establish potentials and measure the reaction currents in an ECD system are relatively straightforward.



There are several sub-variations of ECD, most notably amperometry, voltammetry, and coulometry; in each of these sub-techniques, a sample is analyzed by measuring the electrical response (either the change in current or voltage) in an electrochemical cell containing the analyte under study [6]. Bulk electrolysis refers to analyses that are performed in a fixed volume. However, there are several variations of dynamic flow techniques including flow-through, flow-over, and stopped-flow situations where “flow” describes travel of the analyte stream and stands in stark contrast to bulk analysis. Regardless of the flow specifics, all required electrodes in dynamic analyses are situated inside the flow stream and are exposed directly to the analyte. The current or voltage at these electrodes is either recorded or controlled, depending on the type of experiment. Analysis of the chemical reaction is performed by inspecting the magnitude and/ or duration of the signals recorded, again depending on the specific type of electrochemical analysis. Thus, in its simplest form, the experiment requires a high-fidelity recording of the electrical signals generated by a well-controlled chemical reaction.

Using ECD as an *in-the-field* analytical technique, particularly when recording signals or repeatedly performing experiments over long periods of time, requires periodic calibration against well-known and available standards to confirm accuracy of the measurement. Calibration is performed in virtually every measurement technique both to ensure that the analytical equipment is functioning properly, and to mitigate the influence of experimental anomalies unrelated to the analysis being performed that might interfere with the measurement signal. Beyond the confines of a well-controlled lab environment, sensor dependability can diminish over time through fouling from environmental interferences, consumption of the active materials that are part of the sensor, or drifting of

the sensor response due to temperature variations and extended-use hysteretic effects. Confidence in measurement results can be critical in cases where detection events are used as an emergency condition that triggers some other, more involved investigation or response.

One ECD concept in particular, *exhaustive coulometry*, has the potential to eliminate this calibration requirement for long-term in the field electrochemical analysis. This *calibration free* technique requires a finite, precisely controlled reaction volume. Typically, as in many ECD experiments, the current generated during an oxidative or reductive process is recorded over time, producing what is referred to as a chronoamperogram (Figure 1.1).

As the electrode reaction goes to completion, the reactants are exhausted and the current being measured decays to zero (ideally), or back to background current levels

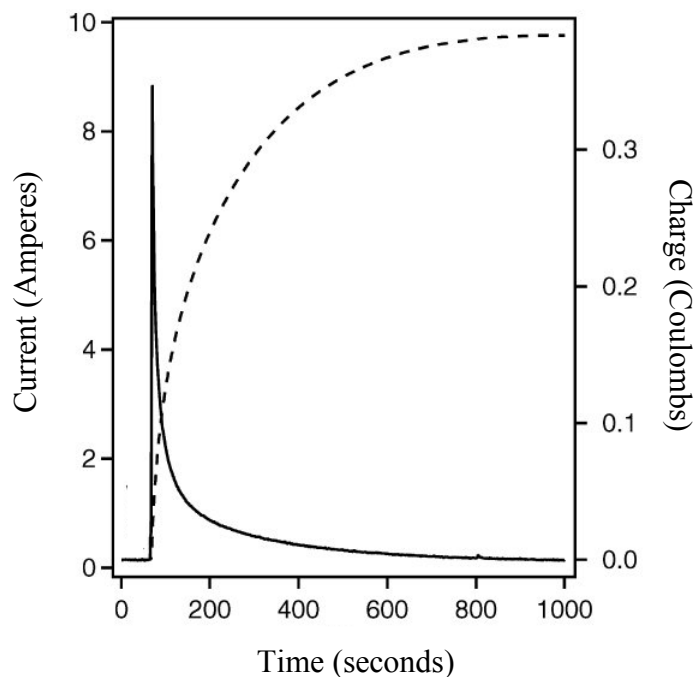


Figure 1.1 – Sample reaction current vs. time chronoamperogram (Left Y-axis; solid line) and integrated reaction current (right Y-axis; dotted line). Adapted from [7]

(practically). By numerically integrating the magnitude of the current signal (measured in amperes), the concentration of the analyte can be determined since the area under the curve of this plot is the total charge generated. The total charge is determined by Faraday's first law of electrolysis, represented by the equation

$$Q = n \cdot F \cdot N \quad \text{Equation 1.1}$$

where  $Q$  is the total charge generated by a reaction (coulombs),  $n$  is the number of electrons transferred per mole of analyte,  $F$  is Faraday's constant, and  $N$  is the moles of analyte in the sample (moles). Since  $N$  by definition can be obtained by multiplying the concentration of analyte by the volume of the sample, and the total charge transferred can be obtained directly from the data, Equation 1.1 can be rewritten, solving for concentration, and expressed as

$$c = \frac{Q}{n \cdot F \cdot V} \quad \text{Equation 1.2}$$

where  $c$  is concentration and  $V$  is volume. By controlling all the terms in this equation (most notably, by design of the experimental setup, volume),  $c$  can be determined *absolutely*.

Perhaps the best characteristic is that, in principle, coulometry is more tolerant of electrode fouling and temperature variations. Over time, as the active area of the electrodes become altered due to contamination or fouling, or when the reaction conditions cause the electrode to disintegrate over time due to repeated use, the total charge recorded (the integrated reaction current signal) should stay the same. While the experiment may take longer as these problems arise, the total charge measured should be the same, and therefore a calibration free analysis could be realized. Finally, this

robustness promotes reusability and suggests repeatability over hundreds of analytical determinations.

## 1.1 Purpose of Study

The overall goal of this collaborative project is *to evaluate the feasibility of exhaustive coulometry as a viable calibration free analytical technique*. The studies presented in this work focus (1) on the design and fabrication of the electrochemical detection cell prototype using Finite Element Analysis, computer-aided design tools, computer controlled machining processes, and flow visualization, and (2) the control of the associated electrochemical experiments with both commercially available equipment and a custom designed control system. In conjunction with our work, our chemistry collaborators will utilize this system to perform exhaustive coulometry experiments on a range of analyte concentrations. A secondary goal of this work is *to design and fabricate a custom analysis and control system* in order to support the electrochemical cell prototype and to promote an autonomous system suitable for remote deployment. This will be done by creating a compact potentiostat with control software modeled after a commercially available, benchtop-scale laboratory system.

## 1.2 Specific Aims

The specific aims for this project are:

**Specific Aim 1:** *To design and construct an electrochemical cell that contains and isolates the microfabricated electrode platform inside a specific, repeatable volume of analyte*. This cell will also provide a manifold system to establish inlet and outlet flow for the analyte and waste fluids, respectively. The electrochemical cell will be designed

using commercially available solid-modeling software and fabricated using precision, computer controlled machining techniques.

**Specific Aim 2:** *To design and fabricate a custom potentiostat sufficiently compact to allow for remote deployment.* The custom potentiostat will operate under battery power, consider the necessity of low-noise, high-precision measurements, and allow for the determination of several ranges of analyte concentration magnitudes via adjustable gain settings.

**Specific Aim 3:** *To design and program a control interface that manages and establishes parameter settings for multiple analysis types including amperometry and cyclic voltammetry.* The control interface will be designed in LabVIEW and provide the user control over the specific settings required for each type of experiment, establish precise timing and switching configurations, and provide visualization, archiving and post-processing for the data generated.

**Specific Aim 4:** *To combine and validate all components of the system in a working prototype that enables coulometric determination of specific electrochemical species.* The sample analyte *ferricyanide* (hexacyanoferrate(III)) will be used as a model to test the system. This anion is reversibly converted to the *ferrocyanide* ion via the reductive process described by Equation 1.3.



Several concentrations of this analyte will be tested to evaluate the performance of the complete system. Finally, the results will be validated against theory and compared to a commercial electrochemical detector.

### 1.3 Significance of the Study

In this project, a stopped-flow electrochemical cell with a well-defined volume will be fabricated. Inside this device, a microfabricated electrode platform with integrated working and reference electrodes will interrogate a chemical sample with the aid of a custom potentiostat that contains the necessary circuit components and appropriate electrical connections. A custom control interface with supporting algorithms will be developed to provide a remotely operated, programmable, continuous, calibration-free monitoring system.

This project aims to mitigate the shortcomings of existing electrochemical analysis techniques by developing a true *calibration-free* analytical measurement prototype that exploits Faraday's law of electrolysis by performing *exhaustive coulometry*. Incorporation of a small analysis volume will allow rapid and repeatable quantitative determination of analyte concentration. To date, calibration-free, remote sensing systems for continuous environmental monitoring have not been reported.

## CHAPTER II

### BACKGROUND

This chapter presents a survey of the advancements in prototyping and manufacturing technologies that were used in this project, including desktop design techniques and microfabrication technologies that are directly impacting developments in the field of analytical chemistry. Additionally, the fundamentals behind variations of electrochemical detection (ECD) will be explored. Finally, current research in electrochemical systems will be examined to demonstrate the relevance of the calibration-free, electrochemical detection system that was developed in this study.

#### 2.1 Microtechnology and Microfluidics

Since the birth of the integrated circuit in 1959 and the first silicon and gallium arsenide integrated circuits (IC) that utilized this discovery [8], modern IC's have evolved to contain close to a billion discrete components [9]. The near linear, every-two-year doubling of the number of transistors on an IC design, referred to as Moore's Law, is, as of this writing, 47 years old [10]. The turn of the century has added another direction of development, the so-called System-on-Chip (SoC), which takes advantage of the increase in density and complexity of the circuits, and integrates many different types of IC's (processor, memory, graphics, etc.) onto a single platform [11]. This type of chip, and this conceptual train of thought where multiple disparate systems are included on a

single platform, has led the way for an explosion in embedded systems and has influenced a rapid and wide ranging evolution in dozens of industrial, environmental, and biomedical industries.

### 2.1.1 Microtechnology

Coincidentally, also in 1959, Dr. Richard Feynman, gave a lecture that would forecast the discovery, development, and eventual maturation of micro-electro-mechanical-systems (MEMS) and nanotechnology [12]. His insightful comment that “there’s plenty of room at the bottom” alluded to the ability to manipulate individual atoms to create unique structures and devices and is generally associated with the birth of nanotechnology. MEMS can be seen as a direct descendent of the IC revolution, as MEMS technologies borrowed many of the fabrication methodologies developed to enhance the capabilities of IC designers. As early as 1967, Nathanson et al. used surface micromachining to create what is essentially a miniature tuning fork in silicon [13]. In 1970, Kulite, the company that gave the world the first bare silicon strain gauges circa 1959 (it was an important year), developed the first micromachined accelerometer [14]. These early developments gave birth in the late 80’s and early 90’s to miniaturization of not just electrical components buried within small slivers of silicon, but fully functional mechanical components that were smaller, faster, accurate, highly reproducible and when made in bulk, due to parallel processing, could be made more cheaply compared to previous generations of the same devices. Publications describing micro-miniaturized cars [15], internal combustion engines [16], even thermal actuators used to drive sophisticated stepper motors were developed to show the possibilities of this burgeoning technology [17]. New sensors deployable in any environment imaginable were



developed, often with integrated instrumentation and temperature compensation schemes, drastically reduced from previous generations, all without sacrificing the accuracy or reliability of the larger, traditionally manufactured versions [18]. In fact, MEMS-based pressure sensors, accelerometers, and temperature sensors are being used in nearly every vehicle sold since the late 1990's.

### 2.1.2 Microfluidics

A companion to the evolution of MEMS was the development of miniaturized fluidic components and systems, called *microfluidics*, where the scale of fluidic channels is reduced down to microns (and below) [19]. The same (or adapted) fabrication techniques used to create MEMS components were used to create drastically smaller flow channels and chambers, where sample volumes are reduced to microliters, nanoliters, picoliters, and femtoliters. While flow is still often initiated actively through the use of pumps, the reduction in scale promotes the movement of a sample and media with far lower power requirements, such as the natural phenomenon of capillary action, which is negligible at the macro-scale [20].

Mentioned in book form as early as 1996 [21], the role miniaturization would play in the development of analytical chemistry instrumentation was extensively explored by Manz, et al. in 2001 [22]. As this sub-category evolved, the concept of the *Lab-on-a-Chip (LOC)* and *μTAS* (micro Total Analysis Systems) was proposed and developed. These conceptual platforms seek to combine all the elements of a chemical process (sampling, sample injection, sample pretreatment, mixing, reacting, detection, etc.) on a single platform. Major advantages of LOC and μTAS platforms are faster analysis times, smaller sample and reagent consumption, higher efficiency, and ease of use [23-26]. As a

result, there has been an explosion in recent years of new micro analytical tools with analytical chemistry applications in the areas of environmental monitoring [27, 28] and healthcare and point-of-care diagnostics [29, 30].

## 2.2 Modern Analytical Chemistry

One of the industries to reap the rewards from this manufacturing revolution would be analytical chemistry, and it can be argued that, in the past 25 to 30 years of research in the area of analytical chemistry, the greatest advancements have been due to refinements in existing analytical methods, as opposed to the invention or discovery of new techniques [31]. Early qualitative analyses, what are now referred to as the “classical methods”, are generally performed as qualitative tests: for example, the test used to indicate the presence of blood (the Kastle-Meyer test that uses reduced phenolphthalein [32]) or the acid test to verify whether or not gold is present in a particular sample [33]. While many of these simple tests are still in use today and can be seen as the building blocks of the more modern analytical methods, they have been largely overshadowed by highly sophisticated, computer-controlled, quantitative techniques.

The rapid evolution of existing detection techniques has come in the form of improvements in the design of the analytical equipment resulting in enhanced sensitivity, response to a wider range of analytes, marked improvements in reliability, decreased system costs, etc. General technological improvements have promoted miniaturization of entire systems; and from a practical standpoint, this latter development has many benefits, including the obvious reduction in both reagents needed and sample used to perform experiments. Experiment time can be a common limitation with traditional detection techniques; for example, a typical gas chromatography experiment can take 5 to

10 minutes to complete [34, 35]. Reductions in the scale of the experimental platform (column lengths, cross-section, volumes, etc.) also offer an associated reduction in time.

Unfortunately, while the analytical techniques behind the machines have been enhanced by improvements in the design of the equipment, device complexity has remained high, a factor affecting absolute minimum costs for equipment, elevated repair and maintenance costs, and lack of true portability. Figure 2.1 shows the size of typical bench top sized, generic gas chromatograph (GC) capable of analyzing any volatile sample. When the various parts of a large analytical system become more closely



Figure 2.1 - Benchtop Gas Chromatograph (public domain image)

integrated, equipment costs can be greatly reduced, allowing for more widespread application of analytical techniques typically tied to laboratory use.

As a result, bench-top scale systems are slowly being reduced in size and moving from the lab to the field. Figure 2.2 includes an image of the 3000 Micro GC portable, MEMS-based, field-deployable gas chromatograph from Infinicon Petrochemical [36]. These miniaturized systems claim to have a 10x sensitivity compared to traditional systems and include all carrier gases and batteries internally for remote use. This comes at a cost, however, since these devices are constructed in application specific configurations limited to a narrow range of analytes.



Figure 2.2 – Micro GC 3000 from Infinicon Petrochemical

### 2.3 Analytical Instrumental Methods of Detection

The most powerful analytical techniques involve some form of transport of a sample, in many cases for the purpose of separating a mixture of analytes, and there is a wide variety of analytical detection techniques associated with the various separation technologies. The previous figures highlight one of these separation techniques (gas

chromatography), but there are others including liquid chromatography and electrophoresis that are designed to accept a sample mixture at one end of some form of column or separation medium, and then produce a separated sample at the other. While these separation techniques are not the object of this study, mated to each analytical separation methodology is some form of detector, where one or more physical, chemical, optical, or electrical property of a sample is exploited to gain insight into the contents of the sample at hand.

Some of these detection methods are associated with simple optical absorption, such as volumetric titrations involving a sample changing color after reaching a certain pH [37]. Another commonly utilized detection technique is laser induced fluorescence (LIF) where a sample either natively, or after specialized treatment, is excited with a laser or specialized narrow band optical light source and is detected via the resulting fluorescence [38]. Separation techniques such as capillary and gel electrophoresis often utilize LIF [39, 40]. DNA analysis in particular has benefitted from adapting this technique in miniaturized microfluidic devices [41]. More recently, Mainz et al. used a LIF detection technique to determine the concentration of nitrous oxide (NO) on a microfluidic platform [42]. This study quantified NO production in control and externally stimulated Jurkat cells, whose subsequently lysed cell contents were sent through the microchip capillary electrophoresis device. While these studies are promising, ultimately, optical techniques are complicated by sophisticated lensing systems and light sources, and complicated procedures are often necessary to complex the sample with a fluorescent label. Alternatively, many analytical samples respond to a simple excitation with an external voltage or current stimulus, and this response establishes a method of detection

that harnesses the electrochemical properties of samples for detection and analysis purposes.

## 2.4 Electrochemical Detection

Electrochemically based analytical methods have garnered increased attention due to both the lower costs associated with the simplicity of the instrumentation required to carry out the associated techniques, but also due to the flexibility and adaptability regarding the physical size of the detection system. This combination of attributes suggests a system ripe for widespread deployment, allowing for autonomous or remotely operated, in-the-field analysis.

One of the disadvantages of this type of analysis is the requirement that a sample be electroactive - i.e., it can be oxidized or reduced: However, this limitation can be mitigated by either functionalizing the electrodes directly or complexing the sample under study with an electrochemical mediator to enhance or facilitate the electron transfer process. The review paper by Kahlert contains an extensive description of types of carbon electrode functionalization via chemical modification, covalent bonding, physical adsorption, and film formation, specifically for creating pH-sensitive carbon electrodes used in electrochemical measurements [43]. Eremenko et al. have shown that manganese dioxide nanostructures can serve as a mediator for the electrochemical detection of thiols [44]. Additionally, it should be noted that specificity of detection as related to mixtures of analytes can limit the effectiveness of electrochemical techniques. When several electroactive species are present in a detection chamber, all will react if the necessary energy (voltage) is present to initiate the reaction. However, there are several adaptive

methods that can be used to get around this limitation, and these will be explored in a following section.

#### 2.4.1 Principles of Electrochemistry

The fundamental physics behind the electrochemical techniques can be attributed collectively to the discoveries of many early scientists in the 1800's such as William Gilbert (magnetism), von Guericke (static electricity), de Coulomb (electrostatics), Galvani ("animal electricity"), Nicholson/Ritter (electrolysis of water, thermoelectric currents), Seebeck (thermoelectricity), Wollaston (the galvanic cell), and Davy (electrolytic cells) [45]. With the invention of the electrovoltaic cell in the late 1800's, the turn of the century brought the founding of the Electrochemical Society in 1902. Perhaps the most original and definitive work related to electrochemistry are the coincidental publications by Bronsted and Lowry regarding a theory behind acids and bases and their behavior in 1923 [37]. The first major development that harnessed the charge state of dissolved species to separate proteins, was a device reported by was reported by Tiselius in 1937, and he was awarded the Nobel Prize for his electrophoresis work in 1948 [46]. In 1949, the International Society of Electrochemistry was founded.

Regarding *quantitative* electrochemistry, the 1959 Nobel Prize in Chemistry was awarded to Jaroslav Heyrovsky who developed a technique that used a mercury electrode to promote the reduction of organic molecules. His experiments in polarography indicated that the measured reduction current was a quantitative representation of the concentration of the analyte. Additionally, he noted that the shape of the current recorded when compared to the applied potential was indicative of the analyte under study [47].

These first bold steps laid the foundation for electrochemistry as a primary detection technology.

#### 2.4.1.1 Redox Reactions

At the heart of any electrochemical process is the *redox* reaction, which is a portmanteau of the companion processes, reduction and oxidation. As visualized in Figure 2.3, each of these involves the transfer of electrons to (reduction) or from (oxidation) a molecule or ion. These processes change the *oxidation state* of the species in question and can be initiated by the application of an external voltage, which is essentially the application of an amount of energy sufficient to make the reaction happen spontaneously. Chemical energy can also initiate oxidative and reductive processes, but in this discussion, we will limit our scope to the electrical activation of redox reactions.

As a brief review, fundamentally, redox reactions are made possible due to the presence of electrons in the outermost shell of an ion or molecule. This previously mentioned *oxidation state* is a hypothetical representation of the resting charge possessed by an atom or ion. It is generally explained that if an analyte donates an electron to

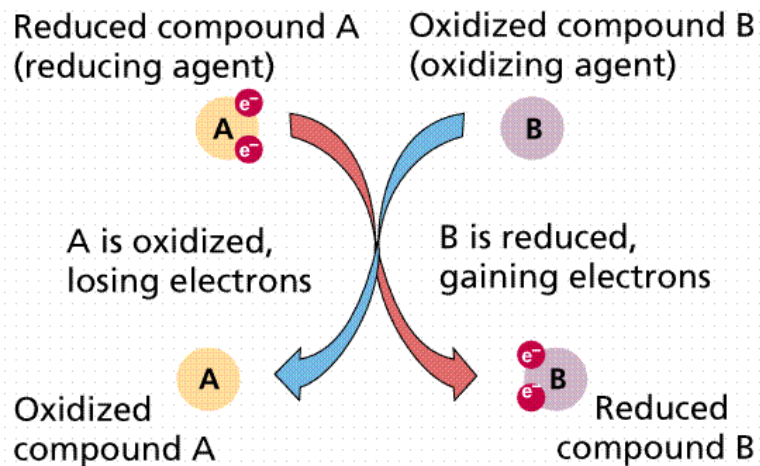


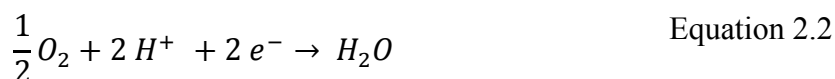
Figure 2.3 - Schematic of a basic redox process



another ion or molecule, it has undergone an oxidation state increase, while the acceptor has undergone an oxidation state decrease. A redox reaction is a coupled process in which a reduction is always accompanied by an oxidation. Either the oxidation or reduction by itself is a “half-reaction” or collectively, the combination constitute a complete redox reaction. Equation 2.1 represents perhaps the simplest oxidation, where a molecule of hydrogen releases its electrons in the process defined by



where  $H_2$  represents a molecule of hydrogen, the superscript “+” indicates a positive charge, and the lowercase “e” represents an electron that is negatively charged, as indicated by the superscript “-“. Equation 2.2 shows a companion reduction process, in this case where oxygen accepts the two electrons provided by the hydrogen oxidation and then combines with the  $H^+$  ion to form water.



By knowing the analyte electron configurations as well as the oxidation state as related to their ionic concentrations at any particular pH, and the necessary energy levels to initiate the oxidation or reduction, the electron transfer process can be measured. The electron(s) liberated in this process are directly exploited in electrochemistry. Due to several factors including, but not limited to, background redox processes and electrical noise in the supporting circuitry, there is a theoretical sensitivity limit to this type of detection, with some electrochemical methods generating only qualitative results [cyclic voltammetry (CV) for example]. However, measuring the expected electron transfer can

be a quantitative process, and the following sections outline the details behind how this is accomplished.

#### 2.4.1.2 The Electrochemical Cell

In electrochemistry, the *electrochemical cell*, herein referred to simply as the cell, describes both the volume that contains the sample and the particular configuration of detection electrodes. During his pivotal research on electrical decomposition of materials in the early 1800's, Michael Faraday coined the name electrode from the Greek words for “amber” (elektron) and “a way” (hodos) [48]. While there is an entire industry dedicated to studying the subject, briefly stated, an electrode is an electron conductor that is used to interface with non-metallic media such as an electrolyte [6]. Fundamentally, electrochemistry seeks to explore the various mechanisms that modulate the transport of charge at the interface between the electrode and electrolyte, where charge is transported in the electrolyte via ions, and in the electrode material via electrons. The interface between the electrode and the electrolyte is where the electron exchange happens and this region will be examined in the next section.

##### 2.4.1.2.1 Electrochemical Electrodes

An electrochemical cell is typically implemented using either a two or three electrode configuration. The two electrode configuration is shown in Figure 2.4, with a single cathode (where reduction occurs) and a single anode (where oxidation occurs). This type of cell is typically used in galvanic electrochemical cells (batteries) and electrochemical cells where the working electrode potential is not or does not need to be monitored (electroplating, for example).

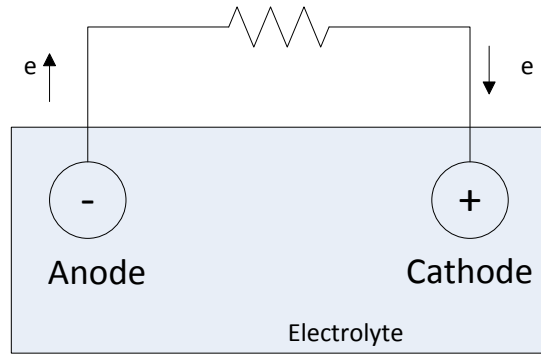


Figure 2.4 – Simple two electrode galvanic cell where current is controlled by an external resistor. Oxidation occurs at the anode; reduction happens at the cathode.

In this configuration, there is an open-circuit potential that exists if the voltage is measured between the two electrodes. This potential, also called the standard cell potential or the electromotive force ( $E^{\circ}$ ), is established by the two half reactions occurring at each electrode, each of which describe the chemical/electrical exchange occurring at the interface. Since each half reaction responds to the potential difference at each electrode differently, a potential gradient is established between the electrodes. For example, a standard Hydrogen electrode half-cell potential is 0.0 V as measured with a platinum plate acting as the anode, while a corresponding cathode potential, a Silver Chloride half-cell potential in the same electrolyte solution is +0.2223 V. The overall resting half-cell potential is given by

$$E^{\circ} = E_{\text{cathode}} - E_{\text{anode}} \quad \text{Equation 2.3}$$

and is, in this case, equal to the cathode half-cell potential. In general, a positive standard cell potential implies that the full redox reaction is favorable (thermodynamically) and will proceed spontaneously. The best example of this situation is a battery, which will provide external power when a load is placed across the anode and cathode. The current

that flows can be used to do useful work via the natural flow of electrons through the completed circuit; this will continue to do so until the internal voltage drop is reduced due to the redox reaction proceeding towards a lower resting potential. For example, in a rechargeable lead acid battery, lead is converted to lead (ii) sulfate at the (cathode) and lead (iv) oxide is converted to lead (ii) sulfate. As this process proceeds towards completion (mostly lead (ii) sulfate remaining), the resting potential is reduced and the battery is seen as being “dead.” Recharging the battery essentially reverses the process, with lead (ii) sulfate being converted back to lead and lead (iv) oxide, and the battery is restored to its former, energy providing state. The efficiency of this process does diminish over time, as the integrity of the electrodes is compromised by some degree with each cycle [49].

Negative standard cell potentials, on the other hand, imply that the electrochemical reaction requires the application of external energy to proceed. The three electrode configuration arises from the necessity that this energy, an externally applied potential, needs to be tightly controlled or monitored. The basic three electrode configuration in an electrochemical cell, depicted in Figure 2.5, includes the working, reference, and counter (or auxiliary) electrode. Only two of the three electrodes in this configuration, namely the working and counter electrodes, actually participate actively in the redox reaction.

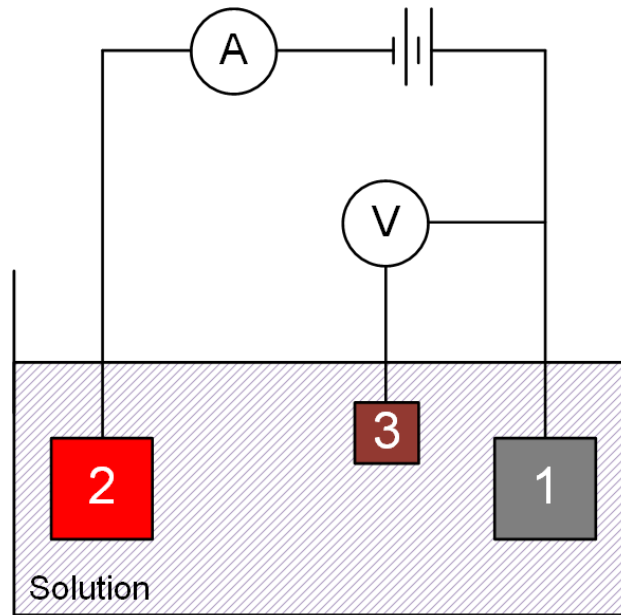


Figure 2.5 - Simplified three electrode configuration showing the working electrode (1), reference electrode (2), and counter electrode (3)

As in the two electrode configuration, all electrodes are in direct contact with the sample, typically an electrolytic buffer containing the sample under interrogation.

The working electrode is where the reaction of interest in the redox couple occurs and all of the reaction kinetics, mass transfer, physical chemistry, and electrode size and material properties associated with this electrode and the electrolyte are of primary concern. The importance of each of these parameters will be addressed in following sections. Simply stated, the working electrode establishes the potential that enables the redox reaction and provides the charge (electrons) as required by the reaction kinetics [34]. The complimentary reaction occurs at the counter electrode and while this reaction is secondary and typically ignored, the reaction current at the working electrode is balanced by an equal and opposite current at the counter electrode. In the supporting electronics configuration, the reaction current is measured through the counter electrode

(block 3 in Figure 2.5). Each electrode participates in half of the full redox equation. Depending on whether the externally applied potential is driving a reduction (negative voltage applied) or oxidation (positive voltage applied) at the working electrode, the working and counter electrodes can either act as the cathode or anode.

To maintain the necessary energy level required to drive the redox reaction, it is imperative to hold the reaction potential constant at the working electrode. Since the collective impedance through the electrolytic solution is constantly changing as reactions occur, this is difficult to do while current is flowing. The reference electrode is included in the circuit to passively monitor the potential applied to the working electrode and, via feedback to the potentiostat circuit, hold the reaction potential constant. The reference electrode is typically a high impedance electrical path and ideally passes no current, and therefore, does not alter or participate in the redox reaction. The details of the types of reference electrodes used and potentiostat circuitry and will be outlined in a later section.

#### 2.4.1.2.2 Electrode Materials

The types of metals that are used as electrodes typically are associated with their stability, i.e. low-activity, inert metals that act as good oxidizing agents. Unstable metals and associated compounds containing these metals typically lose electrons easily and are therefore considered more active, and therefore are generally good reducing agents. The term agent is used because it is not the electrode that is oxidizing or reducing, but rather assisting in the process, or acting as an agent to facilitate the process. Table 2.1 contains a brief list of commonly used metallic electrode materials listed in general order of stability. Inert carbon materials are also used as electrodes, for example, glassy and pyrolytic carbon [50]. The type of material that is actually chosen depends on the size


needed, cost, reusability, durability, and the effective potential window. This latter term refers to the range of voltages applied to the electrode material that are effective in causing the desired oxidation or reduction. At the extremes of this range, the applied voltage self-oxidizes or self-reduces the material, often compromising the integrity of the electrode. Some of the inert metals and metal complexes, mainly electrodes made using mercury, have a toxicity factor that also must be considered. One advantage that will be harnessed in this work is that most of the inert metals used in electrochemistry are easily microfabricated which allows for custom, high-precision electrode designs.

Table 2.1

Abbreviated list of metallic electrode materials and their half-cell potentials

Metal	Half Cell Potential (vs. SHE)
Gold (Au)	+1.680 V
Platinum (Pt)	+1.188 V
Silver (Ag)	+0.799 V
Copper (Cu)	+0.340 V
Mercury (Hg)	+0.268 V
Iron (Fe)	-0.409 V
Titanium (Ti)	-1.63 V
Sodium (Na)	-2.71 V
Lithium (Li)	-3.05 V

Stable Metal



Unstable Metal

Platinum has a high electrochemical inertness and is easily fabricated, however hydrogen ions spontaneously reduce at the surface and generate hydrogen gas which can lead to a large background electrochemical signal, especially at acidic pH levels [51]. Similar to platinum, gold is inert and easily fabricated, but is generally only used in reductions since positive potentials will induce oxidation of the surface, which diminishes the effectiveness of the material as a redox agent. So called modified working electrodes typically have a gold substrate to which some form of functionalized species are complexed [52].

Since the stable metals, also referred to as inert metals, do not generally donate electrons (or take up electrons) in the redox process, instead, the electrons are provided by, or removed by, the electronics. For the purposes of promoting a tightly controlled oxidation or reduction, the electrode material concerns mainly are associated with the working electrode only. In general, the counter electrode material is not as critical, since the reaction at that surface is secondary to the one occurring at the working electrode. Size of the counter electrode, however, is important to a certain degree, and this will be outlined in the next section.

#### 2.4.1.2.3 The Reference Electrode

The reference electrode material has an important role in the cell configuration, since the type of reference electrode used will influence the applied required oxidation or reduction potential. The half-cell potentials reported for any working electrode material type are typically reported “with respect to” the reference electrode used. This is due to the natural resting half-cell potential that will be established when this electrode is placed into the same electrolyte as the working and counter electrode and the additional



*uncompensated resistance*,  $R_u$ , that arises from the unavoidable spatial separation between the reference and working electrodes. This phenomenon is typically accounted for by slightly adjusting the applied potential in an experiment to compensate.

Electrically, the impedance of this electrode is much higher than that of the fluidic cell (typically 1 Mohm; much greater with supporting electronics) so none of the resulting oxidation current will be either provided by or consumed via this electrode. Reference electrodes are divided into two general subclasses of *real* versus *pseudo*, where real refers to a reference electrode constructed such that its composition is absolutely stable, meaning that the electrode half-cell potential is fixed, regardless of the surrounding conditions. A typical commercially available Ag|AgCl reference electrode is shown in Figure 2.6. Because these electrodes use a built-in redox *system*, including an isolated chamber of electrolyte to eliminate diffusion of redox products to the surface of the reference electrode, their use in miniaturized systems can be problematic, and

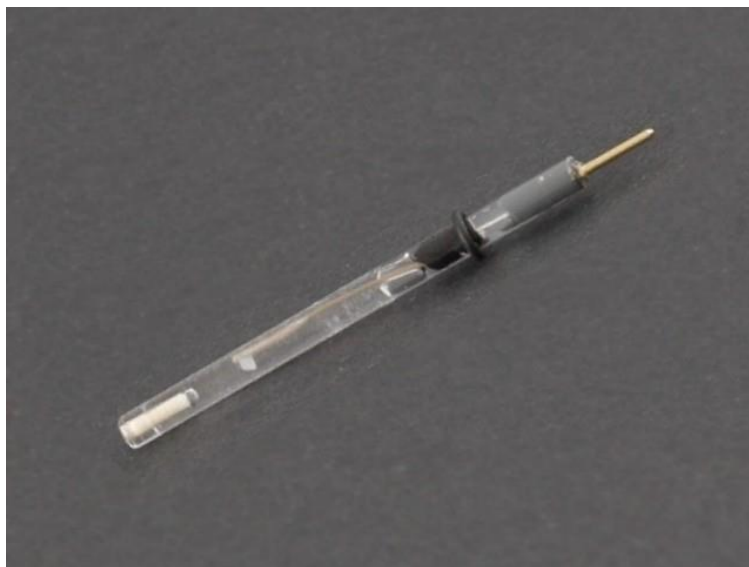


Figure 2.6 – Commercial Reference Electrode

research in this area is active. Pedrotti et al. investigated a mini-reference electrode using microporous polyethylene as the restrictive flow junction [53].

So-called *pseudo-reference electrodes* are also used since these types of electrodes overcome the spatial limitation of the true reference electrodes, albeit with some deficiencies. While these (typically) thin-film electrodes can be easily fabricated *in situ*, and typically at the same dimensions and location of the working electrode in a cell, these electrodes are not as robust as their larger counterparts. While just as effective as real reference electrodes, pseudo Ag|AgCl electrodes are subject to slow disintegration since electrolyte solutions are typically low in Cl<sup>-</sup> ions which can drive a subtle migration of these ions from the electrode surface into the electrolyte. The convenience of the pseudo-reference electrode, however, far outweighs this limitation. Researchers in this area are attempting to overcome the durability issues using unique structures [54] and alternate fabrication techniques [55].

#### 2.4.1.2.4 The Electrode-Electrolyte Interface

There are two basic processes that occur at the interface between the electrode and the electrolyte solution, and both relate to the material, electrolyte, and chemical reaction kinetics. Electrons that flow either from the electrode to the solution or vice versa due to an applied potential are said to be *faradaic* processes. This is due to the fact that the magnitude of the current that flows is governed by Faraday's law of electrolysis, which states that the magnitude of the chemical reaction is directly proportional to the amount of electricity transferred at an electrode [56]. There are other processes unrelated to the direct transfer of electrons that generate measurable currents. These *non-faradaic* processes are typically associated with background processes including adsorption and

desorption of material on the electrode surface, structural changes of the electrode over time, and redox processes associated with the supporting electrolyte, all which can influence analytical measurements. Fortunately the current generated by these occurrences are short-lived transient signals and small in magnitude compared to the main currents measured in ECD. Similar to the noise floor in an electrical or optical measurement, the quantities are typically subtracted from the measured signal after obtaining a blank and said to be background corrected. For low analyte concentrations, where the faradaic current magnitudes are on the same scale as the non-faradaic current (typically in the pico- to single digit micro-amp range), these processes cannot be ignored.

To understand the non-faradaic process, an ideal polarized electrode is described where no current can flow from the electrode surface into the electrolyte. This situation closely resembles an ideal capacitor. When a voltage is applied, there is a charge buildup over time that is related to the size of the capacitor, the potential applied to the capacitor, and the concentration and makeup of the electrolyte solution. Figure 2.7 is a conceptual drawing that describes the inner Helmholtz plane, where ions or molecules are adsorbed to the surface of the electrode, the outer Helmholtz plane, and the diffuse layer of ions from the electrolyte. The inner and outer Helmholtz plane is sometimes referred to as the compact, or Stern layer. Since thermal and convective agitation of the solution will move the ions in the outer layer of electrolyte around, they are non-specifically adsorbed and interact with the ions in the diffuse layer. This properties of this layer (thickness, etc.) is somewhat related to the concentration of the electrolyte.

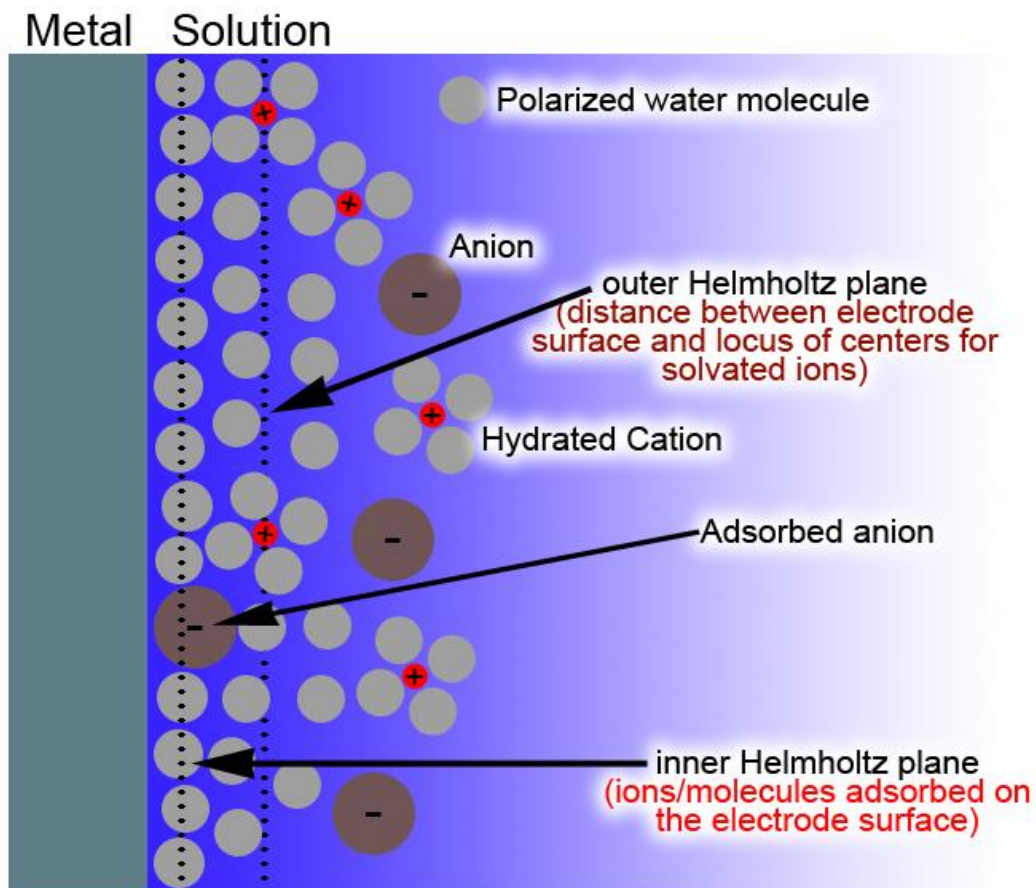


Figure 2.7 - Electrode-Electrolyte Interface

Given that there are at least two half-cell reactions in an electrochemical cell, a rudimentary two-electrode schematic for this configuration can be represented by the simple series circuit shown in Figure 2.8 where  $C_c$  is the capacitance of the counter electrode,  $R_s$  is the resistance of the solution, and  $C_w$  is the capacitance of the working electrode.

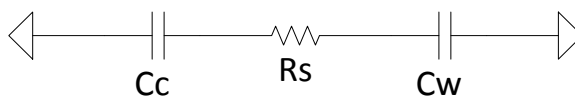


Figure 2.8 - Simple Electrical Equivalent Circuit for Cell

If it is assumed that the counter is an ideal electrode and we neglect the capacitive effect at  $C_c$ , if a voltage step is applied to this circuit, the resulting charging current will resemble an exponential current that obeys

$$i = \frac{V}{R_s} e^{-\frac{t}{R_s C_w}} \quad \text{Equation 2.4}$$

where  $i$  is the charging current responding to the applied step voltage  $V$ , and influenced by both  $R_s$ , the resistance of the electrolyte solution (related to conductivity and chemical activity), and  $C_w$ , the capacitance of the work electrode, which related to the size of the electrode. This charging current is a non-faradaic process that could possibly influence measurements when attempting to record the current passing due to a faradaic redox process. The magnitude of this current (and the charge generated over time) can be estimated by performing a step input to the background solution (no sample present). By convention, this “blank” signal is subtracted from the signal recorded when a sample is present to remove signal contributions by the charging current.

#### 2.4.1.2.5 Electrode Fabrication

One of the benefits of microfabrication is the ability to accurately define custom geometrical shapes at the micron scale. Conveniently, the more favorable electrochemical electrode materials, particularly platinum and gold, are commonly used in microfabrication deposition processes such as sputtering and electron-beam deposition,

which make them ideal for use in miniaturized ECD systems. As mentioned previously,  $\mu$ TAS systems have harnessed this technology as a technique to move away from off-chip, external detection configurations such as laser induced fluorescence, and more towards integrating detection electrodes directly on the chip [57-61].

#### 2.4.2 ECD Electronics

The heart of electrochemical detection depends on accurately measuring the transfer of electrons into and out of the cell during the redox process. The electrodes provide a path for the electrons by acting as the interface between the electrolytic solution and the external analog circuitry necessary to drive the reaction that would not, in the case of unfavorable thermodynamic reactions, not naturally take place. It is the supporting electronics that not only measure the reaction currents, but also control the electrochemical process.

##### 2.4.2.1 The Potentiostat

The three-electrode cell shown in Figure 2.5 includes an externally applied voltage that provides the energy to initiate the redox reaction. Additionally, this figure includes an ammeter that measures the current flowing into (or out of) the cell. These two electrical components are, to some degree, the heart of all electro-analytical instrumentation systems. Since the first potentiostat was introduced in the early 1940's, the introduction of the operational amplifier in 1955 greatly simplified the circuitry required to provide the necessary instrumentation and control [1]. Since then, updates and modifications have been made to the configuration to take advantage of the ever-

improving quality and functionality of this setup; however the basic electrical circuit is shown in Figure 2.9.

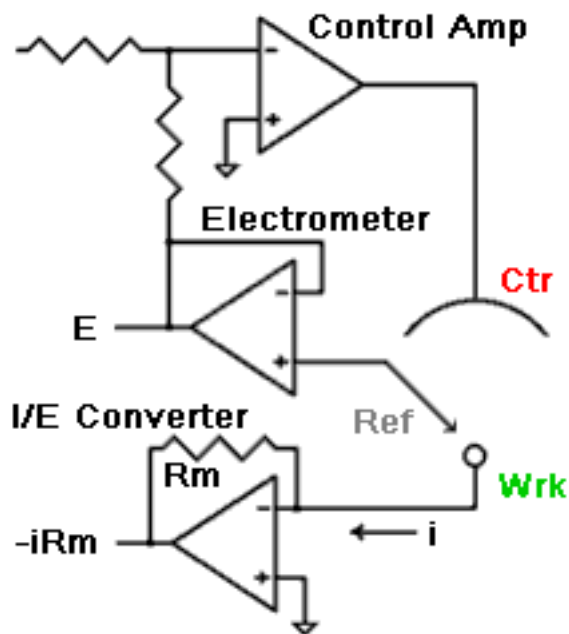


Figure 2.9- Potentiostat Schematic

The most crucial part of this circuit is active control of the applied potential at the working electrode, which, if left in an open-loop situation (i.e. no feedback control), would be affected by the dynamic environment in the electrochemical cell. The oxidation/reduction reaction occurring between the work and counter electrodes would rapidly alter the effective resistance of the cell during the exchange of ions/electrons, and the applied potential would essentially be at the mercy of this change. By providing a measured potential inside the cell (via the reference electrode, further supporting the “reference” nomenclature), this information can be fed back to the operational amplifier that is responsible for holding the applied potential constant.

During the actual redox reaction, changes in the local environment (rapid depletion or additions of electrons provided by the potentiostat and called for by the particular conditions of the cell (electrode type, size concentrations of analytes, etc., all of which immediately affect the resistance of the cell) are accommodated by control of the applied potential. Since the current flowing through the cell is the critical *measurand*, the reference electrode (no matter the type, pseudo, real, or otherwise) is connected to a buffer amplifier that prevents any of the reaction current from diverting through this part of the circuit and the redox current is left undisturbed and free to be measured.

The actual redox current is measured via a trans-impedance amplifier that converts the current flowing into a measureable voltage, regardless of the direction of the current, i.e. either into, or out of the cell. In practice, and on closer inspection of the circuit in Figure 2.9, it can be noted that the working electrode is held at “virtual ground” in order to allow for adjustments to small voltage offsets that may be present in the system. Since this electrode is essentially at ground potential (i.e. zero volts), the reaction potential is actually applied to the counter electrode. For example, if a 400 mV reaction potential is required, - 400 mV is applied to the counter electrode, and therefore the working electrode is 400 mV (positive) with respect to the counter.

### 2.4.3 Volumetric Configurations and Flow Considerations

In the proposed system, a finite volume will be analyzed to determine concentration of a sample using exhaustive coulometry. Exhaustive in this case refers to the analyte which will be completely converted to the oxidized (or reduced) form. The cell volume influences many of the variables associated with ECD, and especially those related to transport of analyte to the surface of the working electrode. This process is



governed by mass transport of three types, *convection*, *diffusion*, and *migration*.

Convection refers to bulk stirring of the electrolyte solution, which can be further defined as *forced convection*. Typically, a magnetic stir bar is used to constantly mix the electrolyte solution to maintain an evenly distributed solution. Diffusion refers to movement of a molecule that is driven by a concentration gradient. Lastly, migration is a phenomenon associated with the movement of molecules under the influence of an electric field. The combination of these three mass transport principles is described by the Nernst-Planck equation described by Equation 2.5.

$$J_a(x) = -D_a \frac{\partial C_a(x)}{\partial x} - \frac{z_a F}{RT} D_a C_a \frac{\partial \phi(x)}{\partial x} + C_a v(x) \quad \text{Equation 2.5}$$

In this representation, the equation is described in a single dimension along the x-axis.

$J_a(x)$  is the flux of analyte  $a$  at some distance  $x$  from the electrode surface,  $D_a$  is the analyte diffusion coefficient,  $\delta C_a(x)/\delta x$  is the gradient of the concentration of  $a$  at distance  $x$ ,  $\delta \phi(x)/\delta x$  is the potential gradient,  $z_a$  and  $C_a$  are the charge and the concentration on the analyte, respectively, and  $v(x)$  is the velocity of electrolyte flowing along the x-axis.

Analytical electrochemistry systems often are specifically configured to control and/or eliminate these contributors to mass transport using various techniques. When the volume is reduced to what is called a *thin-layer cell*, the flow is reduced to zero, with no contribution to flux by a potential or velocity gradient, and therefore Fick's first law of diffusion dominates the process described by Equation 2.5. In this case, the diffusion coefficient for a particular analyte can be used to estimate the time it will take to deplete the cell of analyte in one dimension, and the concentration profile can be represented generally by

$$n(x, t) = n(0) \operatorname{erfc} \left( \frac{x}{2\sqrt{D \cdot t}} \right) \quad \text{Equation 2.6}$$

where  $n$  represents the concentration of analyte in one dimension,  $n(0)$  is the initial boundary concentration at  $x=0$ , and  $\operatorname{erfc}$  is the complimentary error function. The *diffusion length*, which becomes a design criterion for the electrochemical cell, is represented by the value obtained in Equation 2.7.

$$h = \sqrt{2 \cdot D \cdot t} \quad \text{Equation 2.7}$$

A thin-layer cell is generally defined as a cell with a minimized diffusion time, and using this concept with the representative equation for diffusion length, the smallest dimension *is typically less than 100  $\mu\text{m}$* . Since the thickness of the cell (typically considered in a single dimension) effectively maximizes the efficiency of the redox process and all of the electroactive species in the volume undergo electrolysis, the configuration is extremely efficient and contributes directly to the calibration-free concept [62, 63]. By controlling the maximum height of the thin-layer cell, the total time to perform an analysis is greatly reduced. In the following sections, several volumetric configurations will be defined, leading up to the thin-layer configuration incorporated into the system developed for this project.

#### 2.4.3.1 Bulk Electrolysis

Perhaps the most basic electrochemical experiment setup, shown in Figure 2.10 and commonly referred to as *bulk analysis*, is a setup where the electrodes are placed into contact with a large volume of sample undergoing analysis. In this configuration, it is assumed that the volume of sample is sufficiently large enough that reactions occurring at the surface of the electrodes are constant, as the analytes are never depleted. Due to the

large volume, an essentially “infinite” well of analyte is available and a strong diffusion gradient is created during the reaction which drives new analyte near the reaction surface, and dominates the flux described in Equation 2.5. Mechanical stirring is often used to enhance this process. When a step voltage is applied, an initial charging current occurs (as a new electrode-fluid interfacial layer is created), followed by a steady state reaction current that is proportional to the concentration of analyte.

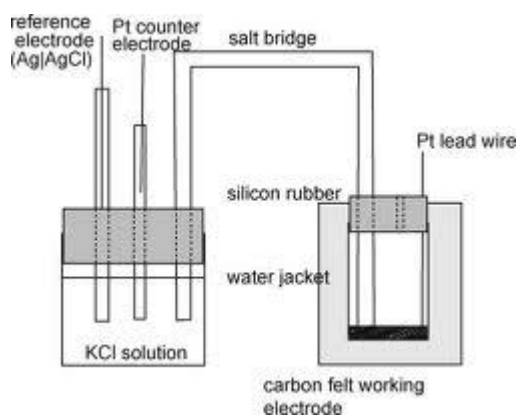


Figure 2.10 - Basic Bulk Electrolysis Experiment Configuration. In this configuration, the salt bridge prevents the diffusion of analyte from the working electrode to the counter electrode.

This large volume experimental setup is used for controlled potential coulometry, as well as a method to characterize and test electrode materials and configurations. Cyclic voltammograms (CV), which are an experimental technique used to identify the potential sufficient to initiate an oxidation/reduction reaction, are often obtained using this configuration. Due to the large volume, this technique is not practical for exhaustive techniques since determination of the concentration of analyte in the sample would take an amount of time that is roughly proportional to the volume of sample. Stirring the solution can minimize the reliance on diffusion, however the time scale for an exhaustive analysis with this setup is impractical.

### 2.4.3.2 Wall Jet Configuration

For sample analysis at a much smaller scale, where the cross sectional dimensions of the flow channels approach the size of the electrodes used in the electrochemical cell, there are several configurations that are used. The wall-jet configuration places a detection electrode on a flat surface and the analyte stream impinges directly onto the electrode [64]. For small channels where the dimensions satisfy

$$L \gg \sqrt{A} \quad \text{Equation 2.8}$$

where  $L$  is the length of the channel and  $A$  is the cross sectional area, and the full Navier-Stokes equation is reduced to Poisson's equation (the momentum equation)

$$\nabla^2 w = \frac{1}{\mu} \frac{dp}{dz} \quad \text{Equation 2.9}$$

where  $w$  and  $z$  are the fluid velocity and flow direction, respectively, and  $\mu$  is the fluid viscosity [65]. This equation describes fully-developed, laminar flow in a constant cross-sectional area, and as such, a constant stream of fresh analyte is delivered to the electrode surface where detection occurs at a diffusion limited rate; furthermore, the steady flow does not disturb the sensitive double layer at the working electrode surface. This setup is used primarily in continuous flow techniques, such as capillary electrophoresis, where the sample stream is continually flowing through the system. The analytes in an injected mixture are initially separated in a long *separation* column upstream from the detector; migration of the analytes through the column or channel are dictated by the charge, flow medium, column construction and separation technique. Each resolved analyte eventually passes to the detector and through the associated oxidation or reduction, is determined.

As can be seen in Figure 2.11 which is depicted magnified but relatively to scale, the size of the detection region is typically larger than the sample channel. Since the flow stream is impinging directly on the electrode, the diffusion gradient that drives fresh unreacted analyte to the electrode surface is supplanted by new sample that is constantly delivered to the electrode surface. However, laminar flow still dominates, and a portion of the sample stream will not reach the electrode surface, but rather will be convectively directed around the detection region. This configuration is also typically cumbersome to assemble due to alignment and fluidic path configuration issues, especially at smaller volumetric scales.

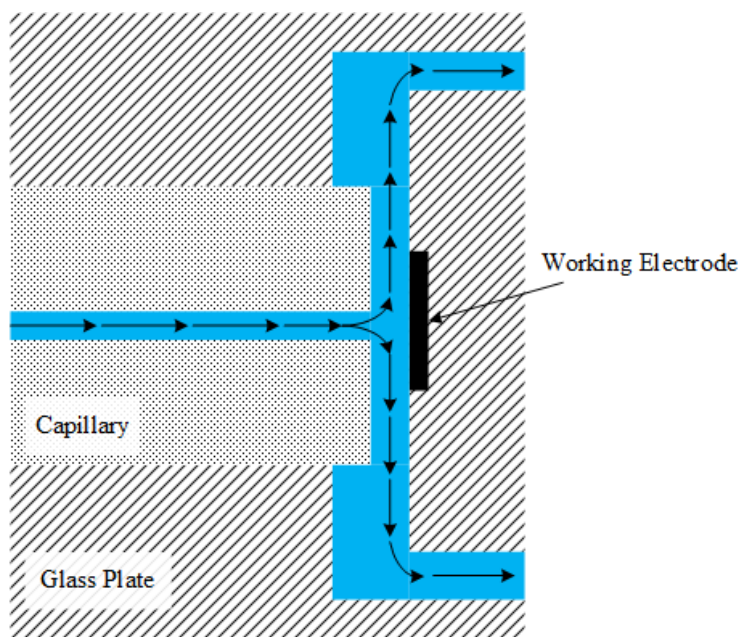


Figure 2.11 – Example of a typical wall-jet detection configuration. Only the working electrode of the three electrode configuration is shown.

#### 2.4.3.3 Flow Over/By Configuration

Similar to the wall-jet configuration, flow-over (also called flow-by) electrode configurations have been utilized in miniaturized electrochemical detection systems due

to fabrication techniques that allow the electrodes to be incorporated directly into the flow stream [57, 58]. Similar to the flow-jet configuration, sample is directed to the detection electrode at the end of sample flow or separation channel, however the sample flows *over* the detection electrode instead of being directed delivered normal to the electrode surface. The ease with which the analyte stream passes through the entire flow path creates a situation where the constant flow carries analyte directly to the detection region regardless of whether or not all of the analyte has been oxidized or reduced. Since the sample is flowing constantly so analyte typically is swept past the detection electrode before every analyte molecule is detected (Figure 2.12). For samples with a constant concentration (heavy metals in a contaminated water stream for example), the detection signal is more or less a constant that is proportional to concentration, however highly sensitive to flow velocity since flow velocity will alter the diffusion profile. This situation will contrasted with stopped flow cells where delivery of the analyte stream is interrupted long enough to completely react all of the analyte in the vicinity of the detection electrode.

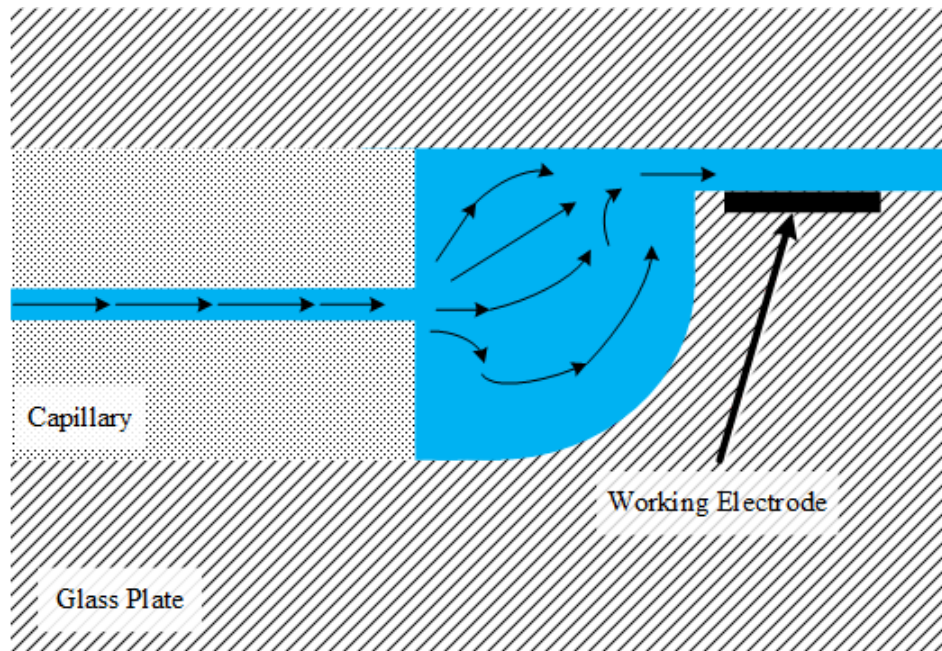


Figure 2.12 – Representative flow-over detection configuration. Only the working electrode of the three electrode configuration is shown.

#### 2.4.3.4 Stopped Flow Thin-Layer Cell

If a similar configuration to the flow-over setup is used under the conditions that after a sample is injected into the system the flow is stopped, the immediate region surrounding the detection electrode becomes what is effectively a reduced-volume bulk electrolysis configuration (Figure 2.13). If the dimensions meet the requirements for a thin-layer cell, when an applied potential is applied, the analyte in the bulk can be oxidized/reduced to completion. It is this particular configuration that will establish the spatial requirements to perform an exhaustive coulometric analysis.

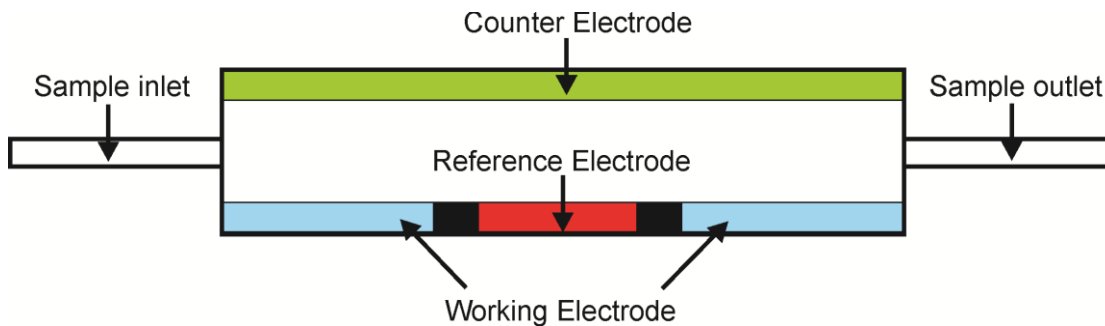


Figure 2.13 – Stopped-flow thin-layer schematic with all three electrodes contained within the fixed volume of the cell

#### 2.4.4 Quantitative Electrochemistry

As described previously, a potentiostat is used to control the voltages at specific electrodes that cause the chemical reaction to progress, while currents generated (or voltage changes) during the chemical reaction are monitored via the other electrodes. Conceptually, this setup is primed for customization, and research has produced miniaturized versions of this setup where the sample size is greatly reduced and will be shown to be the platform of choice for the work presented in this study.

##### 2.4.4.1 Types of Electrochemical Detection

There are several sub-variations of electrochemical methods; however the two primary techniques are *voltammetry* and *amperometry*. In both cases, a sample is analyzed by measuring either the change in current or voltage over time in an electrochemical cell containing the analyte under study. The cell contains a controlled volume of sample, and the current or voltage is either recorded or controlled, depending on the type of experiment, as a reaction takes place. Results of the analysis depend directly on the magnitude and duration of the signals recorded. Thus, in its simplest form,



the experiment is simply the precise recording of the electrical output of a chemical reaction. In general, detection limits are determined by competing background processes that also generate a current (the non-faradaic processes such as the oxidation or reduction of the carrier buffer solution, for example).

#### 2.4.4.1.1 Voltammetric Techniques

Technically, there are two types of voltammetry, sweep voltammetry and step voltammetry although there are subtle variations of each. Perhaps the simplest of electrochemical experiments is the investigation of oxidation/reduction reaction where a voltage applied to a working electrode with respect to a reference electrode is varied linearly over time while the current is measured [66]. The resulting current signal is recorded as the potential is swept linearly between voltages. The range (max-min) of the voltage sweep is chosen based on the analyte and, in general, will be centered on the peak potential ( $E_p$ ) that will generate the greatest oxidation current. The scan rate (V/time), or how fast the voltage is swept, can affect the peak height of the associated voltage vs. current plot, as shown in Figure 2.14, since the diffusion layer at the analyte/electrode interface is a function of the scan rate and the background (charging) current is also affected when the working electrode voltage is changed [67]. For electron processes that are slow, scanning too rapidly will produce what is observed to be a drift in the location of  $E_p$  (not shown).

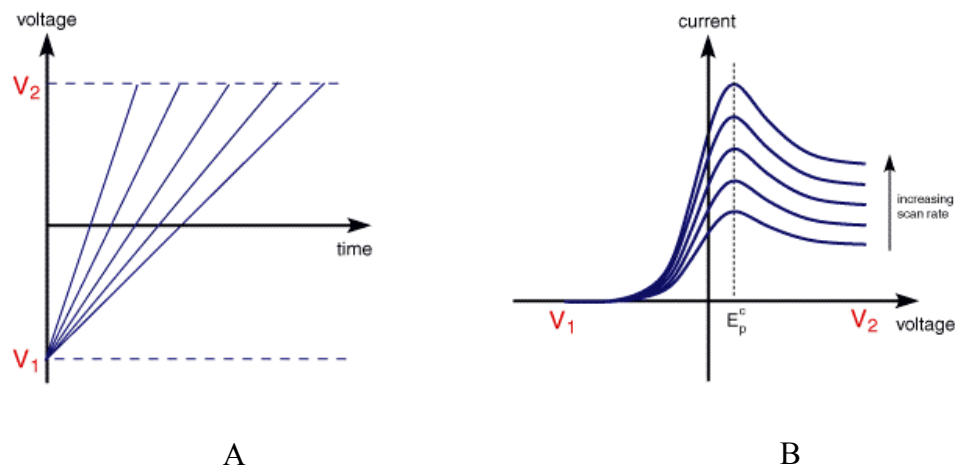


Figure 2.14 - Example of linear sweep voltammetry (A), and corresponding voltage vs. current plots for each scan rate (B)

A *cyclic voltammogram*, shown in Figure 2.15, is a special voltammetric scan that sweeps the voltage beyond both the estimated  $E_p$  for both oxidation and reduction of an analyte. This type of experiment is critical for determining the optimal oxidation or reduction potential in an electrochemical cell since real-world conditions such as electrode material used, electrode fouling over time, and reference electrode inefficiencies will cause a shift in the actual  $E_p$ . For example, Musameh et al. reported a measureable shift in the anodic peak potential when glassy carbon electrodes were modified with carbon nanotubes to detect NADH [68].

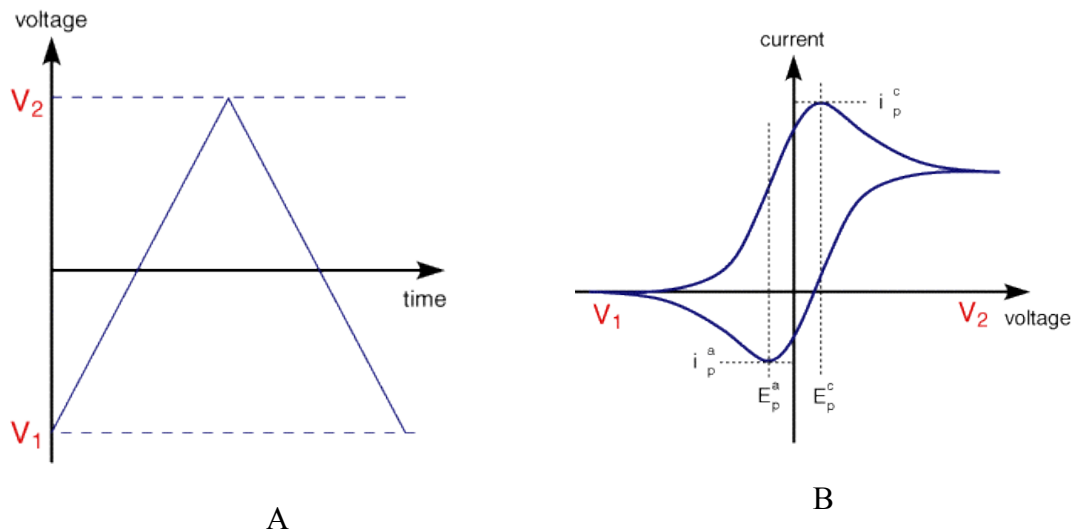


Figure 2.15 - Cyclic voltammogram voltage scan (A) and representative Voltage vs. Current Plot (B)

#### 2.4.4.1.2 Amperometric Techniques

*Amperometry* can be contrasted with voltammetric techniques with a quick examination of the data that is generated from each type of experiment. For voltammetry, as was shown in Figure 2.14B, the scan voltage is plotted against the measured current. In an amperometric experiment, a measured redox current is plotted against time for a particular applied constant potential. A sample amperometric plot is shown in Figure 2.16. As the experiment progresses, the magnitude of the current at any time is proportional to the instantaneous rate of the redox process and each peak corresponds to a different analyte. This technique of detection is used in constant flow techniques such as capillary electrophoresis and liquid chromatography where mixtures of analytes are first separated while traveling down a separation column and are individually detected as each exits the column. In this case, the peak heights are proportional to the concentration of

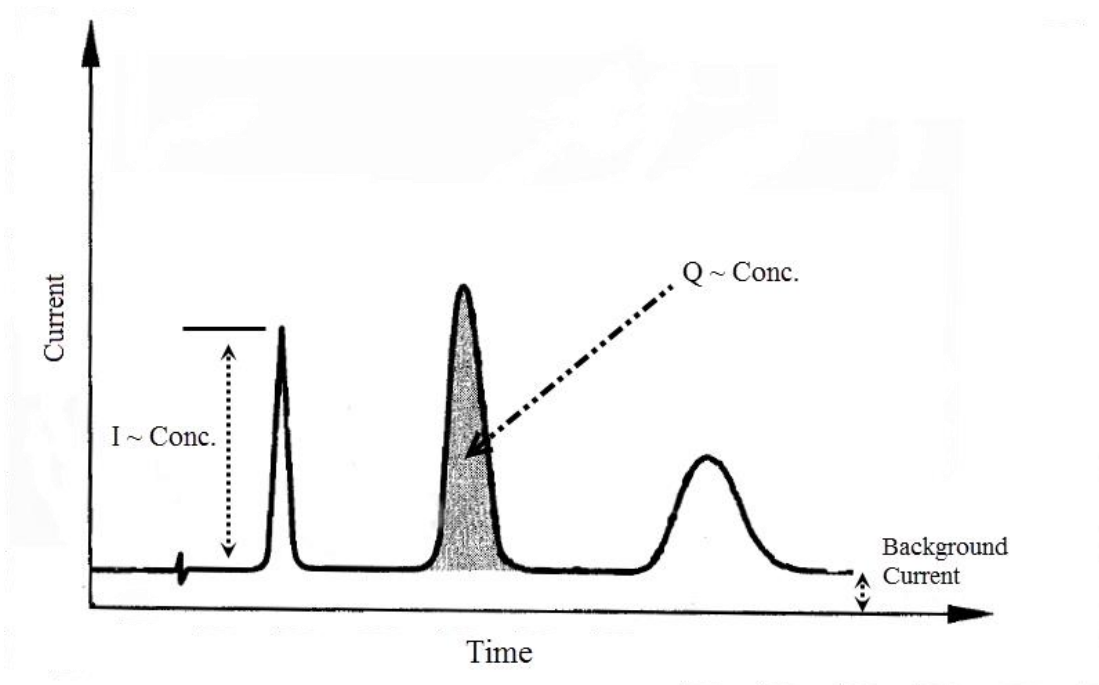


Figure 2.16 – Sample amperogram for a flowing sample that highlights peak heights and area under the curve of a reaction current are both proportional to concentration of analyte.

the analyte and calibration curves can be used to determine the direct relationship of peak height to concentration.

Calibration is required due to the fact that only a very small percentage of the analyte will undergo oxidation or reduction since the analyte stream is flowing past the electrode during detection. Conversion efficiency is flow dependent (mass transfer limited) and is low since the reaction rapidly depletes the analyte near the electrode surface. The flow velocity can be reduced to enhance the residence time, however this will tend to counteract the separation and the separate peaks will overlap and no longer be fully resolved. This calibration requirement is a limiting factor for systems that might be otherwise suitable for in-the-field use.

Taking this one step further is *coulometry*, which considers the area under the curve of the current versus time plot. *Chrono-coulometry*, where the current is obtained with respect to time by integrating the amperometric data curve, a sum of the current over time, and yields the total charge generated during the experiment ( $Q$  in Figure 2.16). This quantity, similar to the peak height, is also directly proportional to concentration. For a well-controlled experimental setup, most notably where the volume is known absolutely, calibration should not be necessary since the non-faradaic background processes that create an offset in the current versus time plot can easily be subtracted from the data. This quantitative determination can be further explained considering the decay of the current to zero as the oxidation/reduction proceeds, represented with

$$i(t) = i(0)e^{(-\frac{\pi^2 D}{L^2}t)} \quad \text{Equation 2.10}$$

where  $i(0)$  is the initial current,  $D$  is the diffusion coefficient of the analyte, and  $L$  is the cell thickness. Carrying this relationship through the expanded version of Equation 2.6, where the complimentary error function is represented by the dimensional equivalent and the concentration gradient is evidenced in time and space by

$$C(x, t) = \frac{4C(0)}{\pi} e^{(-\frac{\pi^2 D}{L^2}t)} \sin\left(\frac{\pi x}{L}\right) \quad \text{Equation 2.11}$$

where  $C(0)$  is the initial concentration, and  $L$  remains the cell thickness. The charge  $Q$  that is transferred over time, independent of location for a planar electrode and fixed height cell volume, then can be shown to be

$$Q(t) = nFVC(0)\left[1 - \frac{8}{\pi^2} e^{(-\frac{\pi^2 D}{L^2}t)}\right] \quad \text{Equation 2.12}$$

where  $n$  is the number of electrons in the reaction,  $F$  is Faraday's constant,  $V$  is the volume of the cell. When  $L \ll (D \cdot t)^{1/2}$ , mass transfer from the bulk no longer dominates and can be neglected, resulting in a simple relationship between charge and concentration of analyte. When  $V$  is known absolutely, the number of moles can be obtained directly from the measured total charge. The current vs. time curve of the charge generated in a thin layer cell is also often described by

$$i(t) = nFACD^{1/2}\pi^{-1/2}t^{-1/2} \quad \text{Equation 2.13}$$

a special form of Equation 2.10 which is referred to as the Cottrell equation, where  $F$  = Faraday's constant,  $A$  is the electrode area,  $D$  is the diffusion coefficient, and  $C$  is the initial concentration of the analyte. The uniqueness of this particular equation is that it takes into account the area of the electrode, in this case derived for a planar electrode. The relatively simple integration of this equation yields the total charge  $Q$  represented by

$$Q(t) = 2nFACD^{1/2}\pi^{-1/2}t^{1/2} \quad \text{Equation 2.14}$$

and is commonly referred to as the Anson equation [69].

In a stopped flow cell, specificity for a particular analyte is not accomplished by prior separation of mixtures of components, but techniques may be employed such as varying the redox potential applied, adjusting the buffer chemistry, as well as using several different electrode materials that have been shown to display an affinity for certain types of analytes in order to quantify mixtures.

#### 2.4.4.2 Applied Electrochemistry

Battery technology notwithstanding, the measurement of pH is perhaps the most common use of the electrochemical techniques [70]. The concentration of  $H^+$  ions in a

particular solution creates a measureable linear potential (roughly 55 mV per pH unit). Typically, a pH probe uses a glass electrode which is an ion-sensitive electrode that is essentially half of a simple galvanic cell and can be used as a detector for changes in concentration [71]. Typically, a probe is placed into solution which completes the circuit and the potential difference established between the anode and cathode is measured and converted to pH using a simple high input impedance circuit. There are dozens of expensive commercial pH meters available; however a quick search of the literature yields active development of customized and miniaturized pH sensors [72, 73], a collection of simple circuits that can be fabricated to accomplish the same task for less than \$100 [74], as well as development of disposable, low-cost pH sensors[75].

Another common example of ECD would be modern glucose meters such as the OneTouch (Figure 2.17) that test for blood sugar using a simple electrochemical technique that is rapid and accurate enough for daily use, and requires only a single drop of patient blood. In this system, a gold microelectrode is pre-coated with a layer of a polymer film infused with an enzyme (glucose oxidase) that is sensitive to  $H_2O_2$ . The response of the sensitized gold electrode is therefore made proportional to the amount of  $H_2O_2$  generated by the reaction of glucose in the sample and the glucose oxidase on the electrode. The benefits of such an easily performed test are obvious; patients require less frequent visits to their physician and diagnostic costs are reduced in every category including the patient, doctors, and insurance company.



Figure 2.17 - OneTouch Glucose Home Diagnostic Kit

When considering other, more traditional, laboratory detection techniques such as Atomic Absorption Spectroscopy (AAS), High Performance Liquid Chromatography (HPLC), or Gas Chromatography combined with Mass Spectrometry (GC/MS), these may be highly sensitive and provide an enhanced level of precision compared to electrochemical techniques, but as explained previously, the equipment is large, expensive (when considering both hardware and operational costs), and typically slow to produce results. Each of these techniques also requires an elevated level of training.

## 2.5 Literature Review

Extending the cost/speed benefits of ECD techniques to other areas where analysis is often performed would provide additional economic benefits. There are many potential industrial applications where various incarnations of ECD are being developed and applied. Apetrei et al. is using a functionalized amperometric biosensor to detect the biogenic amine tyramine which, if present in foods at high levels, can cause dangerous



conditions such as diarrhea [76]. Amperometry was used by Li, et.al, to detect benzophenone, a photoinitiator of UV-cured inks used in food packing materials and a known carcinogen [77]. The authors argue that amperometric techniques are favorable to more traditional techniques such as GC-MS and HPLC-UV because these techniques, while having low detection limits, are bulky and expensive. Environmental studies including water purification/remediation are also using ECD techniques. Grygoliowicz-Pawlak et al. used a coulometric technique to pretreat a seawater sample and remove sodium chloride [78]. It can be envisioned where thousands of miniaturized, inexpensive electrochemical units could be deployed for desalination efforts in countries with little access to fresh water. In the medical industry where hundreds of thousands of measurements are performed regularly, analytical techniques with reduced temporal response and low cost are of great benefit. DNA analysis using electrochemical detection techniques is actively being researched. Zhao et al. is using ECD to detect cancer cells based on the identification of the smaller molecules that link fragments of DNA [79]. ECD would appear to provide a platform with which analyses can be performed in the field at a greatly reduced cost without sacrificing analytical sensitivity or accuracy by creating sensor platforms that are either disposable where they can be quickly replaced or preferably designed for long-term use.

### 2.5.1 Coulometry/Micro-Bulk Electrolysis

The miniaturized thin-layer electrochemical cell proposed in this project is designed to contain a small volume that essentially reduces the electrochemical setup to a miniaturized bulk electrolysis system. There have been attempts in the past to include a fixed volume thin-layer cell in what is essentially otherwise a bulk electrolysis setup. Lee

et al. constructed such a device to detect chemical oxygen demand (COD) using a thin copper layer (Area = 2.5 cm<sup>2</sup>) as a working electrode and the thin-layer of analyte (thickness ~ 150 μm) was created by suspending a glass plate over two 100 μm thick PTFE spacers, as shown in Figure 2.20 [80]. The somewhat crude setup involved introducing the sample into the cell via capillary action, and the in-between times for experiments required 5 minute cleaning steps, including a 2-3 h clean at the start of a day's experiment. Figure 2.19 shows the setup including the external reference electrode and (Pt) counter electrode. The authors mention errors introduced by diffusion of reactants from the edges of the thin-layer portion of the setup during experiments, and non-uniform current distributions due to the counter and reference electrodes placed external to the detection cell. Despite the geometry of the cell, and the estimation of 110 s to completely exhaust the analyte in the cell, the electrolysis typically completed in 3-10 minutes before steady-state was reached.

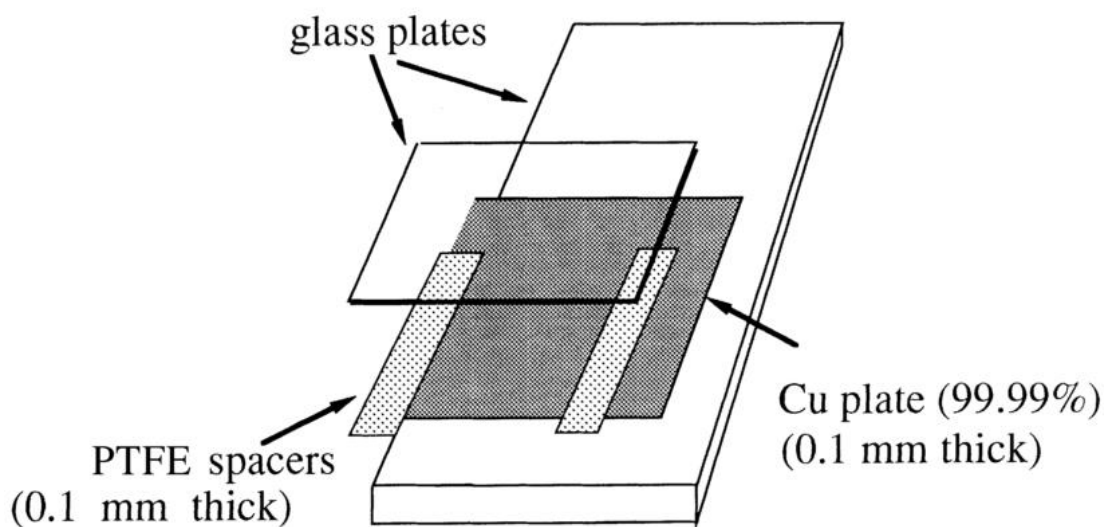


Figure 2.18 – Thin-layer cell created from Cu plate and PTFE spacers for detecting COD (Adapted from [80])

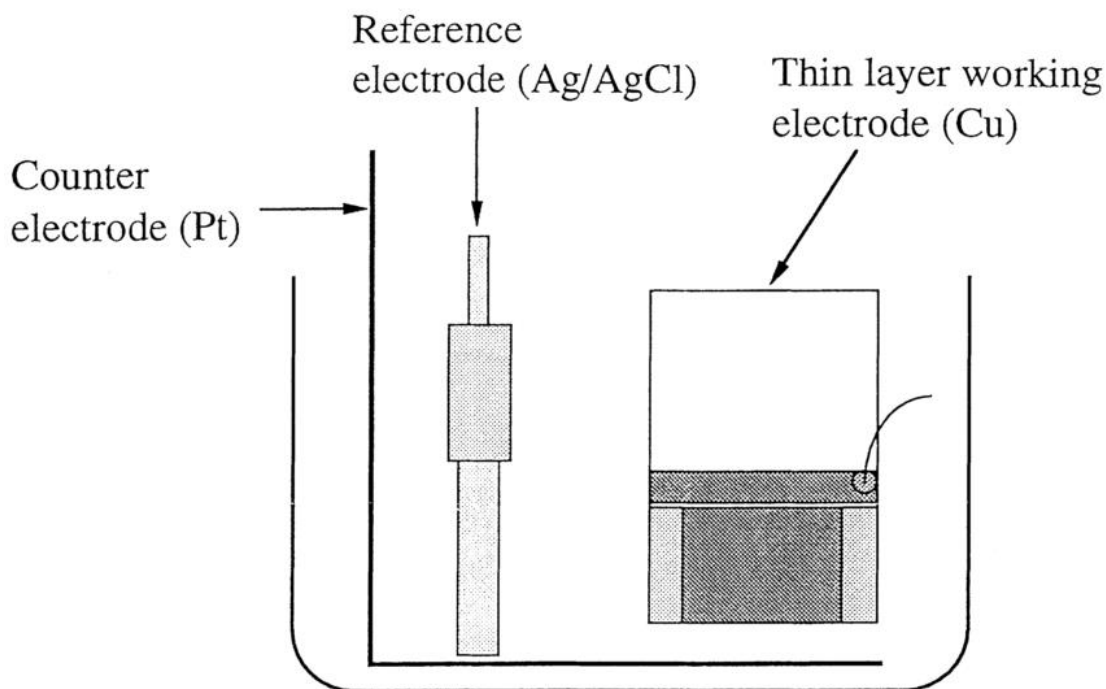


Figure 2.19 – Schematic diagram of the electrochemical cell described by Lee et al (Adapted from [75])

A similar concept was demonstrated by Fukuda et al. who developed a miniaturized open-air “micro-bulk” electrolysis system [81]. The volume of the system was approximately 10-15  $\mu\text{L}$  and complete electrolysis of three oxidoreductases (diaphorase, malate dehydrogenase, and Ketoglutarate) was achieved, as is shown in Figure 2.20. The cell volume was not in a flow or channel configuration, and manual droplets of sample were placed on the open-air cell. Each of the reaction peaks shown in Figure 2.20 occurred when a droplet of analyte was manually placed into the cell volume. The dashed curve shows that the total charge reaches near steady state after a period of time, suggesting complete conversion. However, this data also suggests that even though the cell volume is only 10  $\mu\text{L}$ , the time for each reaction is on the order of 100-200

seconds. Were any of these analytes able to undergo a reverse reaction, these peaks would compete with the desired measurement of the forward reaction.

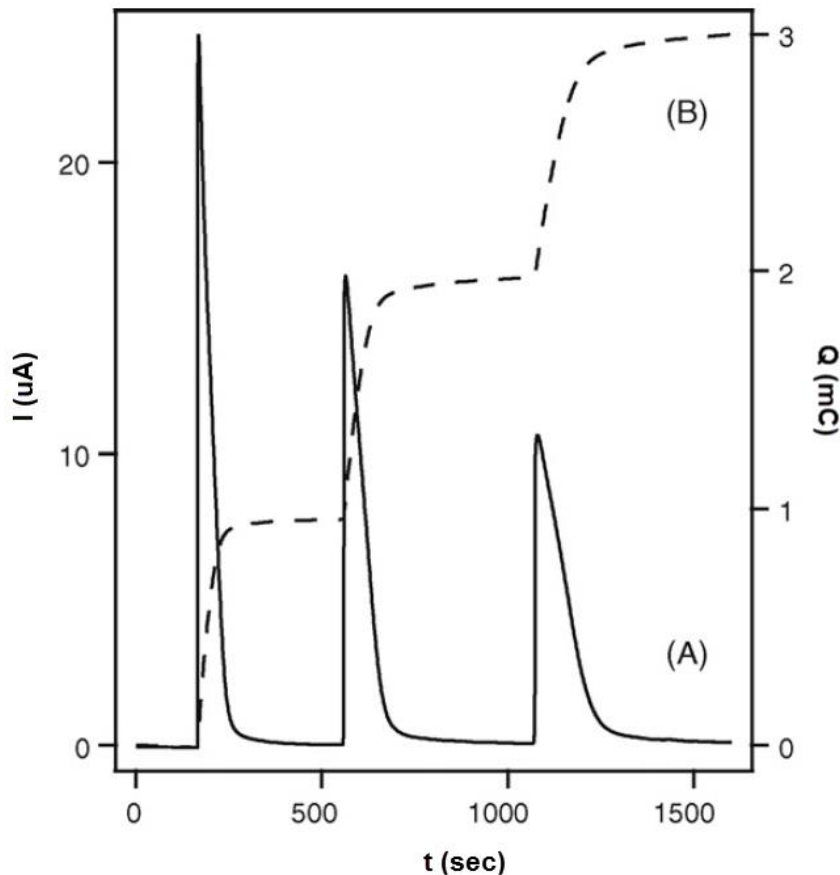


Figure 2.20 – Coulometric analysis of three reductases (diaphorase, malate dehydrogenase, and Ketoglutarate) each placed manually near the detection electrodes; the two plots indicate current (A) and total charge (B); (Adapted from [76])

A more recent work that demonstrates coulometric determination under thin-layer conditions was reported by Sohail et al. on the determination of nitrate in a fresh water sample [82]. In this study, an ion-sensitive membrane was used in a macro-sized circular tubing to establish an approximated thin-layer cell with a critical dimension of 50  $\mu\text{m}$  (Figure 2.21). The authors indicate results showing a small relative standard deviation

between experiments (2.3%) and a limit of detection of 1.1  $\mu\text{M}$ . However, this system has an approximate constant volume, so calibration is required. The low detection limit is attractive, but unfortunately tightly coupled to the large volume of the tubing used. Finally, the authors report exhaustive depletion of sample within about 60 seconds.

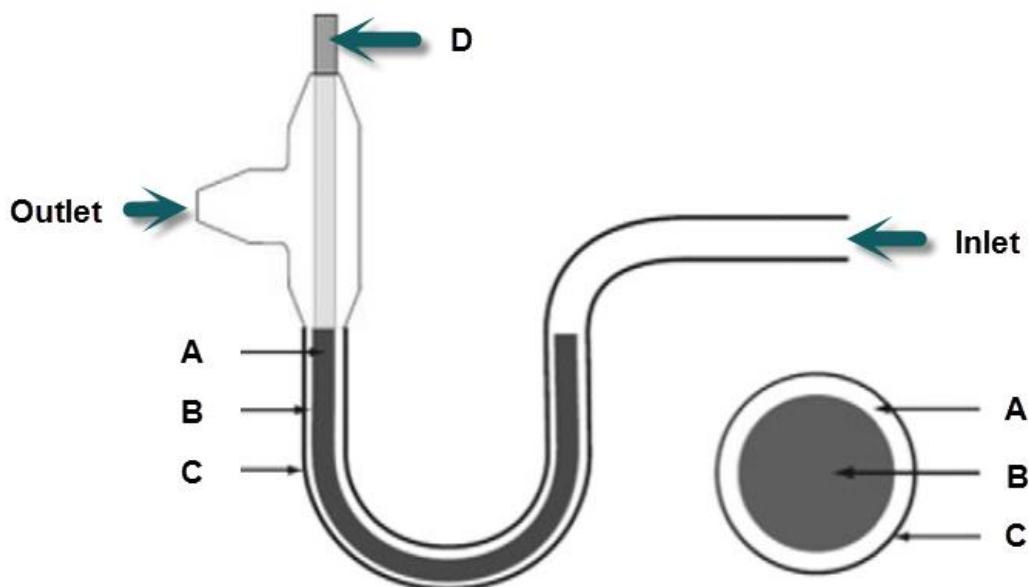


Figure 2.21 – Macro thin-layer cell; A – Ag/AgCl wire; B – thin sample layer; C – membrane. This entire system was placed in an outer solution. (Adapted from [82])

Detection limits in thin-layer cells were explored by Shvarev et al. albeit in a quite complicated experimental setup [83]. In this study, a 50  $\mu\text{m}$  PVDF separator was coiled around the inner silver pseudo-reference electrode to ensure non-contact between the reference and fiber surfaces (Figure 2.22). The porous fiber was an ion-sensitive membrane that separated the sample flow region from the detection electrode region. A multi-pulse technique was required to “reset” the sensor, ostensibly due to some non-specific charge buildup on the large surface area membrane or possibly the PVDF

separator. Detection limits approached 10  $\mu\text{M}$  for calcium and potassium however the large surface areas of all electrodes did not allow detection below this level.

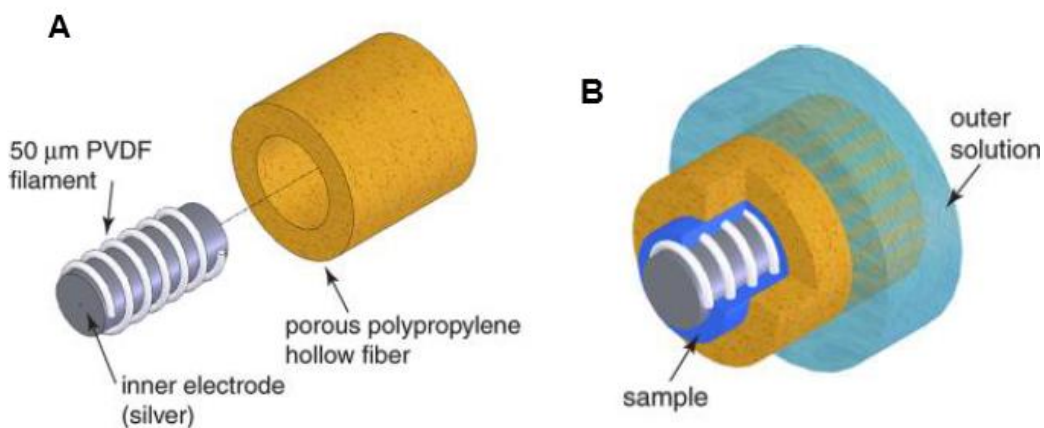


Figure 2.22 – Diagrammatic exploded view of the inner electrode, separating filament, and ion-selective fiber (A), and portion of the assembled system showing the flow regions (From [83])

Finally, Haghighi et al. used a thin-layer electrochemical flow cell to study bromide using a chemoluminescence technique, but explored the platform for amperometric studies as well [84]. In this capacity, a large piece of glassy carbon (20 mm x 10 mm) was used as a working electrode, while a platinum wire was used as the auxiliary (counter) electrode. An inlet was incorporated into the cell to accommodate an external Ag|AgCl electrode. In this flow analysis system, all three electrodes were incorporated into the thin-layer chamber since reversibility was not an issue due to the constant flow stream. -300 mV was applied to the working electrode versus the Ag|AgCl reference electrode and the thickness of the cell was adjusted between 0.1 mm, 0.2 mm, 0.5 mm, and 1 mm. A constant stream of analyte ( $\text{K}_3\text{Fe}(\text{CN})_6$ , 0.1 mM) was flowed into the thin layer cell. The results (Figure 2.23A) indicate an obvious relationship of

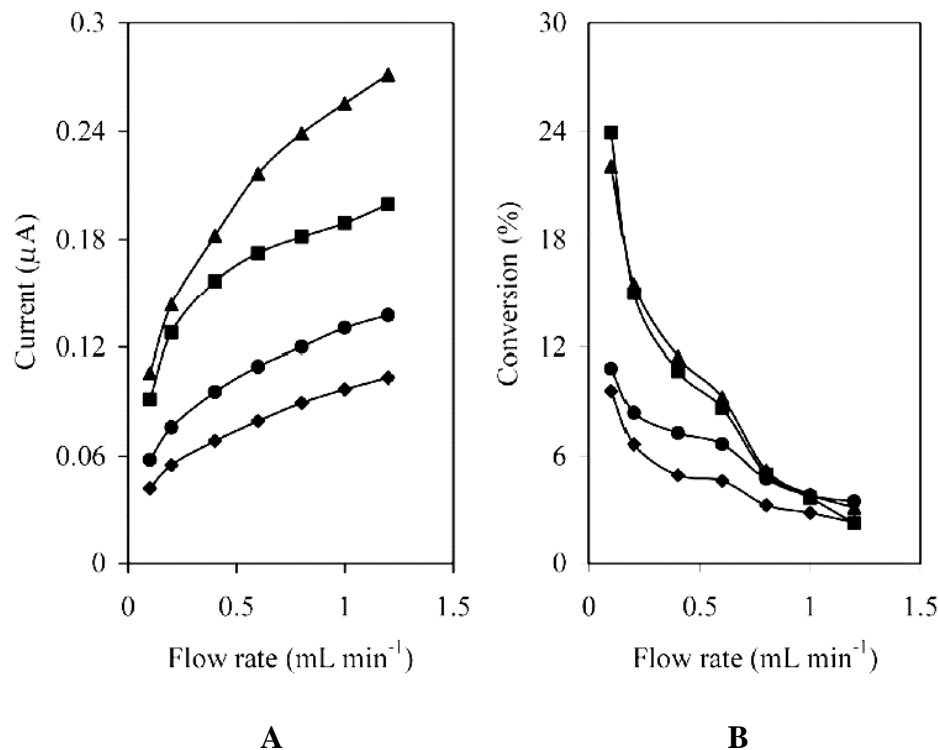


Figure 2.23 – Oxidation current versus flow rate (A) and total analyte conversion (%) for a thin-layer constant flow cell (B) (From [79])

measured current versus to flow rate in that faster flow rates result in a larger oxidation current. Since the reaction at the electrode surface is mass-transport limited, higher flow rates deliver fresh sample to the surface of the electrode to counteract this limitation. Additionally, the authors present data reporting conversion percentage versus flow rate, which does decrease with the increase in flow Figure 2.23(B). It is also not surprising to see that at higher flow rates, the differences in conversion percentage become negligible and the lower flow rates generate the largest reported conversion percentage, near 25%. It is academic to argue that for a stopped flow system, this conversion would certainly increase to 100% over a time specified by the thickness of the cell.

## 2.5.2 Remote Field/Deployable Sensing

The ability to miniaturize the supporting hardware associated with ECD techniques makes this technology ripe for incorporation into portable systems. Despite the obvious advantages, miniaturized systems are only just now starting to surface. Byrne and Diamond have penned a review on remote sensing systems and their inherent limitations in power consumption, high costs, and techniques that require a need for sample treatment and calibration (Figure 2.24) [85]. The authors suggest that “more densely deployed (but less reliable) sensors” may be a solution. Nevertheless,

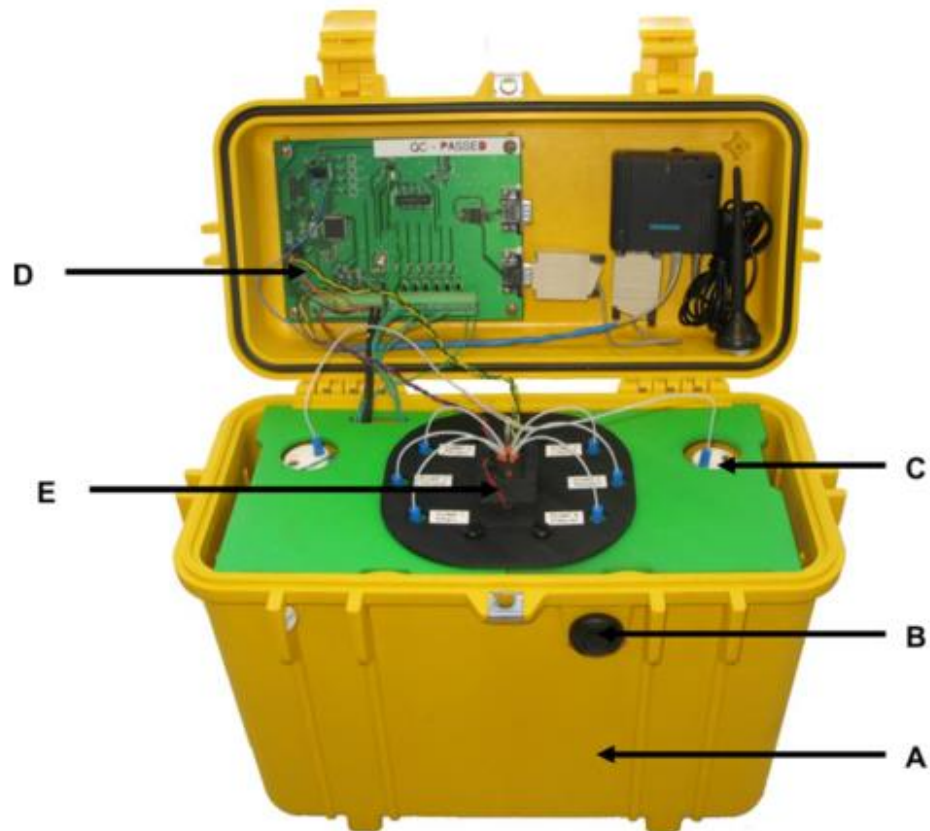


Figure 2.24 – Remote system for measuring phosphate in the field, indicating tough protective case (A), sampling port (B), reagents and waste storage (C), electronics (D) and microfluidics manifold and optical detector housing (E); (From [85])



development is progressing towards remote, autonomous, in the field ECD systems. McGraw et al. reported on an autonomous microfluidic system for detecting phosphate in remote locations [86, 87]. The system records the concentration of phosphate using an optical technique and transmits four sampling results once per day via GSM modem. The battery powered device has a solar panel for regenerating power and could theoretically last indefinitely, however the sensor was shown to show undergo drift after the third week of use. The complexity of the pumping system and related components kept the cost of the prototype somewhere above \$2500 which is not practical for wide scale use.

There are many examples of research in the area of portable flow-based electrochemical techniques, particularly microfluidic systems with separation channels to carry out miniaturized electrophoresis. Our research group reported one of the first such systems that included both the high-voltage and detection electrodes and flow system on a single chip to separate and detect analytes in the catecholamine family such as dopamine and catechol at concentrations down to 4-5  $\mu\text{M}$  [57]. Work continues in this area, such as Fernandez-la-Villa et al. who recently reported on a urine analysis technique designed around a portable microfluidic electrophoresis system. The device was able to separate individual components from a urine sample containing uric acid and interfering compounds such as ascorbic acid and epinephrine [88].

### 2.5.3 Custom Instrumentation

The instrumentation designed to support electrochemical techniques is an area under great development, primarily due to the simplicity of the components, but also due to the precipitous drop in costs associated with the design, development, and fabrication of custom electronics. Flexible and powerful software development platforms also aid in

rapid development of fine-tuned, custom instrumentation systems. In support of our work in the area of capillary electrophoresis, we developed a custom circuit designed to run on standard household batteries and provide all of the low detection-level instrumentation for analyte interrogation, but also include the large ( $\sim 1\text{kV}$ ) voltages fundamental to the implementation of the electrophoretic technique [89]. The uniqueness and novelty of this design warranted the issuing of a U.S. Patent in 2008 [90].

While there are representative examples of custom instrumentation, particularly potentiostats, designed for remote (i.e. outside the lab environment) monitoring, typically they are reported paired with crude, or at best rudimentary electrochemical setups. Yun et al. reported on using a miniaturized wireless system complete with custom potentiostat and radio-frequency (RF) module for sending data back to a base station [91]. The authors state that the electrochemical system was microfabricated, including a mercury working electrode, solid-state reference electrode, and a platinum counter electrode to detect heavy-metal contamination in sample water. The included block diagram, shown in Figure 2.25, includes all of the components necessary to successfully implement this system. The detector was shown to have a limit of detection approaching 5 nM for Cadmium and Lead in the sample using a commercial potentiostat (Figure 2.26; left plot). However, data shown using the custom potentiostat which suggested a detection limit of

1 mM Cadmium (Figure 2.26; Right plot) is debatable and was not directly compared to the commercial detector.

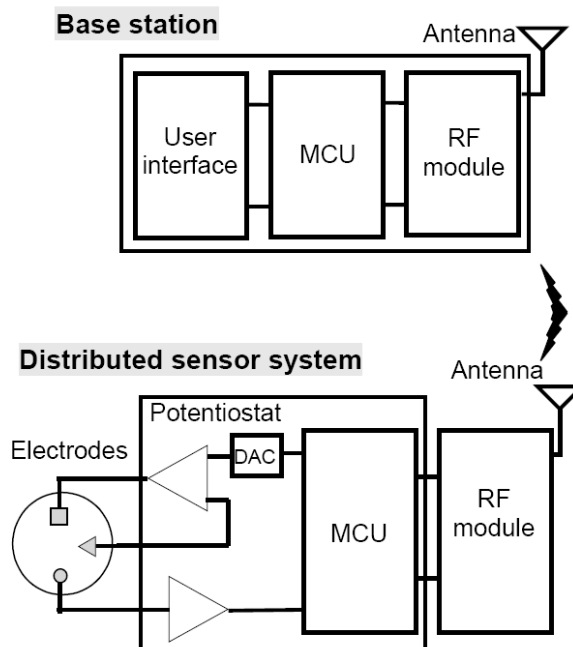


Figure 2.25 – System schematic for remote sensing system as described in [84]

A microcontroller-based data acquisition system (Figure 2.27) was designed by Sangam et al. to evaluate the performance of an amperometric biosensor for the analysis of glucose [92]. The enzyme based biomembrane reacted with glucose and generated a current proportional to concentration in what appeared to be a bulk electrolysis cell. While this system is crude, it does demonstrate the ability to reduce the size of the instrumentation setup for ECD.

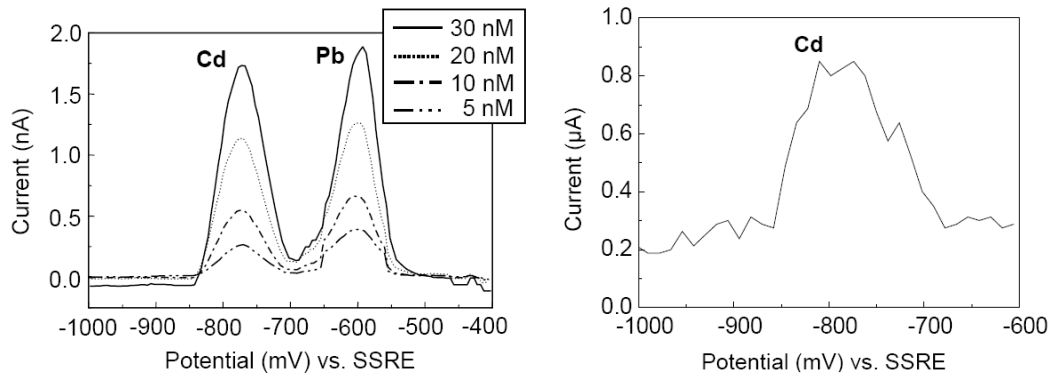


Figure 2.26 – Sample Cadmium and Lead data commercial detector (left) and Cadmium only for the custom potentiostat described in [91]

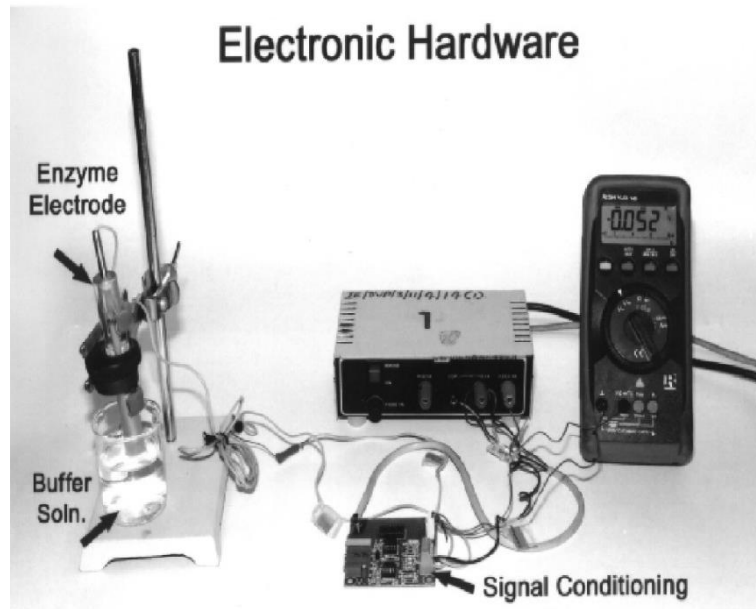


Figure 2.27 – Microcontroller-based instrumentation configuration for interrogating an amperometric biosensor as described in [92]

Huang et al. reported an embedded solution for incorporation into a portable potentiostat based on a SOC package that incorporated many electronic components on a single chip [93]. This prototype was used to measure current generated when bilirubin attached to an enzymatically treated polymer layer. The conditioning circuit described is

essentially a transimpedance amplifier and the reported response for a range of concentrations was described as linear and within 1.5% compared to a benchtop detector.

Perhaps the most representative example of a miniaturized instrumentation prototype for ECD is the embedded system reported by Kwakye et al. which describes a microcontroller with custom software to process, display and store the signal generated by an electrochemical reaction (Figure 2.28) [94]. The microcontroller used (MSP430F449, Freescale Semiconductor, Austin, TX) was designed to transmit data to another device by means of serial communication. The authors include a schematic of a two electrode potentiostat, but do not describe the fabrication of such, nor do they describe the reference electrode used. Interestingly, since the microcontroller chosen does not have a dedicated analog output, a pulse width modulated (PWM) output was converted to an analog signal. A simple transimpedance amplifier configuration was used

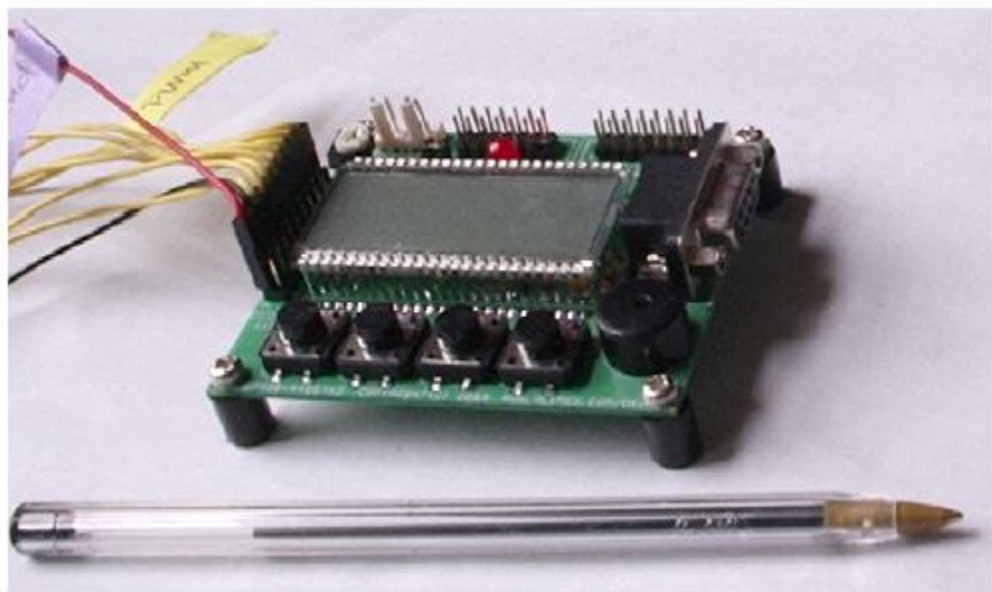


Figure 2.28 - Microcontroller-based instrumentation described in [76]

to convert electrochemical current to voltage which was measured by the microcontroller. The device was battery operated and could run on as little as 3.6 V, with a current draw low enough to run intermittently for many days. The final prototype was sent to an external company for assembly before testing. Both static (droplet) and flow studies were performed using ferri/ferrohexacyanide (0.01 to 50  $\mu\text{M}$ ) and the authors describe results that indicate percent error against a benchtop detector of between 6% and 3% for the static and flow studies, respectively. This study is representative of an *embedded* system, where the detection technique (hardware included) is separated from an upstream controlling device such as a PC or laptop computer where most of the work takes place. The hardware and software are finely tuned to perform all of the fundamental steps to complete a measurement which reduces costs and allows for the possibility of remote deployment.

Recently, Novell et al. have reported on a miniaturized instrumentation device based on radio frequency identification (RFID) which is a low power, narrow band wireless technology [95]. This system uses a potentiometer to report the instantaneous magnitude of ion transport over RFID. While this particular detection technique does not directly compare to electrochemical instrumentation as described previously in this chapter, the study is a good example of the drive towards the miniaturization of supporting electronics for analytical techniques as well as opening the door for wireless transmission of measurement data and remote deployment.

## 2.6 Summary

In this chapter, the background information needed to develop and engineer a highly specialized, custom coulometry cell was presented. This material covered both the

fluidic concepts and geometric restrictions of the flow cell, as well as the materials used for creating electrodes and the instrumentation necessary to implement exhaustive coulometry. Finally, a short study of the analytical chemistry techniques involved and other researchers exploring this area was presented. In the next chapter, the specific materials and techniques used to implement the chosen design will be examined.

## CHAPTER III

### MATERIALS AND METHODS

In this chapter, the techniques used to design and fabricate each part of the full ECD system are described. First, the sensor materials and design will be outlined, including several electrode patterns and fabrication details. Second, the electrochemical flow cell will be explored, including the intricate features that were incorporated to establish a finite volume, thin-layer cell. The assembly required to bring disparate parts together to form the assembled manifold will be explained. Third, the potentiostat circuit that was designed specifically to interrogate the analytical sample will be explained as well as the control software developed to support the instrumentation. Finally, the experimental plan to evaluate the performance of the system will be outlined.

#### 3.1 Electrochemical Sensor Platform

Gold was selected as the primary electrode material due to the near ideal electrochemical properties described in Chapter Two. Fortunately, this noble metal is commonly used in microfabrication processes, particularly in sputtering and electron beam evaporation techniques, used to apply thin-films. Pattern layout and design techniques using these methods allow for near absolute precision, intricate control of shapes and sizes of the electrode area, and, when combined with batch processing, allows



for rapid design changes to the sensor electrode geometry. Batch processing increases yield and provides multiple devices at the end of each complete fabrication cycle.

### 3.1.1 Sensor Electrode Design

Initially, an oval area (4 mm wide x 8 mm long) was used in order to define a maximum electrode area of 25 mm<sup>2</sup>. This general shape matches the design of the flow cell area which was designed as an oval to maximize clear-out of the injected sample and eliminate dead volume within the thin layer cell, and is further described in a separate section.

Multiple variations of the silicon-based sensor platform were microfabricated using the process flow outlined below by adding the designs to a single mask. The electrode pattern and supporting features on the photolithography mask were drawn in AutoCAD (Autodesk, San Rafael, CA) and submitted to the Micro/Nano facility for fabrication on a chrome coated 5" by 5" square quartz plate using a laser pattern generator (DWL66FS, Heidelberg Instruments, Heidelberg, Germany) with a 1 μm minimum resolution. Figure 3.1 shows a sensor layout containing a two-electrode design that includes a single large work electrode (~ 22 mm<sup>2</sup>) with a smaller electrode (~ 4 μm<sup>2</sup>) to be used as a reference electrode. This particular design was the basic design used to test the exhaustive capabilities of the coulometric cell.

Other variations in the sensor electrode pattern using the 4 mm x 8 mm elliptical shape include a design with two electrodes that are interdigitated and close to equal in

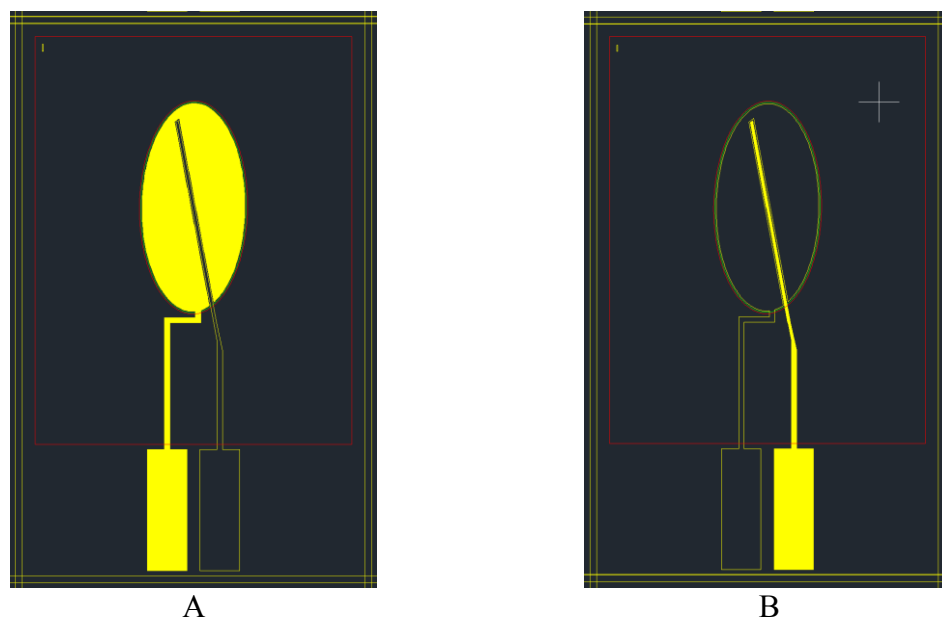


Figure 3.1 – Primary sensor layout (AutoCAD drawing); Working electrode area highlighted in gold (A); Reference electrode area highlighted in gold (B)

area (Figure 3.2A) to simulate electrode fouling, and a six electrode design to test for redundancy and possible long term use in the field (Figure 3.2B). For this latter design, one electrode is used as the reference electrode, and the others are used as individual working electrodes; if the electrode in use becomes fouled or fails after long-term use, the next electrode can be used as the working electrode.

### 3.1.2 Thin-film Sensor Fabrication:

The electrochemical sensors were fabricated in the cleanroom facility operated by the University of Louisville Micro/Nano Technology Center. Figure 3.3 is a simplified graphic of the stepwise fabrication process. The various electrode patterns were transferred to oxidized Si wafers using an image reversal photolithographic liftoff technique. The stepwise process flow began with the growth of a ~500 nm oxide

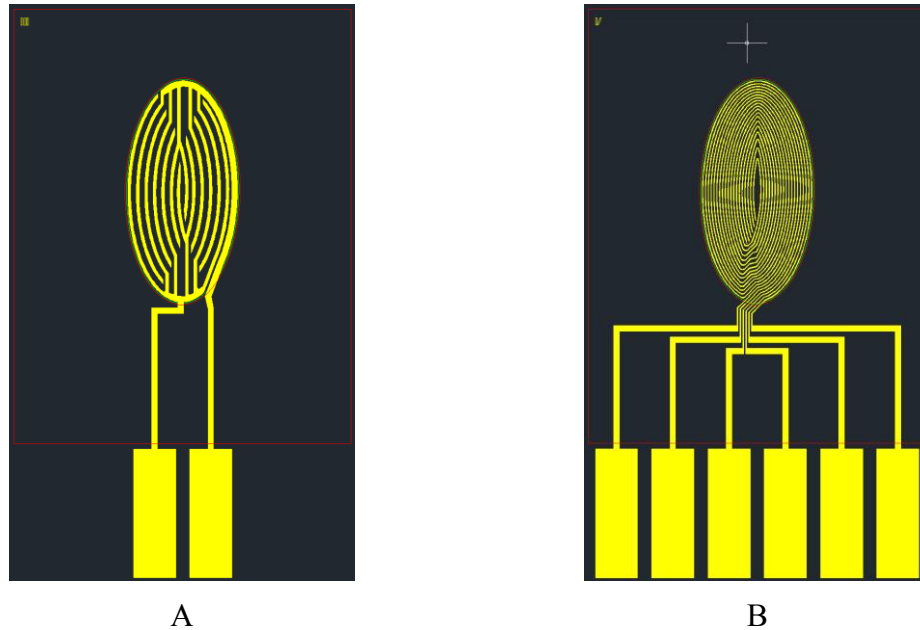


Figure 3.2 – Sensor designs (AutoCAD drawing) with two interdigitated electrodes (A), and six concentric spiral electrodes (B)

insulating layer on a 4-inch (100 mm), 525  $\mu\text{m}$  thick Si wafer (Wafer source). The  $\text{SiO}_2$  coated wafers were then coated with Shipley 1827 positive photoresist to yield the inverse of the electrode pattern, with an additional  $\text{NH}_3$  exposure (gaseous) to improve liftoff. This process produced wafers covered in a sacrificial photoresist with exposed oxide regions that defined the electrode patterns. Next, a buffered oxide etch step produced a recessed region in the oxide layer only ( $\sim 210$  nm). Two sputtering steps were then conducted successively without breaking vacuum ( $\sim 100$  mTorr) in a multi-target sputtering system (Series 4064, Technics) to fill the etched regions. The two resulting layers consisted of a primary nickel adhesion layer (100  $\text{\AA}$ ), followed by gold (2100 $\text{\AA}$ ) which would serve as the final thin-film gold electrode layer. A final liftoff process step removed the excess metal deposits on top of the sacrificial photoresist layer, and resulted in the final patterned wafer with thin film electrodes buried just below the wafer surface.

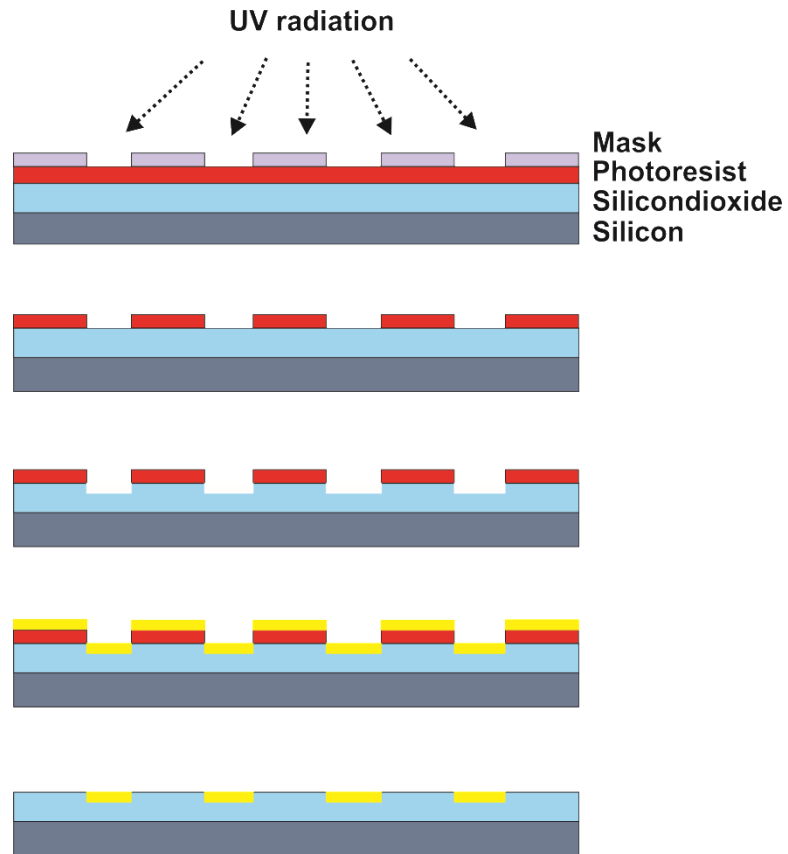


Figure 3.3 – Microfabrication process flow steps with showing the: 1) bottom layer of silicon; 2) light blue layer SiO<sub>2</sub>; 3) red layer photoresist; 4) gray layer is the mask; and, 5) yellow layer is gold.

### 3.1.3 Estimated Sensor Yield

One of the benefits of using microfabrication to create the sensors is the inherent parallel or batch processing to produce many devices from a single wafer. Since the entire wafer goes through the stepwise process flow, multiple device designs can be included on a full wafer. There are a theoretical maximum number of devices that can be included on a full wafer, depending on the size of the wafer and the size of the devices included in the design. The maximum gross Die Per Wafer (DPW) yield can be estimated

using [96]

$$DPW = d\pi \left( \frac{d}{4S} - \frac{1}{\sqrt{2S}} \right) \quad \text{Equation 3.1}$$

where  $d$  is the wafer diameter (mm), and  $S$  is the target sensor size ( $\text{mm}^2$ ). Figure 3.4 is an AutoCAD drawing that shows a full wafer of thin-film electrochemical sensors for a 100 mm diameter Si wafer and a sensor size of 1.3 cm x 2.1 cm.

### 3.1.4 Wafer Dicing

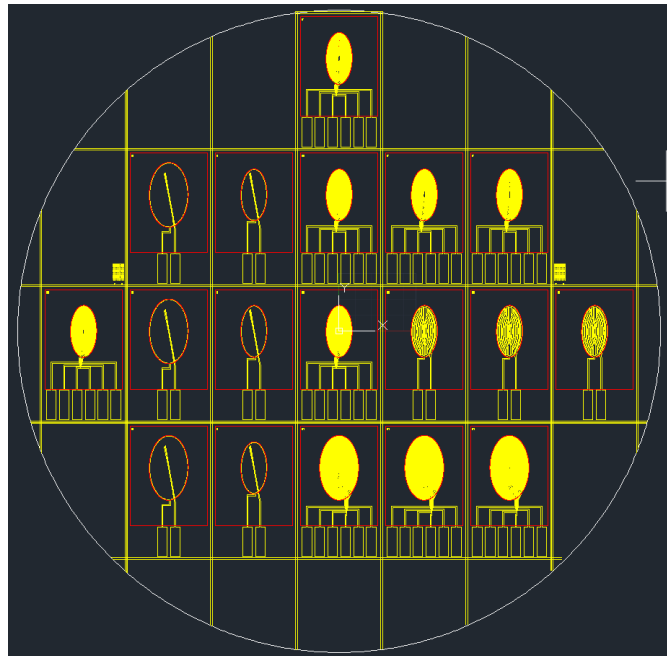


Figure 3.4 – Full Si wafer photolithography mask that includes various sensor designs. Diameter of outer circle is 4 inches (100 mm)

The Si wafer was placed into a dicing saw (DAD 321, Disco, Tokyo, Japan) and the individual sensors were separated from the wafer. Figure 3.5 emphasizes two sets of geometrical patterns included on the photolithography mask. Feature set A in Figure 3.5 is included to aid in alignment of features during successive fabrication steps, while the

features (lines) annotated by B are included to indicate where the dicing blade should travel and cut the wafer in order to minimize errors related to variations in the length and width of the sensors. For many microfabricated devices, the final chip area produced after dicing is not a critical feature. In this project, fluidic ports will be aligned to either end of the oval shape when inserted into the flow cell; therefore, minimizing the variation in the chip dimensions will affect proper alignment of the assembled flow cell.

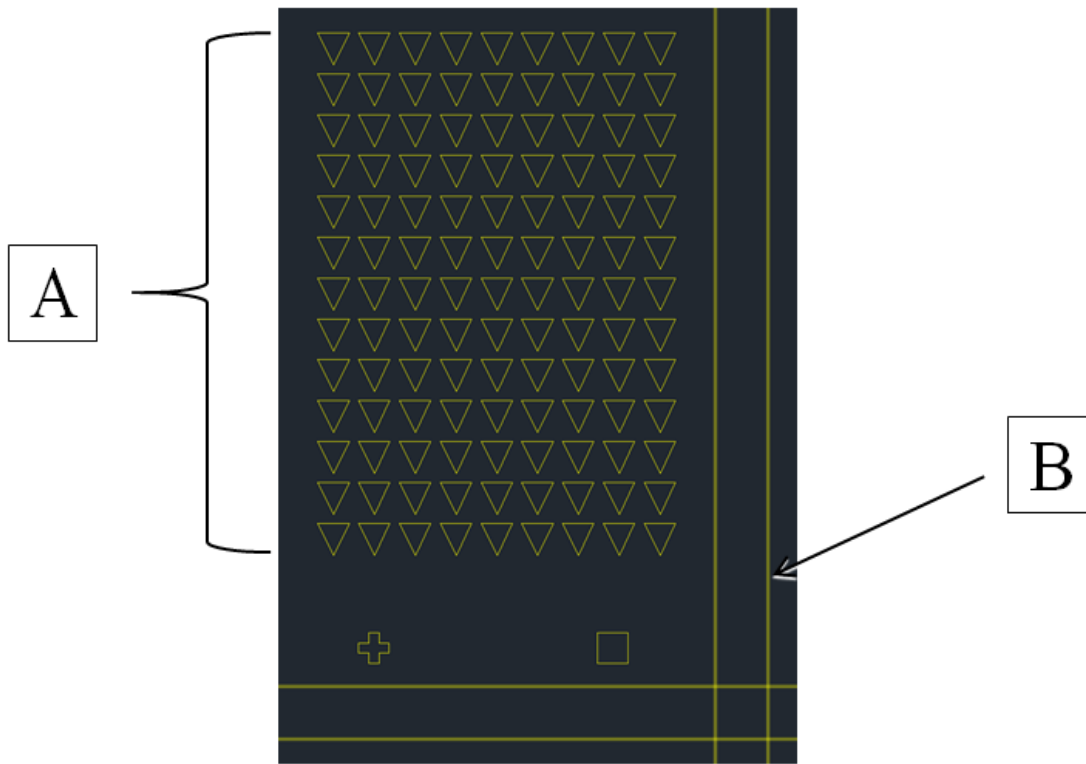


Figure 3.5 - Photolithography fiducial alignment markers (A), and dicing streets (B), 200  $\mu\text{m}$  (W)

### 3.1.5 Sensor Gasket Mask Design

To establish the volume of the working electrode chamber, a rubber gasket layer with the central portion removed was placed directly on top of the silicon surface. Since

the area of the electrode and the supporting gasket area is roughly fixed at  $25 \mu\text{m}^2$ , the thickness of this electrode gasket would define the final volume of the cell using the equation

$$V = \pi abH \quad \text{Equation 3.2}$$

where  $a$  and  $b$  are one-half the length and width of the ellipse, and  $H$  is the height of the cell, in this case the thickness of the electrode gasket layer. A 55A durometer, high-purity silicone rubber was chosen as the gasket material (Part no. 87315K71, McMaster-Carr, Chicago, IL) and a laser etching printer (Mini 18, Epilog, Golden, CO) was used to fabricate the gasket. The specified thickness of this material is 0.005 inches, or  $\sim 127 \mu\text{m}$ , which is reduced by compression to  $\sim 80\text{-}100 \mu\text{m}$  after final assembly of the electrochemical cell. Figure 3.6 shows the gasket layout in relation to the electrode pattern.

### 3.1.6 Ag/AgCl Pseudo-Reference Electrode

A true reference electrode can be described as an electrode terminal that has a stable and predictable electrode half-cell potential. The stability is typically due, particularly in the case of traditional Ag|AgCl reference electrodes, to the establishment of an isolated redox system that contains a constant concentration of each reactant in the redox couple. These electrode systems require some type of isolation (i.e. a glass frit is typically used), which can complicate their use in miniaturized electrochemical cells. To circumvent this limitation, a gold electrode in close proximity to the working electrode (to minimize the uncompensated drop in voltage through the cell due to solution

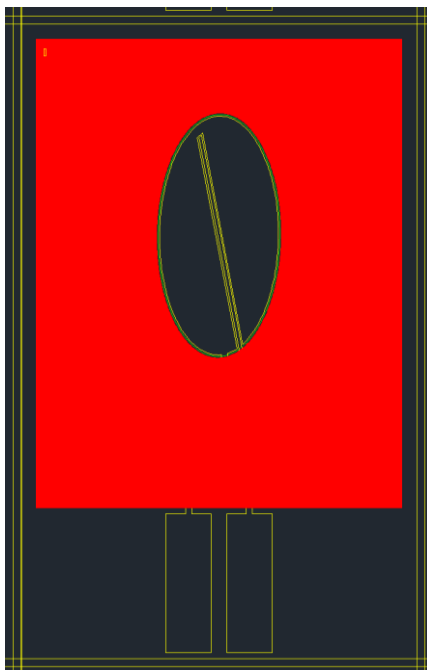


Figure 3.6 - Sensor Gasket Mask Design (red area)

resistance) was converted to a Ag|AgCl *pseudo*-reference electrode via electrodeposition. This two-step process, described in detail by Bard et al. [6], first converts a Ag<sup>+</sup> ion plus an electron to Ag (metal) via the reductive (left to right) process described schematically by:



followed by an oxidation whereby a free Cl<sup>-</sup> ion is oxidized and combines with the Ag (metal) described in the (right to left) process described by:





A commercially available, cyanide-free silver plating solution (Silver Cyless II RTU, Technic, Inc., Cranston, RI) was used in a pulse/reverse pulse technique similar to what is described by Chandrasekar et al. [97]. The square pulse technique combined with stirring, allows a quiescent period to enhance mass transport of silver to the electrode surface during the plating process which ensures a quality conversion to a stable electrode material. The first step of the conversion first deposits a thin layer of Ag on the gold surface where a Ag coated wafer is used as the anode and the gold electrode to be converted is used as the cathode (Figure 3.7); both were placed in a stirred bath of silver

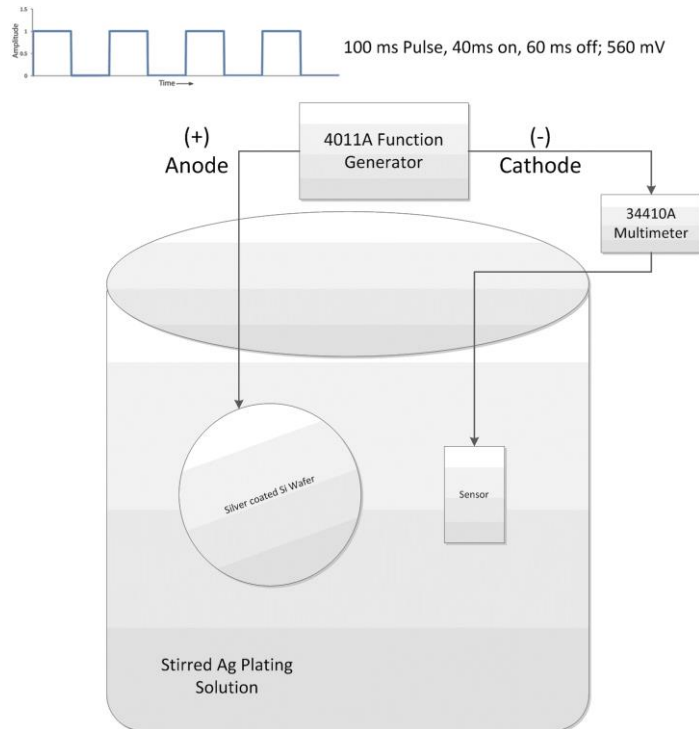


Figure 3.7 – Schematic outlining Step 1 in the Pseudo-Reference Electrode conversion plating solution. A 560 mV pulse train (100 ms; 40 ms on/60 ms off) was applied using a function generator (4011A, B&K Precision, Yorba Linda, CA) for 70 minutes with a target current density of 0.7 mA/cm<sup>2</sup>.

At the end of the electroplating step, a chlorination step was performed using the newly coated silver electrode as the anode, and a bare Pt wire acting as the cathode (Figure 3.8); these were placed in a stirred solution containing 1M NaCl for 15 seconds, using a 50 mV square pulse applied with the same instrumentation. The current generated during both of these processes was measured and a software program was created (details described in section 3.4.1) to report and display the magnitude of the current density during the peak of the applied square wave so adjustments to the magnitude could be made during the process.

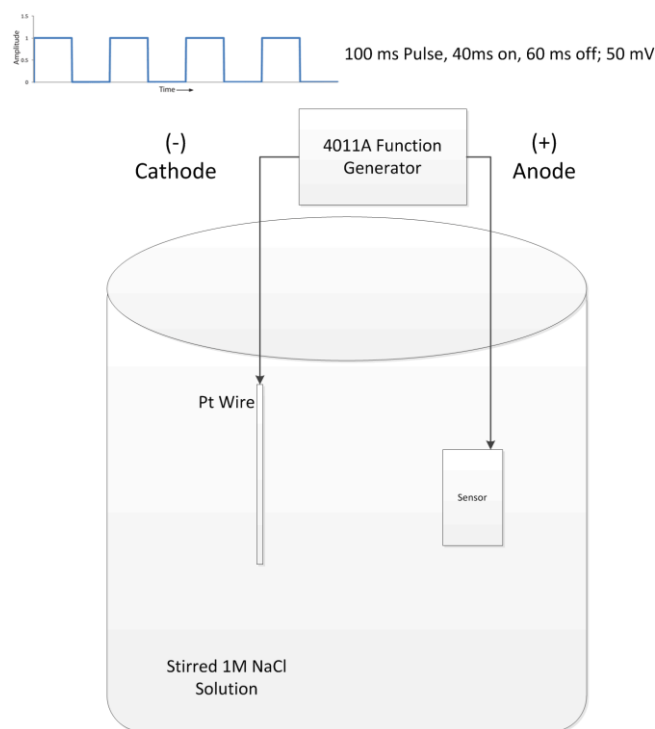


Figure 3.8 – Schematic outlining Step 2 in the Pseudo-Reference Electrode conversion

## 3.2 Flow Cell Design and Fabrication

The fluid component of the electrochemical system was designed around the concept of a stopped-flow, thin-layer electrochemical cell. The zero-flow, finite-volume condition allows all analytes to be oxidized or reduced to completion, while the thin-layer designation assures that the reaction will occur in a reasonable amount of time. At the heart of the fluidic manifold is a precisely-controlled volume designed to satisfy all of the requirements of the thin-layer flow cell.

### 3.2.1 Flow Cell Considerations and Specifications

The schematic in Figure 3.9 (not to scale) shows a vertical/side-view cross-section of a generic thin-layer cell indicating inlet and outlet flow paths that are blocked to upstream and downstream flows, the height of the cell is defined by  $h$ , and for a thin-layer cell, this dimension is typically *restricted to less than 100  $\mu\text{m}$* . The cell height defined by the critical thin-layer dimension,  $h$ , is an important consideration when designing a three-electrode potentiostat intended to position all electrode surfaces in close proximity to one another in the reaction chamber. In the case of processes that are reversible, minimizing this volume creates a situation where reactants at one electrode are free to diffuse to the opposite reactive surface and undergo the reverse process in a

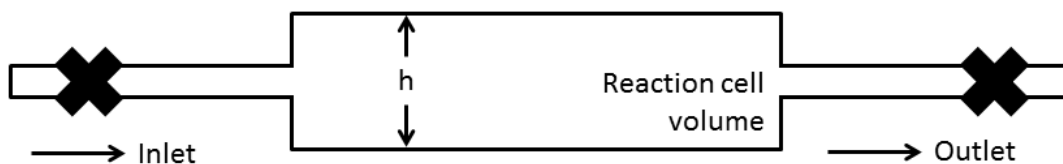


Figure 3.9 - Simplified coulometric flow cell schematic

cyclical manner. This process would prevent an electrochemical reaction from proceeding to completion, which ideally would be indicated by an electrochemical current decaying to zero (or at least to a constant value). Placing all electrodes in close proximity would allow an oxidized analyte to diffuse to the counter electrode, undergo a reductive process there, then diffuse back to the working electrode and reoxidize. In the case of electrochemical cells that are under constant flow (streaming), where reactants created at the work and counter electrodes are immediately carried away by the flow stream, reversible processes are not an issue.

Therefore, to allow experimentation on both reversible and non-reversible analytes in a volume that is essentially stagnant, a dual-chamber design was necessary to separate and, by including a selectively permeable membrane between the two volumes, electrochemically isolate the counter and working electrode. A schematic of this type of design is shown in Figure 3.10 (not to scale). The bottom reaction cell volume will contain the working electrode, and the height of this volume will be restricted according to the thin-layer flow cell specifications. The upper cell volume will include the counter electrode; the height/volume of this chamber is not critical since the reaction current measured at this electrode is optional and any current generated from a reversible process will drastically lag the working electrode current since the reaction species will spend time migrating through the membrane separating the working and counter electrode chambers.

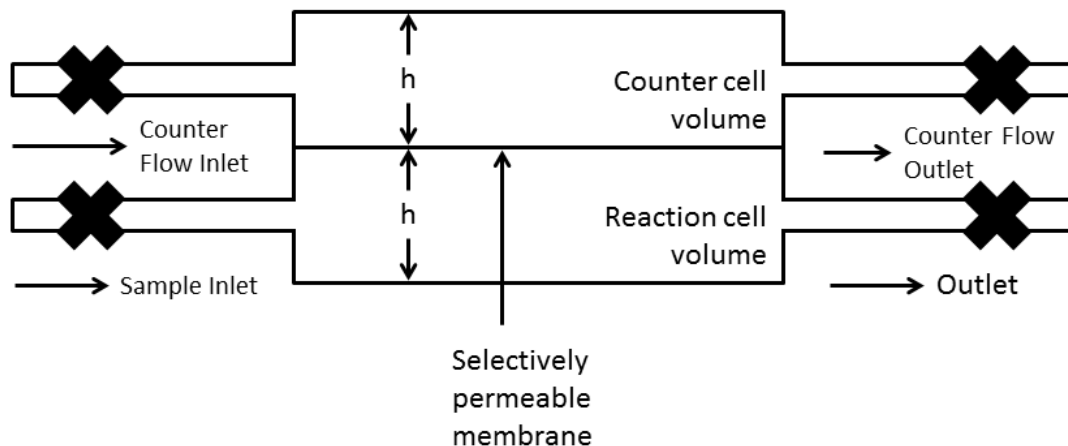


Figure 3.10 - Simplified flow cell schematic to account for reversible reactions

### 3.2.2 Computational Fluid Dynamics

Previous research performed by our group has indicated problems with clearout of injected sample and complications from permanently trapped bubbles in microfluidic channels that are designed with sharp geometries [57, 58]. To prevent these problems from occurring, preliminary two and three-dimensional computational fluidic dynamic studies (CFD) of the oval shaped flow cell were performed using finite element analysis (COMSOL, Waltham, MA). These investigations established an analytical solution for the analysis of the pressure drop through the system considering a flow cell with an overall area that matches the sensor design and a cell height that conforms to the thin-layer theory. Additionally, this study was performed to obtain flow visualization results to confirm that the proposed oval cell geometry would provide an effective flow that would successfully flush out reactants between experiments. In chromatography and electrochemical terms, the fluidic dead volume is any amount of fluid within the flow system that is not swept by the mobile phase. In the case of a stopped flow thin-layer cell,

any dead volume retained between experiments could (deleteriously) affect the determination of total charge in the sample.

The calculation of the pressure drop for circular inlet and outlet channels treated as round capillaries is easily calculated (neglecting gravity) using the Hagen-Poiseuille relationship:

$$\Delta p = \frac{8\mu L Q}{\pi r^4} \quad \text{Equation 3.5}$$

where  $p$  is the pressure,  $\mu$  is the dynamic viscosity,  $L$  is the length,  $Q$  is the volume flow rate, and  $r$  is the radius of the channel. The variable-width, thin-layer volume adds considerable complexity to the calculation, an obstacle the CFD software can easily handle. For the simulation, incompressible, laminar flow was assumed since the smallest channel diameter was 500  $\mu\text{m}$ , and this type of undisturbed flow dominates for systems with Reynolds numbers less than approximately 2000 [98]. The simulation boundary conditions used included zero flow condition at the walls, the fluid in the flow chamber was considered to be water ( $\rho = 1,000 \text{ kg/m}^3$ ,  $\mu = 0.0114 \text{ gm/cm-sec}$ ), the outlet pressure was set to 1 ATM, and the flow through the system was varied between 10 and 10,000  $\mu\text{L/min}$ . Using the standard equation for estimating the Reynolds number for channels with circular cross section

$$Re = \frac{\rho U D}{\mu} \quad \text{Equation 3.6}$$

where  $Re$  is the Reynolds number,  $\rho$  is the density of the fluid,  $U$  is the average velocity of the fluid,  $D$  is the diameter of the pipe, and  $\mu$  is the viscosity of the fluid, the calculation yields a maximum  $Re$  of approximately 37, well under the turbulent flow

threshold, and justifying the assumption of laminar flow. Assuming steady-state conditions and a constant viscosity, the momentum balance equation can be reduced to a simpler form

$$\rho(\mathbf{v} \cdot \nabla \mathbf{v}) = -\nabla p + \mathbf{f} \quad \text{Equation 3.7}$$

where  $\rho$  is the density,  $\mathbf{v}$  is the velocity field,  $p$  is the pressure, and  $\mathbf{f}$  is the force acting on the volume (gravity effects). By providing the average volumetric flow rate, the outlet pressure, and the density of the fluid, the calculation of the complete pressure drop through the system will be obtained which will help to determine the theoretical pressure range while injecting analyte sample through the system.

### 3.2.3 Custom Flow Cell Design

To allow experimentation with both reversible and non-reversible reactions, the primary components of the cell were designed in two parts that form the entire flow system after assembly.

Figure 3.11 shows an exploded isometric schematic view of the flow cell including all layers which include the upper and lower portions, the semi-permeable membrane layer, an upper gasket layer, a lower “chip” gasket that defines the thin-layer cell volume, and the microfabricated sensor. Two alignment pins (D=2 mm, not shown in Figure 3.11) were included to aid in alignment during assembly.

The electrochemical flow cell includes inlet and outlet ports for the sample stream containing the analyte, in addition to the pair of inlet and outlet ports for the counter-chamber buffer stream. All manifold channels machined into the body of the flow cell were designed to be 500  $\mu\text{m}$  in diameter. The two separate chamber volumes are

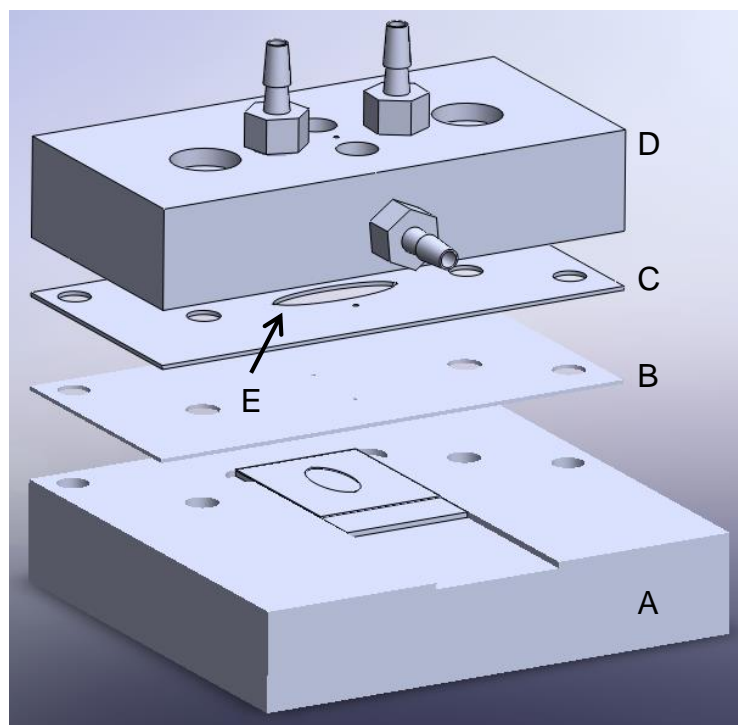


Figure 3.11 - Flow cell three-dimensional model/schematic diagram showing the major layers; (A) Bottom section of the flow cell; (B) Membrane layer; (C) Rubber gasket layer; (D) Top section of the flow cell; and, (E) Outline of the counter electrode chamber volume for the cell.

separated by a selectively permeable membrane with a molecular weight cutoff of 390 g/mol (Koch SelRO MPF-34, Koch Membrane Systems, Wilmington, MA) that can be removed and replaced during assembly; the type of membranes used can vary depending on the analyte under study. Since the area of the reaction chamber is defined by the general elliptical shape described in Section 3.1.1, the third and final dimension of the reaction volume is defined by the thickness of a rubber gasket (ultra-pure silicone rubber, described previously) to establish the vertical dimension  $h$ .

The two main flow cell components are separated first by the semi-permeable membrane followed by a gasket layer to prevent leaks (Silicone Rubber, aka polysiloxane; 70 Durometer, McMaster-Carr). Both of these layers were designed to extend the full width and length of the top cell layer of the flow cell and also contain



holes for alignment, holes for the screws to pull the two main parts together, as well as 500  $\mu\text{m}$  diameter holes to allow passage of sample. Since the volume of the counter chamber is not restricted by the thin-layer criterion, a fixed volume for this chamber is included in the top half of the flow cell. The general shape of this chamber is also elliptical in shape (13 x 4 mm) set at 90° to the thin layer chamber below and is designed to be 500  $\mu\text{m}$  deep. While the depth of this chamber that is included in the top of the cell is not shown in Figure 3.11, the general outline is included in the rubber gasket and is shown in Figure 3.11E.

The bottom portion of the cell (Figure 3.12) contains a trench (depth = 630  $\mu\text{m}$ ) that holds and positions the sensor platform correctly in place prior to assembly of all parts. The fluidic inlet and outlet manifold interfaces normal to the chip surface. To accommodate the slight variability in sensor size due to the dicing process, where the length and/or width of each sensor after separation from a full wafer may be slightly larger or smaller than the specified values, the trench width is designed to be 5% larger than the sensors. All fluidic ports were configured to align with the sensor using only

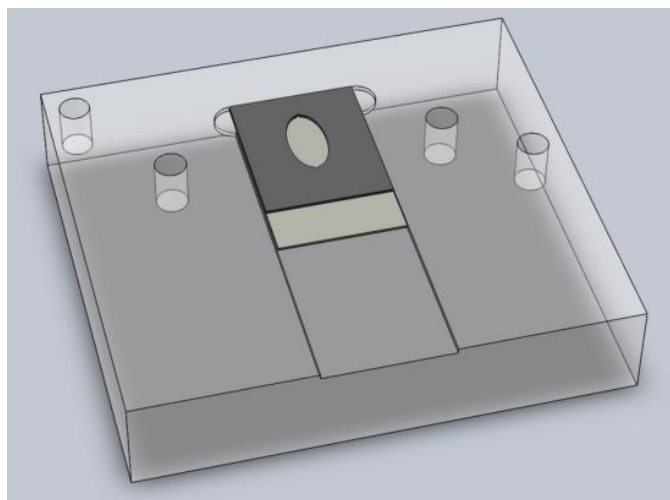


Figure 3.12 - Bottom half of the flow cell indicating the trench, sensor, and sensor gasket

the left and back sides of the diced sensor as positioning features. Therefore, the distance of features on the chip from both the left and back of the chip are the critical distances and should accommodate a variability of several microns.

#### 3.2.4 Flow Manifold Materials

Polycarbonate (commercially known as Lexan™) was used to fabricate the flow cell due to its availability, relative low cost, ease of tooling, and inertness with regard to the types of chemicals used in this study. Compared to other possible machineable plastic platform materials such as PEEK or Teflon, the former is prohibitively expensive, while the latter is difficult to machine within a specified tolerance.

#### 3.2.5 Fabrication

All of the flow cell components described above were designed in SolidWorks™. The design files of the top and bottom components of the flow cell were sent to either a local (Rapid Prototyping Center, University of Louisville, Louisville, KY) or online machine shop (Firstcut, Maple Plain, MN) and fabricated via precision CNC machining with an advertised machining tolerance of 0.0005" (12.7 μm) for polycarbonate. For the external service, turnaround time for fabrication of parts via this service was typically three to five days after model submission (via e-mail) and error checking. Two recessed screw holes were included in the design to secure all layers; however, a screw tap (10-32) was used to create threads in these holes in the bottom half of the cell after receiving the parts from the vendor. This was done primarily to cut down on additional tooling costs, which greatly increased when threading steps were added to the order. All gasket materials and chemical membranes were fabricated using a desktop laser cutter/engraver

(Epilog, Golden, CO) configured for use as a precision cutting tool. Designs for the gaskets and membranes were drawn in AutoCAD and exported to a DXF file format for import into Adobe Illustrator (Version 2011, Adobe Systems Incorporated, San Jose, CA). This vector-based software, combined with the system printer drivers for the laser engraver, allowed the gaskets to be precision cut in the lab, instead of requiring an outsourcing step.

### 3.2.6 Assembly

Figure 3.13 shows an isometric view of 3D model of the assembled flow cell. A portion of the electrochemical sensor is left exposed to allow electrical connection via a custom multi-pin connector (not shown). Two alignment pins at each corner aid in alignment (added in a later generation cell design), and two screws (hand-tightened) firmly pulled the assembly together. The tall columnar feature in Figure 3.13 is the external reference electrode (gold wire, 0.5mm, Alfa Aesar, Ward Hill, MA), which was manually inserted into the counter electrode chamber and glued in place with epoxy to secure and to prevent leaking. A recess was incorporated into the roof of the counter chamber (not shown) that is geometrically positioned at the center of the oval working electrode area. The gold wire was manipulated to coil and fit into this recess in order to expose the gold electrode to the counter flow with a larger surface area than the simple diameter of the wire. A larger counter electrode lowers the density of the current flowing into this electrode. A unique feature of the sensor trench and chip gasket design is shown in Figure 3.14 where the gasket is laid on the sensor, centered on the oval electrode area, and the sensor chip plus gasket is initially higher than the depth of the trench. Upon assembly, the chip gasket is compressed and, therefore, the final cell height is defined by

the thickness of this layer. This allows experimentation of varying cell volumes without having to fabricate new top and bottom components. The trench was designed to be 450

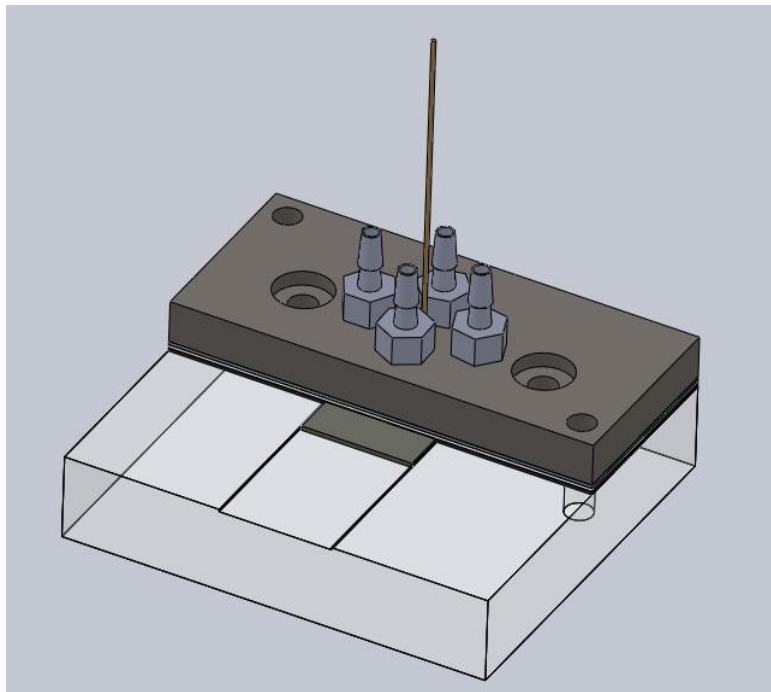


Figure 3.13 – 3D model of the assembled Flow Cell.

$\mu\text{m}$  deep, and the uncompressed gasket (ultrapure silicone rubber) is roughly 120  $\mu\text{m}$  thick.

The gasket material used has a large thickness tolerance (typically +/- 50% of the nominal (specified) thickness, each gasket was measured to ensure the thickness dimension greater than the difference between the trench depth and sensor thickness (~535  $\mu\text{m}$  for a 100mm silicon wafer). The thickness of the full assembly was measured to reveal any deviations from the expected thickness (assumed to be equal to the sum of the two individual thicknesses of the top and bottom cell parts). Additionally, from experimental data, the actual cell volume was back calculated from experimental data using the known analyte concentrations and compared to the expected cell volume.

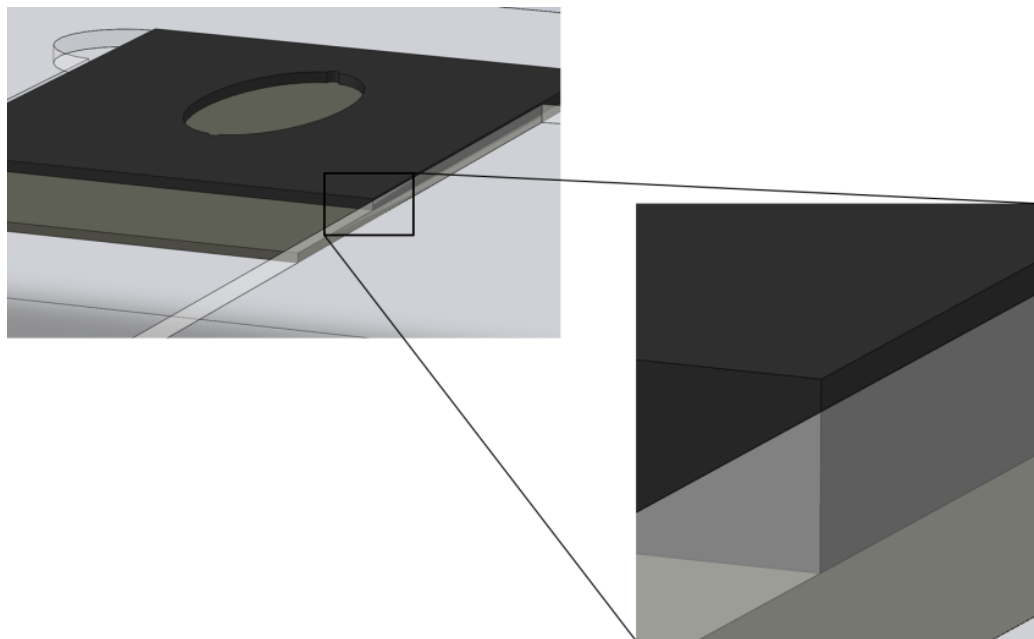


Figure 3.14 – 3D visualization of the chip gasket compression prior to full assembly.

### 3.2.7 Fluidic Connections

Either simple barbed or quick connect fittings (size 4-40, Small Parts Inc, Logansport, IN) and flexible Tygon tubing (6519T14, McMaster-Carr, Aurora, OH) were used to connect all fluidic ports on both the counter and working electrode flow chambers. Separate 100 cc syringes were used to manually inject buffer solution into the counter electrode chamber and sample solution into the working electrode chamber.

### 3.2.8 Pressure Testing

Pressure testing was used to verify success in alignment between the manifold channels and the chip gasket inlet/outlet features and was performed in two ways. First, a digital pressure gauge was connected inline using a “tee” connector to the inlet port and

the system was closed to atmosphere after filling with buffer solution. This assembled system configuration was pressure tested by plunging the syringe closed and noting the increase in pressure while watching for any leaks. Secondly, the system outlet was vented to atmosphere with solution remaining in the system. In this case, the fluid was slowly introduced into the system and pressure monitored as the fluid was ejected from the outlet port. The max pressure recorded was expected to be near the simulated pressure for the pressure drop in the system. While validation of this criterion was not absolutely critical for operation of the system, the eventual incorporation of automated loading techniques such as micro pumps will have a maximum pressure rating, and therefore, the system should be designed to not exceed these values. The system should reveal a pressure test that indicates no leaking occurs at internal pressures below the flow pressure test levels.

### 3.3 Instrumentation

In this section, an overview of the instrumentation used to analyze the sample contained within the exhaustive coulometric flow cell is presented. This will include a description of the custom potentiostat and supporting sub-circuits and the data acquisition (DAQ) equipment and associated electrical connections used by the control software.

#### 3.3.1 Electrochemical Cell Equivalent Circuit

Inarguably, the simplest electrochemical experiment is the application of a fixed (constant) oxidation or reducing potential at a working electrode in the presence of an oxidizable or reducible analyte and the associated measurement of the current that is produced during the chemical reaction. Conversely, an analogous experiment would be to apply a constant current and measure the change in potential as the reaction occurs. To

explain what happens electrically inside the cell during a reaction, Figure 3.15 shows a representative schematic diagram of the three-electrode configuration. Equivalent circuits such as these, also known as “dummy cells”, are used to test and calibrate electrochemical apparatus such as potentiostats and pH meters. In this somewhat idealized circuit,  $I_{reaction}$  is what needs to be monitored and related to the concentration of the analyte. Since there should be no current flowing into the high impedance reference electrode,  $I_{reaction}$  is ideally the only current flowing in the cell and travels between the counter and work electrodes. The resistors included in the circuit represent the equivalent electrical resistance of the fluidic medium experienced by the electrodes. The capacitor  $C_{work}$  represents the double layer capacitance between the working electrode surface and the fluidic medium. This capacitance exists at all electrode-fluid interfaces, but is only shown at the working electrode surface to simplify the diagram. The voltage at the reference electrode is compared to the applied voltage which must be held at a constant value during the reaction. Flowing current and local changes in concentration during oxidation/reduction will induce changes to the overall cell impedance; therefore,

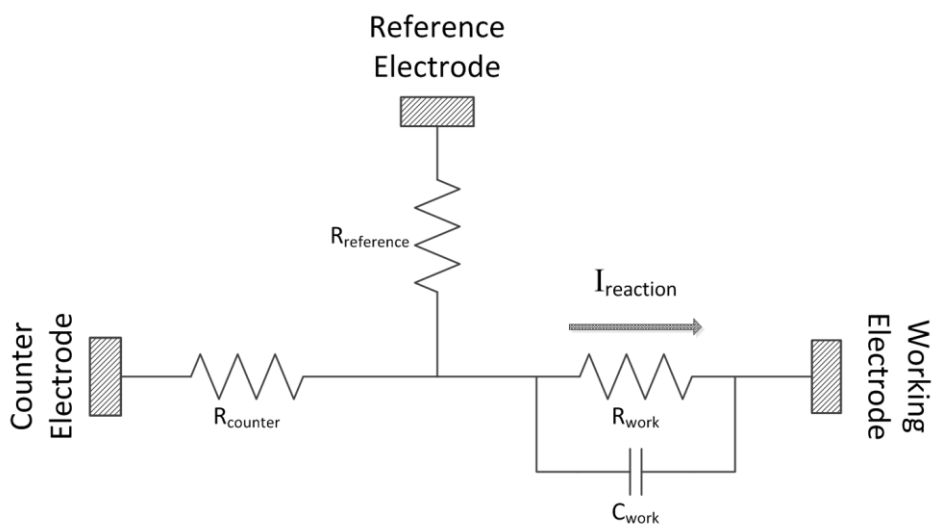


Figure 3.15 – Flow cell equivalent circuit.

feedback is required to hold the applied potential. To accomplish these (and other) tasks, a custom potentiostat was designed to hold a constant applied voltage via feedback from the reference electrode voltage, and measure the current flowing in the cell during a reaction.

### 3.3.2 Potentiostat Circuit

The full potentiostat circuit schematic and printed circuit board layout are included in Figure 4.26 and Appendix E, respectively; however a description of each major component is outlined in the following sections.

#### 3.3.2.1 Trans-Impedance Amplifier Circuit

In Figure 3.15, the magnitude of  $I_{reaction}$  is the critical measurement. This current will vary in proportion to the concentration of the sample, and a trans-impedance amplifier (Figure 3.16) was used to monitor this current at the work electrode. Trans-impedance in this case is indicative of the conversion of current to voltage. The current source in this figure is the current generated by the oxidation/reduction reaction. The amplifier converts this current to a voltage ( $V_{OUT}$ ) that can be measured directly. The “+” input is connected directly to ground and creates a “virtual ground” for the electrochemical cell. This configuration is convenient since by adjusting the value of the feedback resistor (R1), the gain response can be directly adjusted to accommodate the range of current that is expected, which is proportional to concentration.



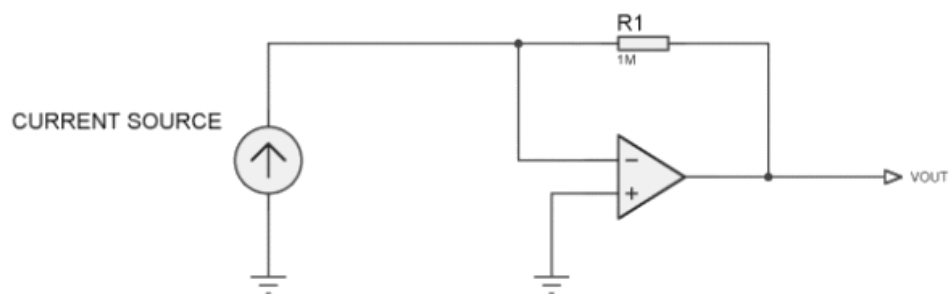


Figure 3.16 – Simplified trans-impedance amplifier circuit; TLC 2202 op-amp used at this stage.

The equation that relates the current flowing in the cell to the voltage at the output of the trans-impedance stage is related by:

$$V = -I_r R \quad \text{Equation 3.8}$$

where  $I_r$  is the reaction current,  $V$  is the voltage at the output of the trans-impedance stage, and  $R$  is the feedback resistor. This simple relationship can be recognized as a slight variation of Ohm's Law, with a negative sign included in the equation due to the use of an inverting op-amp configuration. The gain relationship established by the magnitude of resistor  $R$  has units of Volts/amp, and therefore, increasingly large resistance values of 100 Ohm, 10 kOhms, 1 MOhm, and 100 MOhms were used to measure current responses at 10 mA/V, 100  $\mu$ A/V, 1  $\mu$ A/V, and 10 nA/V, respectively. These magnitudes/ranges were based on previous studies at the concentration levels for the test analyte outlined previously and to make the potentiostat sensitivity range as wide as possible for other possible uses. To indicate how the gain selection affects the voltage measurement for different reaction current magnitudes, Table 3.1 lists the input current magnitudes that establish a one-volt output and the resulting gain settings necessary to

make this happen. Proper selection of the gain will depend on the particular experiment, where larger concentrations yield proportionately larger currents. For example, the highest gain setting, which corresponds to the greatest sensitivity (0.01 nA/V), is used on the lowest concentrations.

Table 3.1

Trans-Impedance Amplifier Feedback Resistor Gain Settings

<i>Current Range</i>	<i>Gain Setting</i>	<i>Resistor Value</i>
+/- 10 mA	10 mA/V → 0.1 V/mA	100 Ohm
+/- 100 μA	100 μA/V → 0.01 V/μA	10 kOhm
+/- 1 μA	1 μA/V → 1 V/μA	1 MOhm
+/- 10 nA	10 nA/V → 0.1 V/nA	100 MOhm

Selection of a particular gain configuration was designed to be set via a rocker switch on the potentiostat printed circuit board. Feedback capacitors were included in the design and were placed in parallel with the feedback resistors (10 μF, 0.1 μF, 1 nF, and 10 pF) to reduce high frequency noise and prevent oscillation in the gain stage. The combination of each of these parallel RC combinations establish a low-pass filter, with a target corner (cutoff) frequency of 160 Hz, and a roll-off of -20 dB/decade. It is important to establish a relatively high cut-off frequency (~ 1200 Hz) since the measurement of the reaction includes a large (in magnitude) initial transient (which is partially due to the charging current at the surface of the electrode) when the applied potential is stepped to the appropriate value. An over-aggressive low-pass filter would artificially suppress the large transient current and would erroneously reduce the calculated total charge.

### 3.3.2.2 Applied Potential Location

While it is necessary to apply the required reaction potential at the working electrode at a level sufficient to initiate the desired oxidative/reductive process, measuring the current flowing through the cell and into/out of this electrode during the reaction is problematic. The dynamic range of the instrumentation is drastically reduced when the output voltage is high due to the applied potential relative to the current being measured. Additionally, the output of many op-amps is often limited to approximately 90% of the supply voltages (in this case, +/- 5V). To ensure that the dynamic range at the trans-impedance stage is maximized, and the full output voltage swing is utilized for the higher sensitivity settings, the working electrode potential is held at a virtual ground established by the op-amp (the positive terminal of the op-amp in Figure 3.16), and a specialized, low-noise, precision op-amp (TLC2202, Texas Instruments, Dallas, TX, Appendix B) that is designed to operate in a rail-to-rail mode was used at this stage.

Accordingly, in order to successfully apply the appropriate reaction potential to initiate the oxidation/reduction reaction at the work electrode, the applied potential is established at the counter electrode and given opposite polarity. For example, a 400 mV applied potential at the work electrode is established by applying -400 mV to the counter electrode. The working electrode is therefore said to be 400 mV positive with respect to the counter electrode and the reaction proceeds as if the requisite potential is applied directly to the working electrode.

### 3.3.2.3 Feedback Circuit

The electrical schematic in Figure 3.17 outlines an expanded version of the potentiostat circuit with the trans-impedance amplifier op-amp removed to simplify the diagram. To monitor the applied potential for use as a feedback control signal, the voltage measured at the reference electrode was fed into an op-amp configured in a follower

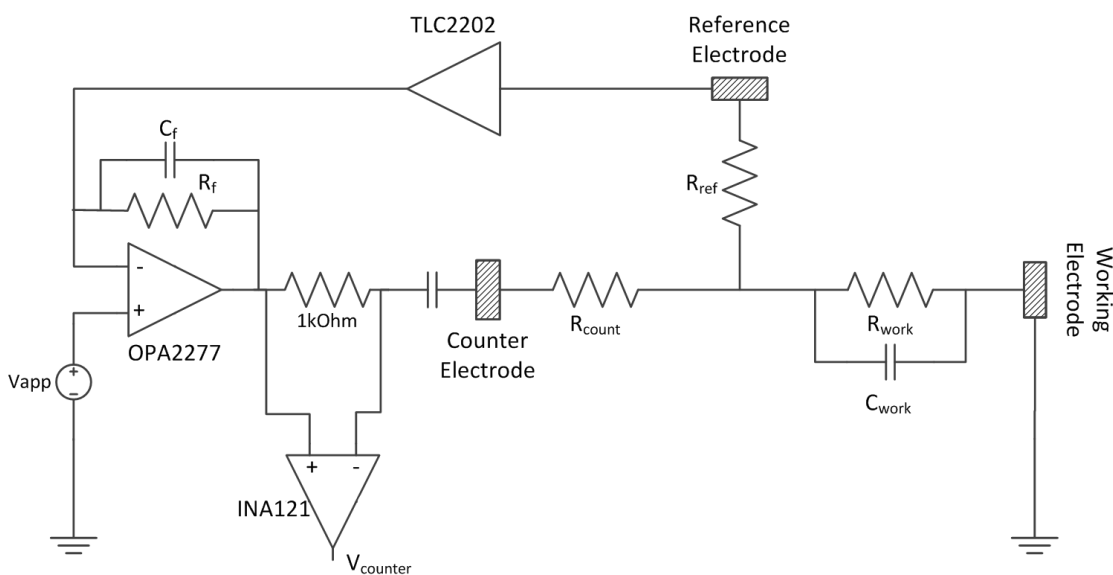


Figure 3.17 - Expanded Potentiostat Schematic showing feedback path through the buffer/follower (TLC2202) and into the control op-amp (OPA2277).

configuration op-amp (TLC2202, Texas Instruments, Dallas, TX). The input impedance of this device approaches 10 GOhms ( $10^9$  ohms), which is beneficial since this property effectively prevents current generated in the electrochemical cell from being drawn into the reference voltage measuring circuit. The ideal assumption is that there is zero current entering into the terminals of the op-amp. In reality, there is a bias current flowing into the op-amp, but it is on the order of pico-amps ( $10^{-12}$  A), which is approximately 100,000

to 1,000,000 times smaller than the current passing through the cell, and therefore is considered negligible and can be ignored in all calculations.

The voltage measured at the reference electrode is used to compare the target applied potential to the actual applied potential. There is no gain in the follower configuration, so the 1:1 voltage at the output of this buffer/follower stage was applied to the negative input of another op-amp (OPA2277, Texas Instruments, Dallas, TX). The applied potential ( $V_{app}$ ) is applied to the positive input of this op-amp and the output is adjusted to hold the voltage constant. A series resistor at the output of the  $V_{Ref}$  buffer amplifier and a parallel resistor/capacitor combination in the feedback path ( $R_f$  and  $C_f$  in Figure 3.17) were included to prevent oscillation. The actual values used (details included in Appendix A) satisfy certain electrical criteria for stability and were determined experimentally [89]. Collectively, the voltage established at the output of this op-amp stage (OPA 2277) establishes the appropriate  $V_{app}$  at the counter electrode and the feedback path provides a measured value so when an oxidation/reduction reaction occurs (an event which will attempt to pull the established voltage away from the set point), the feedback will force the output of the op-amp to compensate and, as a result, hold the applied potential at the desired setting.

The current provided (*sourced* in the case of positive current where current is flowing out of the counter electrode) or consumed (*sinked* in the case of negative current where current is flowing into the counter electrode) by the control amplifier during the reaction is also measured behind the counter electrode through an instrumentation, or differential, op amp (INA121, Texas Instruments, Dallas, TX), which is an alternative configuration to measuring current compared to the trans-impedance amplifier. In this

case, the voltage drop across a “shunt” resistor (the 1 kOhm resistor in Figure 3.17) is measured by connecting the positive and negative terminals of the differential op-amp to the terminals of this resistor. The magnitude of the shunt resistor which is electrically in series with the electrochemical cell, is assumed to be much smaller than the resistance through the cell, and does not, therefore, affect the electrochemical performance of the cell. The gain of this instrumentation amplifier is set by a single resistor, and was chosen appropriately for the range of currents expected in the electrochemical reactions outlined later in this chapter. The counter current may then be calculated using Equation 3.9 which combines Ohm’s Law and the gain of the circuit which sets the relationship between  $V_{out}$  and  $V_{in}$

$$I_{counter} = \frac{V_{out}}{R_{shunt}} \quad \text{Equation 3.9}$$

where  $I_{counter}$  is the current through the resistor  $R_{shunt}$ ,  $V_{out}$  is the voltage measured at the output of the differential op-amp, and  $G$  is the gain of the op-amp. This current should ideally be equal in magnitude to the current measured with the trans-impedance amplifier circuit.

### 3.3.3 Analog-to-Digital Conversion

All analog-to-digital (A/D) and digital-to-analog (D/A) conversion was achieved by using a National Instruments PCMCIA card (DAQCard-6062E; detailed technical specifications are outlined in Appendix C) inserted into a laptop (Latitude D505, Dell, Round Rock, TX) running Windows XP (Microsoft Corporation, Redmond, WA). A laptop was used to allow for portability of the system and to allow rapid development

updates and alterations to the software interface. The A/D converts analog voltages to a digital representation at a 12-bit resolution ( $2^{12}$  levels) at a maximum acquisition rate of 500,000 samples/second with a maximum and minimum measurement level of +10 volts and -10 volts, respectively. The 12-bit resolution establishes the smallest measurement level governed by the following relationship:

$$\frac{Range}{Resolution} = \frac{V_{max} - V_{min}}{2^{12}} = \frac{20\text{ Volts}}{4096\text{ steps}} = 4.883\text{ mV}/step$$

This sensitivity rating, however, assumes a full scale measurement and can be greatly improved by adjusting software settings to restrict the max/min range to the output limits of the actual measurements performed with the system. The practical limits of the outputs in the potentiostat are constrained by the power regulation circuit which was designed to operate at  $\pm 5V$ ; therefore, the A/D sensitivity was appropriately adjusted in software to:

$$\frac{5\text{ V} - (-5\text{ V})}{2^{12}} = 2.441\text{ mV}/step$$

and the resulting smallest change in voltage that can be reported is  $153\ \mu V$ .

The D/A converter output channel, which converts a digital voltage selection chosen in software to an equivalent analog representation, has a range of  $\pm 10$  Volts, and also has a resolution of 12 bits ( $2^{12}$  levels). The smallest voltage increment that can be applied is obtained similarly to the A/D using the following relationship:

$$\frac{V_{max} - V_{min}}{2^{12}} = \frac{10\text{ V} - (-10\text{ V})}{4096} = 4.883\text{ mV}/step$$

The range of applied potentials ( $V_{app}$ ) that will be required were limited to +/- 2 volts since that is the upper range for oxidation/reduction half-cell potentials; applied potentials beyond the half-cell potentials (either positive or negative) tend to cause bubble generation due to the spontaneous oxidation or reduction of water (either  $H_2$  or  $O_2$ , both in the gaseous state). By restricting the voltage range in software to these maximum and minimum values, the output sensitivity of the applied voltage can likewise be improved to the following value.

$$\frac{2 V - (-2 V)}{2^{12}} = 0.977 \text{ mV}/step$$

If this sensitivity is compared to a typical applied potential of 400 mV, an error of +/- 0.977 mV would establish a possible error range of applied voltages between 400.977 mV and 399.033 mV, with an upper and lower percent error of less than 0.1 percent.

### 3.3.4 Physical Connections

The data acquisition card was connected to a breakout board (CB-68LP, National Instruments, Austin, TX) for making the physical connections between the potentiostat circuit input and output channels (Table 3.2). Four physical input channels were used for monitoring the counter electrode current, the reference voltage, and the working electrode current for the electrochemical reaction, as well as two additional inputs for monitoring the battery levels. An additional pin was used as a common (Ground) connection. The full schematic of the physical pin connections for this DAQ card and associated breakout board are included in Appendix C.



Table 3.2

Electrical Connection Breakout Board Connection

<i>CB-68LP Pin Number</i>	<i>DAQCard-6062E Channel</i>	<i>Connection</i>
1	AI08	Counter current
2	AI06	Reference voltage
3	AI12	Work Electrode current
4	AI0	V <sub>cc</sub> +
5	AI1	V <sub>cc</sub> -
6	AO0	Applied Voltage

## 3.3.5 Power Regulation

The potentiostat was designed to be powered by a split power supply using either two traditional 9V cells or two 9V rechargeable battery packs, each containing eight 1.2V NiMH cells. Either power supply was fed into a sub-circuit containing a fixed output regulator (Figure 3.18) set to provide  $\pm 5V$ . Two bypass capacitors were included to minimize high frequency ripple. The regulator circuit (LM340 Family, Texas Instruments, Dallas, TX) was designed to hold a fixed voltage at the output terminal as the battery supply drops from a full charge. Additionally, this regulation ensures that the  $\pm 5V$  provided to all of the op-amps in the potentiostat are at the same potential.

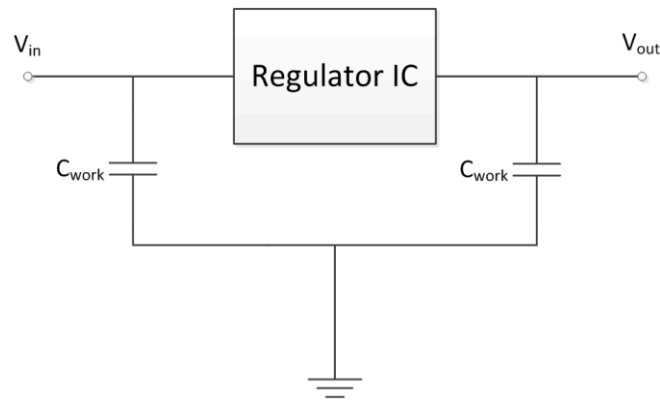


Figure 3.18 – Voltage regulation schematic. The LM340 family of three-terminal regulators was used in the potentiostat circuit.

### 3.3.6 Custom Printed Circuit Boards

Custom design and fabrication of electronic circuits has also reached the desktop, as free, “open-source” software packages allow end users to accurately simulate analog and digital circuits, source all necessary parts and connectors, and then quickly follow through with high-quality prototype printed circuit boards (PCBs) [99]. Typically, electrical (and mechanical) designs containing board geometry, electrical layer number and thickness specifications, and associated electronics component lists can now be checked for errors almost instantaneously via a web page submission or with a quick follow-up e-mail. While custom circuit boards used to be fabricated with messy copper plating solution and crude lithographic masks containing the desired circuit layout to transfer, early prototypes can now benefit from custom production facilities that not only create the circuit boards, but also order the circuit components from a provided bill of materials and populate the board with those parts. These services have experienced fierce competition so costs can be as low as \$33 per board for a 60 in<sup>2</sup> maximum area printed

circuit board design, typically with a three to four day turnaround once error checking has been completed [100].

To take advantage of these modern services and technologies, the potentiostat circuit schematic was created in ExpressSCH schematic software (ExpressPCB, Santa Barbara, CA), transferred to ExpressPCB software, and transmitted to the company headquarters using the MiniBoard option for a quick return of the completed PCB. This option provides a three-day turnaround on three boards for less than \$100, including a solder mask and silkscreen to isolate metal pads and highlight the location of parts on the board, respectively.

### 3.3.7 Electrical Testing

In order to test the individual electrical sub-circuits several electrical tests were performed. Minimization of the high-frequency noise floor and offset voltages were critical to the success of the instrumentation stage of the system. Frequency response of the gain stages were also critical to evaluating the ability of the potentiostat to adequately respond to the current generated by a redox reaction due to the application of a step potential.

#### 3.3.7.1 Ripple and Offset Voltage

A ripple and offset voltage measurement was performed on the regulator circuit and potentiostat amplifier circuit to determine the magnitude of any oscillations that may affect the rest of the potentiostat sub-circuits as well as any zero offset voltage that may artificially influence the amperometric data. The bypass capacitors included in Figure 3.18 were included primarily to short any high frequency signal contained within the DC

power regulation components to ground and smooth the ripple that is often observed at the output of the regulator. This is typically seen in regulation circuits that perform some form of AC to DC conversion, and is not expected to be an issue in this circuit. However, these bypass capacitors will also provide instantaneous current in response to rapid changes in output at the onset of a redox reaction. In any case, any oscillations that enter the operational amplifiers, whether through the power supplies or the input terminals, will show up in the output signal and possibly influence the interpretation of the amperometric data; thus, careful steps must be taken to reduce this possibility.

The magnitude of any ripple present in either supply should be kept to a minimum, ideally less than a single bit on the input resolution of the A/D converter (2.441 mV for a range of -5 V to 5 V). This magnitude was chosen as the maximum voltage allowable at the output with no input; a measured voltage greater than this would require additional steps to null the offset. To measure the ripple, an oscilloscope (DS1052E, Rigol Technologies, Oakwood Village, OH) was used to measure the output of the power regulation circuitry. Additionally, with the inputs of each op-amp stage held at 0 V, the output voltage was measured and recorded to observe any offset voltage or apparent peak-to-peak noise present at each output stage.

### 3.3.7.2 Potentiostat Electrical Performance

To test the electrical characteristics and performance of the entire potentiostat circuit, a small circuit containing fixed resistors and capacitors was constructed. As explained previously, the *dummy cell* was connected to the potentiostat through the counter, reference, and working electrode terminals. By knowing the individual resistor and capacitor values of the components ( $R_{\text{count}}$ ,  $R_{\text{ref}}$ ,  $R_{\text{work}}$ , and  $C_{\text{work}}$  in Figure 3.19), the

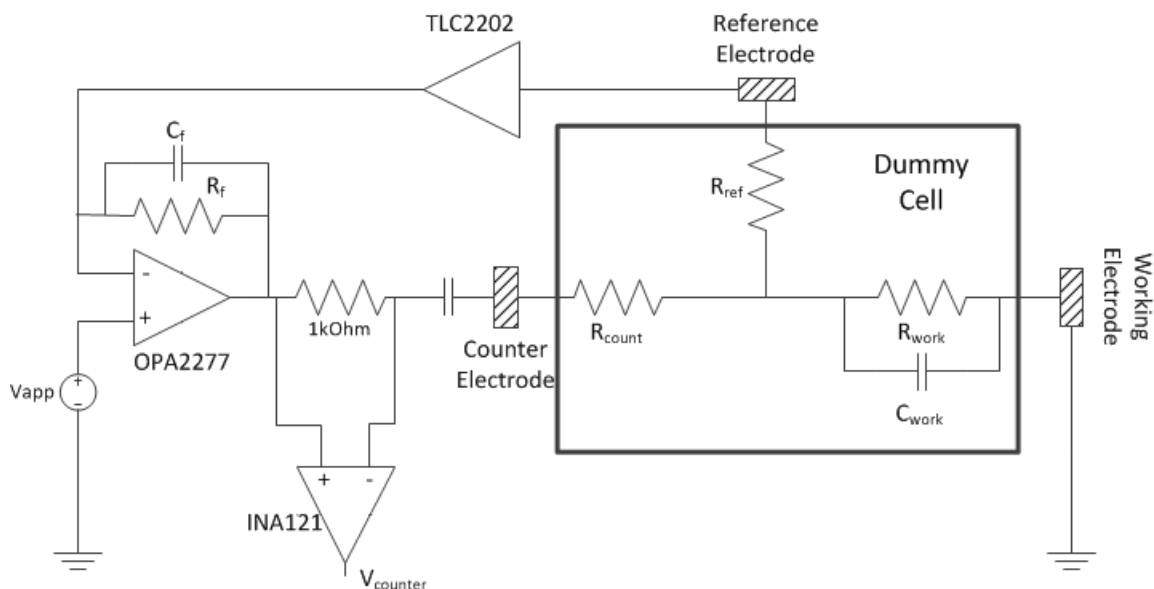


Figure 3.19 - Potentiostat schematic highlighting the *dummy cell* (inside the black box), which is a simple electronic circuit used to mimic an electrochemical cell.

currents and voltages measured in both the trans-impedance circuit and the differential measurement circuit can be evaluated and compared to expected values.

To evaluate the sensitivity and linearity of the trans-impedance circuit, a constant current source supplying currents of 1 pA, 10 pA, 100 pA, and 1 nA were injected into the input of this op-amp stage and the output voltage was measured to test each gain setting. Similar to the ripple measurement, the noise floor was measured by grounding all input electrodes and measuring the output voltage. To evaluate the transient response of the system for the particular RC combination (work electrode), a range of step input voltages from 0 to 1.5 volts in steps of 0.1 V were applied and the output was recorded. The transient response could then be compared to the theoretical curve for a first order system responding to a step input.

Each of the gain resistors in the trans-impedance stage is paired with a corresponding capacitor both to stabilize the feedback signal and to act as a low-pass

filter. At high frequencies, the capacitor acts like a short circuit, which reduces the gain for signals that contain undesirable higher frequencies. The cutoff characteristics for each gain setting was analyzed by injecting a one volt (peak-to-peak) sine wave into the dummy cell counter electrode terminal and recording the output at the work electrode through the trans-impedance amplifier with both an oscilloscope and a simple LabVIEW program to visualize and record the data. The frequency of the sine wave was varied in increments from 1 Hz to 1000 Hz in roughly 10 steps per decade and the output was recorded. The output voltage was divided by the input voltage at each frequency and a frequency versus gain curve was generated to evaluate the filter performance.

### 3.4 Software

The analog potentiostat circuit was developed based on thoughtful analysis of electronic fundamentals. However, the essential functionality of the circuit was fixed by design constraints and the components used to create the circuit. Fortunately, the software that controls the analog circuit via the user (and by extension programmer) interface, has the added benefit of extending this functionality in many ways.

LabVIEW (National Instruments, Austin, TX) was chosen as the development platform to construct the software portion of the potentiostat since this software is a mature, visual programming environment that controls the data acquisition hardware and provides the programmer with the ability to create easy to use and highly functional user interfaces (UI). Several functional software programs were developed to support this work including: 1) a monitoring program for use during the electroplating process; 2) a main control program to perform the analytical experiments; and, 3) data processing

software for post-processing of the Coulometry data generated. All programs were written in LabVIEW (versions 2011SP1 and 2012) due to the rapid development capabilities of the software, as well as the close ties to the data acquisition modules used in the study. Although the data post-processing program was written in native LabVIEW, it was eventually compiled into an executable file to allow its use on any Windows computer. While LabVIEW is a powerful and functional platform for development, it is an extremely large (disk space intensive) program and performing an installation on office computers and laptops for the purposes of visualizing and importing data into other software packages was found to be time consuming, inconvenient, and impractical. All other programs used were coded and then left in the LabVIEW “VI” format (where VI stands for Virtual Instrument and is the native file type in LabVIEW).

#### 3.4.1 Electroplating Software

The setup to perform electroplating of Ag (followed by a chlorination step) required close monitoring of the average peak current flowing from the function generator to the sample under conversion. A 5-digit precision multimeter (34410A, Agilent Technologies, Santa Clara, CA) was used to monitor the current during both plating steps and the magnitude of the square wave applied to the sample was adjusted when the peak current drifted above the required 2 mA. An averaging algorithm using the peak current measured during the “on” phase of the square wave was incorporated into the program so the user could monitor the peak current over a specified period of time. A visualization of the current trend over the entire plating process was also displayed to aid in this step.

### 3.4.2 Electrochemical and Coulometric Analysis Software

In order to perform the necessary electrochemical experiments to successfully evaluate the performance of the coulometric cell and potentiostat, a custom control program with a convenient user interface was developed. The core functionality of this software involved controlling the applied potential and measuring currents during the experimental window. Additionally, the software was designed to measure the voltage of the power supplies unobtrusively in the background.

The control program was designed to run in two modes: 1) Cyclic Voltammogram mode; and, 2) Coulometry mode. In the former setting, the user could program the software to ramp the voltage between two values (with option to sweep between these voltages multiple times) and also control the scan rate between these voltages. The UI mode allowed the user to observe the electrochemical behavior of the electrode installed in the flow cell, both for confirmation that the electrode was functional, but also to observe the voltages where oxidation and/or reduction peaks occurred in a data set containing a standard sample. The latter setting, coulometry mode, was the primary operational mode of the software and allowed the user to set a voltage to which the system would step after a programmed hold period. After stepping to the requested voltage, the potentiostat detected the current generated inside the flow cell, converted the currents to measureable voltages and then the software recorded and converted these back to current and displayed the data to the user.



### 3.4.3 Data Processing and Interpretation

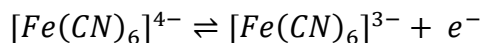
The data generated was saved to disk for post processing in a text-based file that contained details on the acquisition including a time stamp, acquisition rate, as well as the raw coulometric data for all three channels (work, reference, and counter electrode). In order to speed up and enhance the data analysis, a separate data processing program was developed to accurately convert currents into total recorded charge by noting the starting and ending locations of the experimental window and calculating the area under the curve. This program was compiled into an executable file, so data could be processed at any convenient PC since large quantities of data were generated during the experimental gathering phase.

## 3.5 Analytical Technique, Experimental Methods and Conditions

The following section outlines the analytes and electrochemical experiments conducted to evaluate the exhaustive coulometry system performance. In all experiments, analytes and solutions used were not purified after delivery from the manufacturer. Deionized water was obtained from an in-house system.

### 3.5.1 Model Analytes

The electrochemical system could be used for any electroactive species, and (potassium) *ferrocyanide* (VWR International, Batavia, IL) was used as the model analyte to initially evaluate the electrochemical performance of the system. This analyte was oxidized to *ferricyanide* in the reaction process described by the following representation:



This single electron, perfectly reversible process has been well characterized and extensively used in electrochemical studies [101-103]. While many of the salts complexed by cyanide are highly toxic, the ferro- and ferri-cyanide forms have greatly reduced toxicity since the iron form tends to not release free cyanide. Additionally, both of these cyanide salts have been used as a probe of extracellular electron receptors for studying oxidation reduction processes in cells [104].

To prepare the sample solutions, first a potassium nitrate buffer (KNO<sub>3</sub>) at a neutral pH (7.0) was created using 10.11 g of KNO<sub>3</sub> dissolved in one liter of deionized water. A main supply of 10 mM (Potassium)Ferrocyanide was made by dissolving 0.4224 g of the chemical in 100 mL of the KNO<sub>3</sub> buffer. Multiple concentrations (from 10 mM down to 50 μM) of ferrocyanide solution were formulated daily using this main supply. For example, to obtain a sample of 500 μM Ferrocyanide, 2.5 mL of the 50 mM supply was diluted with 50 mL of the KNO<sub>3</sub> buffer solution. Based on a single electron process and a cell volume designed to be 2.2 μL, Table 3.3 lists a sample of the expected charge for a few concentrations of the analyte. These values were calculated using Equation 1.2 using a sample volume of 2.2 μL. All other chemicals used (potassium nitrate and sodium chloride) in this study were purchased from Sigma-Aldrich (Milwaukee, WI) at the highest purity available and not further purified.

Table 3.3

Theoretical Total Charge Generated by the Oxidation of Ferrocyanide for 2.2  $\mu$ L Volume

Concentration ( $\mu$ M)	Calculated Charge ( $\mu$ C)
250	53.07
150	31.84
100	21.23
50	10.61

## 3.5.2 Analytical Chemistry Experiments

In order to evaluate the analytical performance of the system, two primary experiments were performed. First, a coulometric analysis was conducted, where the system was loaded with sample of a known concentration, an oxidation or reduction reaction was performed, and the data analyzed to determine if the reaction current decayed to zero, which would indicate whether or not all of the analyte was converted to the reduced or oxidized form. Secondly, chronoamperometry was performed to show the effectiveness of the membrane and the reversibility of the reaction when the analyte molecule was prevented from diffusing into the counter electrode chamber. A final coulometric determination was conducted using both the prototype potentiostat and a commercial detector as a head-to-head comparison of the analysis technique.

### 3.5.3 Exhaustive Coulometry

For a thin-layer electrochemical cell with critical dimension thicknesses between 2 and 300  $\mu\text{m}$ , the total experimental time for what was essentially a rapid bulk electrolysis process is related to the thickness using the equation:

$$\Delta = \sqrt{2 \cdot D \cdot t} \quad \text{Equation 3.10}$$

where  $\Delta$  is the critical dimension,  $D$  is the diffusion coefficient for the analyte, and  $t$  is time in seconds. Therefore, for a particular cell height that establishes the critical dimension, and assuming one dimensional diffusion (since the electrode area closely matches the cell volume area), the total time to complete the oxidative/reductive process in the cell was estimated. For example, if a one minute determination of total charge was required, using the reported diffusion coefficient for the analyte (Potassium Ferricyanide,  $D = 9.633 \times 10^{-6} \text{ cm}^2/\text{sec}$  [105]), the cell height must be a maximum 340  $\mu\text{m}$ . The rate of the reaction was exponential (the current measured exponentially decayed to zero, and the integrated charge increased exponentially to some constant value)) and was explained by the  $t^{1/2}$  factor in the equation, which is what is being examined in a typical Anson plot, which displays Charge (Y-axis) vs.  $t^{1/2}$  (X-axis). The curve was expected to be linear for a thin-layer cell.

Experiments were performed to observe the complete conversion of the model analyte to the alternate form and to determine the time necessary to reach the expected charge for each concentration of the model analyte. Cyclic voltammograms were taken to determine the appropriate electrolysis voltage for the model analyte. Applying the appropriate reduction potential was done by stepping from a holding potential (ex. 100

mV; no electrolysis) to the desired electrolysis value (ex. 400 mV; electrolysis current is diffusion-controlled). During this time, the current decayed as expected as the reaction progressed. Subsequently, this signal was integrated to obtain the total charge with the data being expected to reach a maximum total charge after a specified number of seconds for the designed electrochemical cell. Figure 3.20 (solid line) shows a sample amperometric curve of current versus time where there was an initial spike of current as the reaction was initiated with a step in the reduction potential, and a gradual exponential decay to value of zero in the current after all of the analyte was reduced. The integral of

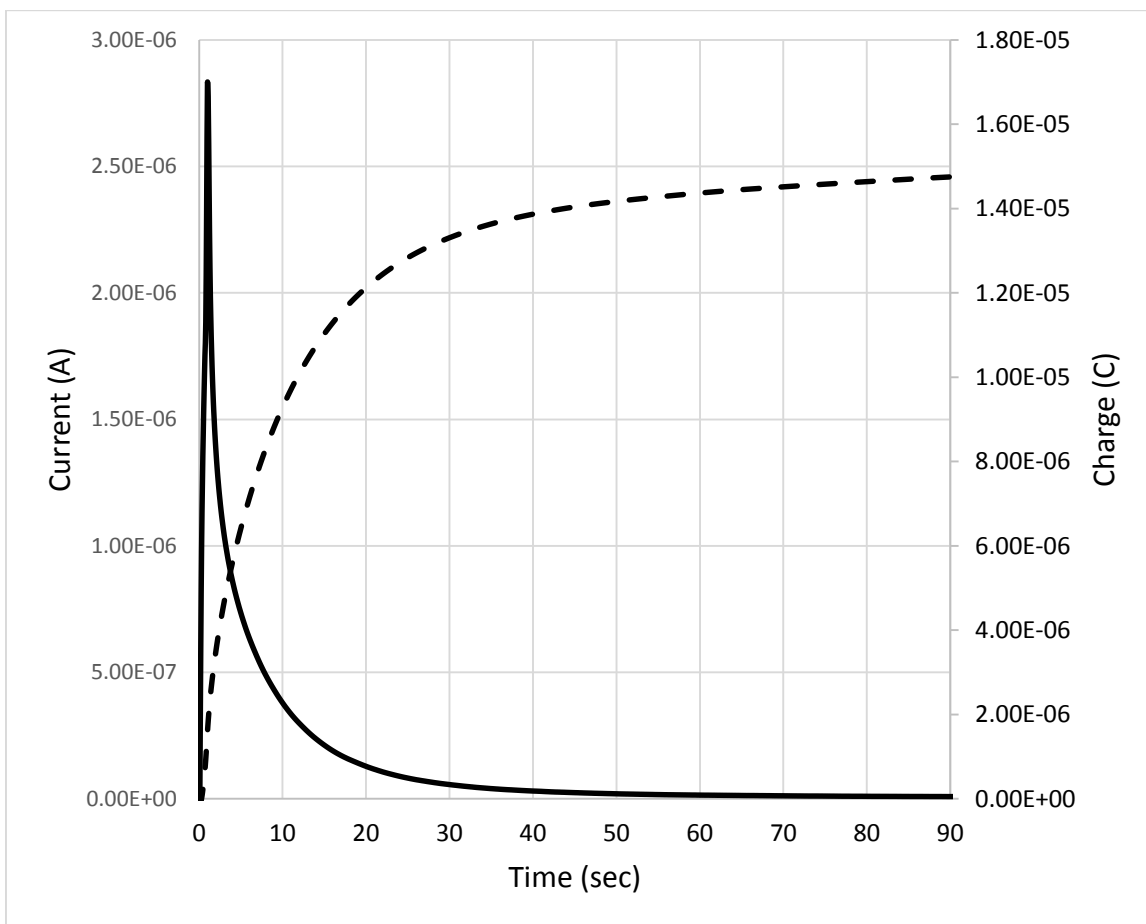


Figure 3.20 – Representative plot showing exponential decay of oxidation/reduction current generated during reaction (solid line) and resulting cumulative asymptotic total charge generated by the reaction (dashed line); magnitudes are normalized to one and not to scale.

this current signal (Figure 3.20, dashed line) was the total charge, which rose rapidly and appeared to approach a constant asymptotic value with a slope of zero that corresponded to the total charge generated by the reaction. The steady-state value was proportional to the concentration, and in the exhaustive coulometry system, was ‘absolutely’ determined as the current decays to zero.

In practical coulometric electrochemistry, the current doesn’t decay to zero, rather it decays to some finite value (the non-Faradaic current) which depends on the electrode, adsorbed species, background electrolyte processes, etc. This so-called background current, was subtracted from the data recorded in all experiments to obtain the current associated with the chemical reaction. When the offset current was subtracted, the slope ideally trended to zero once the analyte within the cell was exhausted.

In addition to the exhaustive capabilities of the system, using the full range of concentrations mentioned previously, the measured charge versus concentration was plotted to determine the linearity of the system (Concentration vs. Total Charge). These curves were then compared directly to the curve of the expected charge (ex. Cottrell plot) for selected concentrations. This direct comparison was used to observe whether or not the cell was acting like a true thin-layer cell, and the shape of the Time vs. Current (or charge) curve followed the expected trajectory. The expected time for total depletion of analyte was determined by comparing the total charge measured for the known concentrations. Verification of the true volume of the cell electrochemically was necessary since this value was difficult to measure directly after assembly of the device.

### 3.5.3.1 Chronoamperometry

In the experimental electrochemical thin-layer cell, the work and counter electrodes were isolated from each other using a semi-permeable membrane. This wetted physical barrier allowed the two electrodes to remain in fluidic and electrical contact with each other via the solution, but prevented the oxidized or reduced species from migrating between electrode surfaces to complete what is commonly a reversible process. To confirm this isolation and to ensure the thin-layer system was in a stopped flow condition, a series of repeated oxidation-reduction-oxidation-reduction steps were executed to capture the current during the entire repeated processes to observe the repeatability and reproducibility of the electrochemical analyses. This experiment was designed to investigate how well the membrane isolated the analyte in the working electrode chamber and proved that none of the analyte was able to migrate through the membrane. The successive current curves were each converted (by integration) to total charge and compared. In an ideal cell, the generated charge for each step should be equal.

### 3.5.3.2 Comparison to Commercial Electrochemical System

To test the accuracy of the custom potentiostat and control software, a BASi Epsilon (BAS instruments, Fort Wayne, IN) was used for direct comparison as the “gold standard” instrumentation setup. Since the functionality of system presented in this work was modeled off of some of the basic functionalities available in the commercial potentiostat, a head-to-head performance was easily delineated. Specifically, for matching sensitivity settings (A/V) and scan rate (V/sec), the data generated by the Epsilon and the custom potentiostat were compared. Successive experiments were

performed where a sample was oxidized first with the Epsilon, then the cell flushed, and the steps repeated. The ability of both systems to accurately resolve the initial charging currents generated by the cell was also compared. Calculation of the total charge obtained in a reaction depended on an accurate representation of the current generated in the cell, especially during the first few microseconds of the experiment where there was a surge in current due to charging of the electrode on the initial step of the oxidation/reduction voltage.

### 3.6 Summary

When taken together, the sections in this chapter have outlined the details of steps taken to fabricate and test a prototype coulometry system designed to provide an exhaustive calibration-free electrochemical analysis method. The exhaustive properties of the system depended on the ability to completely convert all of the analyte in the working electrode chamber to the oxidized or reduced form. This implied that the data reported will be a measured current that ultimately decays to zero in a period of time that is based on a critical dimension, the thickness or height, of the cell. The calibration free capability of the cell was established by data sets that indicated a total calculated charge was equal to the expected charge of a particular concentration of analyte.



## CHAPTER IV

### RESULTS AND DISCUSSION

In this chapter, the results associated with the specific aims outlined in the introduction will be examined. First the flow cell CFD results will be presented and data compared to an assembled prototype. Next, the potentiostat circuit will be tested for basic electrical performance using a dummy cell as a stand-in for the electrochemical cell. The software controlling the experimental conditions will also use the dummy cell as a way to compare expected performance of the circuit since the specific values of the electrical components of the dummy cell can be chosen for this purpose. Finally, the performance of the system components as a whole will be evaluated by introducing known concentrations of analyte into the system, appropriate voltage settings and control timing applied, and electrochemically generated currents measured. This data will be analyzed to investigate the exhaustive capabilities of the system by comparing the total charge measured as well as the time to deplete all of the analyte in the system when compared to the theoretical calculation of these values

#### 4.1 Final Flow Cell Design

Development of the flow manifolds used in the project initially involved the creation of several solid models at the conceptual level, which after fabrication and assembly, was evaluated by examining the fluidic performance that consisted of manually

loading the sample into the inlet port (for both the sample and counter flow channels) and the ejection of sample to a waste container at the outlet. A manifold, with a central reaction cell geometry, satisfying the volume requirements was created keeping in mind that the sample loading would be performed manually with syringes. The geometry of the interior fluid paths for the manifold was chosen to balance the tooling limitations of the fabrication company together with the small size of the fluid paths, which cause large pressure drops through the system and unnecessarily complicate the sample loading and flushing steps. Several designs were considered, all primarily focused on alignment, accommodation with the sensor platform, and establishing an isolated constant volume that interfaced with the electrode surfaces.

#### 4.1.1 Solid Model and Design Features

Fundamentally, the cell design required a few critical features, the most important of those being the thickness of the working electrode chamber (the thin-layer volume). To prevent reversible reactions from occurring, it was required that the working and counter electrode chambers be isolated by a membrane permeable to ions only. The platform design included ports for the fluids entering both the working and counter chambers and allowed for precise alignment of the sample stream to flow and interact with the working electrode.

Each layer of the flow cell was first conceived using a three dimensional CAD package, knowing that these drawings were to be used for simple visualization of conceptualized design and eventually sent out for fabrication when a final design was decided upon. Figure 4.1 shows an exploded view of the final flow cell, including all primary layers (labeled in the diagram).

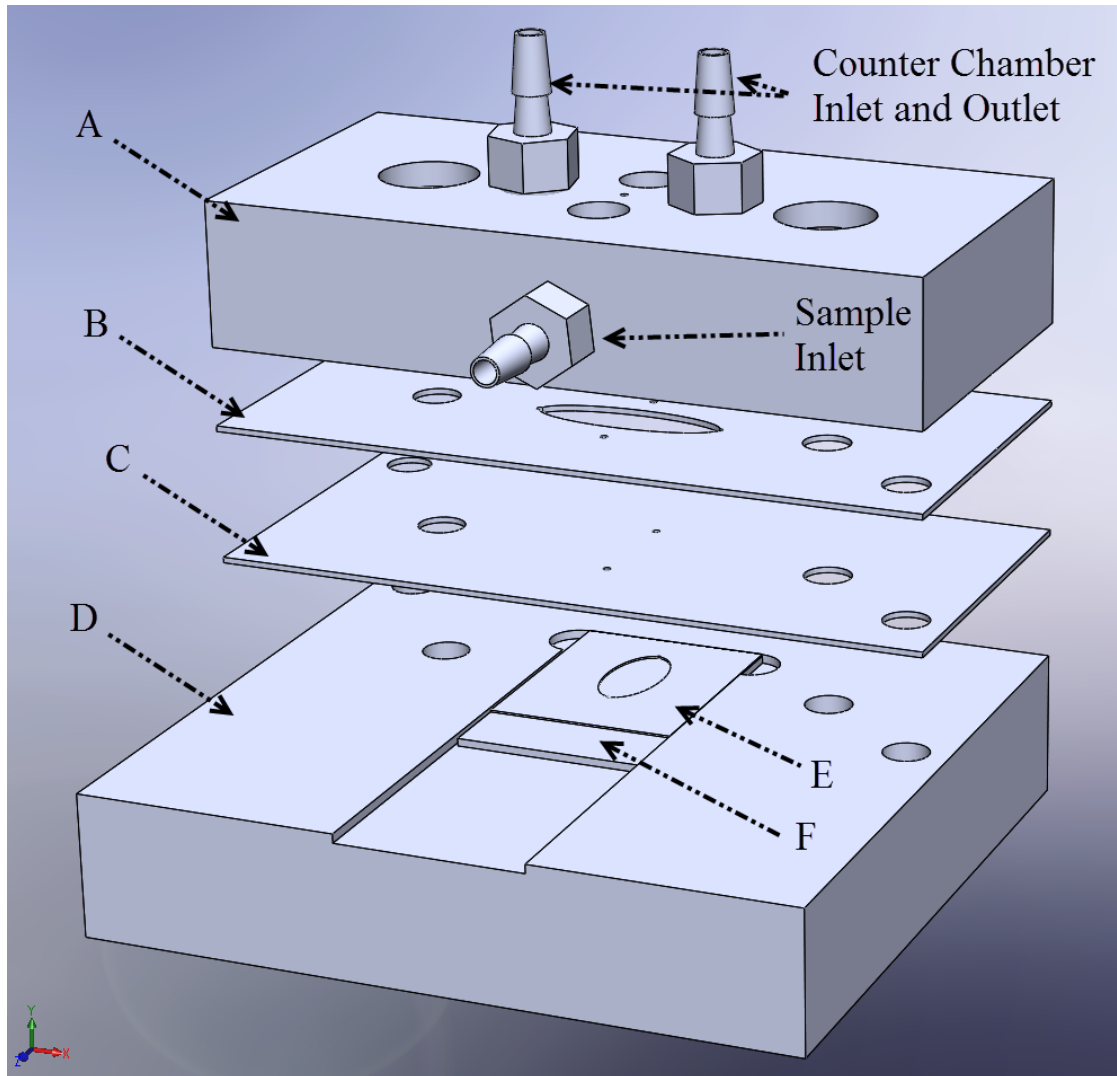


Figure 4.1 - Flow cell solid model (V3) indicating the many layers including the top half of the cell (A), the upper gasket (B), the semi-permeable membrane (C), the bottom of the cell assembly (D), the chip gasket (E), and the sensor (F); for clarity, the counter electrode is not shown, and the sample outlet port is obscured from view.

To elucidate the details of the fluid flow within the cell, the interior flow paths together with the geometry for alignment and design features for securing the two halves of the flow cell are shown in which is a transparent front view of only the top half of the assembly. The primary flow paths for both the sample and counter chamber fluids are indicated (Figure 4.2 C and G); in this particular flow cell design, only the counter flow

path is introduced from the top of this layer, the sample inlet and outlet are in the front and in the rear, respectively, of this part. Figure 4.3 is a right side projected view of the interior of the final flow cell design showing the flow path of the sample stream (Figure 4.3; inlet (A) and outlet (B)). Features C in Figure 4.3 indicate the tool path for blocking pins included in the design to ensure that diffusion of the reactants from the analyte stream was minimized after sample loading.

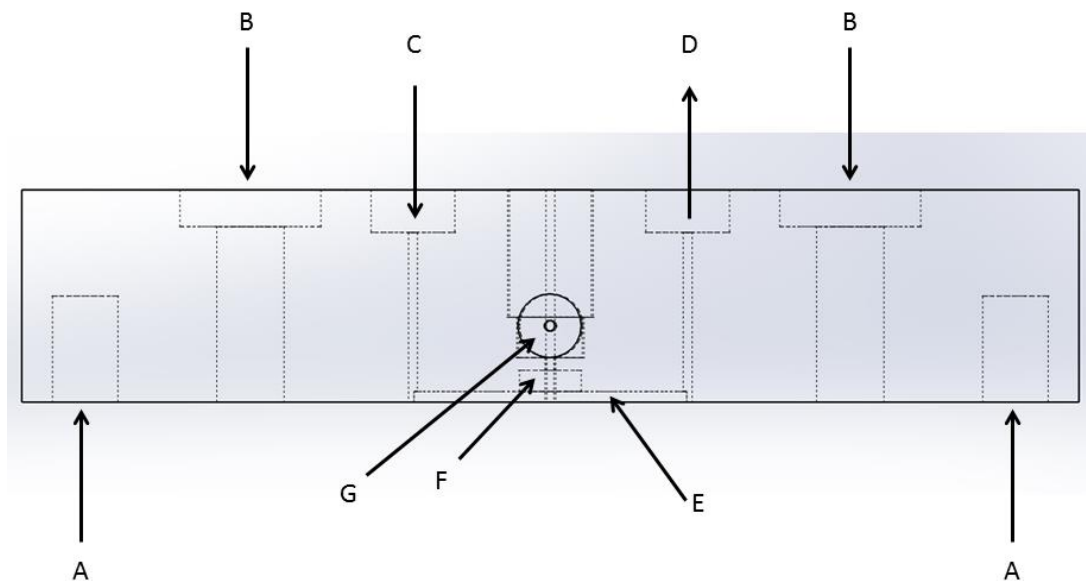


Figure 4.2 – Front projected view of the top section of the flow cell (W=50mm; H=10mm) indicating interior features incorporated into the design including holes for alignment pins (A), holes for the two screws that secure the primary the upper gasket (B), counter-flow inlet (C), counter flow outlet (D), counter chamber volume (E), and counter electrode recessed area (F). For clarity, the screw threads are not shown.

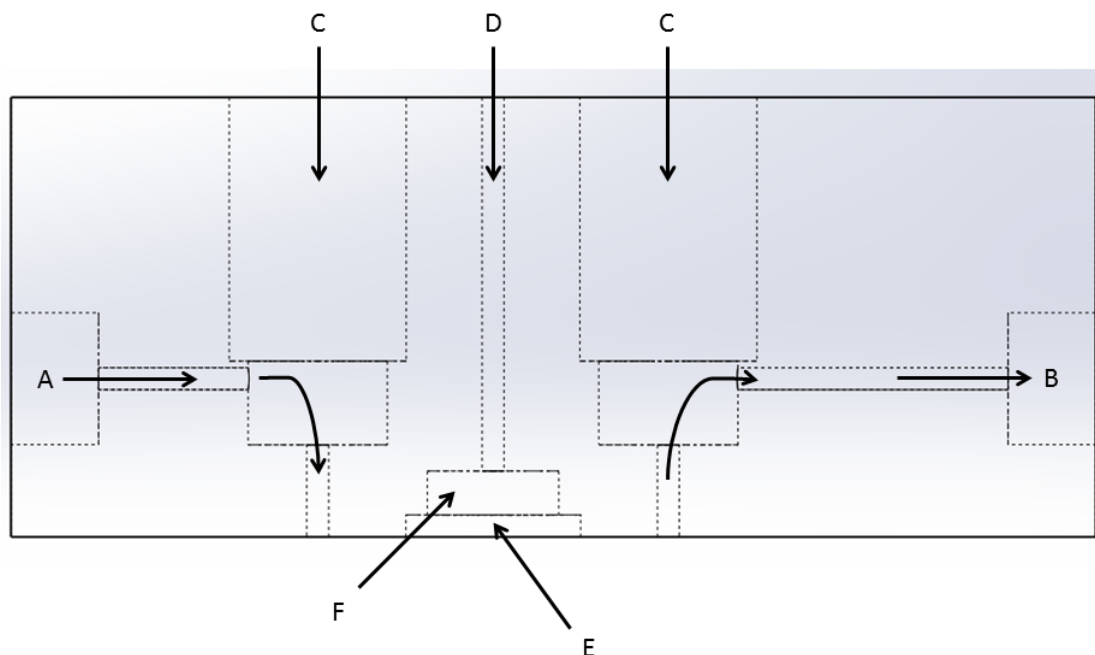


Figure 4.3 – Side projected view of the top section of the flow cell ( $D=24.75\text{mm}$ ) indicating interior features incorporated into the design including sample flow inlet (A) and outlet (B) (thin-layer volume below not shown); tooling paths for spring probes inserted to block analyte diffusion (C; counter electrode hole (D); counter chamber volume (E), and counter electrode recessed area (F). For clarity, the screw threads are not shown and the holes for the alignment pins have likewise been removed.

Details of the membrane layers are identified in Figure 4.4, and show the relationship between the counter flow volume (D) and the thin-layer cell volume (E). The only fluidic features machined into the membrane layer are the  $500\ \mu\text{m}$  holes to allow the passage of the analyte stream (E). Also shown are the machining relief structures due to a limitation of the routing tool not being able to create true  $90^\circ$  corners. In this view, the sensor chip is included and shown to be aligned with the right and back sides of the trench that is milled into the bottom layer.

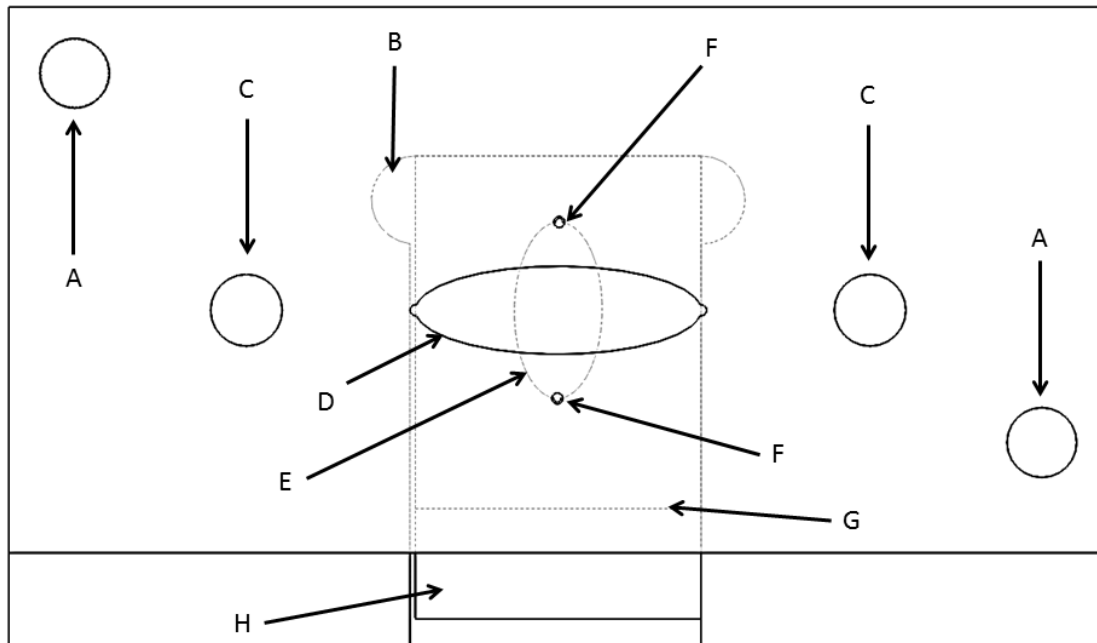


Figure 4.4 – Top view of the bottom flow cell and thin membranes included in the design; Alignment pin holes (A); machining relief features (B); screw holes (C); counter flow geometry in rubber gasket (D); thin-layer volume (E) defined in the chip gasket (G); fluidic ports in membrane layer for analyte stream (F); sensor (H).

## 4.2 Computational Fluid Dynamics

The voids in the geometry created in the solid models represented the fluidic portion of the cell, and these chosen dimensions were used to investigate the flow profile inside the thin-layer cell volume. The smallest dimension for all fluidic ports was designed to be 500  $\mu\text{m}$ , which is the smallest diameter that can be reliably machined according to the fabrication vendor used in this project. Considering that the pressure inside the system would increase as the geometry reduced in size, the fabrication limitation was not seen as a hindrance since the fluids in the prototype system were delivered manually.

#### 4.2.1 Model Details

The CFD model was manipulated in many ways, particularly concerning the meshing routine used to adequately represent the abrupt changes in aspect ratio where the inlet and outlet fluid paths meet the thin-layer geometry. Figure 4.5 is an isometric (ISO) view from the side of the model used in the study. In the solver, the finite elements were set to calibrate for *fluid dynamics*, which instructed the mesh algorithm to consider all bends and aspect ratio changes as possible locations for large gradients. Tetrahedral elements were used for the entire volume, with particular attention paid to the number of elements distributed across the thickness of the cell geometry. The inlet and outlet fluid paths were also meshed using tetrahedral elements, with settings slightly adjusted to allow for larger elements, since the geometry in these structures are much larger than the thin-layer volume. Another benefit to using tetrahedral elements was that they supported adaptive mesh refinement, which enhanced the mesh algorithm calibration setting.

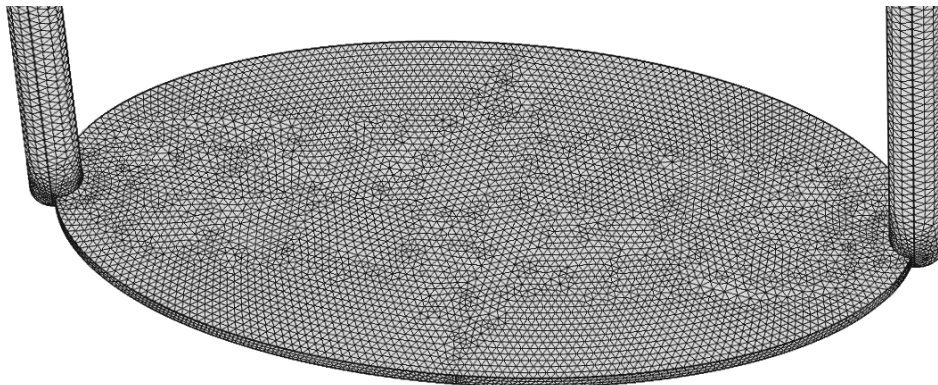


Figure 4.5 – Isometric side view of the CFD model used to estimate the max pressure for the manifold. Aliasing in the image enhances the subtle variations in the element pattern due to the curved geometry.

Figure 4.6 provides more detail regarding the mesh particularly at the interface between the inlet/outlet and the thin-layer cell. The arrow in Figure 4.6A points to the outer edge of the thin-layer which can be shown to have three layers of elements in this particular model. The number of elements in the cross section of the thin-layer geometry was shown to be a critical parameter in the ability of the simulation to properly resolve the pressure differential created at the inlet/thin-layer interface. In many cases, for simulations with higher flow-rates and meshes consisting of less than three elements in

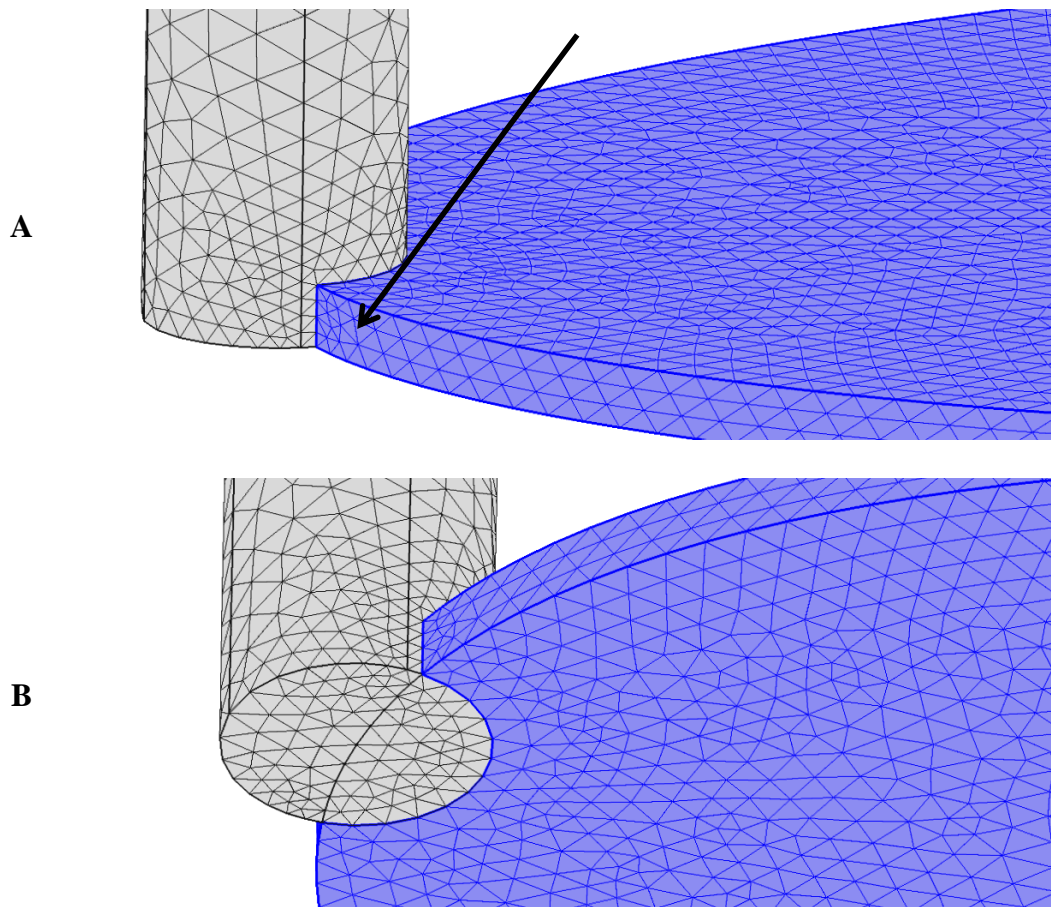


Figure 4.6 – Zoomed in view of the mesh interface between the inlet and the thin-layer cell (highlighted in both for emphasis). The arrow is highlighting the emphasis placed on the number of elements in the thin-layer cross-section.



the thin-layer cross section, the solver crashed and reported that the model could not converge to a solution.

#### 4.2.2 Numerical Analysis

The inlet and outlet geometries as well as the thin-layer oval area were held constant in the CFD model, and the height was parametrically varied from 300  $\mu\text{m}$  to a worst-case scenario of 50  $\mu\text{m}$ . For the 127  $\mu\text{m}$  membrane (0.005 in.) used in the thin-layer cell, the variability was listed at  $\pm 75 \mu\text{m}$  ( $\pm 0.003$  in.). The upper and lower limits for the height of the cell in the model was chosen based on this range. Figure 4.7 shows the maximum calculated pressure resulting from the application of a boundary condition of 0.212 m/s fluid velocity ( $\sim 2.5$  mL/min volumetrically) and venting the outlet to atmospheric pressure (1 ATM). At cell heights below approximately 100  $\mu\text{m}$ , the peak

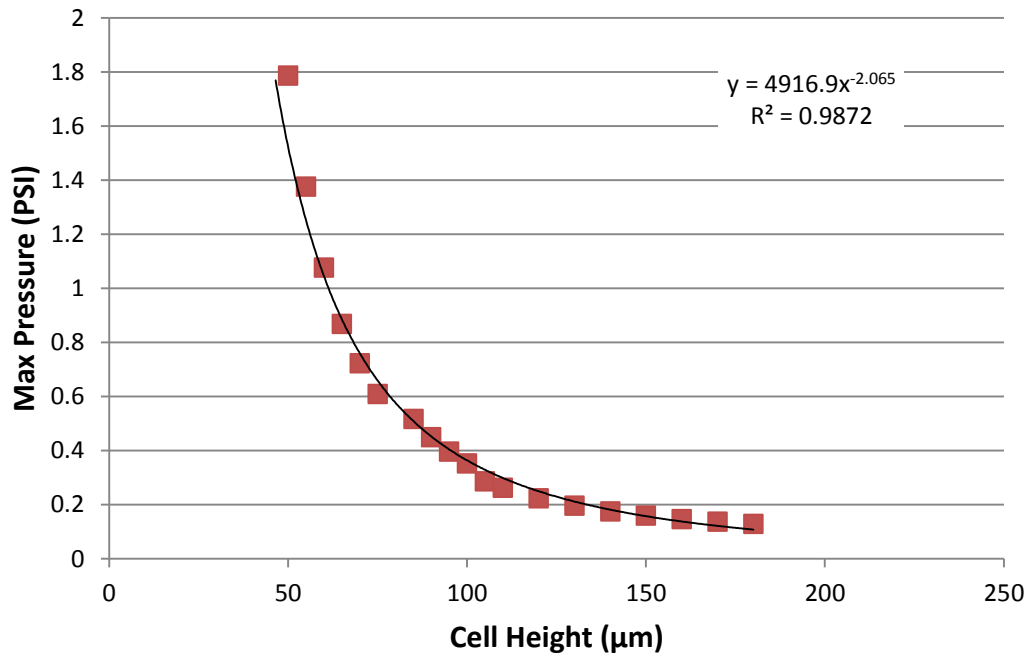


Figure 4.7 – CFD results for simulating the increase in back-pressure with decreasing thin-layer cell height.

pressure appeared to increase dramatically. Fortunately, this two-hundred-fold increase only reached a maximum of 1.79 PSI at the smallest cell height used in the model. While it was interesting to note a change occurring near the 100  $\mu\text{m}$  critical thickness specification for thin-layer electrochemistry, the explanation was purely geometry driven and did not have an effect on the analysis since the experiment was run under stopped flow conditions.

Visual inspection of three-dimensional results showed a gradual increase in the pressure near the inlet/outlet-thin layer junction with increasing flow rate. Figure 4.8 is a series of simulation results showing the increased progression in pressure as the flow rate was ramped from 10 to 10,000  $\mu\text{L}/\text{min}$ . The black ISO lines indicated a path of equivalent pressure. As the flow rate increased, these lines increased in frequency and became compacted as the increasing flow rate began to initiate an ejection event when the two sections of flow intersect. Figure 4.9 is an image showing a similar progression of the increase in velocity with flow rate. The data was obtained from the velocity projected onto a slice through the centroid of the thin-layer volume. As the flow rate at the inlet increased, the velocity of the fluid entering the thin channel increased and spread out to the full width of the channel, slowed down, then reconverged as the fluid entered the outlet channel. The spatial effects were most drastic near the exit of the inlet channel and the entrance from the thin-layer cell to the outlet channel, but in all flow rates, the flow remained laminar.



Figure 4.8 – CFD results for simulating the increase in pressure with increasing flow rate. Color scale indicates pressure magnitude. Black lines indicate equivalent lines of pressure in the volume.

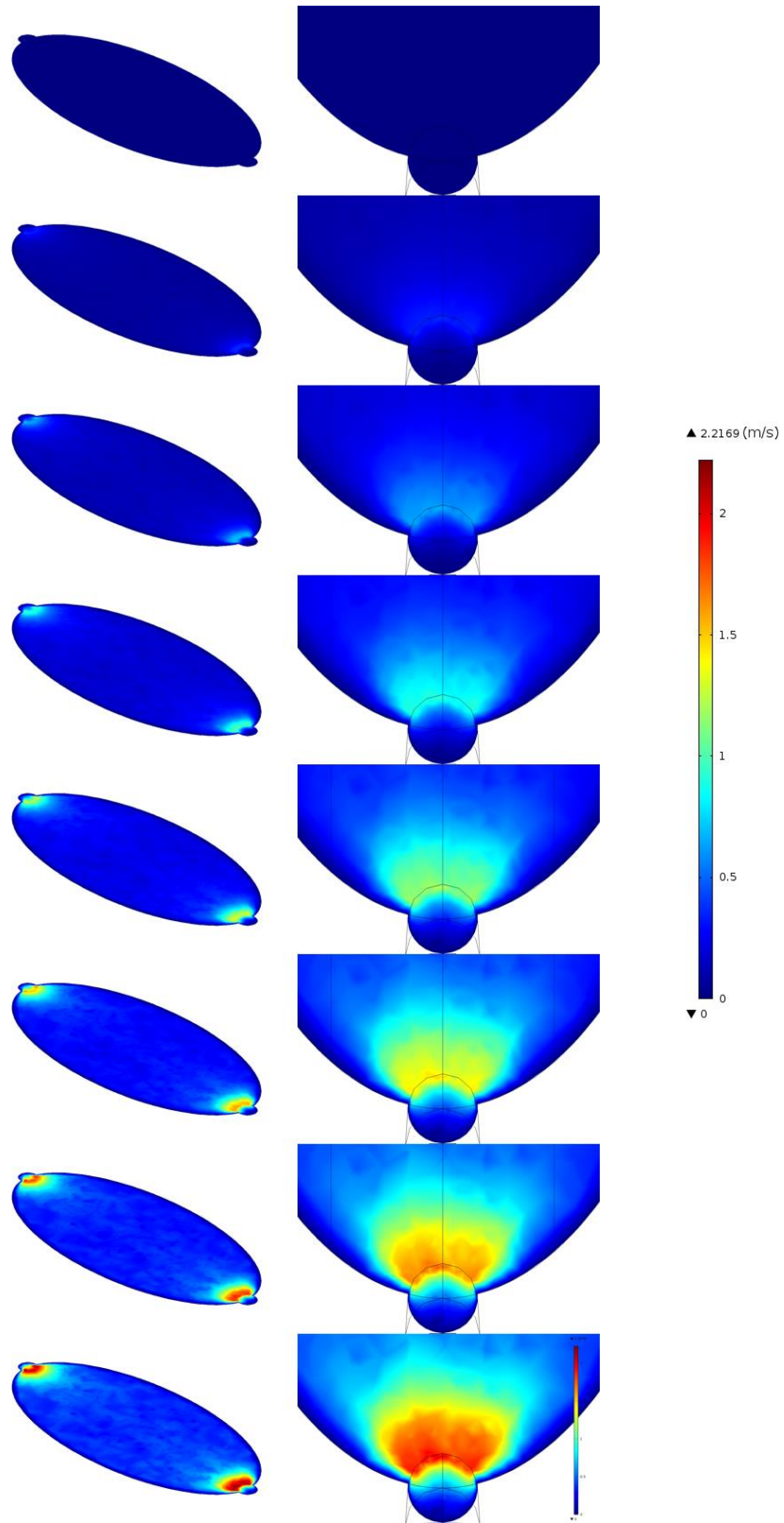


Figure 4.9 – CFD results for simulating the increase in velocity at the thin-layer cell inlet and outlet increasing flow rate

### 4.2.3 Mesh Convergence Test

When considering the accuracy of the results provided by any finite element simulation, along with the application of appropriate boundary conditions and choosing the correct physics (hence, equations) to solve the model, there is a direct relationship between accuracy and the number of elements in the model. In general, this relationship is true since the smaller each element is over the full geometry, the ability for the numerical model to correctly represent the design. Unfortunately, computational time is also directly proportional to the number of elements used in a mesh; therefore, it is advantageous to only use the minimum number of elements needed to attain accurate results. Determination of the minimum number of elements required to achieve repeatable, accurate results requires a process known as *test of convergence*, where the coarseness of the mesh is gradually increased, results are obtained for each mesh and compared over a range of mesh sizes to identify when the output yields the same values regardless of the mesh size. A more sophisticated method for testing the mesh size convergence can be accomplished by using a “fine” mesh in areas where steep gradients in the parameters will occur, and a “coarse” mesh in areas where little change will be occurring.

To confirm the effect of the CFD model mesh density on the max pressure obtained in our simulations, the inlet flow rate was held constant (0.212 m/s) and the meshing parameters were adjusted to modulate the density of elements near where the inlet/outlet and thin-layer meet (Figure 4.6). This modification was specifically performed to modify the number of elements in the cross sectional area of the thin-layer cell volume. Figure 4.10 shows the effects of the mesh adjustments for 1, 2, 4, and 8

elements in the thin-layer cross section and how the curve converges towards what can be considered the correct simulation results, which are a max pressure of 0.5 PSI for an average inlet flow velocity of 0.212 m/s. The final simulation took 47 minutes to complete (vs. 5 minutes for the previous), yet the result is only 0.9% different from the previous result. Based on this result, four elements in the cross section was the minimum number of elements used in future simulations.

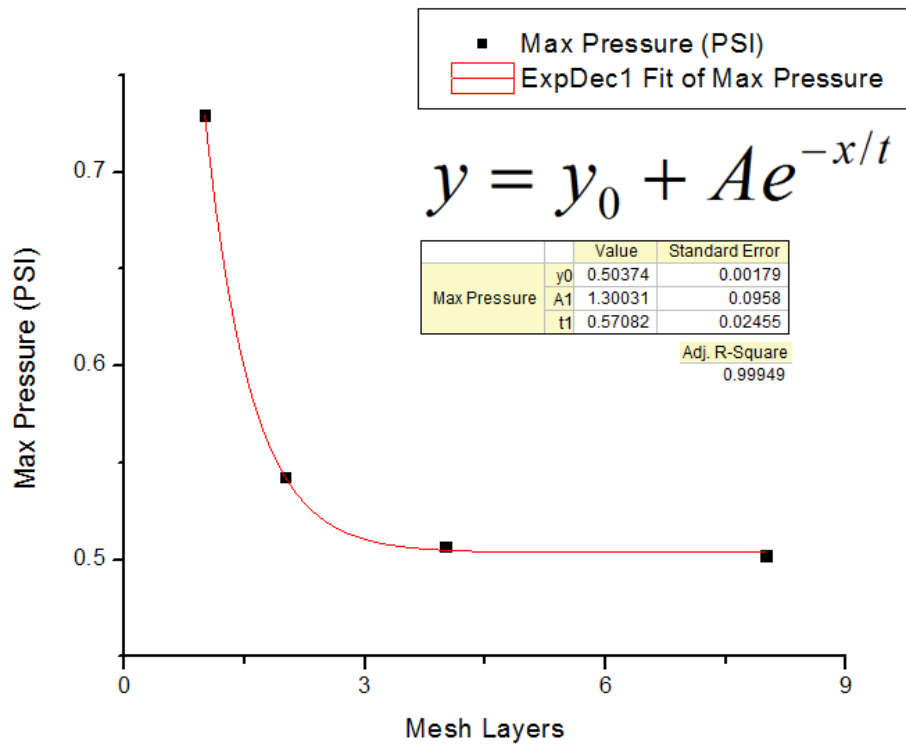


Figure 4.10 – Mesh convergence simulation showing the trajectory towards a final solution. The last two solutions are 0.9 % apart, yet the last solution took 47 minutes to solve, compared to 5 minutes for the previous model.

To investigate the effects of flow rate on the pressure in the cell, another series of simulations was performed where the flow rate was ramped up in ten even steps between 10  $\mu\text{L}/\text{min}$  and 10,000  $\mu\text{L}/\text{min}$ . As can be seen in Figure 4.11, there was a gradual increase in pressure as the flow rate increased.

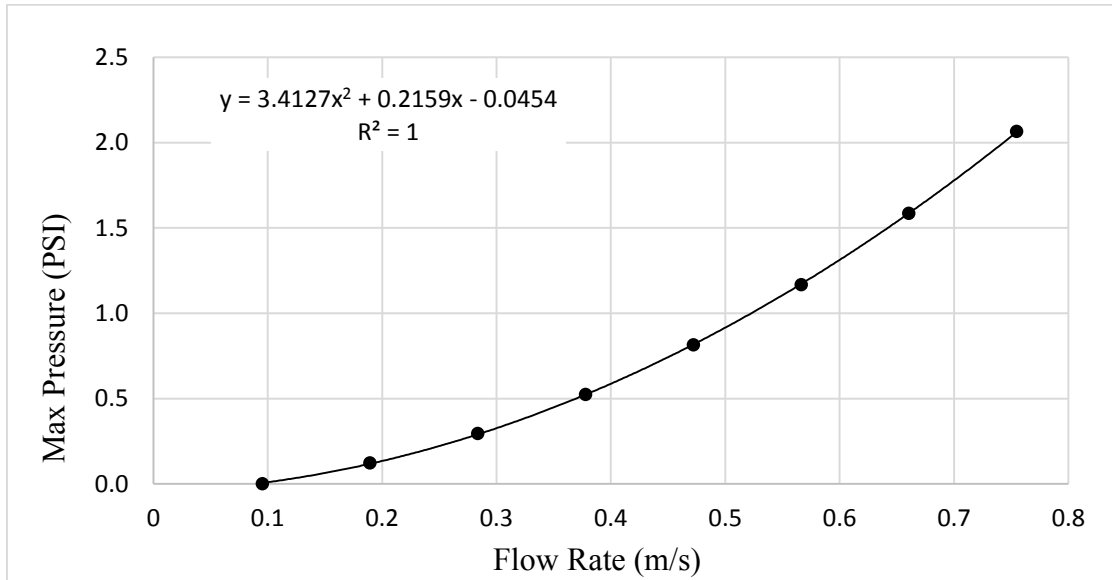


Figure 4.11 – CFD results for simulating the increase in back pressure with increasing flow rate

### 4.3 Final Flow Cell Prototype

Armed with the confidence provided by the CFD results, the top and bottom layer of the solid model were ready for fabrication. Using the detailed specifications in the CAD software, all top and bottom portions of the flow cell were machined using CNC milling. There were four major revisions of the cell during the course of this project, and images of each can be found in Appendix D.

Figure 4.12 is an image of the assembled final cell design used in this study and is the device with features described by the drawings shown in Figures 4.1 through 4.4. The mass of amorphous material that can be seen on the top of the device was hot glue used to seal and secure the counter electrode (a bare gold wire), the yellowish gold object in the image. Barbed fittings were originally used, but quick-connect fittings were used in later experiments when rigid tubing was introduced. These fitting are shown on the counter

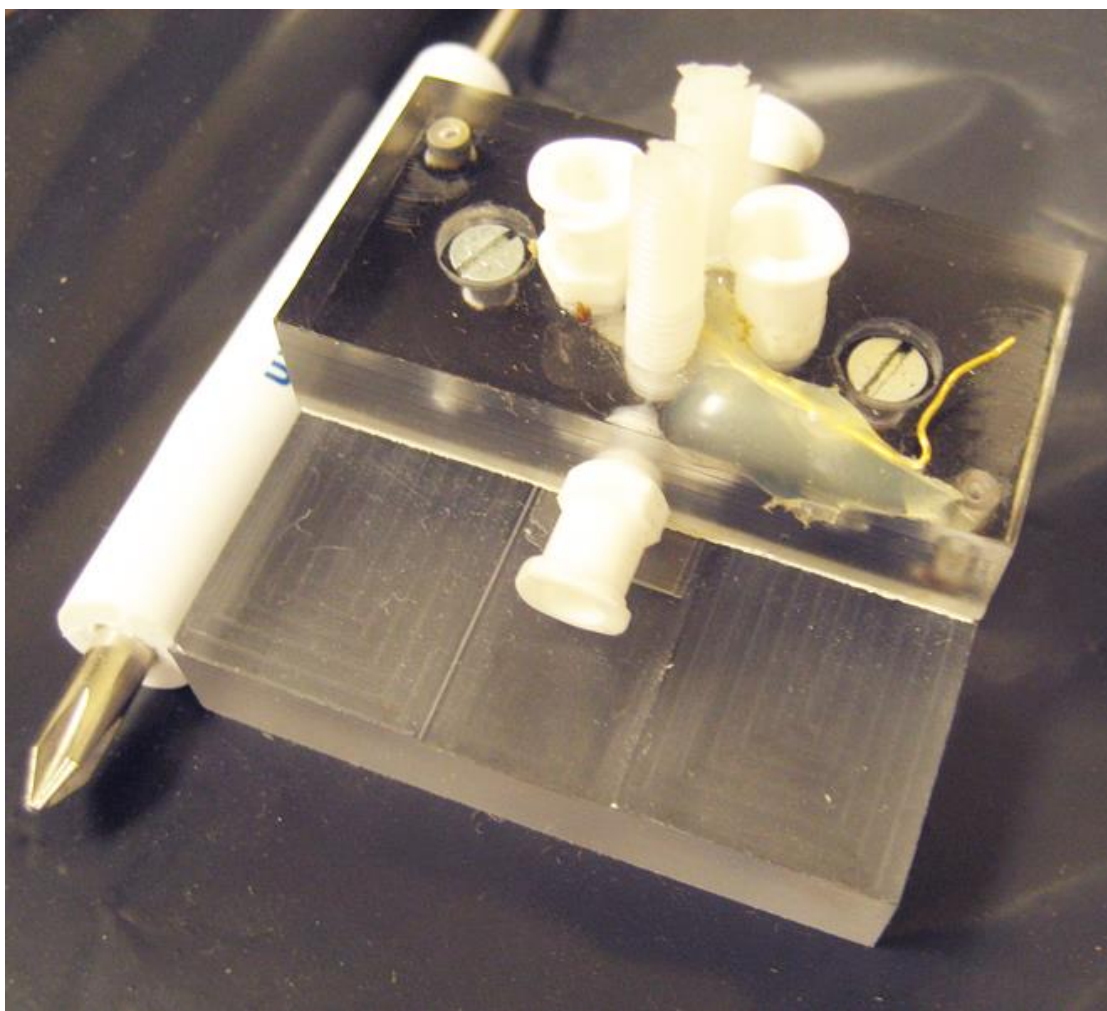


Figure 4.12 – Final flow cell used in this study. Two pairs of inlet/outlet ports, one for the sample (working electrode) chamber (front, rear not shown), and one for the counter electrode chamber (top). Counter electrode inserted manually through an access hole at the center of the top (hidden).



inlet and outlet (top of the cell) and the sample inlet (front of the cell). The sample outlet was in the back and partially hidden by the fluidic connection hardware.

Figure 4.13 is a picture of the underside of the top layer, showing the recessed counter chamber and the gold counter electrode which was spiraled in the hole machined to house this electrode. The coiling was performed to increase the surface area of the counter electrode to decrease current density on the counter electrode which balances the current at the working electrode. Another observation was made concerning the tooling marks that were apparent on these new outsourced parts (Figure 4.12 just left and right of the sensor trench and Figure 4.13). By contrast, the original chips were translucent and showed no tooling marks on the upper surface of the bottom layer. The tooling marks

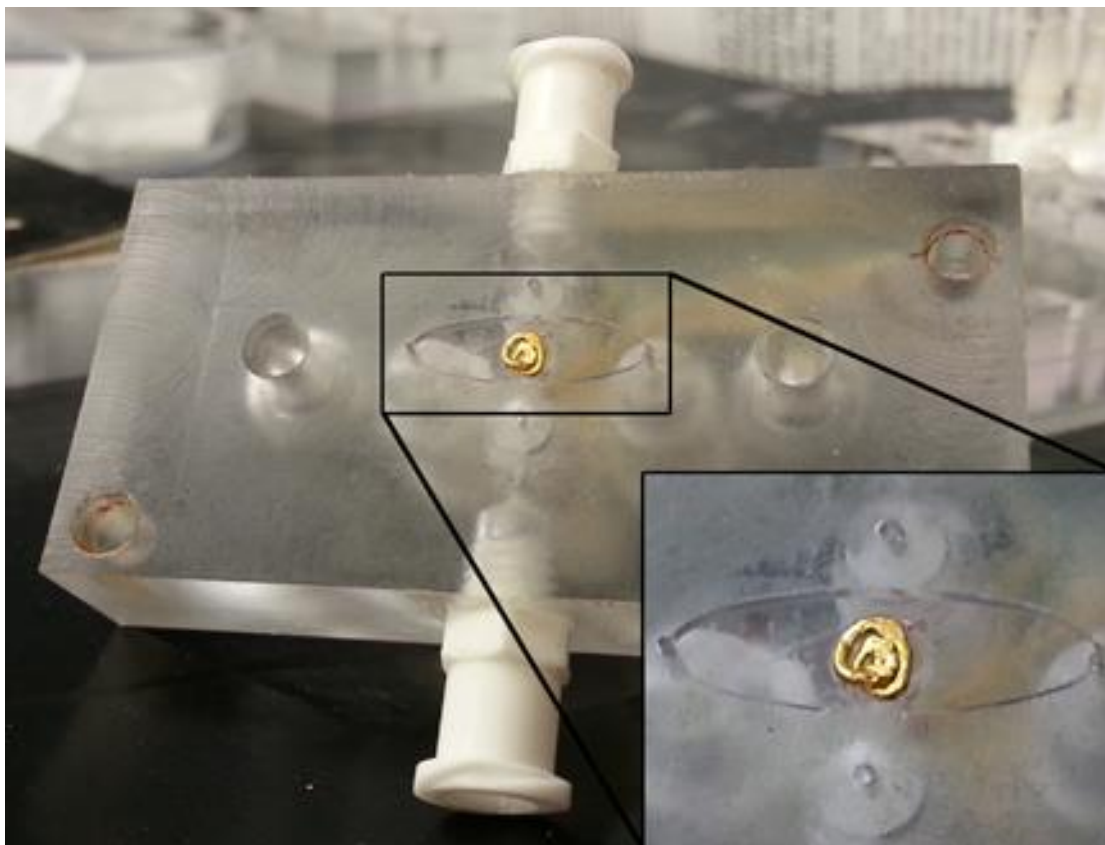


Figure 4.13 – Bottom of the top of the third generation flow cell. The oval recess for the counter electrode volume is shown and counter electrode is coiled up at the center of this volume (with inset for magnified view).

were actually perceived as a slight benefit since their presence increased the surface roughness which may aid in securing the gasket layers, although no specific tests were performed to test this theory.

In all prototypes, two (or more) screws were used to pull the two pieces of the assembly together. In all cases, the screw holes in the bottom layer and manifold inlet/outlet ports were tapped using a 4-40 size tapered machine screw tap. This was done by hand by first soaping up the part and proceeding slowly, turning the tap a quarter turn at a time until the tap reached the bottom. Each design included a minimum of five full turns of the tap from the top of the hole to the bottom of the feature. Burrs were removed, the soap was rinsed off, and finally the connector parts were installed in the tapped holes. In most cases, Teflon tape was not used initially since the plastic threads on both the hole and the threaded part were soft enough to create a tight seal. Figure 4.14 contains an image of the process.

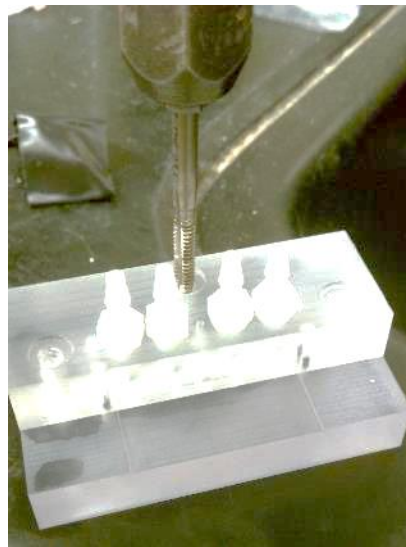


Figure 4.14 – Manually tapping inlet/outlet ports and screw holes.

### 4.3.1 Rubber Gasket Fabrication

Instead of including the membrane layers in the outsourced build of the flow cell prototype, a laser cutting system was used. The masks containing the membrane layers were loaded into the program running the laser system, and the laser was set to 2.5% power (40W laser), 1 inch per second travel (speed), and a 5000 kHz pulse frequency. The upper gasket and chip gasket materials were ordered from McMaster-Carr and typically arrived in a 12"x12" sheet. The thickness of these membranes was measured with calipers and tabulated. Care was taken to not to compress the gasket material when taking the measurements, particularly regarding the extremely compressible chip gasket, which is almost translucent. The 70 durometer material was a stiffer material akin to car

Table 4.1

Measurement Data for Rubber Gaskets Used in the Flow Cell

Gasket	Material	Durometer	Thickness ( $\mu\text{m}$ )	St.Dev ( $\mu\text{m}$ )	n
Upper	Silicone	70	508	60.32	24
Chip	Ultrapure Silicone	55A	114.3	10.4	17

tires, while the 50 durometer material was more flexible. Table 4.1 contains the results of these measurements. Most notable was the large standard deviation of both measurements (more than 10% away from the mean for each), however a much larger value was expected given the specifications from the manufacturer.

Figure 4.16 shows an image of the upper gasket, which was black in color and shows the features for the alignment pin holes, screw holes, and oval opening for the coulometry cell. Figure 4.15 is an image of the chip gasket shown slightly askew and on

top of one of the microfabricated sensors. The chip gasket was so thin that it appeared to be wet when placed on the sensor. Care was taken to align this gasket on top of the sensor, typically with a pair of blunt tweezers, as sharp (pointed) tweezers would puncture the thin material. Flaws seen while fabricating the membrane when either the laser power was set too high during cutting, or there was an irregularity

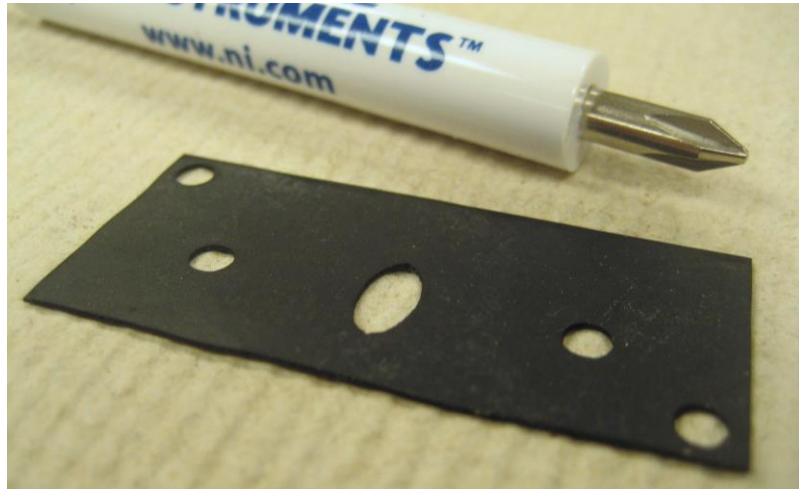


Figure 4.16 – Upper gasket layer created using a laser cutter.

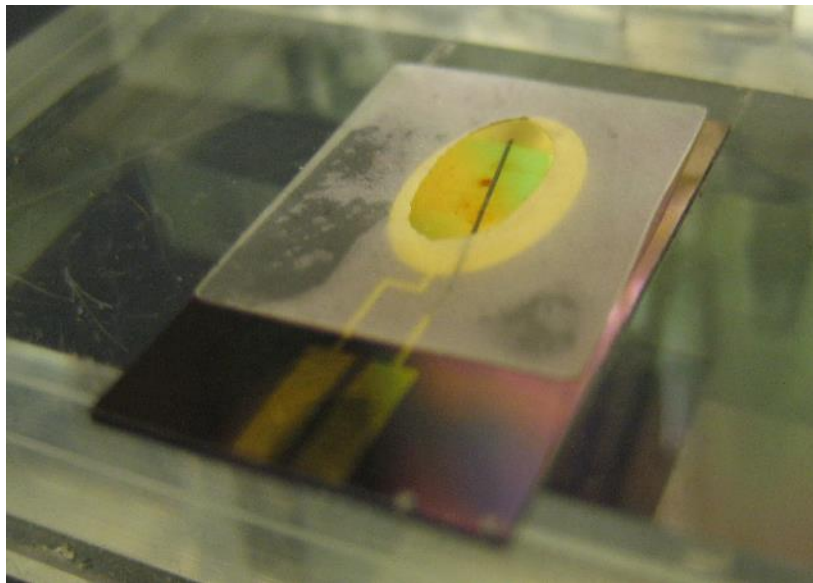


Figure 4.15 – Extremely thin ( $\sim 100$   $\mu\text{m}$ ) chip gasket layer created from a large sheet of stock rubber using a laser cutter.

in the material. All gaskets were inspected for these types of flaws and discarded when appropriate.

#### 4.3.2 Membrane Fabrication

Similar to the rubber membranes, the chemi-selective membrane was also cut and patterned with the laser cutting tool (Figure 4.17). Essentially a paper filter with fiber density set to prevent any materials below a certain molecular weight to pass through, this material was more difficult to work with considering the manufacturer's requirement of keeping the stock hydrated. Allowing the membrane to dry would cause cracking and render it useless for experimentation. Since the sample was always at least slightly wet

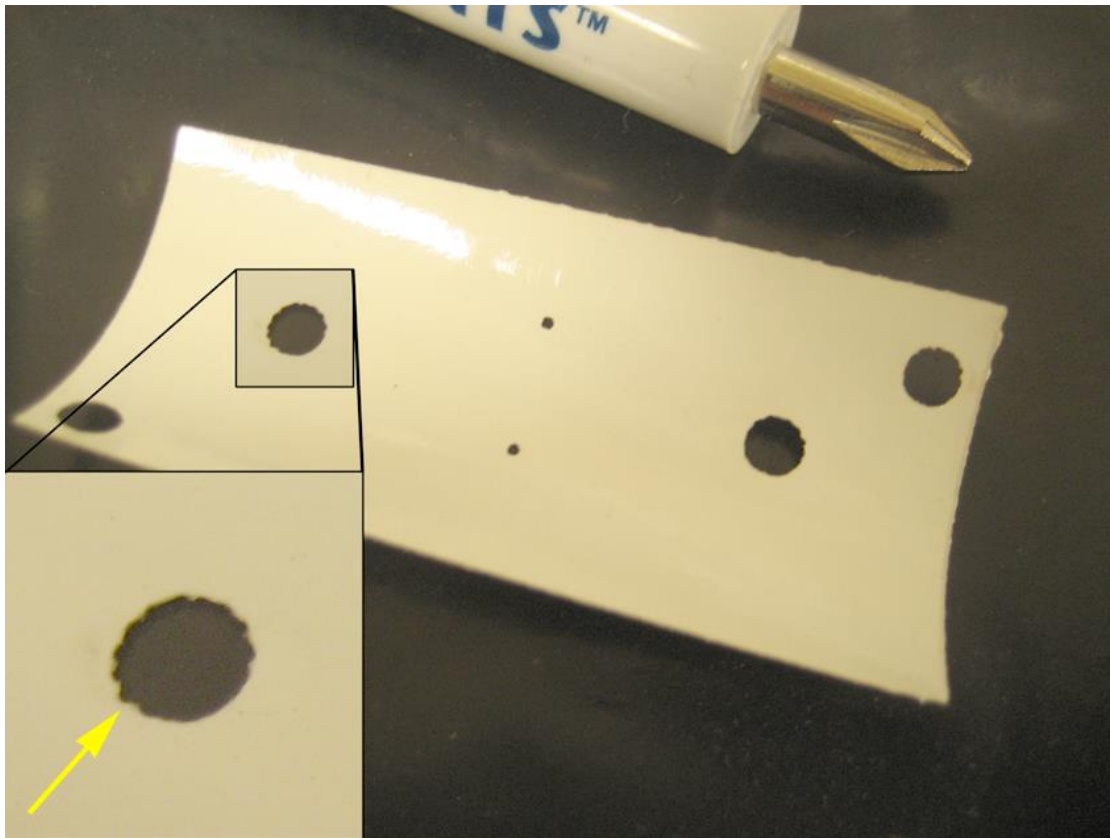


Figure 4.17 – Paper-based chemi-selective membrane; One side is paper backing for structural support, the other (shiny) side (displayed) is the microporous media. Yellow arrow is pointing to errors in the laser cutting path.

during fabrication of the membrane patterns, the laser tended to vaporize the water and create fenestrations or pockets along the interior cuts as can be seen in as can be seen in Figure 4.17. The laser settings (both power and feed rate) were manipulated to minimize this problem. The small size of the two central holes (1 mm, larger than the 0.5 mm holes in the main manifold) represent the critical inlet and outlet flow paths of the analyte.

### 4.3.3 Assembly Issues

Despite the inclusion of alignment pins, the obvious limitation to a successful assembly was the “floating” chip gasket, which required manual placement. The thickness, or perhaps more appropriately, the thinness of this membrane proved problematic mainly due to a sticking issue with the silicon sensor surface during placement. This caused the gasket to stretch and distort in shape and complicated planar alignment with the sensor active area. With practice and a set of blunt tweezers, the process of laying the gasket down properly was much improved. The trench design situated the sensor beneath the upper edge of the trench, and the chip gasket also aligned with the walls of the trench.

Another assembly complication was the electrical connection, which was partially blocked by the front inlet port (shown in Figure 4.18). The upper manifold of this flow cell was modified primarily by relocating the inlet and outlet ports for the sample stream. This was done to incorporate a flow constriction feature to prevent diffusion after sample loading. Since there were no internal routes for the fluid (i.e. all flow paths either begin or end at a surface), the relocation was necessary. Adapters were made to accommodate the change and experiments continued.

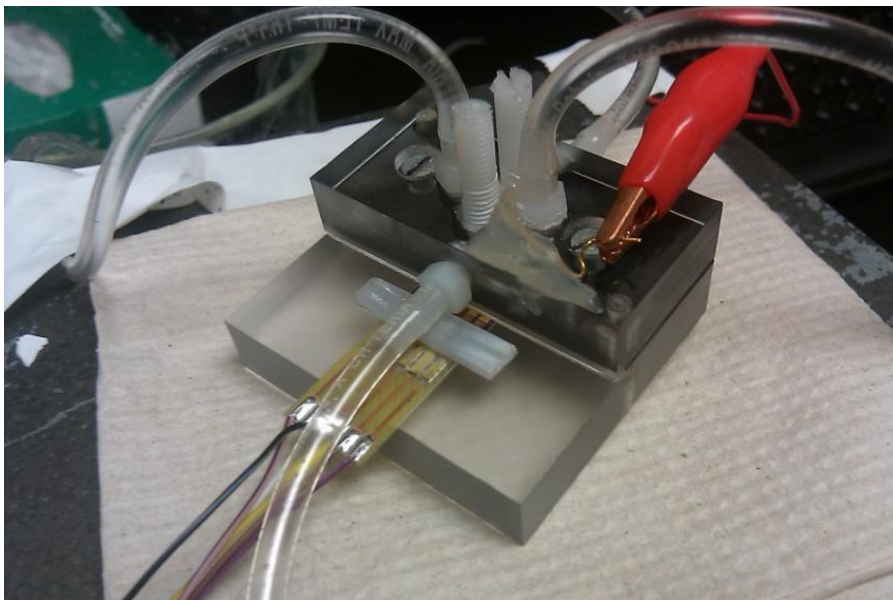


Figure 4.18 – Fully assembled prototype flow cell including sample tubing, counter electrode connection, and work/reference electrode connection.

#### 4.3.4 Pressure and Leak Testing

To determine the system's ability to withstand the pressures necessary to provide the required flow rates, the flow cells were subjected to pressure testing over a period of several (non-consecutive) days. DI water was pushed into the flow cell while monitoring the pressure at the inlet until flow was seen exiting the assembly. The maximum pressure during this process was recorded. Figure 4.19 contains a plot of the data recorded over three weeks compared to the computational results. For the 27 measurements obtained, the average peak pressure observed was 2.204 PSI ( $n=27$ , st. dev = 1.647); but, there were a noticeable number of pressures that were considerably higher than the average.

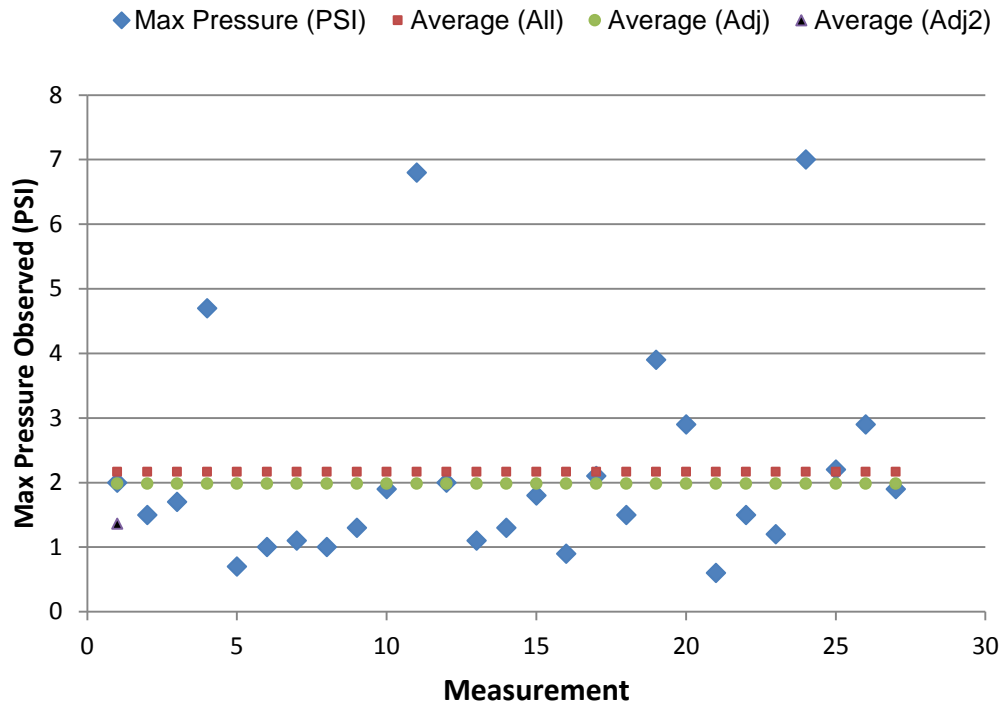


Figure 4.19 – Pressure data over three weeks in an assembled flow cell including the average pressure and the average after removal of perceived outliers; data indicated a few outliers which were believed to be associated with misalignment of the gasket layers.

Calculation of the coefficient of variation (CoV) was used as a means to indicate a relatively high variation. The general rule is that as a CoV approaches unity, the standard deviation is considered out of the ordinary. This value was obtained by dividing the standard deviation by the mean. In the original case above, the CoV calculated for the original data is 0.75, which was not close to unity, yet there was still some doubt given the outliers mentioned above. The Grubbs test (also called the extreme studentized deviate) was also used to test for outliers, which probes the data, point by point, to label a data point as an outlier by calculating a z value using the distance between the mean and the measurement divided by the standard deviation. Using a 95% confidence level, only a single data point (measurement 24, with a PSI measurement of 7) was returned as a



significant outlier. Removing this value adjusted the mean peak pressure to 2.019 (n=26, stdev=1.37), which did not improve confidence that measurement 24 was the only outlier. However, the Grubbs test suffers from *masking*, where two outliers close in value will both affect the standard deviation enough so only one will qualify as an outlier [106]. This appeared to happen with measurements 11 and 24.

Chauvenet's criterion was then applied which used the two standard deviation, three standard deviation, etc., rule, where 95 % of a normally distributed data set should fall within the selected standard deviation range [107]. For the original data, measurements 11 and 24 were 4.796 and 4.596 away from the mean, respectively. The 0.05 probability of a data point falling beyond two standard deviations was multiplied by the number of data points (27) and a statistical value of 1.35. This was much greater than 0.05, so the test for outliers failed. Regardless of the legitimacy of removing the outliers from the pressure data, it was assumed that a misaligned gasket was the culprit during these high pressure readings. When these high pressures were experienced, the cell was disassembled, inspected, and reassembled, and typically the pressure on the next test was more in line with the average. Looking at the data on a day-by-day basis instead of a single collective set (Figure 4.20), there is a general trend that appears to indicate that the peak pressures typically occurred after the first or second assembly during experiments.

The holes for fluid passage in the primary manifold were 0.5 mm and any blockage, even marginal, would cause an increase in pressure during the loading step. Lowering the average value of the max pressure would bring the measurements closer in line with the simulation data. There was a threefold difference between the simulated results at an estimated 80  $\mu\text{m}$  cell height (the height of the compressed gasket after

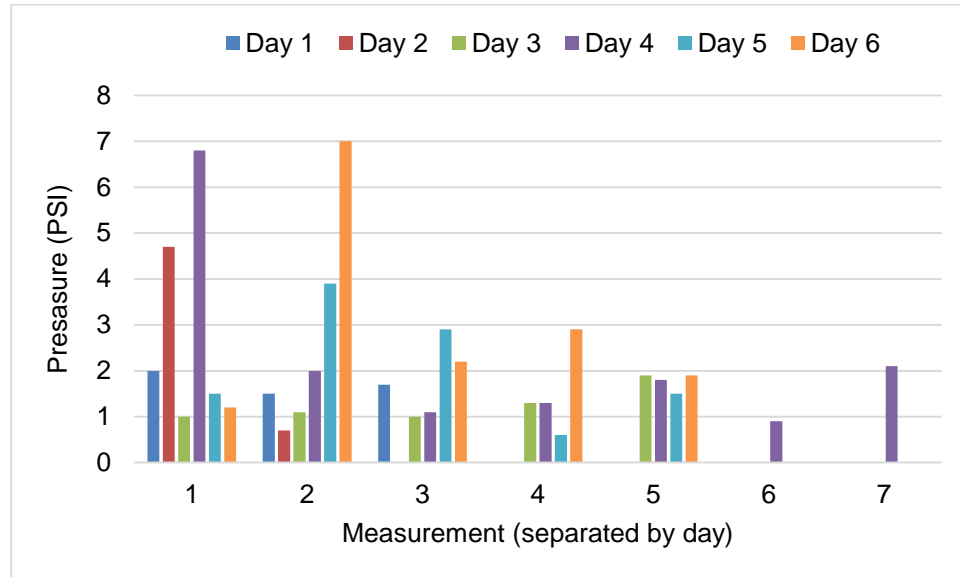


Figure 4.20 – Pressure data separated into different days, showing that the high pressures were typically experienced when the cell was first assembled. It was assumed that gasket misalignment was the cause.

assembly) and the calculated average (0.719 PSI at 80  $\mu\text{m}$  simulated versus 2.019 PSI measured). Removing both outliers would bring the average down even further (1.828 PSI) and closer to the simulated value.

The cell was rather robust and held up well over hundreds of experiments, however leaks began to develop on the top of the cell over time. To try and find which port was the culprit, a leak test was performed by placing soapy water on the outside of the assembled cell and pushing air into the cell with the outlet sealed. This process pressurized the interior volumes, and where air escapes, typically at the weakest point, bubbles formed to indicate the location of the leak. The leaks in this flow manifold were predominantly seen near the isolation screws on the top of the cell. These holes were tapped much deeper (by necessity) compared to other tapped holes and it was assumed

that the threads in the hole were failing and not creating a tight seal. At this point, Teflon tape was used to wrap the threads in an attempt to improve the seal and eliminate leaks.

#### 4.4 Sensor Fabrication

While several electrode patterns were contained on the full-wafer photomask image shown in Figure 3.4, two of these designs were given higher priority in this study. The vast majority of the flow cell experimental data was recorded using the design shown in Figure 4.21A, which has a working electrode area of 25.6 mm<sup>2</sup> (large gold surface area) and a reference electrode area of 0.714 mm<sup>2</sup> (centrally located strip in the center of

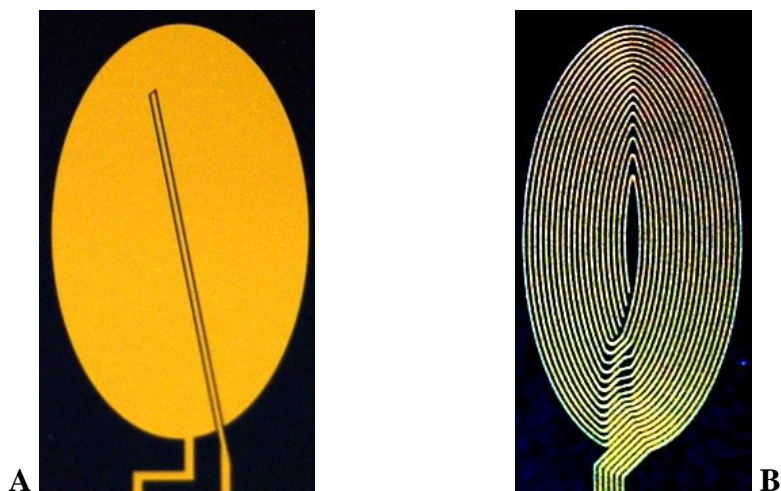


Figure 4.21 - Two versions of the microfabricated sensor electrodes. Sensor A was the version predominantly used in this study. Electrode B contains six finger electrode sensor designed and fabricated to test for redundancy.

the working electrode). This design attempted to one-dimensionalize the diffusion of analyte in the cell by maximizing the work electrode area to fit the area of the cell volume. Except for the area occupied by the narrow reference electrode, the largest diffusion distance for any analyte molecule was the height of the thin-layer cell. The second design used in the study (Figure 4.21B), contained a total of six electrodes, five

working electrodes and one converted to serve as a pseudo reference electrode. The areas of the working electrodes varied from 1.73 mm<sup>2</sup> up to 2.49 mm<sup>2</sup> (average= 2.035 mm<sup>2</sup>, st.dev.=0.268). This particular electrode was used to test for redundancy of a field deployable system so if one electrode fails, the system could simply switch to the next alternate electrode.

A full wafer of sensors before dicing is shown in Figure 4.22. Liftoff of the gold layer in the connection pad area of the six-electrode design is demonstrated in the inset of Figure 4.22, which was due to poor adhesion of the Tantalum adhesion layer. This issue was mitigated after fine-tuning a few of the fabrication steps. The height of the gold layer from the oxidized Si substrate was measured with a profilometer (Zygo) and found to be 97 nm (n=3, stdev=18.451) for the single electrode oval area and 59 nm (n=3, stdev=16.352) for the six-electrode chip. Figure 4.23 represents a cross-sectional view of

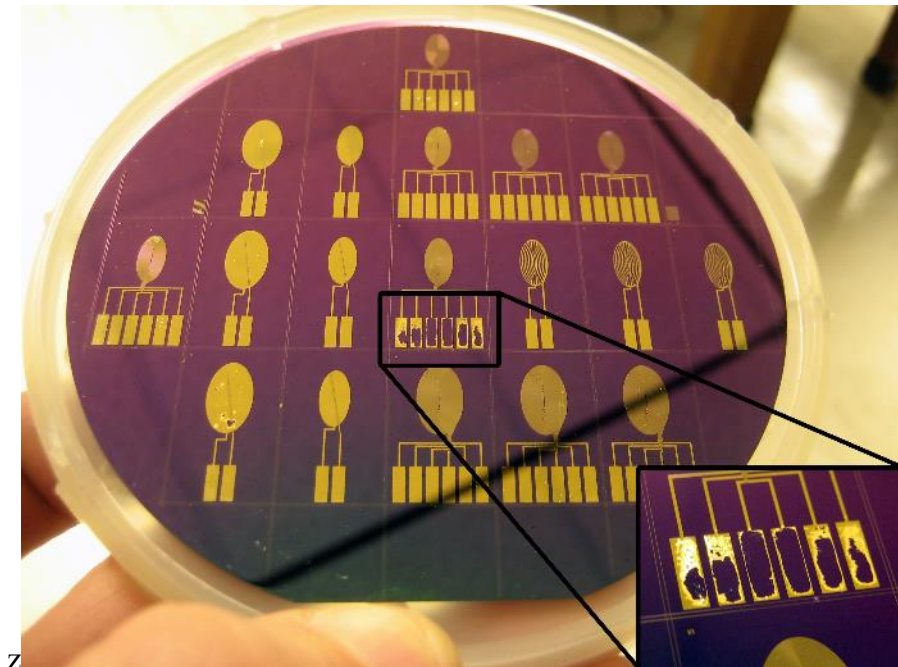


Figure 4.22 – Full wafer of sensors. Liftoff of the gold layer was the primary mode of failure in the first few fabrication attempts.

the central reference electrode showing the space between the large oval area and the line electrode was 43  $\mu\text{m}$ . Statistical data on this particular geometric feature was not compiled.

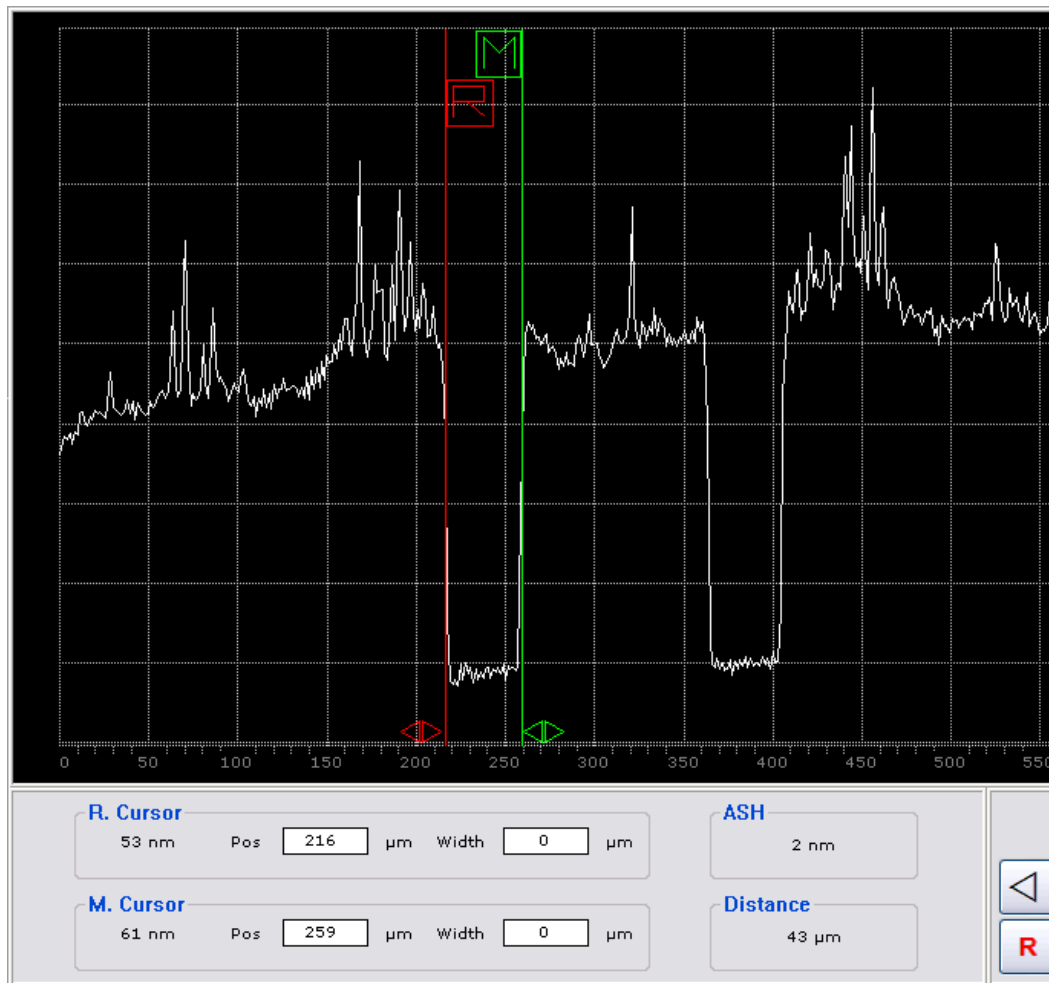


Figure 4.23 – Large surface area electrode undergoing profilometry tests. The spacing between the large area and the line electrode is 43  $\mu\text{m}$  in this measurement.

#### 4.4.1 Pseudo Electrode Fabrication Results

In both chip designs, a single electrode was chosen to be converted into a pseudo-reference electrode using the technique described in Section 3.1.6. This process was fundamentally an electrochemical deposition where Ag molecules suspended in solution

were electrically attracted to the plating gold surface, which was biased appropriately to foster the process. As a result of this process, the original yellowish gold appearance of the sensor area transitioned to a smooth darkened color (blackish) from the Ag coating step. The second step in the deposition process consisted of a chloridation step where the Ag was converted to AgCl yielding a drastically different texture on the pseudo reference electrode surface (Figure 4.24 A and B). In both images, the converted electrode stood out in stark contrast to the original gold electrode(s) which was (were) unaffected by the process. Upon closer inspection (Figure 4.25), the relatively smooth area of the unmodified gold electrode ( $\sim 40$  nm surface roughness) was clearly distinguishable from the new surface of the modified electrode. Surface roughness measurements were not performed on the Ag|AgCl electrodes after conversion to protect the integrity of the new material.



Figure 4.24 – Post processing photographs of the Ag|AgCl pseudo-electrodes for the two electrode (A) and six electrode (B) sensors. Arrow indicated pseudo reference

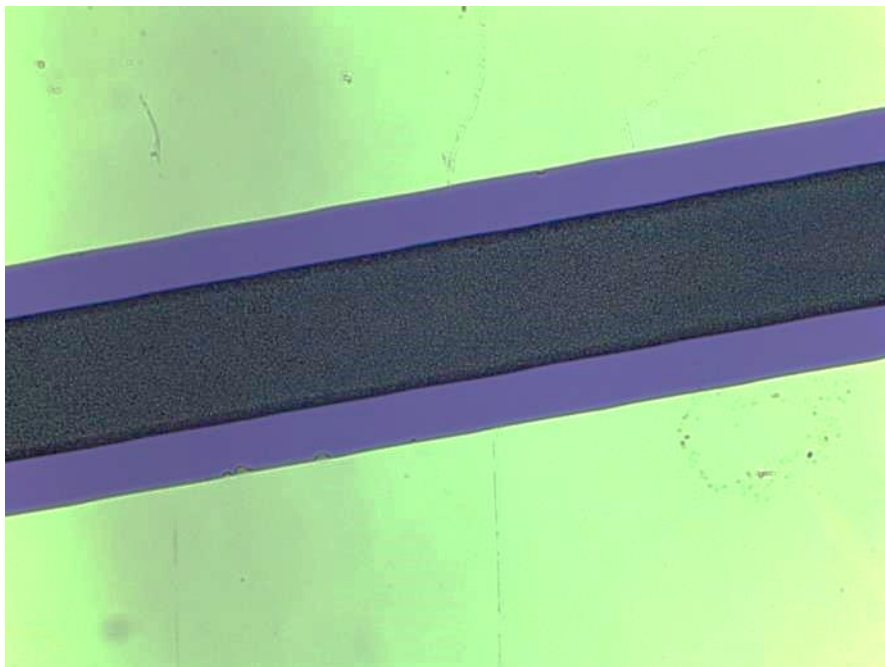


Figure 4.25 – Magnified view (4x) of a gold electrode that has been converted to an Ag|AgCl pseudo-reference electrode. The color change and surface roughness of the new material was easily visible.

## 4.5 Electronics

Using the individual schematics for each sub-circuit of the potentiostat which included the power regulation stage, the trans-impedance amplifier stage, and the working electrode feedback/regulation stage, a full schematic of the electronics was created in Multisim (National Instruments, Austin, TX) and ExpressSCH (ExpressPCB, Santa Clara, CA) schematic capture software. These types of electronics CAD packages tracked all pins, nodes, headers, and electrical buses, including a database of the specific parts that represent the circuit. This functionality allowed an easier transition from the schematic to the actual board layout, which required not only the necessary connections, but also the footprints of the specific parts used in the design. ExpressPCB, which included a sister program called ExpressSCH, was finally chosen due to the quick

turnaround time (2-3 days) and low cost (~\$79 for three boards including a white silkscreen and green solder mask) of a 3.8 in. x 2.5 in. board that contained the potentiostat circuit.

#### 4.5.1 Final Schematic and Board Layout

The schematic of the final design used to fabricate the board with industry standard nine-pin header connectors to enable the circuit to be controlled beyond a PC with an associated DAQ card as outlined in Chapter 3 is shown in Figure 4.26. This design schematic was transferred into the ExpressPCB software to layout the circuit board. The final silkscreen of the board shown in Figure 4.27 represented the final design and location of the electronic components.



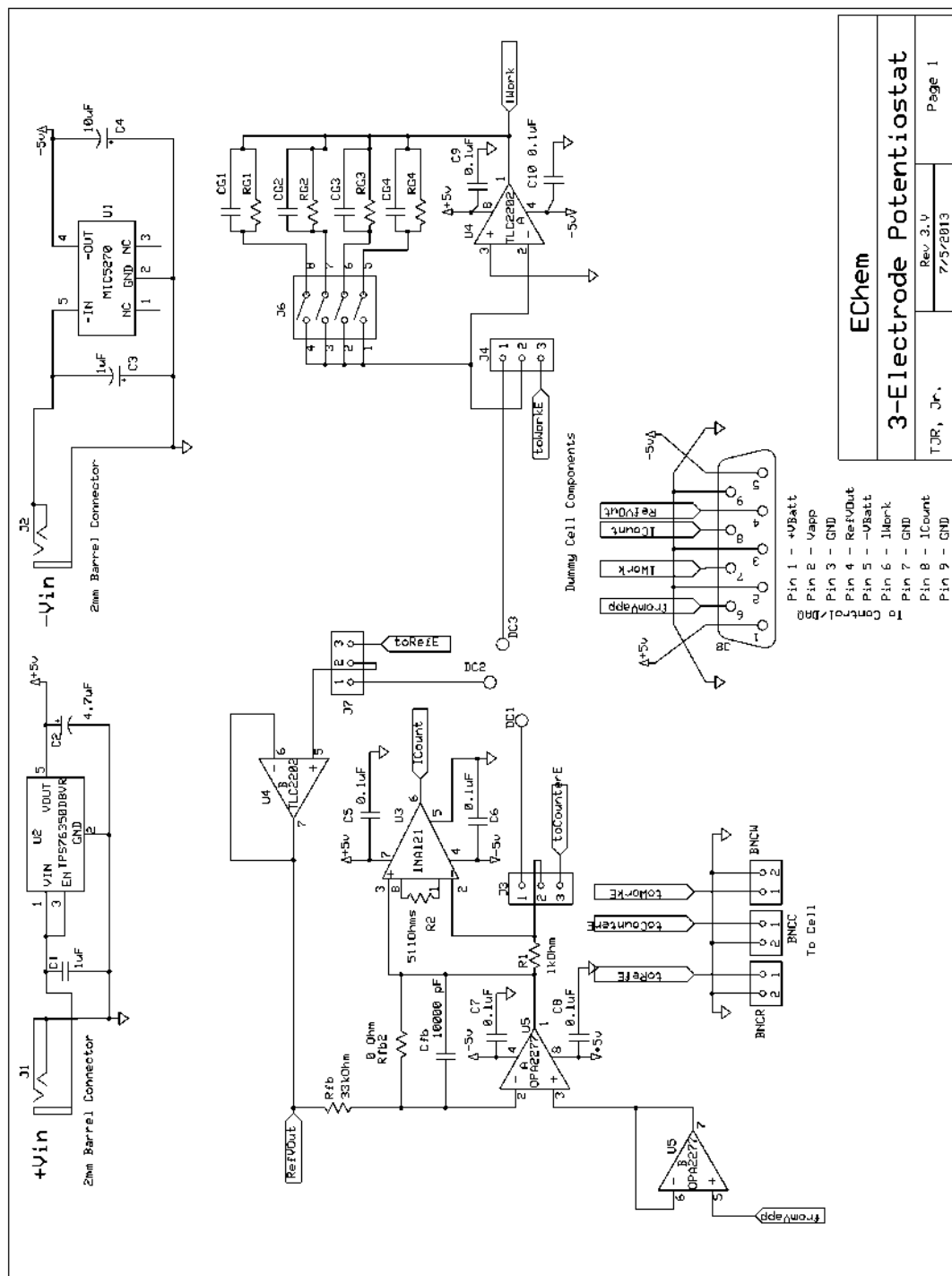


Figure 4.26 – Final schematic of the custom potentiostat including all stages outlined in Chapter 3, as well as the headers for connecting to power and the connector to send data to the DAQ card.

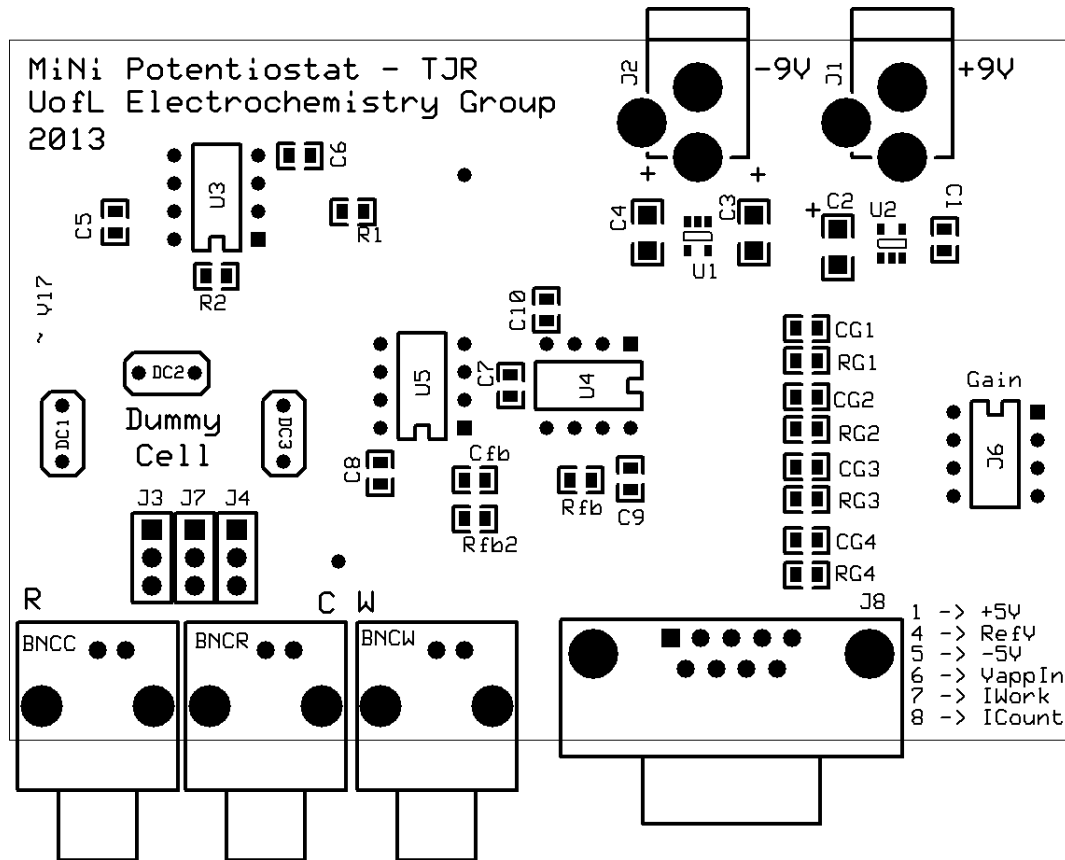


Figure 4.27 – Silkscreen image of the final printed circuit board design layout.

#### 4.5.2 Final Printed Circuit Board

The final board design (Figure 4.28) was limited to the size restrictions outlined by the ExpressPCB “MiniBoard” option, a footprint of 3.8” x 2.5”. The largest components on the board were the BNC connections attached to the leads of the work, reference, and counter electrodes on the sensor. These could easily be replaced by a more compact, three terminal equivalent, albeit at an increased cost. The DB9 connector as

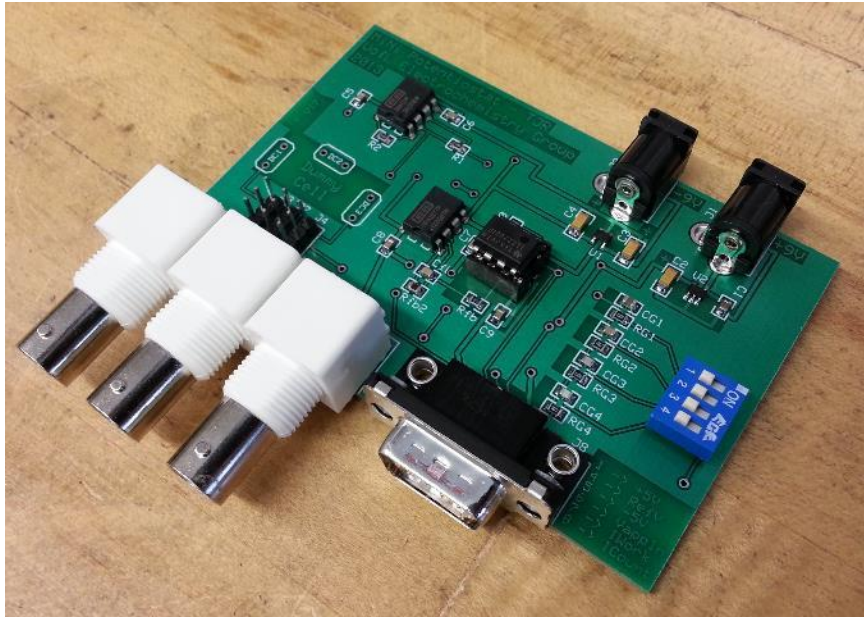


Figure 4.28 – Final populated board containing the potentiostat circuit designed via control by custom software.

well could be adapted to some alternative, less bulky component. This connector tethered the potentiostat circuit to whatever device controlled it, for example, a laptop computer as in the current configuration, or perhaps an embedded system. Additionally, a more complex circuitry could be added to the design to reduce the power requirements to a single supply (perhaps run completely from a USB port, for example) instead of a split supply. Figure 4.29 shows an image of the potentiostat connected to the DAQ breakout board, ready for analysis.

#### 4.5.3 Electrical Testing and Performance Evaluation

In order to test the electrical performance of the individual sub-circuits on the custom potentiostat, several measurements were taken and evaluated. Comparisons were

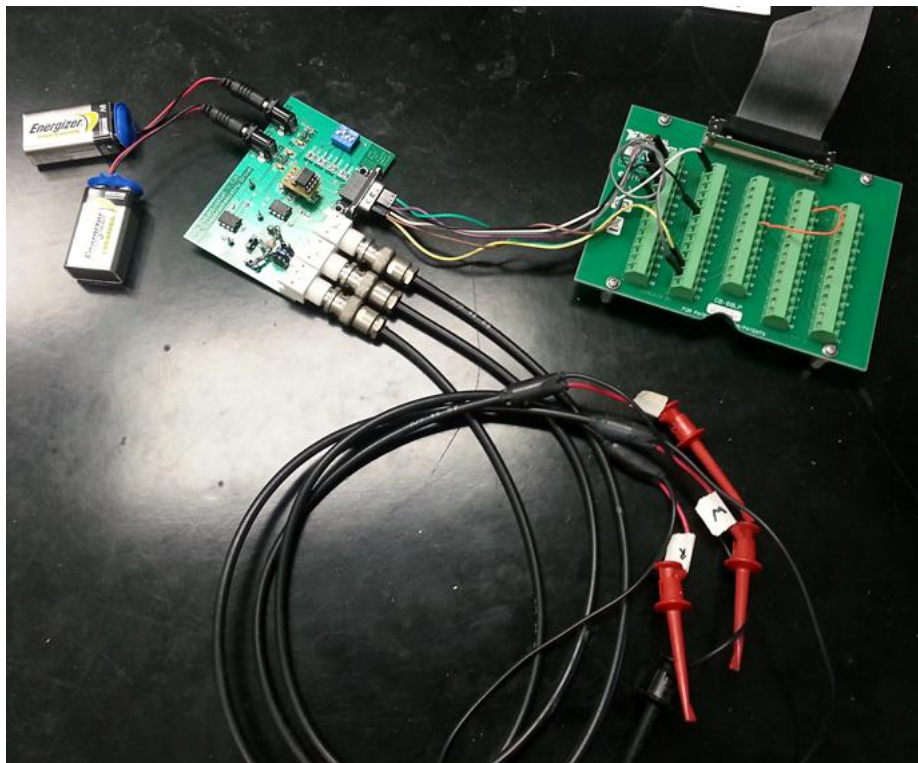


Figure 4.29 – Custom potentiostat with working, counter, and reference electrode leads, connected to DAQ breakout board and ready for analysis.

drawn between the theoretical precision of the A/D and D/A board when connected to the potentiostat, as well as the performance of the circuit using an electrical dummy cell in place of the electrochemical cell.

#### 4.5.3.1 Reference Electrode/Feedback Circuit Testing

Table 4.2 contains the results of electrical tests performed on the reference electrode using a fixed resistor network to compare the input voltage to what the feedback control circuit was attempting to apply to the counter electrode. For an input of

Table 4.2

Measurement Data on Feedback Control

Measurement Type	Input Voltage	Average Data	Std Dev	n
Offset Voltage	0 V	555 $\mu$ V	76 $\mu$ V	100
Noise Floor	1 V	1.0034 V	.00032 V	100

zero volts, the measured offset value of 555  $\mu$ V may have come from the D/A converter on the DAQ board or either of the two operational amplifiers in the potentiostat circuit, but less than a single millivolt of output was acceptable. The offset was compared to the specifications for the 6062E DAQ card which listed an average offset accuracy of 1.0 mV after calibration. Therefore the 555  $\mu$ V measurement is within specifications. For a one volt input at the counter electrode, the ripple measured by the reference electrode was held within two bits on the A/D, representing a fluctuation of approximately 0.32 mV. The specifications document lists a post-calibration relative accuracy after calibration of  $\pm 3$  LSB, so two bits of fluctuation is also within normal range.

In order to observe the regulation capabilities of the feedback in response to a pulse input, measurements were taken via the differential measurement stage of the circuit for a pulse input of 100 mV for 1 millisecond. The results of this test are shown in Figure 4.30, which indicated no ringing of the regulation stage when the pulse was applied. If this part of the circuit struggled to maintain the voltage output, an oscillation would appear in the measurement just after the pulse input. The plot of the output showed no oscillations were observed for both a positive and negative pulse. This measurement also ran the risk of pushing the limits of the op-amps, which have a hardware limitation (slew rate) that limits how fast the output can track the input. Once again, no problems were observed.

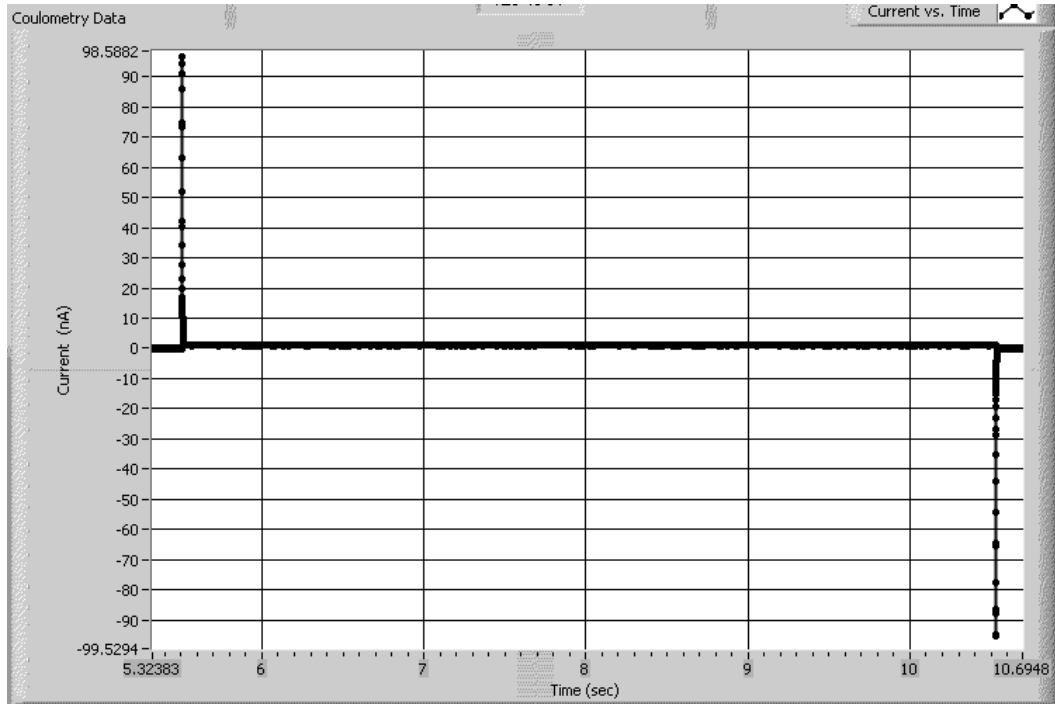


Figure 4.30 – Data showing the stability of the system to a pulse input. No ringing of the measured signal was seen after a pulse input was applied to the dummy cell.

#### 4.5.3.2 Power Regulator Output Stage Evaluation

When the power supplies were first connected, a quick check of the output voltages of the regulators revealed that the output of the +5V supply appeared to be shorted (0V reading at the output pin), while the -5V supply was outputting the correct voltage. A comparison of the schematic drawing to the PCB layout and continuity test revealed no problems. The datasheet of the part in question was inspected, and revealed that the footprint, which matched the pin in the schematic to the pin on the device to be used on the PCB, had two pins switched (the enable pin). A remedy for this problem was to add a small jumper wire over the P50 component to engage the enable pin (Figure 4.31). The accuracy of the libraries that contained parts with errors was a common

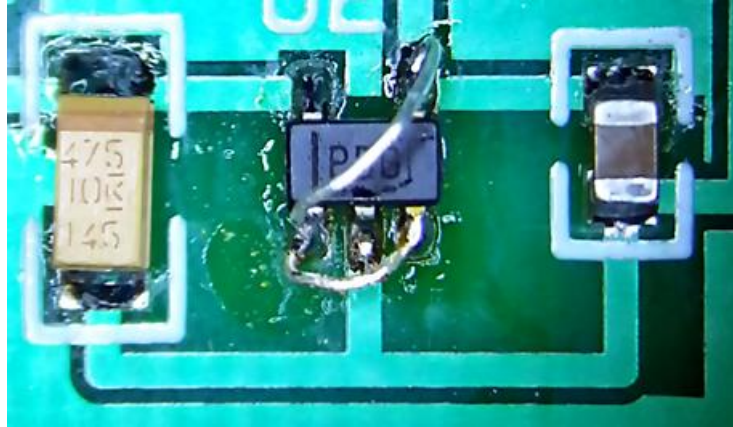


Figure 4.31 – Image showing the quick repair of enable pin connection using a jumper wire (~ 8X magnification).

problem with the free software. Once the repair was made, the output of the regulator adjusted to the correct value and the details of the regulator stages were assessed.

Measurements were also obtained at the output connector of each of the voltage regulators in an attempt to observe any ripple that may trickle through the op-amp stages and potentially alter the electrochemical data. Table 4.3 contains representative data for this measurement. Each of these measurements showed approximately 3-4 bits of ripple representing a range of  $\pm 3.908$  mV. This value was acceptable given the fact that it is 0.078% of full-scale.

Table 4.3

Measurement data for +5 and -5V supply voltages

Output Voltage	Average (V)	Std Dev (V)	n
5V	5.0155	0.00017	100
-5V	-5.0144	0.00024	100

#### 4.5.3.3 Transimpedance Stage vs. Differential Input Evaluation

The potentiostat has built-in redundancy when measuring the electrochemical current due to the inclusion of both a differential measurement technique as well as the transimpedance amplifier stage. The latter of these two was the more flexible of the two due to the switchable gain settings included on the board. The gain setting on the transimpedance stage was set to 100  $\mu\text{A}/\text{V}$ , which roughly matched the fixed gain on the differential stage (100) and a comparison between these measured values was performed to obtain a percent difference value.

Table 4.4 outlines the measurements for the current measured at each stage for a 0.100 V input applied across a 1 M $\Omega$  resistor, which should generate a current of 100  $\mu\text{A}$  due to the simple Ohm's law relationship ( $V/R = I$ ). Using the transimpedance measurement as the assumed correct value, the results indicated a percent difference of 3.26% and a simple program was written to monitor these currents and calculated the percent error during the experiment (Figure 4.32). This dual measurement allows the system to confirm that flow in the cell is balanced and no other sources or sinks of current are contributing to the current measurement. If the currents did not balance, there

Table 4.4  
Comparison of Current Measurement Between Differential and Transimpedance Stage

Stage	Average Data ( $\mu\text{A}$ )	StDev ( $\mu\text{A}$ )	n
Differential	104.4	0.034	100
X-Impedance	101.1	0.019	100



would be some other source of current in the cell besides the electrochemical reaction and would have to be discovered and eliminated.

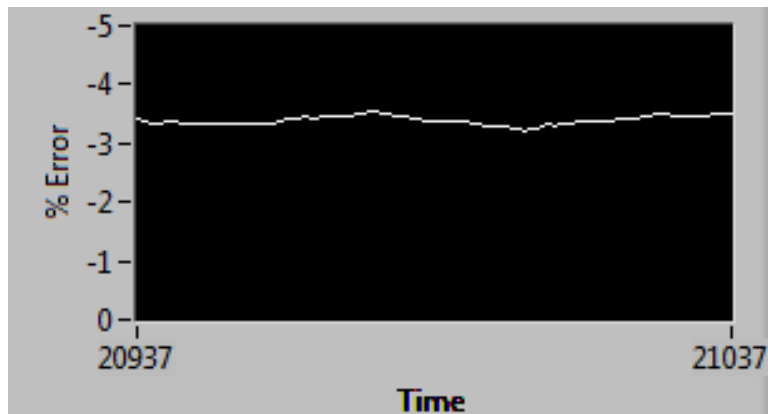


Figure 4.32 - Image indicating percent error between current measuring techniques (differential vs. transimpedance stage)

#### 4.5.3.4 Transimpedance Amplifier Gain Stage Analysis

The current to voltage amplification was designed with four selectable gain settings by incorporating a four-position DIP-switch in the feedback path of this stage to select the resistor that establishes the gain. To test each gain stage, a 1 MOhm (1% tolerance) resistor was used to inject a range of currents into the amplifier input and the output voltage was measured. In all cases, ten measurements were taken at each setting ( $n=10$ ) and the average and standard deviations were calculated. The lowest gain setting was not examined due to the large voltages necessary to establish a sizeable voltage output with this setting. Figure 4.33 shows the results of 10 kOhm gain stage which was designed to produce a 0.1 V output for a 1  $\mu$ A input. The trend was linear and had a negative slope due to the inverting configuration of the operational amplifier used in this stage. The input range was -4 to 4  $\mu$ A in steps of 1  $\mu$ A.

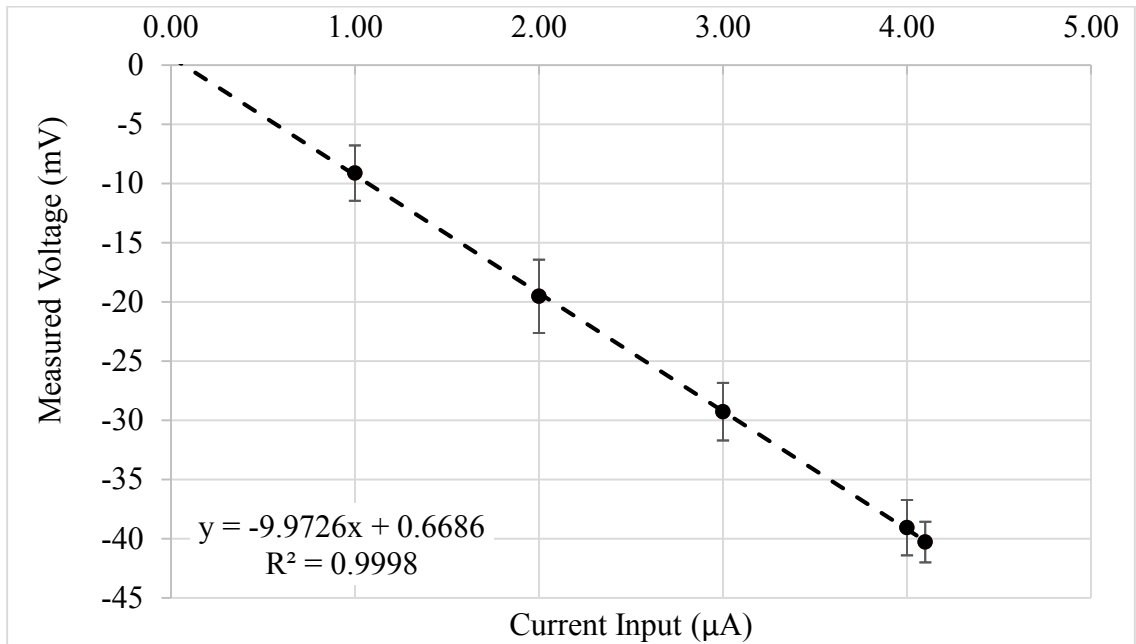


Figure 4.33 – Plot of 10kOhm gain stage setting of the transimpedance amplifier over and input range of 0 to 4.1 Volts. The trend line is linear with an offset that agrees closely with the measurement in Table 4.2.

The 1MOhm gain setting, which was designed to generate a 1V output voltage for a 1 μA input current, showed an extremely linear response and correlation value equal to one as a result of a calculated standard deviation that had to be scaled up by 10x to register on the plot (Figure 4.34). The input range covered a span of -4 to 4 μA in 1 μA steps. The calculated slope value of -998.35 would ideally be -1000 for a perfectly linear relationship, and only represented an error of 0.165%.

A range 100 times lower than this (-40pA to 40pA) was tested on the 1 MOhm gain setting to observe the ramifications of choosing the correct setting for the measurement. Measuring current at the picoamp scale is a complicated task and there are

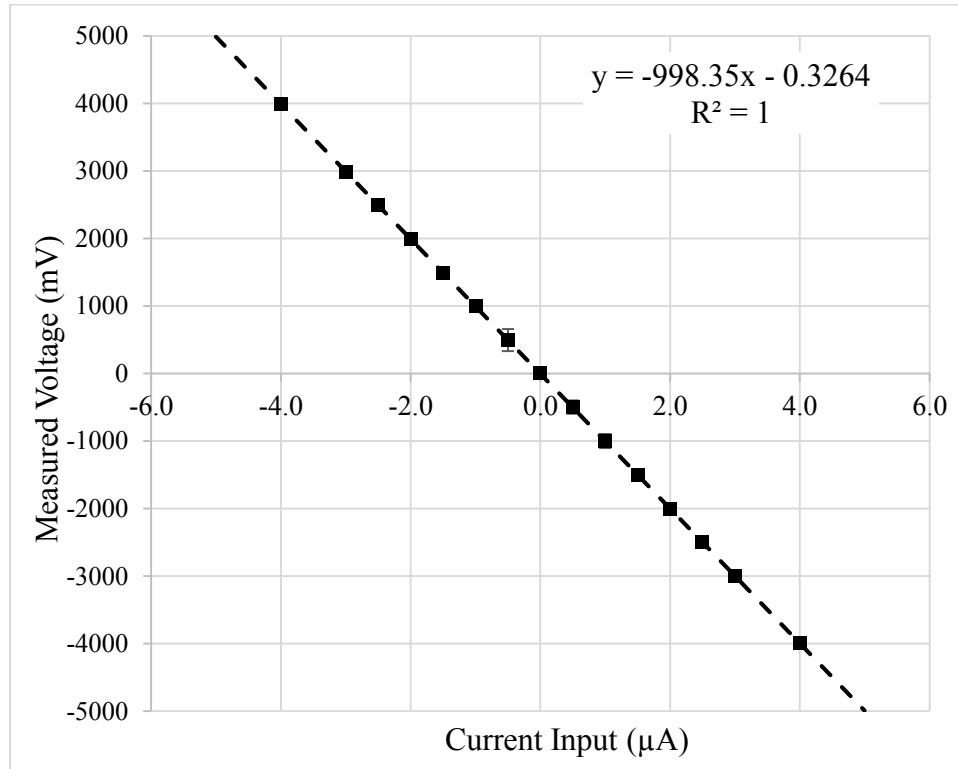


Figure 4.34 - Plot of 1M $\Omega$  gain stage setting of the transimpedance amplifier over an input range of -4 to 4 Volts in 1 Volt increments. The linear trendline is reporting a perfect correlation. The error bars, normally representing one standard deviation, have been multiplied by 10 so the bars show up on the plot.

instrumentation techniques specifically designed for this. Not surprisingly, at this gain setting there was considerable noise indicating the circuit was struggling with accurately resolving the small current, as represented visually in the error bars seen in Figure 4.35.

While there was still a general linear relationship, the calculated slope, ideally at -1000 for this gain stage, dropped to -926.99, an error of 7.3% from the desired relationship.

The error increased dramatically at values close to ground potential, and can be attributed to the intricacies of measuring picoamp (and smaller) currents, which are typically on the order of the bias currents driving the measurement circuits.

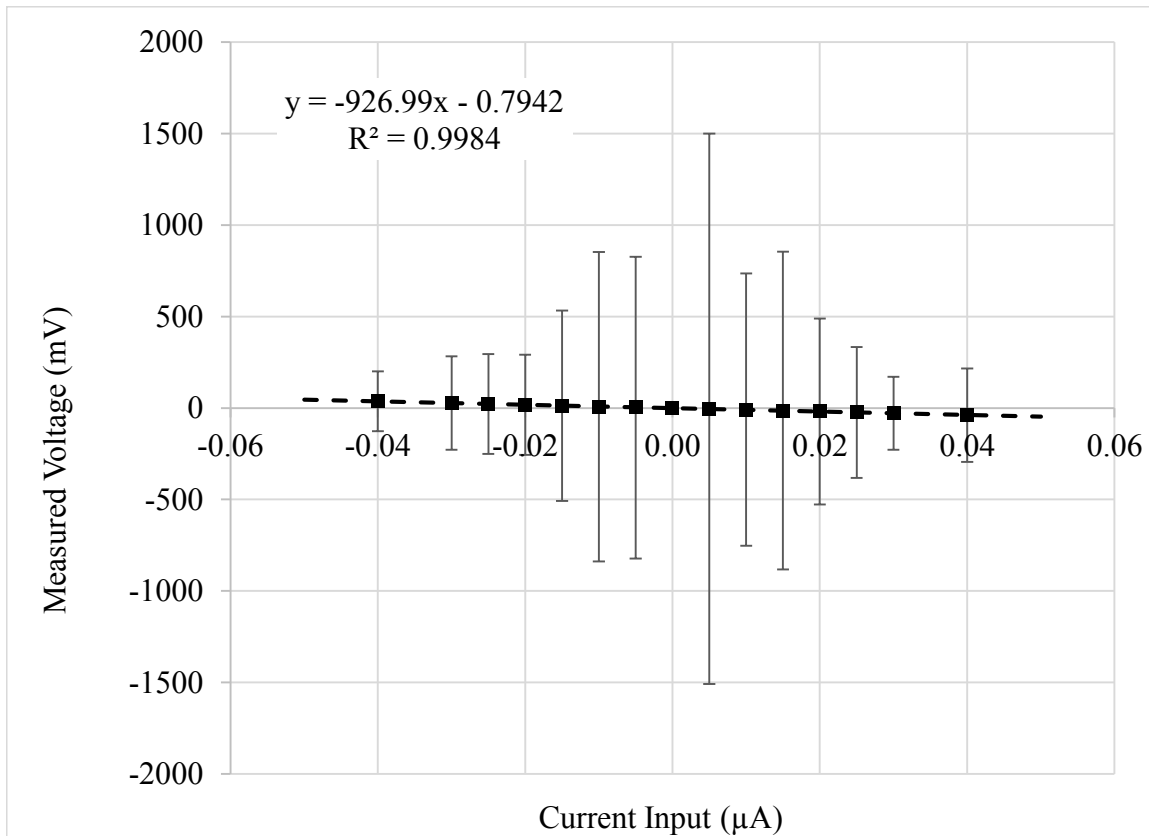


Figure 4.35 - Plot of 1MΩ gain stage setting of the transimpedance amplifier over an input range of -0.04 to 0.04  $\mu\text{A}$  in 0.01  $\mu\text{A}$  increments. While the correlation calculated on the average values at each data point is high (0.9984), the error bars, representing one standard deviation, show a large deviation from the average, especially close to ground potential.

The gain setting was increased to the most sensitive setting included on the transimpedance stage (100 MΩ), and the same range of currents were injected into the amplifier. Figure 4.36 shows an improved conversion of the picoamp magnitude currents with a correlation of near unity (0.9987); however, a similar pattern that occurred in the previous measurements was observed. Measurements closer to ground potential displayed a much larger standard deviation than those away from ground. Interestingly, the percent error calculated for the slope of the trend line in this measurement was also high (7.33%). These deviations close to zero most certainly affected the measurements for small

currents. The range of reduction and oxidation voltage used in the coulometry experiments switched between -0.1 Volts and 0.4 Volts. Fortunately, the experiments using those values stepped between them and never dwelled near 0 Volts.

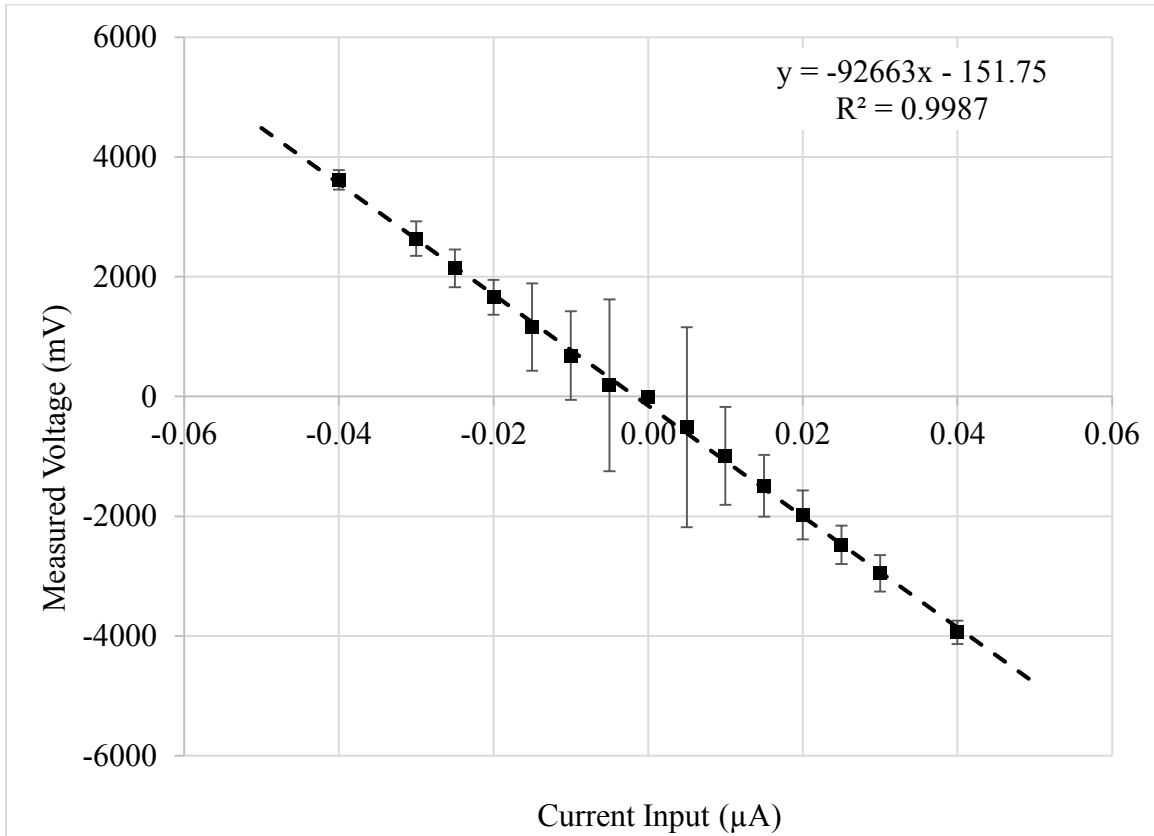


Figure 4.36 - Plot of 100M $\Omega$  gain stage setting of the transimpedance amplifier over and input range of -0.04 to 0.04  $\mu$ A in 0.01  $\mu$ A increments. The linear trend line is reporting a near perfect correlation, but issues do exist. The error bars representing one standard deviation and increase for data points closer to ground potential.

To examine the frequency response of the transimpedance stage, a sine wave was applied across a 1 M $\Omega$  resistor to generate a sinusoidal input current, and the  $V_{pp}$  output of the amplifier was measured. For each gain setting there was a feedback capacitor to stabilize the circuit, and the presence of the capacitor created a low-pass filter. At input frequencies greater than the RC combination of the gain stage, the output voltage began to drop. It was critical that this filtering effect did not dampen the output

signal when the potential was stepped up to the oxidation potential or down to the reduction potential from the holding potential. The range of frequencies was approximately 10 Hz to 2500 Hz (Figure 4.37). The RC combination for this particular gain setting (1 MOhm feedback resistor; 1 nF feedback capacitor) was designed to be 159.16 Hz using:

$$F_c = \frac{1}{2\pi RC} \quad \text{Equation 4.1}$$

where  $F_c$  was the theoretical cutoff frequency for the low pass filter, R was the resistor in the feedback path and C was the feedback capacitor. The measured cutoff frequency for the filter was estimated by projecting the linear portion of the curve (a logarithmic expression due to the X-axis scale) to the 0 dB crossing. The last ten data points were used to fit a trendline and a correlation of 0.998 was generated. Using the resulting equation of fit, setting 'y' to zero and solving for 'x', the measured cutoff was 153.27 Hz, for an error of only 3.7 percent. The data points used in this graph were generated from the averages of 10 measurements at each frequency, and for each measurement, the percent standard deviation was less than one percent, so no error bars were included in the plot. Table 4.5 contains the theoretical and measured cutoff frequencies for other gain settings.

Table 4.5

Theoretical vs. Experimental Cutoff Frequencies For Three Gain settings

	Device		Unit	Theoretical $F_c$		Measured $F_c$		% Error
Gain 2	CG2	100	nF	159.16	Hz	148.32	Hz	6.807829
	RG2	10	k $\Omega$					
Gain 3	CG3	1	nF	159.16	Hz	153.27	Hz	3.696296
	RG3	1	M $\Omega$					
Gain 4	CG4	10	pF	159.16	Hz	151.85	Hz	4.589865
	RG4	100	M $\Omega$					

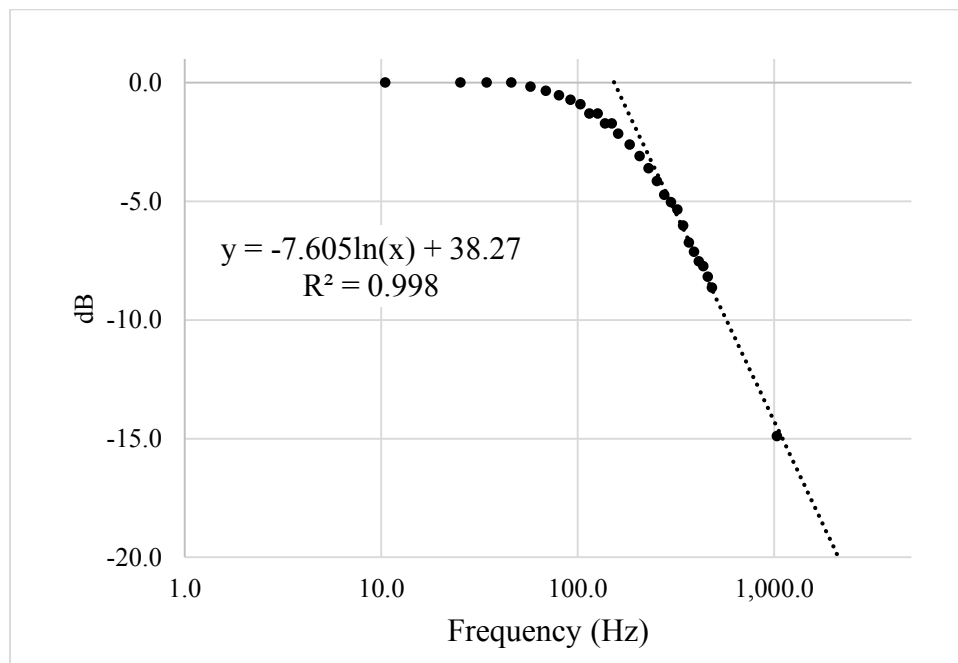


Figure 4.37 - Frequency response plot of the transimpedance amplifier circuit. The curve fit is generated on the last ten data points, where a straight line demarcates the -20 dB/decade drop after the filter kicks in.

#### 4.5.3.5 Dummy Cell Testing

As outlined in Chapter 3, the fluid-electrode interface was modeled by an electrical analogue composed of a parallel resistor/capacitor combination. This setup mimicked using a real capacitor-resistor combination in a dummy cell to test the ability of the potentiostat to track the current during a step potential. Figure 4.38A contains simulation results of the transimpedance stage (including the op-amp used in the potentiostat circuit) for a dummy cell that contained a resistor (1 M $\Omega$ ) and capacitor (0.1  $\mu$ F) in parallel. The time scale in this window was one ms/division and the amplitude scale was 50 nA/division so the current spike decayed in approximately 5 milliseconds. Figure 4.38B is a snapshot of data from the potentiostat using a step potential from 0 V to -0.01 V and also showed a decay of approximately five milliseconds. The negative potential step was simply to provide a positive output since the transimpedance amplifier stage was inverting. When the step was applied, the sharp rise of input contained high frequencies, which viewed the capacitor as a short circuit. The huge current spike was due to this virtual short, right after the step happens. The magnitude was indeed huge compared to the steady state, final current, which could almost not be seen at this scale. Once the input step reached a steady value, which for all intents and purposes was a DC bias, the capacitor transferred the current over to the resistor in a time frame proportional to the RC time constant. The RC time constant was calculated using the inverse of Equation 4.1. However, attaching the RC circuit to the transimpedance amp modulated the time constant, and the simulation allowed visualization of this effect with good agreement to the measured value.



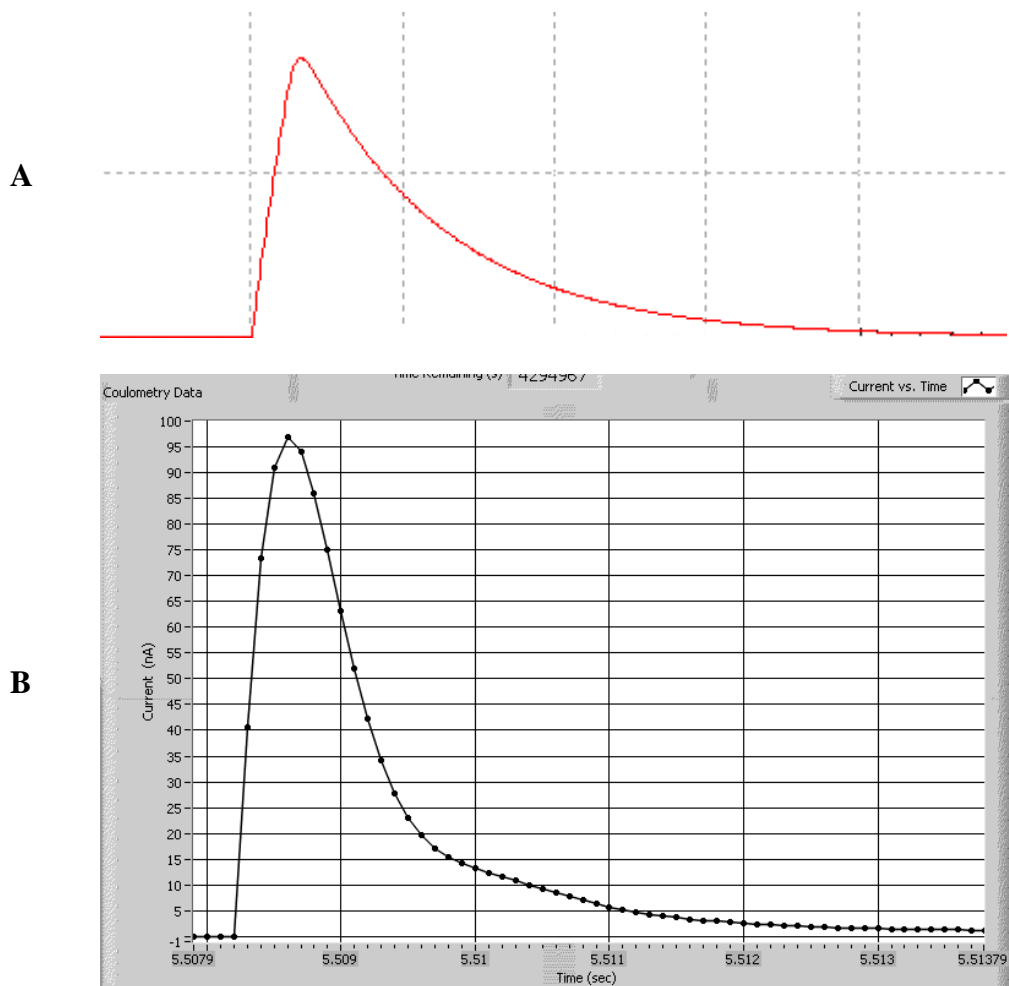


Figure 4.38 – Fast scan of a resistor/capacitor parallel pair acting as a dummy cell of the working electrode; (A) simulation results; (B) Measured results

## 4.6 Software

Controlling the potentiostat via software extended the capabilities of the fixed hardware. Multiple software programs were written, both to directly control the hardware and to manipulate data generated after experiments were completed. The primary software used allowed the user to control the steps of a coulometric measurement, including the initial hold time and voltage, step potential, experiment time, and final voltage (Figure 4.39). The software controlled the timing of the data acquisition (samples

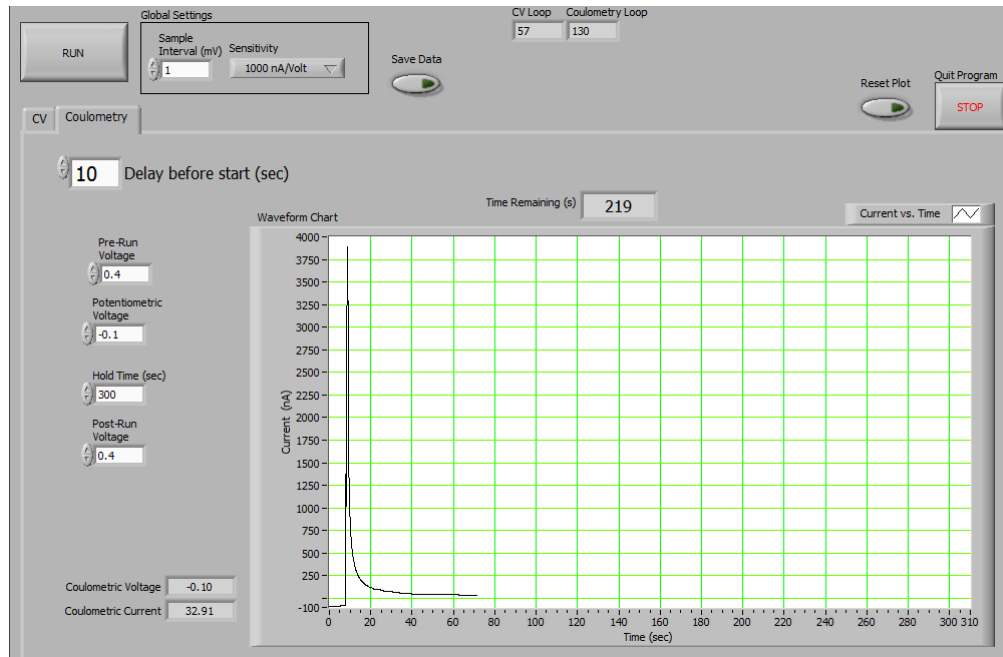


Figure 4.39 – Software user interface for controlling the coulometry experiments. This particular image has an active experiment underway, and the current being generated by the cell can be seen in the plot area.

per second) as well as provided an entry for the gain setting used for the experiment so the current was calculated from the output voltages measured. Data was easily saved at the end of an experiment.

Besides the coulometric analysis, the software contained a cyclic voltammetry (CV) mode to allow the user to build a ramp input and scan the voltage while measuring current. The ramp rate was included since this parameter affected the ability of an electrode to respond to the rapidly changing voltage. In Figure 4.40, the ramp rate 100 mV/sec for the RC dummy cell caused a hysteretic effect as the slope of the ramp changed. If the scan rate was slow enough, then voltage would look like a DC voltage to the RC couple and produce a straight line, representing Ohm's law (where the slope would be resistance; not shown).

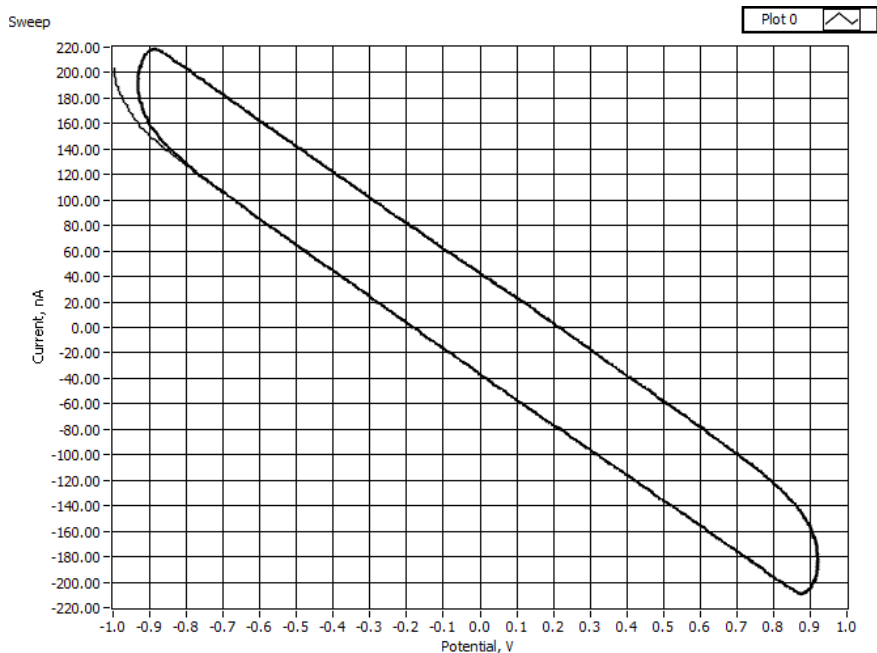


Figure 4.40 – 100 mV/sec CV scan with dummy cell showing the hysteretic effect that distorts the typical linear curve described by Ohms' law.

#### 4.6.1 Web Interface Control

The software was exported to be used by web control, and the user interface was pulled up over the internet using a special web address. To use this functionality, a plugin (much like Adobe Flash) provided by National Instruments called the LabVIEW RunTime Engine (V.2011) was installed and the web browser-based components were installed. The user interface looked and operated no differently than the computer-based version, despite being controlled remotely. Experiments were performed with the dummy cell to ensure the remote access was working correctly and that all features of the software were accessible via web control (Figure 4.41).

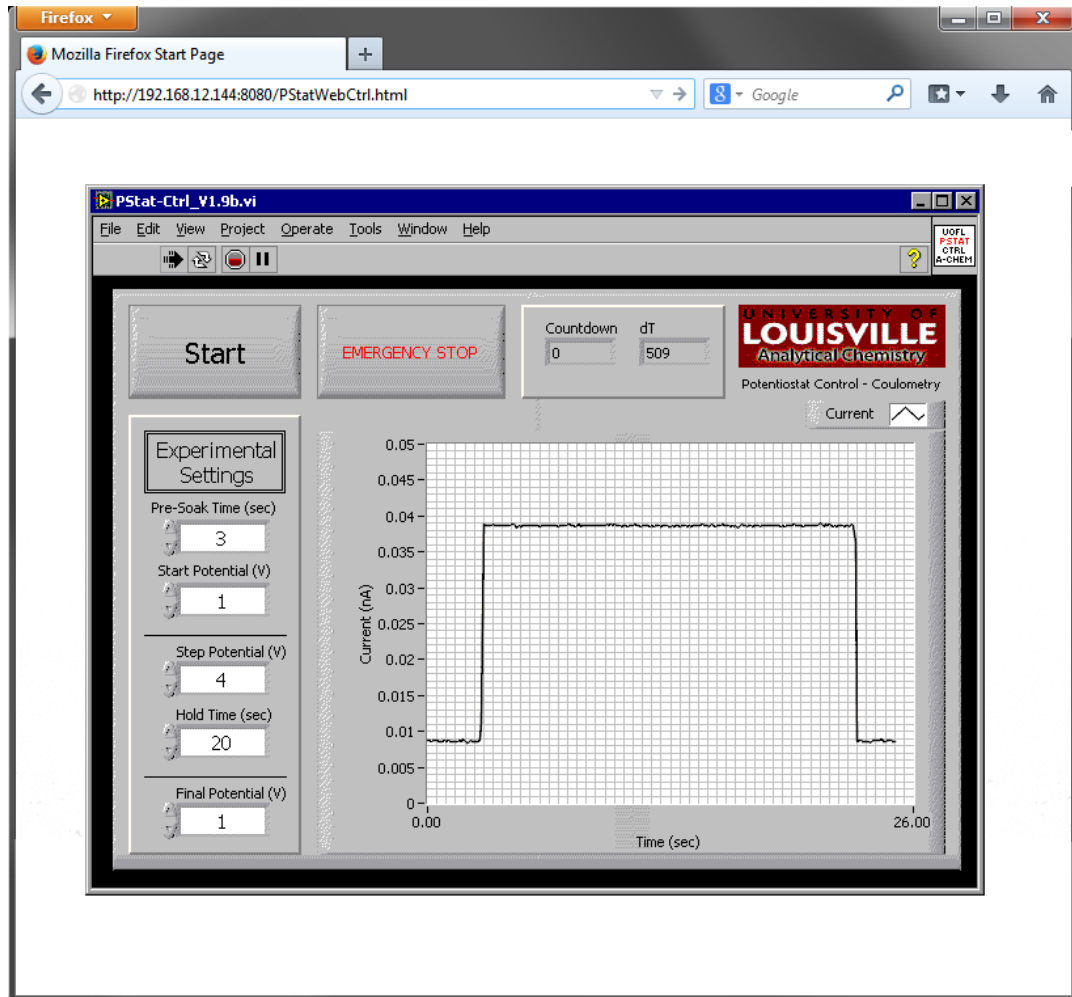


Figure 4.41 – Web interface provided over the internet via Firefox web browser running a LabVIEW plugin (LabVIEW Runtime Engine) to allow remote control of the software. A step potential of 4 V is being applied to a fixed, 1M $\Omega$  resistor. A newer coulometry program, with basic functionality (no CV control, for instance) is shown.

#### 4.6.2 Ag/AgCl Conversion Interface

In order to prevent damage to the wafers during the silver plating and chloridization processes, a software interface was developed to monitor the full current flowing in the electrical circuit during both processes. In the software, (UI shown in Figure 4.42), the instantaneous current was plotted in real time, and the max and min

currents were extracted from this stream of data and plotted on separate graphs, which allowed the user to quickly respond to sudden spikes in current during the process being observed. Currents that were much higher than those specified in the processing outline (avg. 20 mA) tended to create failure points in the electrodes under regular use, provided failure (sudden open circuit, for example) did not occur during one of the conversion steps.

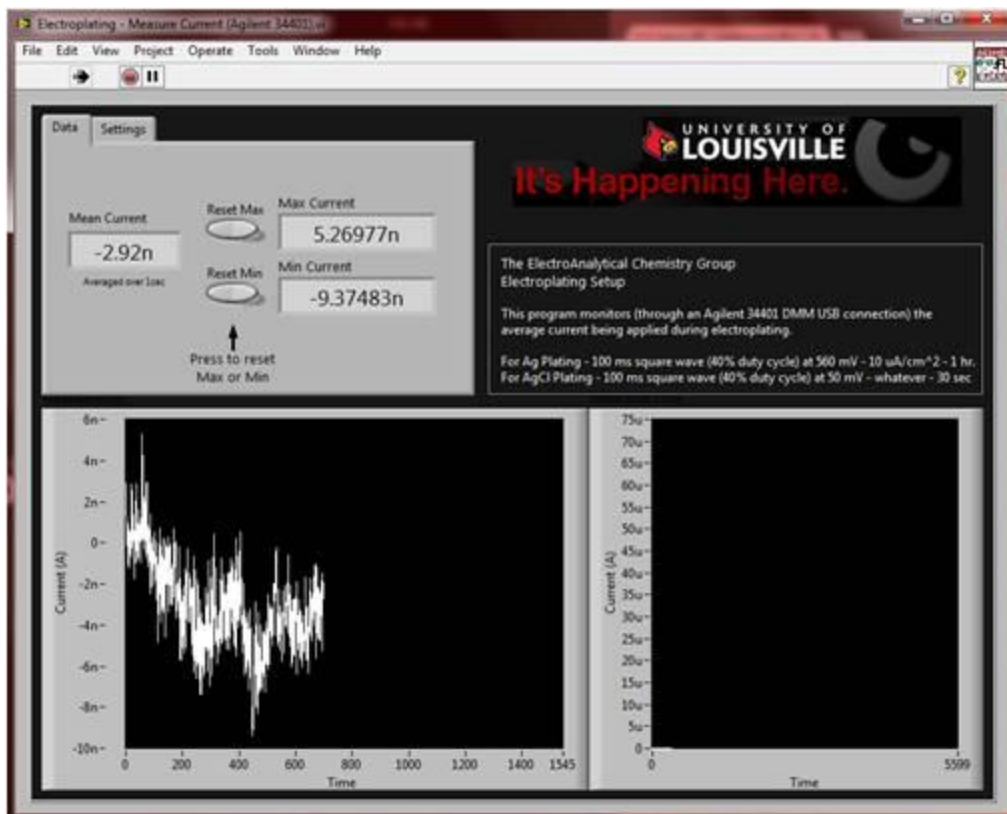


Figure 4.42 – Pseudo Reference Electrode Current Monitoring Program that allows the user to visualize the instantaneous, max, and min currents during the electrode conversion process. In this screen capture, the Y-axis has not yet been autoscaled.

### 4.6.3 Data Processing

One of the most difficult steps in the project was inspecting, analyzing, sorting and ultimately processing the multitudes of data generated during the coulometry experiments. Typically, each data set contained (for a 1 kHz sample rate) two columns of data, each with upwards of 300,000 rows (for experiments that gathered data up to 300 seconds in length). Three sets of data for each step in the range of analytes used, as well as three sets (or more) of coulometry performed on blank solution. Therefore, each data set typically generated millions of data points. Other programs such as Matlab were ideally suited for large data sets, however, since the control programs were written in LabVIEW, and this software has an exhaustive library of subroutines to handle, process, sort, and display data, custom code for processing the data was written. While at least a dozen programs were written specifically for manipulating data, only two will be mentioned here.

The original data processing program developed processed the coulometric data by subtracting the averaged background and integrating the signal to obtain the total charge for each experiment. In this early software, the processing was a mostly manual process, and the user actively manipulated the cursors to choose where the beginning and end features of a coulometry data set. Figure 4.43 shows the user interface of the original “Area Under the Curve” program, which was compiled into an executable file and distributed to multiple computers for post processing data.

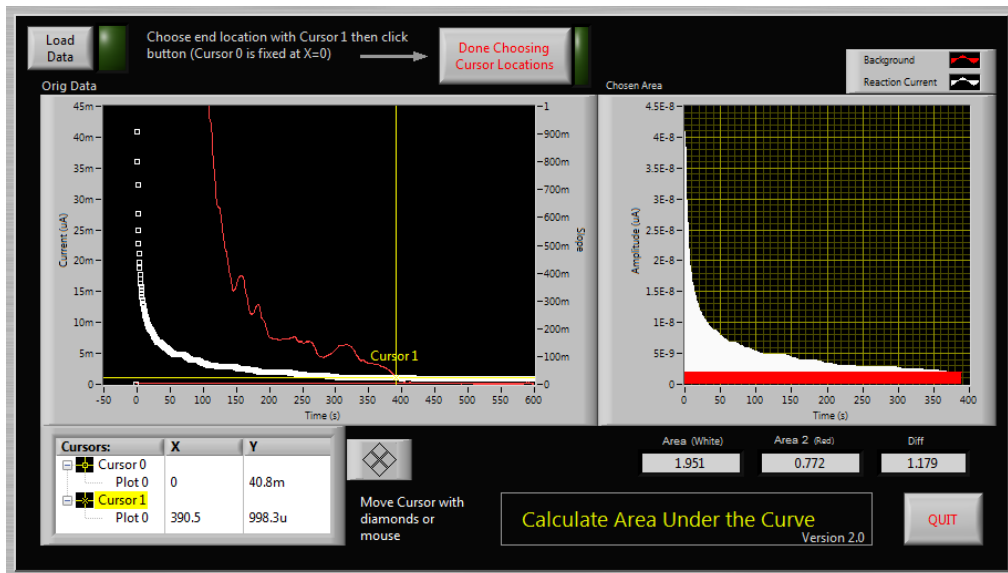


Figure 4.43 – First major coulometric data processing program. The instantaneous derivative was plotted along with the raw data in an attempt to visualize where the slope of the curve was sufficiently close to zero and the area could then be calculated.

Once it was determined that the coulometric cell appeared to be performing satisfactorily, the processing software was further developed in order to provide the ability to process more than a single concentration of analyte at a time. Additionally, for a majority of the experiments, multiple runs at each concentration were conducted to obtain an average signal and to perform statistical analysis for evaluating run-to-run variability. For a single experiment, a set of data typically consisted of three runs to attain both background data and a set of data at each concentration. Figure 4.44 is a screen capture of the user interface for the software used to process these multi-run experiments. The user first entered the particular concentrations used in the experiment as well as the expected charge at each concentration into the software. The software then prompted the user to identify three sets of data representing the background coulometry measurement, and automatically found the first three runs for each of the concentrations entered.





After loading, averaging and background correction of the full set of experimental data, the software calculated and plotted a calibration curve (including correlation) for each concentration until the reaction progressed towards 100% conversion of analyte over time. The particular set of sample data contained in Figure 4.44 shows the results of four concentrations, which were background corrected and shown to display a correlation coefficient of 0.965 over the concentrations used in the experiment.

#### 4.7 Electrochemical Analysis

Coulometric analysis with the prototype thin-layer flow cell involved loading the cell with a known concentration of analyte, followed by the application of an appropriate potential to initiate conversion of the model analyte to the alternate oxidized or reduced form. In all experiments, *ferrocyanide* was oxidized to *ferricyanide* by stepping from -100 mV to 400 mV, and *ferricyanide* was reduced to *ferrocyanide* by stepping from 400 mV to -100 mV. The appropriate oxidation and reduction potentials were determined experimentally in previous studies by examining the results of cyclic voltammogram in a bulk coulometric cell. Figure 4.45 shows the results of such a study where the redox potentials were determined (commercial BASi potentiostat used for this measurement). This type of analysis was also used to observe the effects of using a pseudo-reference

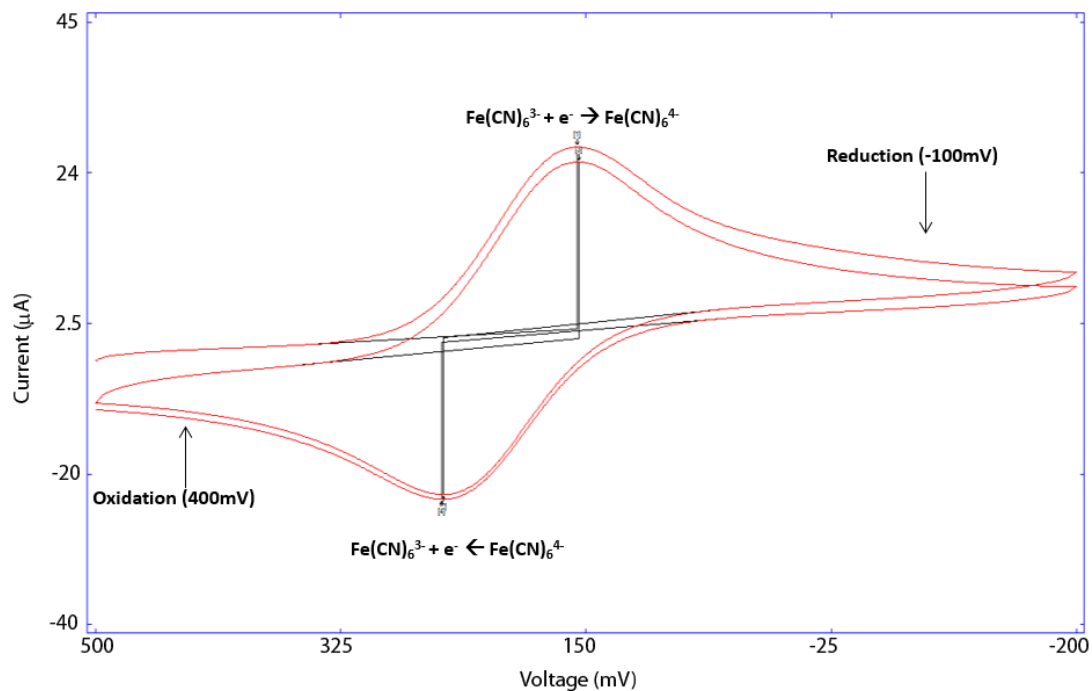


Figure 4.45 – Cyclic voltammetry experiment to determine the appropriate potentials for carrying out oxidation and reduction.

electrode (as well as electrode spacing considerations), which can shift the peaks by several millivolts (ex, 50 mV for an Ag|AgCl pseudo-reference electrode). If this type of shift occurred and went unnoticed, the redox process still ensued, but took longer to complete in the thin-layer cell, which was actually an attractive feature of the technique.

#### 4.7.1 Chronocoulometry Experimental Results

Due to the presence of the membrane, the analyte was sequestered in the working electrode chamber while the electrical connection between the working and counter electrodes for the passage of electrons during the electrochemical process was maintained. Chronocoulometry experiments were performed to show reversibility of the redox process inside the thin-layer cell [108]. Figure 4.46 is a sample set of data for such

an experiment where 250  $\mu\text{M}$  ferrocyanide was first oxidized to ferricyanide then reduced back to the ferro- form. This oxidation-reduction process was repeated four more times over a period of 425 seconds. In each step, the applied potential was stepped between -0.100 mV and 400 mV and held until the reaction appeared to proceed to completion (near zero current). The plot of the data showed a current spike that immediately followed the step potential, with a gradual decay of the current as the analyte was either oxidized or reduced completely inside the cell. Switching back to the opposite, original potential caused an oppositely charged current spike and decay. Each process appeared to take approximately 30 seconds to complete.

Examining the calculated charge for each successive experiment showed a general trend supporting the expected full conversion and recovery between the reduction and oxidation steps (Table 4.6). However, it was apparent that the reduction step produced a

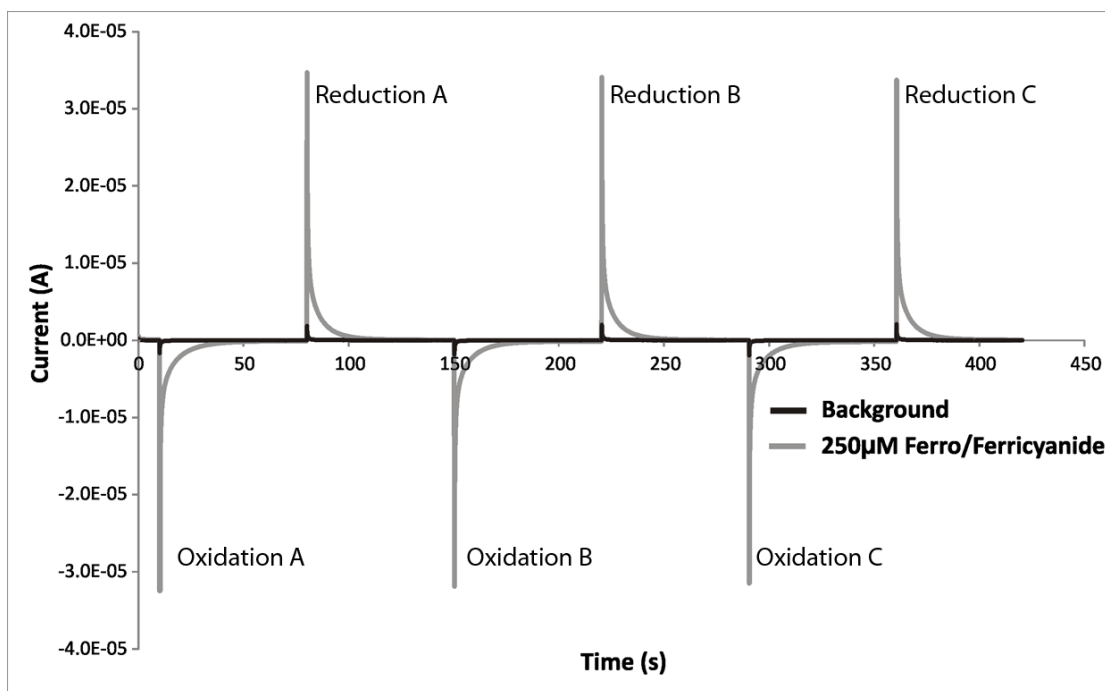


Figure 4.46 – Repeated reduction/oxidation experiment carried out the test the membrane and reversibility of the reaction [108].

charge less than the previous oxidation, and correspondingly, each oxidation step produced a calculated charge that was greater than the previous reduction. Further examination of single oxidations proved crucial in determining the cause of this phenomenon.

Table 4.6

Chronocoulometry Results Showing the Charge from Successive Redox Reactions

Step	Calculated Charge ( $\mu\text{C}$ )	Percent of Previous
Oxidation A	67.37	N/A
Reduction A	60.3	89.5%
Oxidation B	64.6	107.1%
Reduction B	58.46	90.5%
Oxidation C	65.6	112.2%
Reduction C	57.5	87.6%

#### 4.7.2 Coulometric Experimental Results

The expected volume of the cell for an 80  $\mu\text{m}$  final gasket thickness was 2  $\mu\text{L}$ . Successive coulometric experiments were performed on increasing concentrations of analyte to examine the details of the curves and determine the total time required to exhaustively convert each sample. A coulometry experiment was performed before the analyte concentrations were analyzed to determine the magnitude of charge in the measured signal due to the charging current and background processes. This data was subtracted from the analyte data, and therefore, said to be “background corrected.”

Multiple concentrations of analyte were prepared and injected in order of increasing concentration, with a clean step (with blank solution, 0.1 M  $\text{KNO}_3$ ) between each run. Figure 4.47 shows the results from this type of experiment with concentrations

from 50  $\mu\text{M}$  to 250  $\mu\text{M}$ . The current response tracked with concentration for each successive experiment, and the pre-and post-blank measurements appeared to be superimposed, which was a good indication that the analyte was indeed completely flushed out of the cell at the end of the experiments. Had the post-run blank measurement shown a larger current, there would have been some concern as to what caused the increase, perhaps analyte adsorbed onto the membrane, etc. The concentrations were increased specifically to ensure that any lingering analyte in the subsequent concentration would be at a lower concentration and have less of an impact on the measurement.

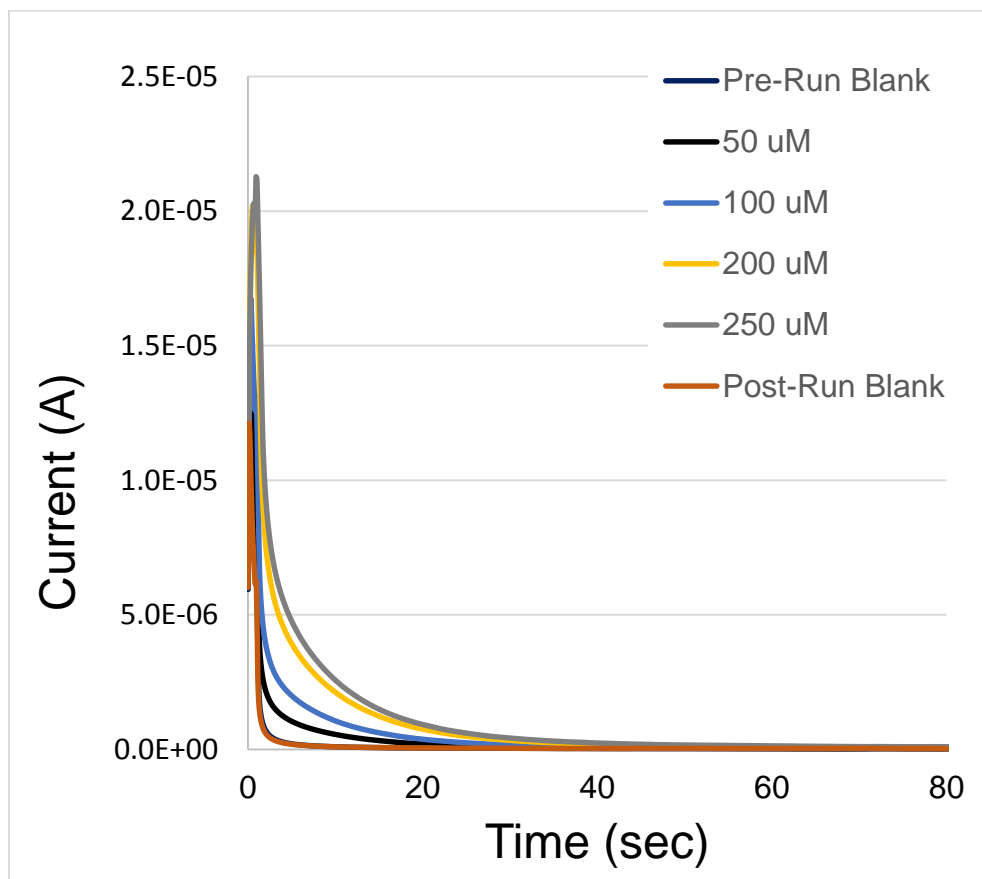


Figure 4.47 – Amperogram displaying 80 seconds of current measured during the oxidation of ferrocyanide for increasing concentrations (50 – 250  $\mu\text{M}$ ). Peak heights increase for increasing concentration.

A closer inspection also showed that higher concentrations took longer to completely oxidize compared to the lower concentrations. This could be due to the increased current density at the counter electrode, which in this study was a coiled gold wire with an area much smaller than the working electrode. Further analysis revealed that although the current appeared to decay to background levels, the currents measured do not drop below the background current. Figure 4.48 provides a close up view of the current measurement between 80 and 85 seconds after applying the potential steps. It was clearly seen that each successive concentration appeared to be holding constant at levels above the background current, and interestingly, in the order of concentration. This

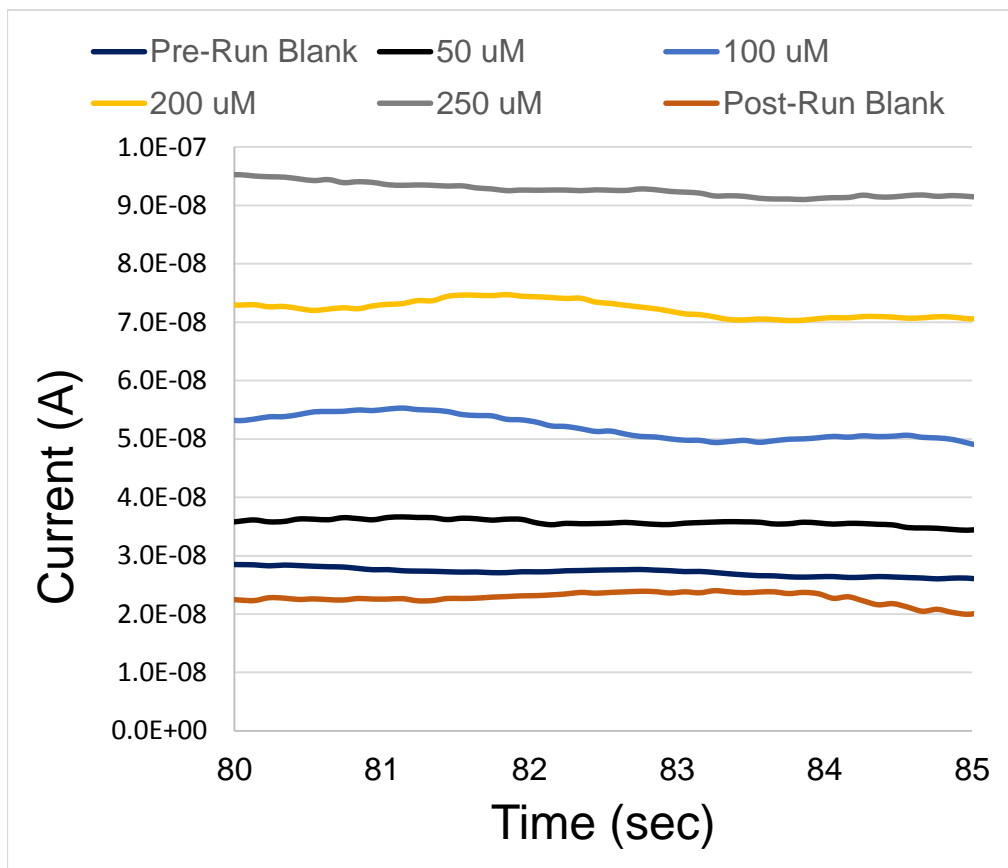


Figure 4.48 – Coulometric analysis long after electrolysis is done and the curves do not reach the background level. The offset is proportional to concentration.

persistence suggested that some process, either diffusion of analyte from the inlet/outlet port, or convection after sample loading, was delivering fresh, unreacted analyte into the thin-layer cell.

#### 4.7.3 Linear response of concentration range

To observe the linearity of the total charge measured with respect to concentration, a range of analyte concentrations from 50  $\mu\text{M}$  up to 10,000  $\mu\text{M}$  were formulated and analyzed. Figure 4.49 contains the results from one such study that showed perfect correlation with respect to concentration and calculated charge (Adapted from [108]). The error bars included in the plot show increasing variability at the higher concentrations; however, the results were still quite impressive, and the linearity observed was typical for all such studies. Table 4.7 contains the results for several

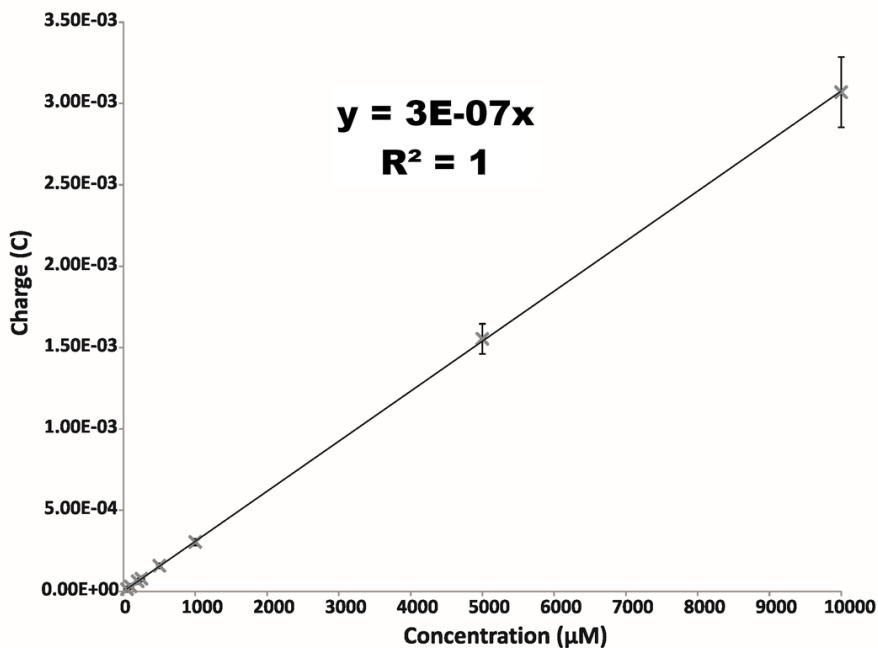


Figure 4.49 – Plot showing linear response of system over wide range of concentrations.

experiments performed over non-consecutive days for concentration range 50  $\mu\text{M}$  to 250  $\mu\text{M}$ ).

Table 4.7

Coulometric Analysis Results Showing Linearity over Several Days

Date	Regression Equation	R <sup>2</sup>
18-Nov	$y = 1\text{E-}07x - 7\text{E-}07$	0.9978
23-Nov	$y = 1\text{E-}07x - 1\text{E-}06$	0.9971
30-Nov	$y = 2\text{E-}07x - 2\text{E-}07$	0.9999
01-Dec	$y = 2\text{E-}07x - 3\text{E-}07$	0.9997
06-Dec	$y = 2\text{E-}07x - 5\text{E-}08$	0.9999

#### 4.7.4 Coulometric Determination over Time

The goal of exhaustive coulometry was to determine the total charge obtained in a fixed volume thin-layer cell. To analyze the coulometric determination of total charge over the estimated period of time for the designed cell geometry, the measured current was integrated and plotted over time. Figure 4.50 is the integrated total charge from the data in Figure 4.47 for four concentrations (50  $\mu\text{M}$  to 250  $\mu\text{M}$ ), and included the background current obtained with the blank solution (once again, 0.1M  $\text{KNO}_3$ ). While the total charge appeared to level off at the lower concentrations, the higher concentrations had an obvious constant slope beyond approximately 30 seconds, which confirmed the possibility that a constant supply of fresh, unreacted analyte was being delivered into the



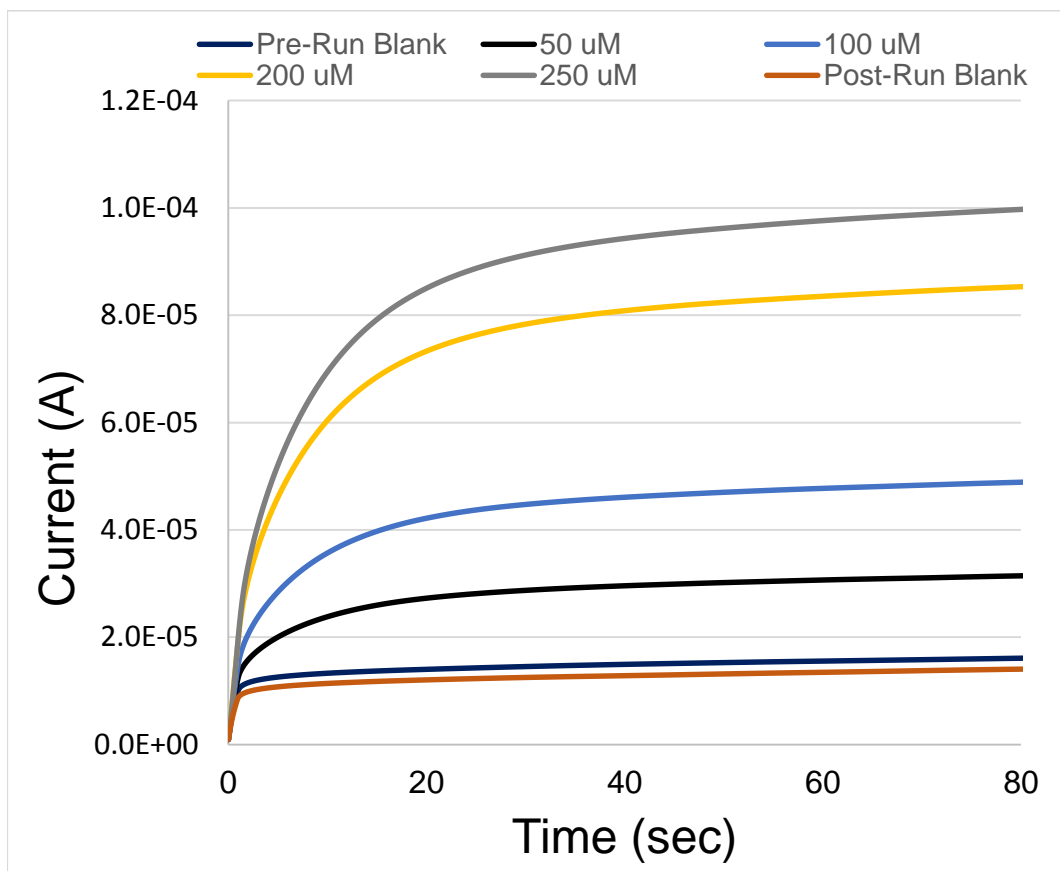


Figure 4.50 – Integrated coulometric signals for four concentrations. Each curve should ideally level off and have a zero slope indicating reaction has gone to completion.

thin-layer cell. This was further examined by calculating the total charge at each concentration and comparing them to the expected charge for the estimated volume of the thin-layer cell ( $\sim 2 \mu\text{L}$ ). Table 4.8 (adapted from [108]) listed the expected charge at each concentration, followed by the measured charge after 10, 30 and 60 seconds for both oxidation and reductions of the model analyte. The ‘n’ in this data set represented the number of different days for each concentration and the relative standard deviation for each time calculation was also included. It was observed that the expected charge for both the oxidation and reduction steps was reached shortly after 10 seconds; however, the charge continued to increase apparently unabated beyond that point.

Table 4.8

Calculate Charge over Time for Increasing Concentrations for both Oxidations and Reductions

<b><i>Reductions</i></b>	<b>Expected Charge (<math>\mu\text{C}</math>)</b>	<b>Charge after 10s</b>	<b>Charge after 30s</b>	<b>Charge after 60s</b>
<b>50<math>\mu\text{M}</math> (n=4)</b>	10.61	9.71 (+/- 0.47)	12.56 (+/- 0.72)	13.50 (+/- 1.19)
<b>100<math>\mu\text{M}</math> (n=4)</b>	21.23	20.33 (+/- 0.54)	26.50 (+/- 0.58)	28.28 (+/- 0.66)
<b>150<math>\mu\text{M}</math> (n=4)</b>	31.84	30.78 (+/- 0.99)	40.40 (+/- 1.54)	42.88 (+/- 1.23)
<b>250<math>\mu\text{M}</math> (n=4)</b>	53.07	51.30 (+/- 2.41)	67.37 (+/- 4.38)	71.30 (+/- 4.58)
<b><i>Oxidations</i></b>	<b>Expected Charge (<math>\mu\text{C}</math>)</b>	<b>Charge after 10s</b>	<b>Charge after 30s</b>	<b>Charge after 60s</b>
<b>50<math>\mu\text{M}</math> (n=5)</b>	10.61	9.95 (+/- 0.89)	13.45 (+/- 1.16)	14.68 (+/- 1.50)
<b>100<math>\mu\text{M}</math> (n=5)</b>	21.23	20.57 (+/- 1.10)	27.92 (+/- 1.61)	30.3 (+/- 2.09)
<b>150<math>\mu\text{M}</math> (n=3)</b>	31.84	31.25 (+/- 0.71)	42.31 (+/- 1.92)	46.47 (+/- 2.49)
<b>200<math>\mu\text{M}</math> (n=2)</b>	42.45	41.51 (+/- 1.79)	56.46 (+/- 1.68)	60.53 (+/- 1.82)
<b>250<math>\mu\text{M}</math> (n=5)</b>	53.07	51.97 (+/- 0.58)	69.88 (+/- 1.29)	75.32 (+/- 1.87)

#### 4.7.5 Flow Cell Comparison to Thin Layer Theory

Selected data for the background corrected oxidation of 100  $\mu\text{M}$  ferrocyanide was compared to thin-layer theory, particularly in relation to the Cottrell equation, which further refines thin-layer theory based on electrode area. The simulated data presented assumed a diffusion coefficient for ferrocyanide ( $D=0.667 \text{ cm}^2/\text{s}$ ) and an electrode area of  $0.28 \text{ cm}^2$ . Figure 4.51 shows the results of this comparison and indicated that for the first few seconds of the experiment, the curves were nearly identical, but diverged after perhaps five seconds (Adapted from [108]). It was assumed that this divergence was due to the lingering, near constant current that was measured long after the current should have decayed to background levels. Despite the divergence from theory, the data indicated that our cell falls somewhere in between a true thin-layer cell, and the results obtained by the free linear diffusion suggested by the Cottrell derivation.

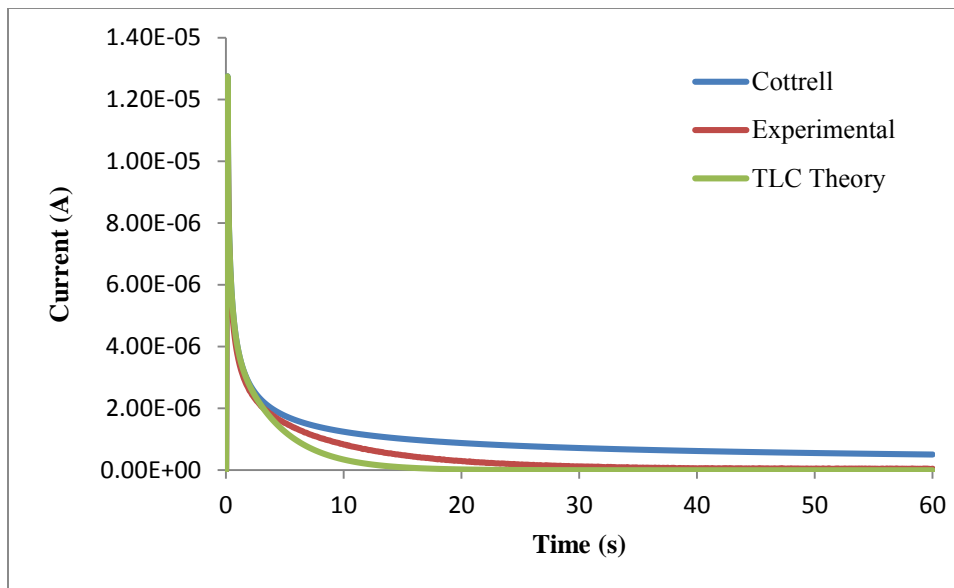


Figure 4.51 – Plots comparing the performance of the flow-cell to theoretical equations for idealized flow cells with equivalent geometries and electrode areas.

#### 4.7.6 Comparison of Commercial Detector and Custom Potentiostat Data

A direct comparison of the instrumentation performance was made to compare the custom potentiostat and a commercial electrochemical analyzer. Table 4.9 is a direct comparison of the two instruments for the background corrected oxidation of ferricyanide 50  $\mu\text{M}$ , 100  $\mu\text{M}$ , 150  $\mu\text{M}$ , and 250  $\mu\text{M}$ . The data showed good, but not perfect agreement between the systems. This data is also plotted in Figure 4.52 and both results showed near perfect linearity over the concentration range that was tested.

Table 4.9

Comparison of Total Charge Recorded after 30 Seconds - Commercial Detector and Custom Potentiostat

Concentration ( $\mu\text{M}$ )	Commercial $\mu\text{C}$	StDev	Custom Pstat $\mu\text{C}$	StDev	% Difference
50	14.1	-	15.1	-	7.09
100	28.6	0.94	32.1	1.7	12.24
150	44.4	1.9	48	1.2	8.11
250	77.8	5.9	77.6	1	0.26

Figure 4.53 is a representative example of a coulometric study for the background corrected oxidation of 250  $\mu\text{M}$  ferricyanide performed on different days, but with the same cell and sensor. Minor differences in assembly may have contributed to some of the subtle differences in the curves, but both appeared to decay to similar background levels after 15 to 20 seconds. What stood out was the drastic difference in the data obtained during the first second or two. The first data point obtained by the commercial detector was sharply positive, while the custom detector captured the charging current as it progresses from zero. This may have been simply be due to the methods used in the

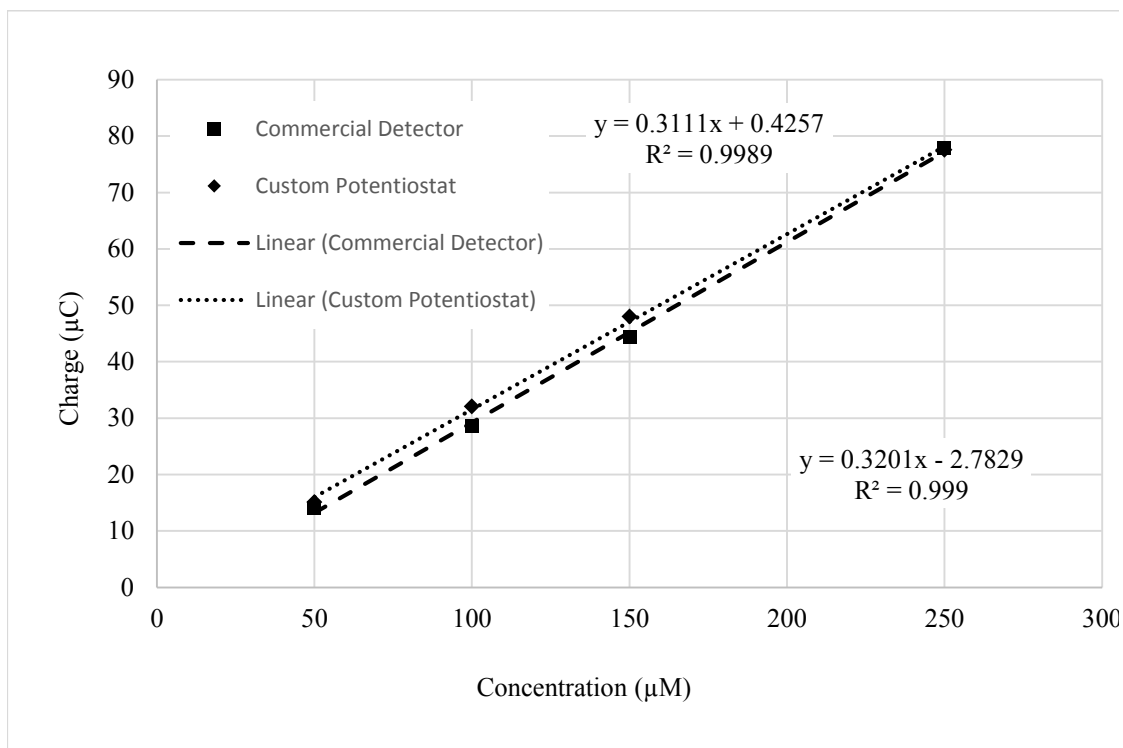


Figure 4.52 – Plots comparing the performance of the custom potentiostat and commercial electrochemical system.

software or hardware on the commercial detector to sync the step potential initiation with data acquisition. The data gathered by the custom potentiostat, which was triggered internally to start at the precise moment the voltage was stepped to the oxidation potential, seemed to contain more information on the charging current. There were other advanced settings in the potentiostat software, such as filter settings, and data acquisition rate that may have contributed to what seems like a premature truncation of some possibly useful information.

The first few seconds of data plotted in Figure 4.54 showed features on the peaks during the charge up current that were never captured by the commercial detector. It was not determined if these features, which in this data are present in the background as well as the varying concentrations of analyte, were artifacts of some anomalous process worth

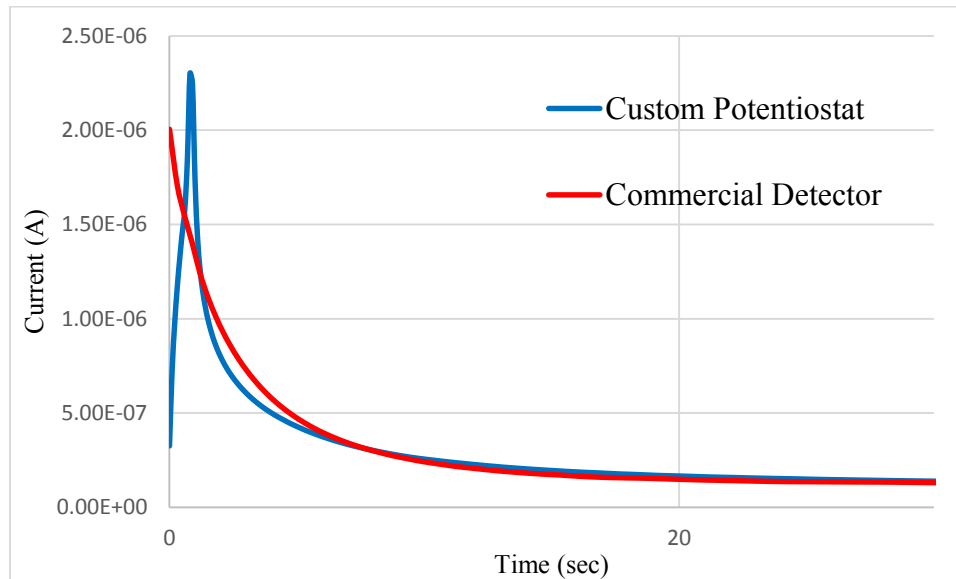


Figure 4.53 – Head to head coulometric data for the custom potentiostat (blue) and commercial detector (red).

investigating, such as subtle electrode-fluid interactions due to sensor geometry, or perhaps merely the indication of a bubble near the surface of the reference/working electrode transition. These features were only observed on occasion when inspecting sets of data gathered with the custom potentiostat and software. Regardless, the performance of the custom potentiostat seems to be at least as good as the commercial detector.

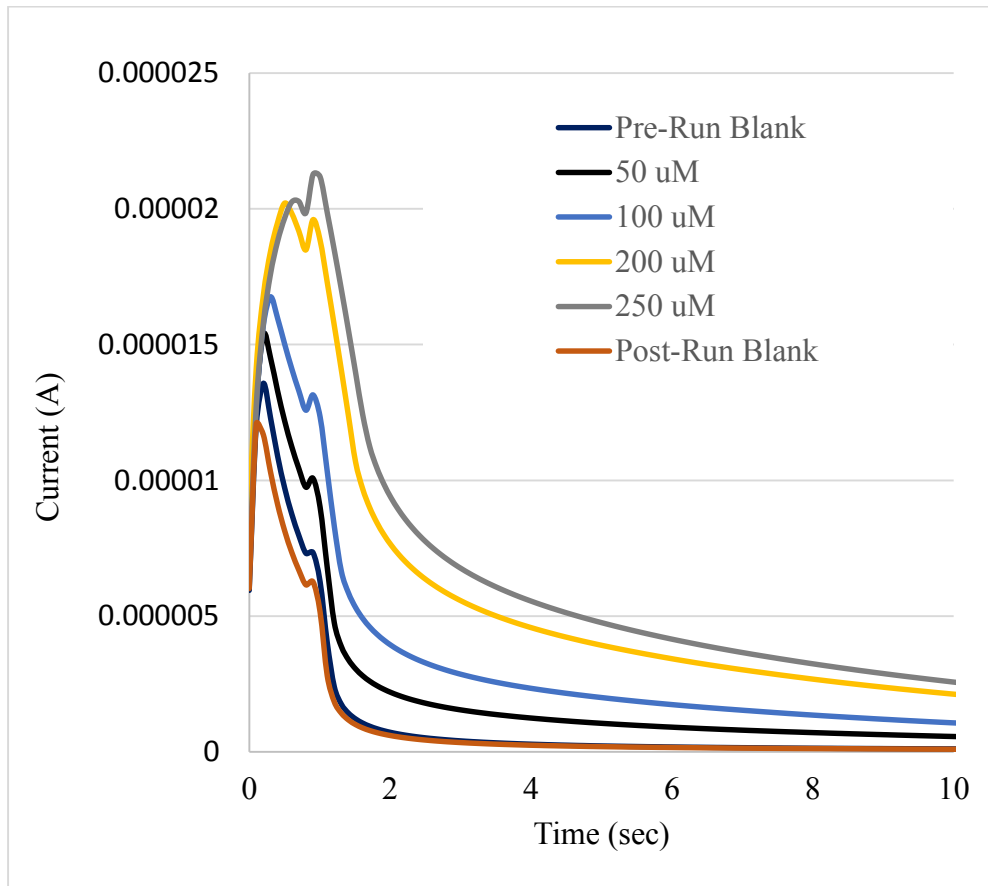


Figure 4.54 – The first ten seconds of a coulometric analysis for increasing concentrations (50 – 250  $\mu\text{M}$ ). The odd-shaped peaks are part of an electrochemical process that does not show up with the dummy cell. Peak heights increase for increasing concentration.

#### 4.8 Thin Layer Cell Redesign

In order to explore the possibility of convective flow contributing to the constant, greater than background currents seen in the data obtained with the first generation cell, a second generation flow-cell was created (Figure 4.55). Using similar layers and manifold inlets and outlets for the counter and thin-layer flow volumes, this updated design was created around a second-generation sensor (Figure 4.56) designed with the same sensor

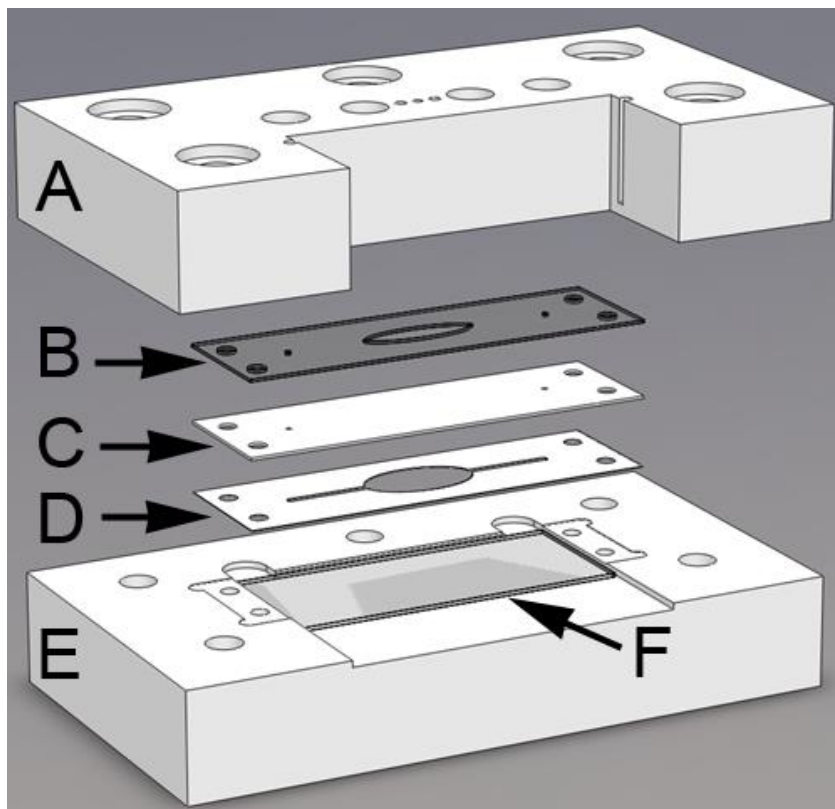


Figure 4.55 – Second generation flow cell solid model indicating the many layers including the top half of the cell (A), the upper gasket (B), the semi-permeable membrane (C), the bottom of the cell assembly (D), the chip gasket (E), and the sensor (F); for clarity, the counter electrode is not shown, and the sample outlet port is obscured from view.

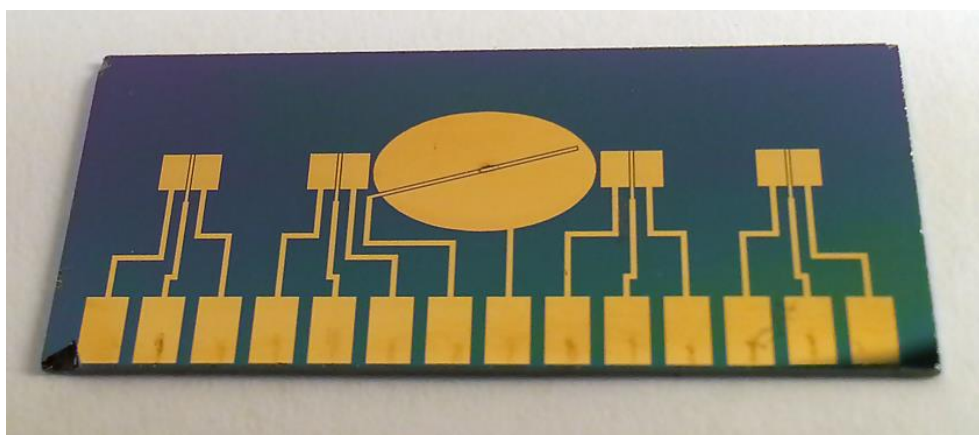


Figure 4.56 – Second generation electrochemical sensor. The central working electrode area is equal to the first generation sensor ( $\sim 25 \text{ mm}^2$ ), but is rotated  $90^\circ$ .



area as the original sensor (8mm x 4mm), but the chip was rotated in the fixture by ninety degrees. Additionally, the thin-layer volume was still defined by the thickness of the chip gasket. For brevity, and since the layers of the two generations are similar, the projected views for this final flow cell can be found in Appendix D. The specific features that are different in the second generation platform compared to the first were modifications to: 1) the placement and number of alignment pins; and, 2) the suspension of the chip gasket over the edges of the trench. Both of these changes aided in aligning the chip gasket on the sensor. This second generation flow cell reverted back to having all the inlet/outlet ports on the top of the manifold, so the leakage problems and electrical connection issues were both alleviated by design. Finally, the chip gasket thickness was doubled to eliminate the problems encountered with the first generation cell (sticking on the sensor, etc.).

The flow cell was sent out for fabrication and when received, threads were cut into the device and it was assembled in a similar manner to the first design. Figure 4.57 shows the fabricated second generation cell and some of the internal features are apparent when looking from the side, particularly the inlet and outlet ports. Figure 4.58 shows all of the components collected to assemble the flow cell.

#### 4.8.1 Particle Image Velocimetry

Of the two theorized possible sources of the extra current lingering in the cell after the coulometry process should be completed, convective flow was theorized to be the one that could possibly deliver a sizeable volume of analyte into the thin-layer cell over the time span of an experiment. Diffusion on the other hand, a process that, while no less an issue, would not be able to deliver as large a quantity of

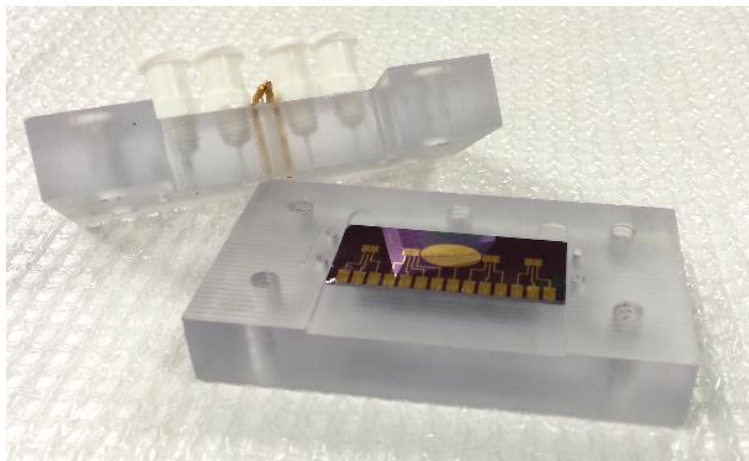


Figure 4.57 – Second flow cell prior to assembly. A version of the second generation sensor is also shown. The shadows cast inside the upper half of the cell hint at the geometry of the sample and counter chamber inlet/outlet flow paths. The gold counter electrode can be seen as well.



Figure 4.58 – View of all parts needed for assembly of the second generation flow cell.

analyte in only a few dozen seconds of experimental time. In order to visualize the flow, particle image velocimetry was used to visualize the flow inside the cell during the delivery of sample. In order to carry this out, the bottom of the thin layer cell was polished to make it transparent to visible light, and a glass spacer with similar thickness was inserted in place of the silicon sensor (Figure 4.59). A solution containing two micron fluorescent particles (Fluoro-Max R02000, polystyrene based) was added to 50 mL of DI water to create a sample solution for injection into the flow cell. The system was placed on an inverted microscope (Nikon Eclipse Ti-U, Nikon Instruments, Inc., Melville, NY) and images were taken at approximately 9 frames a second (Pico Sencicam

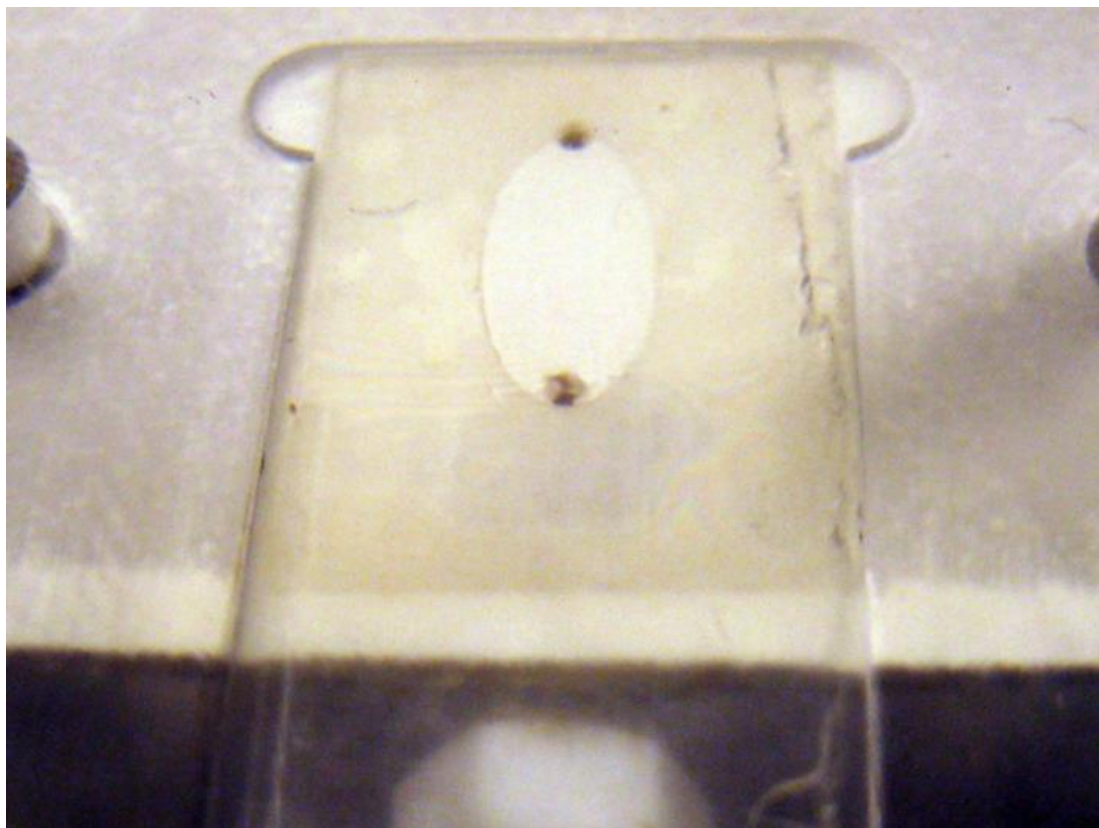


Figure 4.59 – Image of the glass spacer installed in the flow cell (viewed from the bottom) that was polished to be as transparent as possible. This setup was used to visualize the motion of suspended particles flowing through the thin-layer cell.

QE camera, PCO AG, Kelheim, Germany) during sample loading and after stopping the injection process. The flow cell was fitted with rigid tubing and flow valves were added to stop the flow after injection. Images were compiled and showed a drastic difference between images gathered with the valves open after injection, and with them closed.

Figure 4.60 shows an integrated snapshot of both configurations, where A was the cell with valves open after injection, and B was the cell with valves closed (adapted from

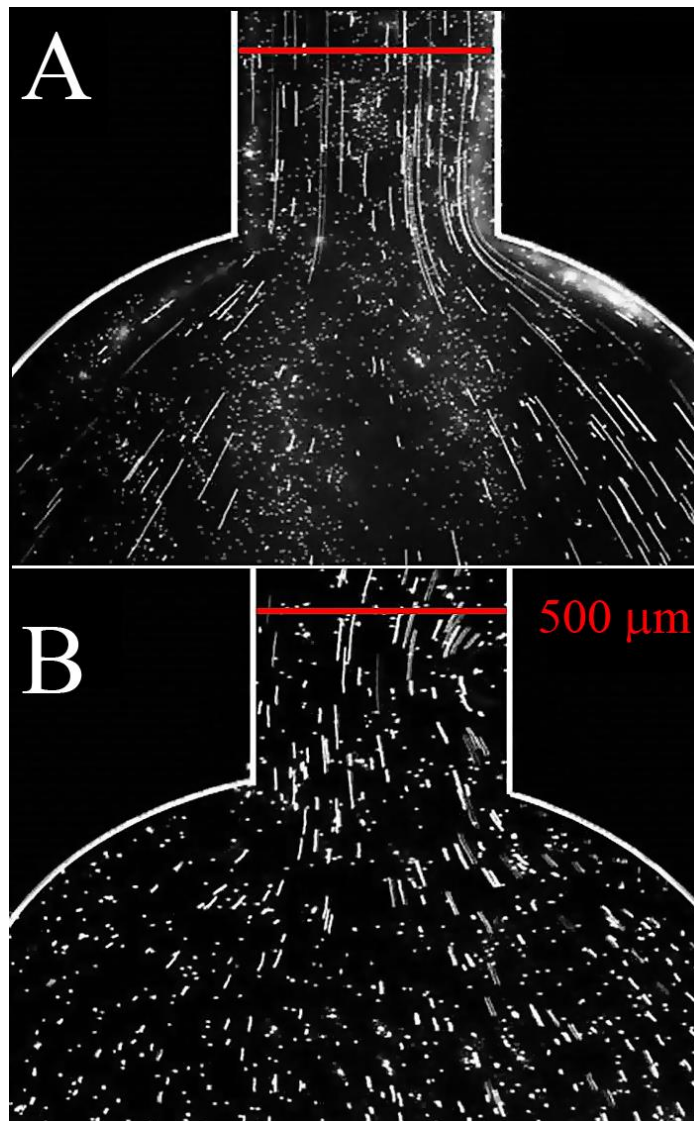


Figure 4.60 – Flow visualization of particles still moving after injection of sample. Open valves (A) estimated average flow rate 4 mm/min, and closed valves (B), estimated average flow rate 0.9 mm/min.

[109]). Careful tracking of the particles over multiple frames in the inlet cross section revealed an estimated flow of approximately 3.9 mm/min flow when the valves remained open, and 0.9 mm/min flow when the valves were closed. The addition of valves did not completely eliminate the flow, but did reduce it by a factor of four. Knowing the cross sectional area of the inlet, the volumetric flow rate was estimated to be 0.5  $\mu\text{L}/\text{sec}$ , and for a volume of approximately 2  $\mu\text{L}$  in the thin-layer portion of the flow cell, this suggests that every 30 seconds, 10 percent of the cell volume could be replaced with new analyte. This could easily replace enough fluid to produce the current magnitudes observed in the coulometry data.

#### 4.8.2 Electrochemical Analysis

Confident that stopping the flow would at least mitigate what was evidently a convective flow issue in the original cell, a coulometry experiment was performed where all of the flexible Tygon tubing was replaced with rigid equivalent connectors and stop flow valves on every inlet. Figure 4.61 is an image of this configuration. Coulometric data was gathered with this cell and showed an immediate improvement over the previous generation results. Figure 4.62 shows a set of data from the first flow cell adapted to show percent oxidized over time for the  $\sim 2 \mu\text{L}$  cell volume. The dashed line in the plot indicates the estimated total charge (100% conversion) and is where the curve should reach zero slope. The data obtained with the original coulometry cell reaches 100% conversion after approximately 12 seconds and shows signs of increasing

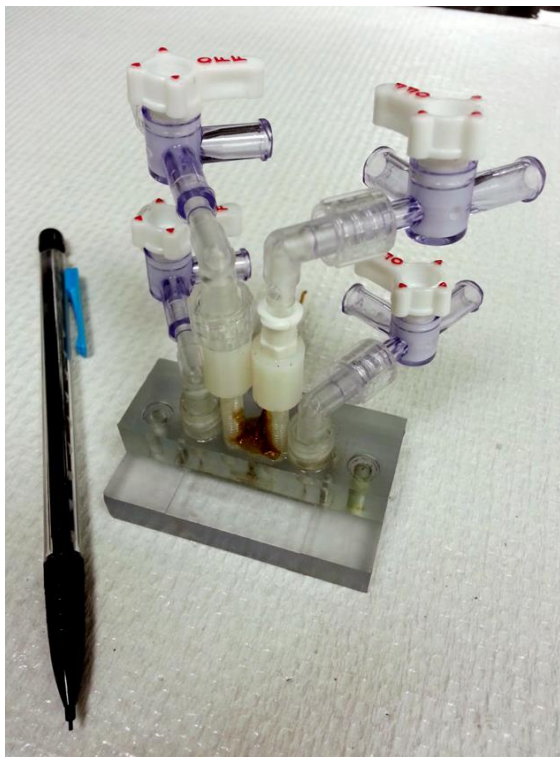


Figure 4.61 –Valves added to inlet and outlet of all channels in an attempt to completely stop the flow.

at a constant rate beyond this point as in previous experiments.

Data obtained with the new cell showed much improved coulometric determination, however the residual flow is obviously still present. Figure 4.63 shows data collected in the new cell design with all rigid tubing and all fluidic ports closed after loading the cell with sample. The coulometric analysis reaches 100 % conversion in approximately 70 seconds (the volume of the thin-layer cell was estimated to be 3.73  $\mu\text{L}$  in the redesigned cell), and the constant slope after 100% is reached is present in the data indicating that the flow of analyte is still taking place. However, over after two hundred seconds, the total charge has increased only to 106 %, when in the original cell, the charge had reached nearly 140 % in only 60 seconds. While there are obviously still some

changes that need to be made to completely stop the flow, adding valves and rigid tubing was a simple change that improved the results dramatically.

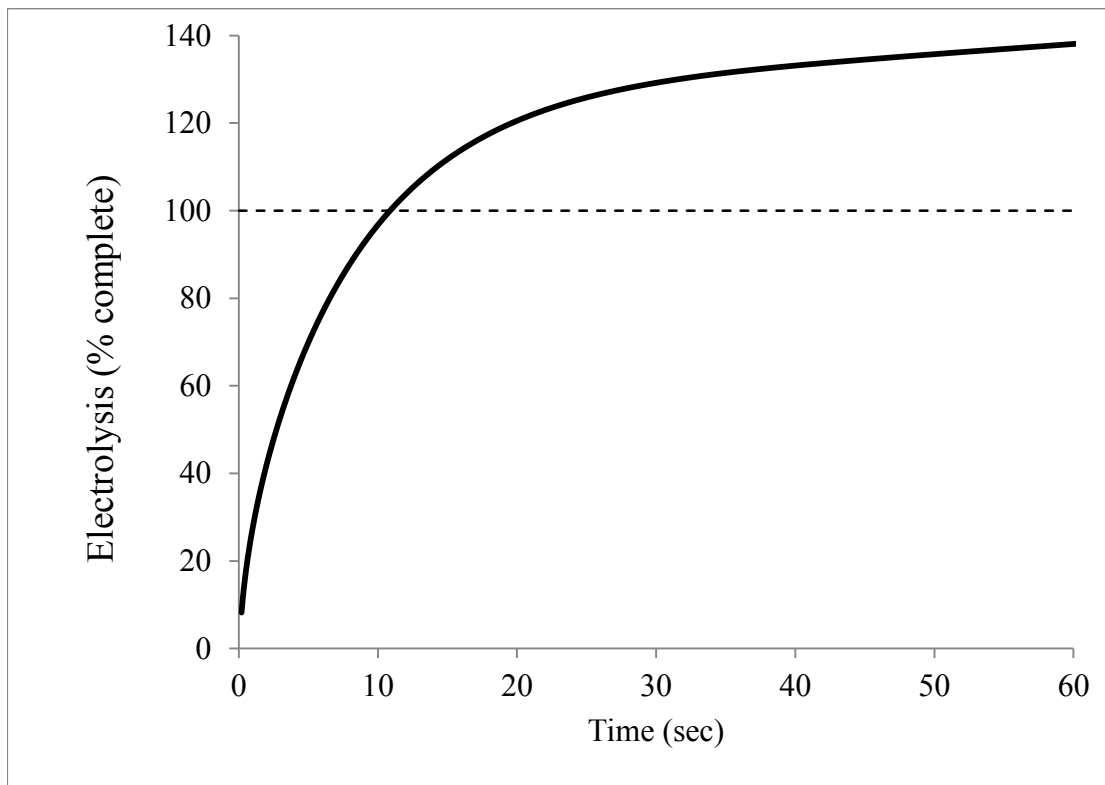


Figure 4.62 –Plot with valves open for oxidation of 500  $\mu\text{M}$  ferrocyanide showing percent converted over time. The dashed line is placed at 100 % of the theoretical charge for the thin-layer coulometry cell in used in this study.

#### 4.9 Future Work

Though the results presented in this chapter are promising, there is more work to be done, particularly on the fluid mechanics of the flow cell. It is assumed that the pressure drop inside the flow-cell (examined in the simulations) continues to drive flow through the thin layer from the inlet even after force on the syringe is removed. Perhaps

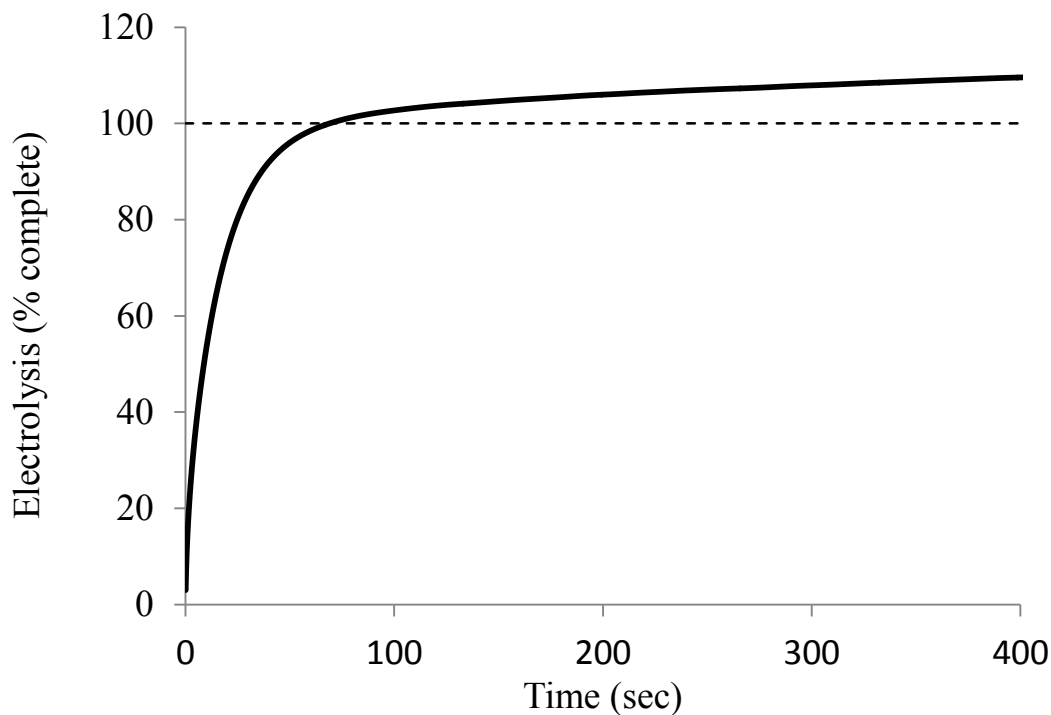


Figure 4.63 –Plot with valves closed for oxidation of 500  $\mu\text{M}$  ferrocyanide showing percent converted over time. The dashed line is placed at 100 % of the theoretical charge for the thin-layer coulometry cell in used in this study.

the flexible tubing stores enough of this pressure to deliver flow magnitudes as large as the ones measured in the visualization study. This phenomenon could be modeled using CFD by performing a transient simulation with appropriate boundary conditions applied. The residual flow problem will have to be eliminated if the system development is to move towards a more automated, remotely, and perhaps autonomously operated device. The requirement of a membrane is probably the most limiting factor in the design of the flow cell itself. It would be advantageous to microfabricate all of the fluidics and sensor, electrical connection, etc. into a single device, but somehow a membrane will have to be incorporated into the design. There are other types of semi-permeable materials, such as rigid glass frits, as well as polymeric membranes that should be explored.



Recent studies with the prototype have shown it is effective for determining the concentration of practical analytes such as heavy metals. For example, alternate electrochemical techniques such as anodic stripping coulometry (ASC) are being used with this flow cell to detect ppb levels of copper. Regarding the instrumentation, a move away from the requirement of computer-based data acquisition seems imminent and timely, considering the capabilities of modern microprocessors. A miniaturized, low-power version of the potentiostat could be deployed and the system could be powered from batteries that are charged using solar technology. Passive delivery of sample into the cell could be handled using gravity fed techniques or perhaps capillary action. All of these design modifications would promote the possibility of a system that could run autonomously for an extended period of time with little need for operator or technician intervention.

## CHAPTER V

### CONCLUSIONS

The primary goal of this project was to develop and create a prototype electrochemical cell to exploit the implications of Faraday's first law of electrolysis, which explains the relationship between the quantity of electrons generated (or consumed) in a redox reaction and the concentration of analyte in a sample. The study sought to deliver specific components of a system including

- A miniature flow cell with a known analyte volume and critical cell height dimension less than 100  $\mu\text{m}$ ;
- A custom-designed potentiostat circuit with electronics uniquely chosen for fast response, high-precision and low-noise;
- Supporting software to set the correct potentials, control the timing, and measure the experimental data;

Collectively, these individual components provided an experimental platform to explore *exhaustive coulometry*, a technique that in theory should allow the determination of analyte concentration based solely on total charge measured. This method of sample analysis is potentially calibration-free since the current should ideally decay to zero and, knowing the volume of the cell and analyte in question, the concentration can be determined directly from the total charge obtained without having to refer back to some form of calibration curve. Other external factors such as temperature variations and electrode degradation due to fouling will only alter the kinetics of the reaction, not the

total charge. The reaction may take longer to complete, but the total charge will be unaffected by these changes.

The results presented in Section 4 described the performance of the prototype and showed favorable outcomes. The simulation data showed a manageable increase in pressure inside the cell, which suggested there would be no problems manually loading the sample into the system and that laminar flow would ensure all analyte would be cleared between experiments. The flow cell, after correct assembly techniques were developed, was used to perform hundreds of experiments and was reliable over many months of use. Evaluation of the electronics indicated that the performance of the circuit was in line with specifications, functioned as designed, and was small enough to be packaged for use in the field. The software developed proved to be an integral part of the system, including both the experimental control interface as well as post experiment data processing methods. The experimental data revealed that the total measured charge approached the theoretically determined values within the expected time window set by the flow cell height and nearly perfect linearity was seen when comparing charge obtained with increasing concentration. While the original flow-cell design displayed a subtle analyte flow after injection, presumably due to residual internal pressure, the simple addition of rigid tubing and valves reducing the flow to a fraction of the original value.

Continued development of the platform explored in this study will confirm an accurate and essentially calibration-free method of electrochemical detection for samples containing electroactive components. Ultimately, this will provide a platform to develop remotely deployable systems intended for fully automated operation.

## REFERENCES

1. Gabe, D.R., *Bibliography of Potentiostat Design*. British Corrosion Journal, 1972. **7**(5): p. 236-238.
2. Weber, S.G. and J.T. Long, *Detection Limits and Selectivity in Electrochemical Detectors*. Analytical Chemistry, 1988. **60**(15): p. 903A-913A.
3. Elliott, S., et al., *ICP-MS: When sensitivity does matter*. Spectroscopy, 2007: p. 36-+.
4. Welz, B., *Atomic absorption spectrometry*. 3rd, completely rev. ed. 1999, Weinheim ; New York: Wiley-VCH. xxii, 941 p.
5. Adamek, M., et al. *The electrochemical sensor with integrated chip of potentiostat*. in *Electronics Technology, 2008. ISSE '08. 31st International Spring Seminar on*. 2008.
6. Bard, A.J. and L.R. Faulkner, *Electrochemical methods : fundamentals and applications*. 2nd ed. 2001, New York: Wiley. xxi, 833 p.
7. Tsujimura, S., et al., *Micro-coulometric study of bioelectrochemical reaction coupled with TCA cycle*. Biosensors & Bioelectronics, 2012. **34**(1): p. 244-248.
8. Kilby, J.S., *Invention of Integrated-Circuit*. Ieee Transactions on Electron Devices, 1976. **23**(7): p. 648-654.
9. Toton, E., et al. *Comparing the power and performance of Intel's SCC to state-of-the-art CPUs and GPUs*. in *Performance Analysis of Systems and Software (ISPASS), 2012 IEEE International Symposium on*. 2012.
10. Moore, G.E., *Cramming more components onto integrated circuits*. Electronics, 1965. **38**(8): p. 114.
11. Badawy, W.J., G., *System-on-chip for real-time applications*. 2003: Kluwer.
12. Feynman, R.P., *There's Plenty of Room at the Bottom*. Amer. Phys. Soc. Meeting, 1960.
13. Nathanson, H.C., et al., *The resonant gate transistor*. Electron Devices, IEEE Transactions on, 1967. **14**(3): p. 117-133.
14. *Kulite.com*. 10/1/2012]; Available from: <http://www.kulite.com/>.
15. Teshigahara, A., et al., *Performance of a 7-Mm Microfabricated Car*. Journal of Microelectromechanical Systems, 1995. **4**(2): p. 76-80.
16. Dae-Eun, P., et al. *Design and fabrication of micromachined internal combustion engine as a power source for microsystems*. in *Micro Electro Mechanical Systems, 2002. The Fifteenth IEEE International Conference on*. 2002.
17. Comtois, J.H. and V.M. Bright, *Applications for surface-micromachined polysilicon thermal actuators and arrays*. Sensors and Actuators a-Physical, 1997. **58**(1): p. 19-25.
18. Madou, M.J., *Fundamentals of microfabrication and nanotechnology*. 3rd ed. 2012, Boca Raton, FL: CRC Press.

19. *Microfluidics: History, Theory and Applications*. 1 ed. 2006: Springer.
20. Hitzbleck, M., et al., *Capillary soft valves for microfluidics*. *Lab on a Chip*, 2012. **12**(11): p. 1972-1978.
21. Technical Insights Inc., *Lab-on-a-chip : a revolution in instrumentation*. Emerging technologies. 1996, Fort Lee, NJ: Technical Insights. 114 leaves.
22. Manz, A. and J.C.T. Eijkel, *Miniaturization and chip technology. What can we expect?* *Pure and Applied Chemistry*, 2001. **73**(10): p. 1555-1561.
23. John Wiley & Sons. Technical Insights., *Lab-on-a-chip : the revolution in portable instrumentation*. 3rd ed. 2000, New York: J. Wiley. xxvi, 259 p.
24. Royal Society of Chemistry (Great Britain), *Lab on a chip*. 2001, Royal Society of Chemistry: Cambridge, UK. p. v.
25. Smith, L.A., et al., *Lab-on-a-chip : platforms, devices, and applications : 26-28 October, 2004, Philadelphia, Pennsylvania, USA*. SPIE proceedings series,. 2004, Bellingham, Wash.: SPIE. ix, 240 p.
26. Herold, K.E. and A. Rasooly, *Lab on a chip technology*. 2009, Norfolk, UK: Caister Academic Press. <v. 1>.
27. Gardeniers, J.G.E. and A. van den Berg, *Lab-on-a-chip systems for biomedical and environmental monitoring*. *Analytical and Bioanalytical Chemistry*, 2004. **378**(7): p. 1700-1703.
28. Chin, C.D., V. Linder, and S.K. Sia, *Lab-on-a-chip devices for global health: Past studies and future opportunities*. *Lab on a Chip*, 2007. **7**(1): p. 41-57.
29. Kricka, L.J., *Microchips, microarrays, biochips and nanochips: personal laboratories for the 21st century*. *Clinica Chimica Acta*, 2001. **307**(1-2): p. 219-223.
30. Chin, C.D., V. Linder, and S.K. Sia, *Commercialization of microfluidic point-of-care diagnostic devices*. *Lab on a Chip*, 2012. **12**(12): p. 2118-2134.
31. Baldwin, D.R., *Conversation about advancements in Analytical Chemistry in the past 10-20 years*. 2012.
32. Gaensslen, R.E., *Sourcebook in forensic serology, immunology, and biochemistry*. 1983: University of Michigan Library.
33. Bunge, M., *Philosophy of Science: From Explanation to Justification*. 1998: Transaction Publishers.
34. Harris, D.C., *Quantitative Chemical Analysis*. 6 ed. 2003.
35. Skoog, D.A., D.M. West, and F.J. Holler, *Fundamentals of analytical chemistry*. 7th ed. Saunders golden sunburst series. 1996, Fort Worth: Saunders College Pub.
36. Inficon Petrochemical, I. *3000 Micro GC Gas Analyzer*. 2012 October 1, 2012]; Available from: <http://www.inficonpetrochemical.com/en/3000microgcgasanalyzer/index.html>.
37. Petrucci, R.H., *General chemistry ; principles and modern applications*. 1972, New York,: Macmillan. xxviii, 637 p.
38. Kinsey, J.L., *Laser-Induced Fluorescence*. *Annual Review of Physical Chemistry*, 1977. **28**(1): p. 349-372.
39. Chen, Z., et al., *Potent Method for the Simultaneous Determination of Glutathione and Hydrogen Peroxide in Mitochondrial Compartments of Apoptotic Cells with Microchip Electrophoresis-Laser Induced Fluorescence*. *Analytical Chemistry*, 2010. **82**(5): p. 2006-2012.

40. Wise, E.T., N. Singh, and B.L. Hogan, *Argon-laser-induced fluorescence detection in sodium dodecyl sulfate-capillary gel electrophoretic separations of proteins*. Journal of Chromatography A, 1996. **746**(1): p. 109-121.
41. Shrinivasan, S., et al., *A low-cost, low-power consumption, miniature laser-induced fluorescence system for DNA detection on a microfluidic device*. Clin Lab Med, 2007. **27**(1): p. 173-81.
42. Mainz, E.R., et al., *Monitoring intracellular nitric oxide production using microchip electrophoresis and laser-induced fluorescence detection*. Analytical Methods, 2012. **4**(2): p. 414-420.
43. Kahlert, H., *Functionalized carbon electrodes for pH determination*. Journal of Solid State Electrochemistry, 2008. **12**(10): p. 1255-1266.
44. Eremenko, A.V., et al., *Manganese Dioxide Nanostructures as a Novel Electrochemical Mediator for Thiol Sensors*. Electroanalysis, 2012. **24**(3): p. 573-580.
45. Ebbing, D.D., *General chemistry : ap edition*. 9th ed. 2007, Boston, MA: Houghton Mifflin Co.
46. Tiselius, A., *Electrophoresis of Purified Antibody Preparations*. J Exp Med, 1937. **65**(5): p. 641-6.
47. *Electrochemical Methods for Neuroscience*. 2007: CRC Press.
48. Faraday, M. *On Electrical Decomposition*. in *Philosophical Transactions of the Royal Society*. 1834.
49. Chang, T.G., E.M. Valeriotte, and D.M. Jochim, *Effects of Fast Charging on Hybrid Lead/Acid Battery Temperature*. Journal of Power Sources, 1994. **48**(1-2): p. 163-175.
50. Gross, E.M.K., Richard S.; Cannon, Donald M. Jr., *Analytical Electrochemistry: Potentiometry*. 2008, asdlib.org: Analytical Sciences Digital Library.
51. Kelly, R.S., *Analytical Electrochemistry: The Basic Concepts*. 2009: asdlib.org.
52. Yi, X., J. Huang-Xian, and C. Hong-Yuan, *Direct electrochemistry of horseradish peroxidase immobilized on a colloid/cysteamine-modified gold electrode*. Analytical biochemistry, 2000. **278**(1): p. 22-28.
53. Pedrotti, J.J., L. Angnes, and I.G.R. Gutz, *Miniaturized reference electrodes with microporous polymer junctions*. Electroanalysis, 1996. **8**(7): p. 673-675.
54. Suzuki, H., et al., *Problems associated with the thin-film Ag/AgCl reference electrode and a novel structure with improved durability*. Sensors and Actuators B: Chemical, 1998. **46**(2): p. 104-113.
55. Simonis, A., et al., *New concepts of miniaturised reference electrodes in silicon technology for potentiometric sensor systems*. Sensors and Actuators B: Chemical, 2004. **103**(1-2): p. 429-435.
56. Strong, F.C., *Faraday's laws in one equation*. Journal of Chemical Education, 1961. **38**(2): p. 98.
57. Baldwin, R.P., et al., *Fully integrated on-chip electrochemical detection for capillary electrophoresis in a microfabricated device*. Analytical Chemistry, 2002. **74**(15): p. 3690-3697.
58. Pai, R.S., et al., *Fully Integrated Three-Dimensional Electrodes for Electrochemical Detection in Microchips: Fabrication, Characterization, and Applications*. Analytical Chemistry, 2009. **81**(12): p. 4762-4769.

59. Wang, J., B.M. Tian, and E. Sahlin, *Integrated electrophoresis chips/amperometric detection with sputtered gold working electrodes*. Analytical Chemistry, 1999. **71**(17): p. 3901-3904.
60. Wilke, R. and S. Buttgenbach, *A micromachined capillary electrophoresis chip with fully integrated electrodes for separation and electrochemical detection*. Biosens Bioelectron, 2003. **19**(3): p. 149-153.
61. Yan, Y.M., et al., *Integrated Electrically Contacted Glucose Oxidase/Carbon Nanotube Electrodes for the Bioelectrocatalyzed Detection of Glucose*. Journal of Physical Chemistry C, 2008. **112**(46): p. 17883-17888.
62. Deangelis, T.P., et al., *Thin-Layer Differential Pulse Voltammetry*. Analytical Chemistry, 1977. **49**(12): p. 1792-1797.
63. Hubbard, A. and F. Anson, *The theory and practice of electrochemistry with thin layer cells*. Electroanalytical Chemistry A Series of Advances, 1970. **4**: p. 129-131.
64. Kurita, R., et al., *Fabrication and electrochemical properties of an interdigitated array electrode in a microfabricated wall-jet cell*. Sensors and Actuators B: Chemical, 2000. **71**(1-2): p. 82-89.
65. Shah, R.K. and A.L. London, *Laminar flow forced convection in ducts : a source book for compact heat exchanger analytical data*. Advances in heat transfer : Supplement. 1978, New York: Academic Press. xiv, 477 p.
66. Kissinger, P.T. and W.R. Heineman, *Laboratory techniques in electroanalytical chemistry*. 2nd ed. 1996, New York: Marcel Dekker, Inc. xvii, 986 p.
67. *Linear Sweep and Cyclic Voltammetry: The Principles*. [cited 2013 May 29]; Available from: <http://www.ceb.cam.ac.uk/pages/linear-sweep-and-cyclic-voltammetry-the-principles.html>.
68. Musameh, M., et al., *Low-potential stable NADH detection at carbon-nanotube-modified glassy carbon electrodes*. Electrochemistry Communications, 2002. **4**(10): p. 743-746.
69. Hubbard, A.T., R.A. Osteryoung, and F.C. Anson, *Further Study of the Iodide-Iodine Couple at Platinum Electrodes by Thin Layer Electrochemistry*. Analytical Chemistry, 1966. **38**(6): p. 692-697.
70. Gama, M.D. and J.C. Afonso, *From Svante Arrhenius to the digital pH meter: A century of acidity measurement*. Quimica Nova, 2007. **30**(1): p. 232-239.
71. Kahlert, H., et al., *Application of a new pH-sensitive electrode as a detector in flow injection potentiometry*. Electroanalysis, 2005. **17**(12): p. 1085-1090.
72. Veeramani, M.S., et al., *A Miniaturized pH Sensor With an Embedded Counter Electrode and a Readout Circuit*. Ieee Sensors Journal, 2013. **13**(5): p. 1941-1948.
73. Abdul-Majid, H., et al., *A Low-Cost Single-Chip Readout Circuit for Ph Sensing*. Informacije Midem-Journal of Microelectronics Electronic Components and Materials, 2009. **39**(2): p. 100-104.
74. Douchamps, D. *Tiny pH-Meter*. 2013; Available from: [http://damien.douxchamps.net/elec/ph\\_meter/](http://damien.douxchamps.net/elec/ph_meter/).
75. Goldcamp, M.J., et al., *Inexpensive and Disposable pH Electrodes*. Journal of Chemical Education, 2010. **87**(11): p. 1262-1264.

76. Apetrei, I.M. and C. Apetrei, *Amperometric biosensor based on polypyrrole and tyrosinase for the detection of tyramine in food samples*. Sensors and Actuators B-Chemical, 2013. **178**: p. 40-46.
77. Li, H.D., et al., *An amperometric sensor for the determination of benzophenone in food packaging materials based on the electropolymerized molecularly imprinted poly-o-phenylenediamine film*. Talanta, 2012. **99**: p. 811-815.
78. Grygolowicz-Pawlak, E., et al., *Coulometric Sodium Chloride Removal System with Nafion Membrane for Seawater Sample Treatment*. Analytical Chemistry, 2012. **84**(14): p. 6158-6165.
79. Zhao, J., et al., *A new electrochemical method for the detection of cancer cells based on small molecule-linked DNA*. Biosensors & Bioelectronics, 2013. **49**: p. 329-333.
80. Lee, K.H., et al., *Chemical oxygen demand (COD) sensor using a stopped-flow thin layer electrochemical cell*. Electroanalysis, 1999. **11**(16): p. 1172-1179.
81. Fukuda, J., S. Tsujimura, and K. Kano, *Coulometric bioelectrocatalytic reactions based on NAD-dependent dehydrogenases in tricarboxylic acid cycle*. Electrochimica Acta, 2008. **54**(2): p. 328-333.
82. Sohail, M., et al., *Thin layer coulometric determination of nitrate in fresh waters*. Analytica Chimica Acta, 2012. **744**: p. 39-44.
83. Shvarev, A., B. Neel, and E. Bakker, *Detection Limits of Thin Layer Coulometry with Ionophore Based Ion-Selective Membranes*. Analytical Chemistry, 2012. **84**(18): p. 8038-8044.
84. Haghghi, B., et al., *Fabrication and Characterization of a Thin-Layer Electrochemical Flow Cell and Its Application for Flow Analysis*. Analytical Letters, 2011. **44**(1-3): p. 258-270.
85. Byrne, R. and D. Diamond, *Chemo/bio-sensor networks*. Nature Materials, 2006. **5**(6): p. 421-424.
86. McGraw, C.M., et al., *Autonomous microfluidic system for phosphate detection*. Talanta, 2007. **71**(3): p. 1180-1185.
87. Diamond, D., et al., *Integration of analytical measurements and wireless communications - Current issues and future strategies*. Talanta, 2008. **75**(3): p. 606-612.
88. Fernandez-la-Villa, A., et al., *Fast and reliable urine analysis using a portable platform based on microfluidic electrophoresis chips with electrochemical detection*. Analytical Methods, 2013. **5**(6): p. 1494-1501.
89. Jackson, D.J., et al., *Portable high-voltage power supply and electrochemical detection circuits for microchip capillary electrophoresis*. Analytical Chemistry, 2003. **75**(14): p. 3643-3649.
90. Jackson; Douglas J., R., Jr.; Thomas J., Crain; Mark M., Baldwin; Richard P., Keynton; Robert S., Naber; John F., Walsh; Kevin M., Edelen, John G., *Capillary electrophoresis-electrochemical detection microchip device and supporting circuits*, U.S.P.a.T. Office, Editor. 2008, The University of Louisville Research Foundation: United States.
91. Yun, K.S., et al., *A miniaturized low-power wireless remote environmental monitoring system based on electrochemical analysis*. Sensors and Actuators B-Chemical, 2004. **102**(1): p. 27-34.



92. Sangam, V.G.P., B. M., *Performance Evaluation of an Amperometric Biosensor using a Simple Microcontroller based Data Acquisition System*. World Academy of Science, Engineering and Technology, 2008. **13**.
93. Huang, C.Y., et al., *A portable potentiostat for the bilirubin-specific sensor prepared from molecular imprinting*. Biosensors & Bioelectronics, 2007. **22**(8): p. 1694-1699.
94. Kwakye, S. and A. Baeumner, *An embedded system for portable electrochemical detection*. Sensors and Actuators B-Chemical, 2007. **123**(1): p. 336-343.
95. Novell, M., et al., *A novel miniaturized radiofrequency potentiometer tag using ion-selective electrodes for wireless ion sensing*. Analyst, 2013. **138**(18): p. 5250-7.
96. Rabaey, J.M., A.P. Chandrakasan, and B. Nikoli. , *Digital integrated circuits : a design perspective*. 2nd ed. Prentice Hall electronics and VLSI series. 2003, Upper Saddle River, N.J.: Pearson Education. xxii, 761 p., 4 p. of plates.
97. Chandrasekar, M.S. and M. Pushpavanam, *Pulse and pulse reverse plating - Conceptual, advantages and applications*. Electrochimica Acta, 2008. **53**(8): p. 3313-3322.
98. White, F.M., *Fluid mechanics*. 7th ed. 2011, New York, N.Y.: McGraw Hill. xv, 862 p.
99. Fritzing. 2012 [cited 2012 October 1]; Available from: [www.fritzing.org](http://www.fritzing.org).
100. 2-Layer PCB Manufacturing. 2012 [cited 2012 October 1]; Available from: <http://www.4pcb.com/33-each-pcbs.html>.
101. Oreilly, J.E., *Oxidation-Reduction Potential of Ferro-Ferricyanide System in Buffer Solutions*. Biochimica Et Biophysica Acta, 1973. **292**(3): p. 509-515.
102. Shaw, B.R., F.E. Strillacci, and K.A. Carrado, *Electrochemistry of Ferricyanide on Carbon Paste Electrodes Containing an Anion-Exchanging Clay*. Journal of the Electrochemical Society, 1987. **134**(3): p. C140-C140.
103. Taurino, I., et al., *Comparison of two different carbon nanotube-based surfaces with respect to potassium ferricyanide electrochemistry*. Surface Science, 2012. **606**(3-4): p. 156-160.
104. Baoutina, A., R.T. Dean, and W. Jessup, *Trans-plasma membrane electron transport induces macrophage-mediated low density lipoprotein oxidation*. The FASEB Journal, 2001. **15**(9): p. 1580-1582.
105. Konopka, S.J. and B. Mcduffie, *Diffusion Coefficients of Ferricyanide and Ferrocyanide Ions in Aqueous Media, Using Twin-Electrode Thin-Layer Electrochemistry*. Analytical Chemistry, 1970. **42**(14): p. 1741-&.
106. Montgomery, D.C. and G.C. Runger, *Applied statistics and probability for engineers*. 1994, New York: John Wiley & Sons.
107. Taylor, J.R., *An introduction to error analysis : the study of uncertainties in physical measurements*. 2nd ed. 1997, Sausalito, Calif.: University Science Books. xvii, 327 p.
108. Carroll, S., et al., *Microfabricated electrochemical sensors for exhaustive coulometry applications*. Sensors and Actuators B: Chemical, 2011. **160**(1).
109. Marei, M.M., et al., *Electrochemical and microfabrication strategies for remotely operated smart chemical sensors: application of anodic stripping coulometry to*

*calibration-free measurements of copper and mercury.* Anal Chim Acta, 2013.  
**803**: p. 47-55.

## Appendix A

### Potentiostat Bill of Materials

#### Part 1

<b>Part Label</b>	<b>Detail</b>	<b>Equivalent Digikey Part Number</b>
BNCC	BNC Connection (Counter)	ARF1065NW-ND
BNCR	BNC Connection (Reference)	ARF1065NW-ND
BNCW	BNC Connection (Work)	ARF1065NW-ND
C1	1uF	399-1284-1-ND
C2	4.7uF	399-3696-1-ND
C3	1uF	399-10114-1-ND
C4	10uF	399-8268-1-ND
C5	0.1uF	399-7999-1-ND
C6	0.1uF	399-7999-1-ND
C7	0.1uF	399-7999-1-ND
C8	0.1uF	399-7999-1-ND
C9	0.1uF	399-7999-1-ND
C10	0.1uF	399-7999-1-ND
Cfb	10000 pF	399-9280-1-ND
CG1	10uF	399-7411-1-ND
CG2	100 nF	399-1170-1-ND
CG3	1 nF	478-3759-1-ND
CG4	10 pF	399-11158-1-ND
DC1	NC	NC
DC2	NC	NC
DC3	NC	NC

Part 2

<b>Part Label</b>	<b>Detail</b>	<b>Equivalent Digikey Part Number</b>
J1	9V Header	CP-202A-ND
J2	-9V Header	CP-202A-ND
J3	Jumper Block	952-2264-ND
J4	Jumper Block	952-2264-ND
J6	4 Position Switch	450-1364-ND
J7	Jumper Block	952-2264-ND
J8	9Pin D-Sub	A2096
R1	1kOhm	P1.00KCCT-ND
R2	511Ohms	P511CCT-ND
Rfb	33kOhm	RHM33kBUCT-ND
Rfb2	0 Ohm	RHM0.0BMCT-ND
RG1	100 Ohm	RHM100CHCT-ND
RG2	10 kOhm	RHM10.0KCHCT-ND
RG3	1 MOhm	RHM1.00MCHCT-ND
RG4	100 MOhm	HMC0805JT100MCT-ND
U1	-5V Regulator	576-1294-1-ND
U2	+5V Regulator	296-11023-1-ND
U3	INA121	INA121PA-ND
U4	TLC2202	296-7071-5-ND
U5	OPA2277	OPA2277PA-ND

## Appendix B

### TLC2202 Datasheet (First Ten Pages)

#### TLC220x, TLC220xA, TLC220xB, TLC220xY Advanced LinCMOS™ LOW-NOISE PRECISION OPERATIONAL AMPLIFIERS

SLOS175B – FEBRUARY 1997 – REVISED JANUARY 2008

- B Grade Is 100% Tested for Noise  
30 nV/√Hz Max at f = 10 Hz  
12 nV/√Hz Max at f = 1 kHz
- Low Input Offset Voltage . . . 500 μV Max
- Excellent Offset Voltage Stability  
With Temperature . . . 0.5 μV/°C Typ
- Rail-to-Rail Output Swing
- Low Input Bias Current  
1 pA Typ at T<sub>A</sub> = 25°C
- Common-Mode Input Voltage Range  
Includes the Negative Rail
- Fully Specified For Both Single-Supply and  
Split-Supply Operation

#### description

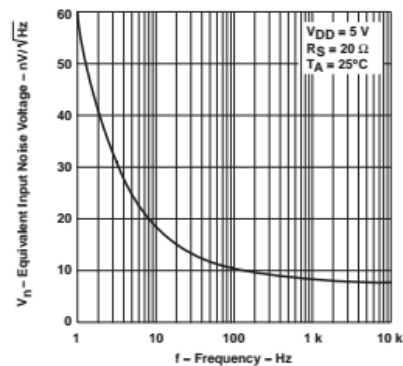
The TLC220x, TLC220xA, TLC220xB, and TLC220xY are precision, low-noise operational amplifiers using Texas Instruments Advanced LinCMOS™ process. These devices combine the noise performance of the lowest-noise JFET amplifiers with the dc precision available previously only in bipolar amplifiers. The Advanced LinCMOS™ process uses silicon-gate technology to obtain input offset voltage stability with temperature and time that far exceeds that obtainable using metal-gate technology. In addition, this technology makes possible input impedance levels that meet or exceed levels offered by top-gate JFET and expensive dielectric-isolated devices.

The combination of excellent DC and noise performance with a common-mode input voltage range that includes the negative rail makes these devices an ideal choice for high-impedance, low-level signal-conditioning applications in either single-supply or split-supply configurations.

The device inputs and outputs are designed to withstand –100-mA surge currents without sustaining latch-up. In addition, internal ESD-protection circuits prevent functional failures at voltages up to 2000 V as tested under MIL-PRF-38535, Method 3015.2; however, care should be exercised in handling these devices as exposure to ESD may result in degradation of the parametric performance.

The C-suffix devices are characterized for operation from 0°C to 70°C. The I-suffix devices are characterized for operation from –40°C to 85°C. The M-suffix devices are characterized for operation over the full military temperature range of –55°C to 125°C.

TYPICAL EQUIVALENT  
INPUT NOISE VOLTAGE  
VS  
FREQUENCY



Please be aware that an important notice concerning availability, standard warranty, and use in critical applications of Texas Instruments semiconductor products and disclaimers thereto appears at the end of this data sheet.

Advanced LinCMOS is a trademark of Texas Instruments Incorporated. All other trademarks are the property of their respective owners.

PRODUCTION DATA information is current as of publication date.  
Products conform to specifications per the terms of Texas Instruments  
standard warranty. Production processing does not necessarily include  
testing of all parameters.

TEXAS  
INSTRUMENTS

POST OFFICE BOX 655303 • DALLAS, TEXAS 75265

Copyright © 1997–2008, Texas Instruments Incorporated

On products compliant to MIL-PRF-38535, all parameters are tested  
unless otherwise noted. On all other products, production  
processing does not necessarily include testing of all parameters.

1

**TLC220x, TLC220xA, TLC220xB, TLC220xY**  
**Advanced LinCMOS™ LOW-NOISE PRECISION**  
**OPERATIONAL AMPLIFIERS**

SLOS175B – FEBRUARY 1997 – REVISED JANUARY 2008

**TLC2201 AVAILABLE OPTIONS**

T <sub>A</sub>	V <sub>IO</sub> max AT 25°C	V <sub>n</sub> max f = 10 Hz AT 25°C	V <sub>n</sub> max f = 1 kHz AT 25°C	PACKAGED DEVICES				CHIP FORM† (Y)
				SMALL OUTLINE† (D)	CHIP CARRIER (FK)	CERAMIC DIP (JG)	PLASTIC DIP (P)	
0°C to 70°C	200 µV	35 nV/√Hz	15 nV/√Hz	TLC2201ACD	—	—	TLC2201ACP	TLC2201Y
	200 µV	30 nV/√Hz	12 nV/√Hz	TLC2201BCD			TLC2201BCP	
	500 µV	—	—	TLC2201CD			TLC2201CP	
-40°C to 85°C	200 µV	35 nV/√Hz	15 nV/√Hz	TLC2201AID	—	—	TLC2201AIP	—
	200 µV	30 nV/√Hz	12 nV/√Hz	TLC2201BID			TLC2201BIP	
	500 µV	—	—	TLC2201ID			TLC2201IP	
-55°C to 125°C	200 µV	35 nV/√Hz	15 nV/√Hz	TLC2201AMD	TLC2201AMFK	TLC2201AMJG	TLC2201AMP	—
	200 µV	30 nV/√Hz	12 nV/√Hz	TLC2201BMD	TLC2201BMFK	TLC2201BMJG	TLC2201BMP	
	500 µV	—	—	TLC2201MD	TLC2201MFK	TLC2201MJG	TLC2201MP	

† The D packages are available taped and reeled. Add R suffix to device type (e.g. TLC220xBCCR).

‡ Chip forms are tested at 25°C only.

**TLC2202 AVAILABLE OPTIONS**

T <sub>A</sub>	V <sub>IO</sub> max AT 25°C	V <sub>n</sub> max f = 10 Hz AT 25°C	V <sub>n</sub> max f = 1 kHz AT 25°C	PACKAGED DEVICES					CHIP FORM† (Y)
				SMALL OUTLINE† (D)	PLASTIC SMALL OUTLINE (PS)	CHIP CARRIER (FK)	CERAMIC DIP (JG)	PLASTIC DIP (P)	
0°C to 70°C	500 µV	30 nV/√Hz	12 nV/√Hz	TLC2202BCD	—	—	—	TLC2202BCP	TLC2202Y
	500 µV	35 nV/√Hz	15 nV/√Hz	TLC2202ACD	—	—	—	TLC2202ACP	
	1 mV	—	—	TLC2202CD	TLC2202CPSR	—	—	TLC2202CP	
-40°C to 85°C	500 µV	30 nV/√Hz	12 nV/√Hz	TLC2202BID	—	—	—	TLC2202BIP	—
	500 µV	35 nV/√Hz	15 nV/√Hz	TLC2202AID	—	—	—	TLC2202AIP	
	1 mV	—	—	TLC2202ID	—	—	—	TLC2202IP	
-55°C to 125°C	500 µV	30 nV/√Hz	12 nV/√Hz	TLC2202BMD	—	TLC2202BMFK	TLC2202BMJG	TLC2202BMP	—
	500 µV	35 nV/√Hz	15 nV/√Hz	TLC2202AMD	—	TLC2202AMFK	TLC2202AMJG	TLC2202AMP	
	1 mV	—	—	TLC2202MD	—	TLC2202MFK	TLC2202MJG	TLC2202MP	

† The D packages are available taped and reeled. Add R suffix to device type (e.g. TLC220xBCCR).

‡ Chip forms are tested at 25°C only.

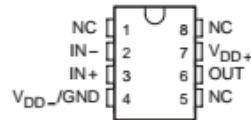


POST OFFICE BOX 655308 • DALLAS, TEXAS 75265

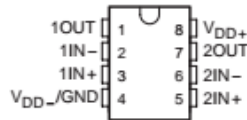
**TLC220x, TLC220xA, TLC220xB, TLC220xY**  
**Advanced LinCMOS™ LOW-NOISE PRECISION**  
**OPERATIONAL AMPLIFIERS**

SLOS175B - FEBRUARY 1997 - REVISED JANUARY 2008

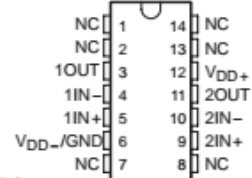
**TLC2201**  
**D, JG, OR P PACKAGE**  
**(TOP VIEW)**



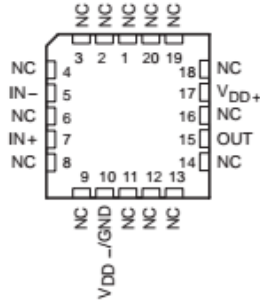
**TLC2202**  
**PS, JG, OR P PACKAGE**  
**(TOP VIEW)**



**TLC2202**  
**D PACKAGE**  
**(TOP VIEW)**

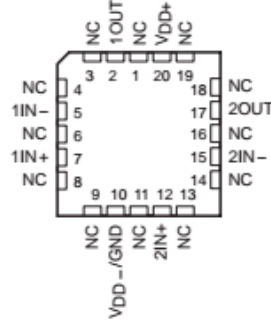


**TLC2201**  
**FK PACKAGE**  
**(TOP VIEW)**



NC - No internal connection

**TLC2202**  
**FK PACKAGE**  
**(TOP VIEW)**

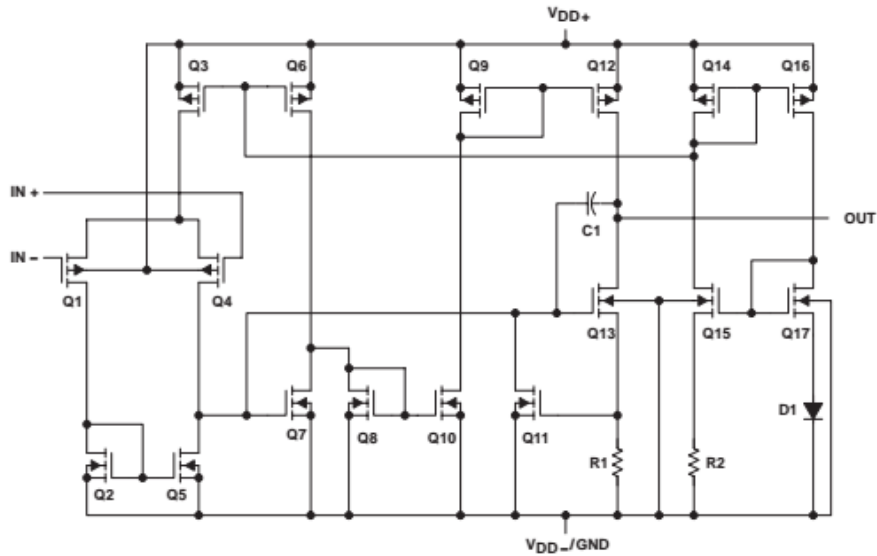


POST OFFICE BOX 655303 • DALLAS, TEXAS 75265

**TLC220x, TLC220xA, TLC220xB, TLC220xY**  
**Advanced LinCMOS™ LOW-NOISE PRECISION**  
**OPERATIONAL AMPLIFIERS**

SLOS175B – FEBRUARY 1997 – REVISED JANUARY 2008

equivalent schematic (each amplifier)



ACTUAL DEVICE COMPONENT COUNT		
COMPONENT	TLC2201	TLC2202
Transistors	17	34
Resistors	2	2
Diodes	1	4
Capacitors	1	2

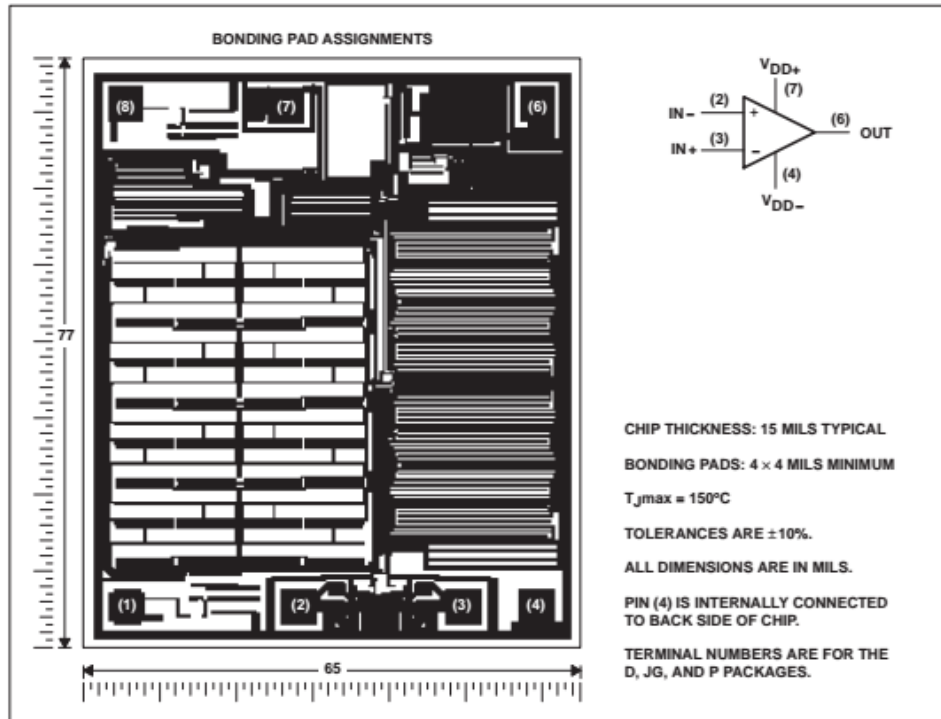


**TLC220x, TLC220xA, TLC220xB, TLC220xY**  
**Advanced LinCMOS™ LOW-NOISE PRECISION**  
**OPERATIONAL AMPLIFIERS**

SLOS175B – FEBRUARY 1997 – REVISED JANUARY 2008

**TLC2201Y chip information**

This chip, when properly assembled, displays characteristics similar to the TLC2201C. Thermal compression or ultrasonic bonding may be used on the doped-aluminum bonding path. Chips may be mounted with conductive epoxy or a gold-silicon preform.

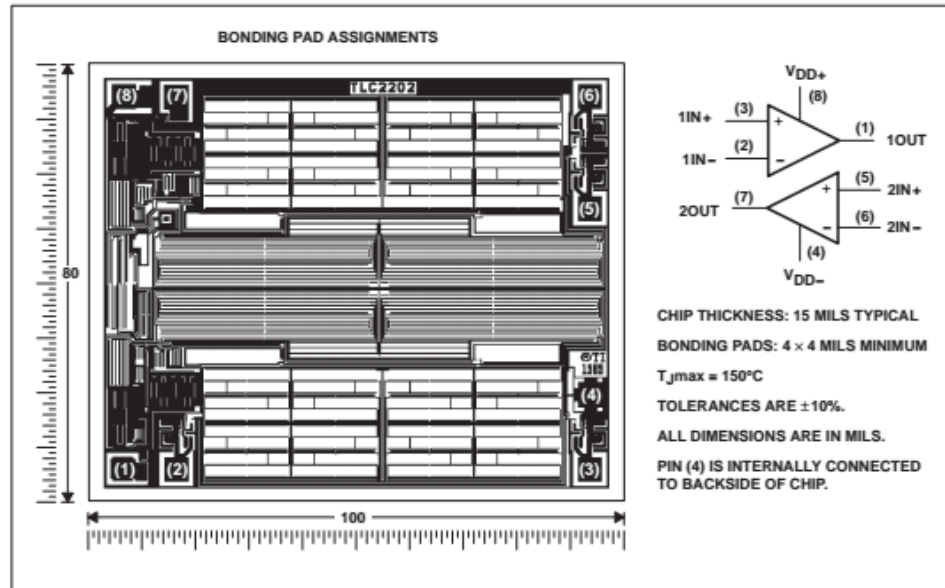


**TLC220x, TLC220xA, TLC220xB, TLC220xY**  
**Advanced LinCMOS™ LOW-NOISE PRECISION**  
**OPERATIONAL AMPLIFIERS**

SLOS175B – FEBRUARY 1997 – REVISED JANUARY 2008

**TLC2202Y chip formation**

This chip, when properly assembled, displays characteristics similar to the TLC2202C. Thermal compression or ultrasonic bonding may be used on the doped-aluminum bonding pads. Chips may be mounted with conductive epoxy or a gold-silicon preform.



**TLC220x, TLC220xA, TLC220xB, TLC220xY**  
**Advanced LinCMOS™ LOW-NOISE PRECISION**  
**OPERATIONAL AMPLIFIERS**

SLOS175B – FEBRUARY 1997 – REVISED JANUARY 2008

**absolute maximum ratings over operating free-air temperature range (unless otherwise noted)†**

Supply voltage, $V_{DD+}$ (see Note 1)	8 V
Supply voltage, $V_{DD-}$	-8 V
Differential input voltage, $V_{ID}$ (see Note 2)	$\pm 16$ V
Input voltage, $V_I$ (any input)	$\pm 8$ V
Input current, $I_I$ (each input)	$\pm 5$ mA
Output current, $I_O$ (each output)	$\pm 50$ mA
Duration of short-circuit current at (or below) 25°C (see Note 3)	unlimited
Continuous total dissipation	See Dissipation Rating Table
Operating free-air temperature range, $T_A$ : C suffix	0°C to 70°C
I suffix	-40°C to 85°C
M suffix	-55°C to 125°C
Storage temperature range	-65°C to 150°C
Case temperature for 60 seconds: FK package	260°C
Lead temperature 1,6 mm (1/16 inch) from case for 10 seconds: D, PS, or P package	260°C
Lead temperature 1,6 mm (1/16 inch) from case for 60 seconds: JG package	300°C

† Stresses beyond those listed under "absolute maximum ratings" may cause permanent damage to the device. These are stress ratings only, and functional operation of the device at these or any other conditions beyond those indicated under "recommended operating conditions" is not implied. Exposure to absolute-maximum-rated conditions for extended periods may affect device reliability.

NOTES: 1. All voltage values except differential voltages are with respect to the midpoint between  $V_{DD+}$  and  $V_{DD-}$ .

2. Differential voltages are at  $IN+$  with respect to  $IN-$ .

3. The output may be shorted to either supply. Temperature and/or supply voltages must be limited to ensure that the maximum dissipation rating is not exceeded.

DISSIPATION RATING TABLE

PACKAGE	$T_A \leq 25^\circ\text{C}$	DERATING FACTOR ABOVE $T_A = 25^\circ\text{C}$	$T_A = 70^\circ\text{C}$	$T_A = 85^\circ\text{C}$	$T_A = 125^\circ\text{C}$
	POWER RATING		POWER RATING	POWER RATING	POWER RATING
D-8	725 mW	5.8 mW/°C	464 mW	377 mW	145 mW
D-14	950 mW	7.6 mW/°C	608 mW	494 mW	190 mW
PS	770 mW	6.2 mW/°C	496 mW	403 mW	155 mW
FK	1375 mW	11.0 mW/°C	880 mW	715 mW	275 mW
JG	1050 mW	8.4 mW/°C	672 mW	546 mW	210 mW
P	1000 mW	8.0 mW/°C	640 mW	520 mW	200 mW

**recommended operating conditions**

	C SUFFIX		I SUFFIX		M SUFFIX		UNIT
	MIN	MAX	MIN	MAX	MIN	MAX	
Supply voltage, $V_{DD\pm}$	$\pm 2.3$	$\pm 8$	$\pm 2.3$	$\pm 8$	$\pm 2.3$	$\pm 8$	V
Common-mode input voltage, $V_{IC}$	$V_{DD-}$	$V_{DD+} - 2.3$	$V_{DD-}$	$V_{DD+} - 2.3$	$V_{DD-}$	$V_{DD+} - 2.3$	V
Operating free-air temperature, $T_A$	0	70	-40	85	-55	125	°C



**TEXAS  
INSTRUMENTS**

POST OFFICE BOX 655308 • DALLAS, TEXAS 75265

7

**TLC220x, TLC220xA, TLC220xB, TLC220xY**  
**Advanced LinCMOS™ LOW-NOISE PRECISION**  
**OPERATIONAL AMPLIFIERS**

SLOS175B – FEBRUARY 1997 – REVISED JANUARY 2008

**TLC2201C electrical characteristics at specified free-air temperature,  $V_{DD\pm} = \pm 5$  V (unless otherwise noted)**

PARAMETER	TEST CONDITIONS	$T_A$ †	TLC2201C			UNIT
			MIN	TYP	MAX	
$V_{IO}$ Input offset voltage	$V_{IC} = 0, R_S = 50 \Omega$	25°C		100	500	$\mu V$
		Full range			600	
$mV_{IO}$ Temperature coefficient of input offset voltage		Full range		0.5		$\mu V/^\circ C$
Input offset voltage long-term drift (see Note 4)		25°C		0.001	0.005	$\mu V/mo$
$I_{IO}$ Input offset current		25°C		0.5	60	pA
		Full range			100	
$I_{IB}$ Input bias current	25°C		1	60	pA	
	Full range			100		
$V_{ICR}$ Common-mode input voltage range	$R_S = 50 \Omega$	Full range	-5 to 2.7		V	
$V_{OM+}$ Maximum positive peak output voltage swing	$R_L = 10 k\Omega$	25°C	4.7	4.8	V	
		Full range	4.7			
$V_{OM-}$ Maximum negative peak output voltage swing		25°C	-4.7	-4.9	V	
		Full range	-4.7			
$A_{VD}$ Large-signal differential voltage amplification	$V_O = \pm 4$ V, $R_L = 500 k\Omega$	25°C	400	560	VmV	
		Full range	300			
	$V_O = \pm 4$ V, $R_L = 10 k\Omega$	25°C	90	100		
		Full range	70			
CMRR Common-mode rejection ratio	$V_{IC} = V_{ICRmin}, V_O = 0, R_S = 50 \Omega$	Full range	85		dB	
		25°C	90	110	dB	
$k_{SVR}$ Supply voltage rejection ratio ( $\Delta V_{DD\pm} / \Delta V_{IO}$ )	$V_{DD\pm} = \pm 2.3$ V to $\pm 8$ V	Full range	85			
		25°C		1.1 1.5	mA	
$I_{DD}$ Supply current	$V_O = 0, \text{ No load}$	Full range		1.5		

† Full range is 0°C to +70°C.

NOTE 4: Typical values are based on the input offset voltage shift observed through 168 hours of operating life test at  $T_A = 150^\circ C$  extrapolated to  $T_A = 25^\circ C$  using the Arrhenius equation and assuming an activation energy of 0.96 eV.

**TLC2201C operating characteristics at specified free-air temperature,  $V_{DD\pm} = \pm 5$  V**

PARAMETER	TEST CONDITIONS	$T_A$ †	TLC2201C			UNIT
			MIN	TYP	MAX	
SR Slew rate at unity gain	$V_O = \pm 2.3$ V, $C_L = 100$ pF, $R_L = 10 k\Omega$	25°C	2	2.7	$V/\mu s$	
		Full range	1.5			
$V_n$ Equivalent input noise voltage	$f = 10$ Hz	25°C		18	$nV/\sqrt{Hz}$	
	$f = 1$ kHz	25°C		8		
$V_{N(PP)}$ Peak-to-peak equivalent input noise voltage	$f = 0.1$ to $1$ Hz	25°C		0.5	$\mu V$	
	$f = 0.1$ to $10$ Hz	25°C		0.7		
$I_n$ Equivalent input noise current		25°C		0.6	$fA/\sqrt{Hz}$	
Gain-bandwidth product	$f = 10$ kHz, $R_L = 10 k\Omega, C_L = 100$ pF	25°C		1.9	MHz	
$\phi_m$ Phase margin at unity gain	$R_L = 10 k\Omega, C_L = 100$ pF	25°C		48°		

† Full range is 0°C to +70°C.



POST OFFICE BOX 655308 • DALLAS, TEXAS 75265

**TLC220x, TLC220xA, TLC220xB, TLC220xY**  
**Advanced LinCMOS™ LOW-NOISE PRECISION**  
**OPERATIONAL AMPLIFIERS**

SLOS175B – FEBRUARY 1997 – REVISED JANUARY 2008

**TLC2201C electrical characteristics at specified free-air temperature,  $V_{DD\pm} = \pm 5\text{ V}$  (unless otherwise noted)**

PARAMETER	TEST CONDITIONS	$T_A$ †	TLC2201AC			TLC2201BC			UNIT
			MIN	TYP	MAX	MIN	TYP	MAX	
$V_{IO}$ Input offset voltage		25°C	80	200		80	200	$\mu\text{V}$	
		Full range		300		300			
$\alpha_{VIO}$ Temperature coefficient of input offset voltage	$V_{IC} = 0, R_S = 50\ \Omega$	Full range	0.5			0.5			$\mu\text{V}/^\circ\text{C}$
Input offset voltage long-term drift (see Note 4)		25°C	0.001	0.005		0.001	0.005	$\mu\text{V}/\text{mo}$	
$I_{IO}$ Input offset current		25°C	0.5	60		0.5	60	$\text{pA}$	
	Full range		100		100				
$I_{IB}$ Input bias current		25°C	1	60		1	60	$\text{pA}$	
		Full range		100		100			
$V_{ICR}$ Common-mode input voltage range	$R_S = 50\ \Omega$	Full range	-5 to 2.7			-5 to 2.7			$\text{V}$
$V_{OM+}$ Maximum positive peak output voltage swing	$R_L = 10\ \text{k}\Omega$	25°C	4.7	4.8		4.7	4.8	$\text{V}$	
Full range		4.7			4.7				
$V_{OM-}$ Maximum negative peak output voltage swing		25°C	-4.7	-4.9		-4.7	-4.9	$\text{V}$	
		Full range	-4.7			-4.7			
$A_{VD}$ Large-signal differential voltage amplification	$V_O = \pm 4\ \text{V}, R_L = 500\ \text{k}\Omega$	25°C	400	560		400	560	$\text{V}/\text{mV}$	
		Full range	300			300			
	$V_O = \pm 4\ \text{V}, R_L = 10\ \text{k}\Omega$	25°C	90	100		90	100		
		Full range	70			70			
CMRR Common-mode rejection ratio	$V_{IC} = V_{ICR\text{min}}, V_O = 0, R_S = 50\ \Omega$	25°C	90	115		90	115	$\text{dB}$	
		Full range	85			85			
$k_{SVR}$ Supply voltage rejection ratio ( $\Delta V_{DD\pm} / \Delta V_{IO}$ )	$V_{DD\pm} = \pm 2.3\ \text{V}$ to $\pm 8\ \text{V}$	25°C	90	110		90	110	$\text{dB}$	
		Full range	85			85			
$I_{DD}$ Supply current	$V_O = 0, \text{ No load}$	25°C	1.1 1.5			1.1 1.5			$\text{mA}$
		Full range	1.5			1.5			

† Full range is 0°C to +70°C.

NOTE 4: Typical values are based on the input offset voltage shift observed through 168 hours of operating life test at  $T_A = 150^\circ\text{C}$  extrapolated to  $T_A = 25^\circ\text{C}$  using the Arrhenius equation and assuming an activation energy of 0.96 eV.



POST OFFICE BOX 655303 • DALLAS, TEXAS 75265

9

**TLC220x, TLC220xA, TLC220xB, TLC220xY**  
**Advanced LinCMOS™ LOW-NOISE PRECISION**  
**OPERATIONAL AMPLIFIERS**

SLOS175B – FEBRUARY 1997 – REVISED JANUARY 2008

**TLC2201C operating characteristics at specified free-air temperature,  $V_{DD\pm} = \pm 5\text{ V}$**

PARAMETER	TEST CONDITIONS	$T_A$ †	TLC2201AC			TLC2201BC			UNIT
			MIN	TYP	MAX	MIN	TYP	MAX	
SR	Slew rate at unity gain $V_O = \pm 2.3\text{ V}$ , $R_L = 10\text{ k}\Omega$ , $C_L = 100\text{ pF}$	25°C	2	2.7		2	2.7		$\text{V}/\mu\text{s}$
		Full range	1.5			1.5			
$V_n$	Equivalent input noise voltage (see Note 5)	$f = 10\text{ Hz}$		18	35		18	30	$\text{nV}/\sqrt{\text{Hz}}$
		$f = 1\text{ kHz}$	25°C	8	15		8	12	
$V_{N(PP)}$	Peak-to-peak equivalent input noise voltage	$f = 0.1\text{ to }1\text{ Hz}$	25°C		0.5		0.5		$\mu\text{V}$
		$f = 0.1\text{ to }10\text{ Hz}$	25°C		0.7		0.7		
$I_n$	Equivalent input noise current		25°C		0.6		0.6	$\text{fA}/\sqrt{\text{Hz}}$	
	Gain-bandwidth product	$f = 10\text{ kHz}$ , $R_L = 10\text{ k}\Omega$ , $C_L = 100\text{ pF}$	25°C		1.9		1.9	MHz	
$\phi_m$	Phase margin at unity gain	$R_L = 10\text{ k}\Omega$ , $C_L = 100\text{ pF}$	25°C		48°		48°		

† Full range is 0°C to +70°C.

NOTE 5: This parameter is tested on a sample basis for the TLC2201A and on all devices for the TLC2201B. For other test requirements, please contact the factory. This statement has no bearing on testing or nontesting of other parameters.



POST OFFICE BOX 655303 • DALLAS, TEXAS 75265

## Appendix C

### DAQCard-6062E Specifications

# NI DAQCard™ -6062E Family Specifications

This document lists the I/O terminal summary and specifications for the NI DAQCard-6062E for PCMCIA.

#### I/O Terminal Summary



**Note** With NI-DAQmx, National Instruments revised its terminal names so they are easier to understand and more consistent among NI hardware and software products. The revised terminal names used in this document are usually similar to the names they replace. For a complete list of Traditional NI-DAQ (Legacy) terminal names and their NI-DAQmx equivalents, refer to *Terminal Name Equivalents* of the *E Series Help*.

**Table 1.** I/O Terminals

Terminal Name	Terminal Type and Direction	Impedance Input/ Output	Protection (V) On/Off	Source (mA at V)	Sink (mA at V)	Rise Time (ns)	Bias
AI <0..15>	AI	100 G $\Omega$ in parallel with 100 pF	25/10	—	—	—	$\pm 200$ pA
AI SENSE	AI	100 G $\Omega$ in parallel with 100 pF	25/10	—	—	—	$\pm 200$ pA
AI GND	—	—	—	—	—	—	—
AO 0	AO	0.1 $\Omega$	Short-circuit to ground	5 at 10	5 at -10	10 V/ $\mu$ s	—
AO 1	AO	0.1 $\Omega$	Short-circuit to ground	5 at 10	5 at -10	10 V/ $\mu$ s	—
AO EXT REF	AI	10 k $\Omega$	25/15	—	—	—	—
AO GND	—	—	—	—	—	—	—
D GND	—	—	—	—	—	—	—
+5 V	—	0.45 $\Omega$	Short-circuit to ground	250 at V <sub>CC</sub>	—	—	—
P0.<0..7>	DIO	—	V <sub>CC</sub> + 0.5	13 at (V <sub>CC</sub> - 0.4)	24 at 0.4	1.1	50 k $\Omega$ pu <sup>f</sup>



Table 1. I/O Terminals (Continued)

Terminal Name	Terminal Type and Direction	Impedance Input/ Output	Protection (V) On/Off	Source (mA at V)	Sink (mA at V)	Rise Time (ns)	Bias
AI HOLD COMP	DO	—	—	3.5 at (V <sub>CC</sub> - 0.4)	5 at 0.4	1.5	50 kΩ pu
EXT STROBE*	DO	—	—	3.5 at (V <sub>CC</sub> - 0.4)	5 at 0.4	1.5	50 kΩ pu
PFI 0/ (AI START TRIG)	AI/DIO	10 kΩ	V <sub>CC</sub> + 0.5/±35	3.5 at (V <sub>CC</sub> - 0.4)	5 at 0.4	1.5	50 kΩ pu, 10 kΩ pd
PFI 1/ (AI REF TRIG)	DIO	—	V <sub>CC</sub> + 0.5	3.5 at (V <sub>CC</sub> - 0.4)	5 at 0.4	1.5	50 kΩ pu
PFI 2/ (AI CONV CLK)*	DIO	—	V <sub>CC</sub> + 0.5	3.5 at (V <sub>CC</sub> - 0.4)	5 at 0.4	1.5	50 kΩ pu
PFI 3/ CTR 1 SOURCE	DIO	—	V <sub>CC</sub> + 0.5	3.5 at (V <sub>CC</sub> - 0.4)	5 at 0.4	1.5	50 kΩ pu
PFI 4/CTR 1 GATE	DIO	—	V <sub>CC</sub> + 0.5	3.5 at (V <sub>CC</sub> - 0.4)	5 at 0.4	1.5	50 kΩ pu
CTR 1 OUT	DO	—	—	3.5 at (V <sub>CC</sub> - 0.4)	5 at 0.4	1.5	50 kΩ pu
PFI 5/ (AO SAMP CLK)*	DIO	—	V <sub>CC</sub> + 0.5	3.5 at (V <sub>CC</sub> - 0.4)	5 at 0.4	1.5	50 kΩ pu
PFI 6/ (AO START TRIG)	DIO	—	V <sub>CC</sub> + 0.5	3.5 at (V <sub>CC</sub> - 0.4)	5 at 0.4	1.5	50 kΩ pu
PFI 7/ (AI SAMP CLK)	DIO	—	V <sub>CC</sub> + 0.5	3.5 at (V <sub>CC</sub> - 0.4)	5 at 0.4	1.5	50 kΩ pu
PFI 8/ CTR 0 SOURCE	DIO	—	V <sub>CC</sub> + 0.5	3.5 at (V <sub>CC</sub> - 0.4)	5 at 0.4	1.5	50 kΩ pu
PFI 9/CTR 0 GATE	DIO	—	V <sub>CC</sub> + 0.5	3.5 at (V <sub>CC</sub> - 0.4)	5 at 0.4	1.5	50 kΩ pu
CTR 0 OUT	DO	—	—	3.5 at (V <sub>CC</sub> - 0.4)	5 at 0.4	1.5	50 kΩ pu
FREQ OUT	DO	—	—	3.5 at (V <sub>CC</sub> - 0.4)	5 at 0.4	1.5	50 kΩ pu

**Caution:** Exceeding the output limit in the Source and Sink columns can damage the NI DAQCard-6062E.

\* Indicates active low.

† P0.<6..7> are also pulled up with a 10 kΩ resistor.

AI = Analog Input    DIO = Digital Input/Output    pu = pull-up  
 AO = Analog Output    DO = Digital Output    AI/DIO = Analog Input/Digital Input/Output

**Note:** The tolerance on the 50 kΩ pull-up resistors is large. Actual value might range between 17 kΩ and 100 kΩ.



## Specifications

The following specifications are typical at 25 °C unless otherwise noted.

### Analog Input

#### Input Characteristics

Number of channels ..... 16 single-ended,  
16 pseudodifferential,  
or 8 differential  
(software-selectable on  
a per-channel basis)

Type of A/D converter (ADC)..... Successive  
approximation

Resolution ..... 12 bits, 1 in 4,096

Max sampling rate ..... 500 kS/s

Input signal ranges

Range (Software-Selectable)	Input Range	
	Bipolar	Unipolar
20 V	±10 V	—
10 V	±5 V	0 to 10 V
5 V	±2.5 V	0 to 5 V
2 V	±1 V	0 to 2 V
1 V	±500 mV	0 to 1 V
500 mV	±250 mV	0 to 500 mV
200 mV	±100 mV	0 to 200 mV
100 mV	±50 mV	0 to 100 mV

**Accuracy Information**

Nominal Range at Full Scale (V)	Absolute Accuracy										Relative Accuracy Resolution (mV)	
	% of Reading		Offset (mV)	Noise + Quantization (mV)		Temp Drift (%/°C)	Absolute Accuracy at Full Scale (mV)	Relative Accuracy Resolution (mV)				
	24 Hours	1 Year		Single Pt.	Averaged			Single Pt.	Averaged			
±10.0	0.0672	0.0714	9.83		6.100	0.975	0.0010	17.945	7.370	1.280		
±5.0	0.0272	0.0314	4.92		3.050	0.488	0.0005	6.983	3.680	0.642		
±2.5	0.0672	0.0714	2.47		1.530	0.244	0.0010	4.502	1.840	0.321		
±1.0	0.0672	0.0714	1.001		0.610	0.098	0.0010	1.813	0.737	0.128		
±0.5	0.0672	0.0714	0.511		0.305	0.049	0.0010	0.917	0.368	0.064		
±0.25	0.0672	0.0714	0.266		0.208	0.029	0.0010	0.474	0.238	0.039		
±0.1	0.0672	0.0714	0.119		0.098	0.012	0.0010	0.203	0.111	0.016		
±0.05	0.0672	0.0714	0.070		0.071	0.008	0.0010	0.113	0.082	0.010		
10 to 0	0.0272	0.0314	4.920		3.050	0.488	0.0005	8.555	3.68	0.642		
5 to 0	0.0672	0.0714	2.470		1.530	0.244	0.0010	6.288	1.84	0.321		
2 to 0	0.0672	0.0714	1.001		0.610	0.098	0.0010	2.528	0.737	0.128		
1 to 0	0.0672	0.0714	0.511		0.305	0.049	0.0010	1.274	0.368	0.064		
0.5 to 0	0.0672	0.0714	0.266		0.208	0.029	0.0010	0.653	0.238	0.039		
0.2 to 0	0.0672	0.0714	0.119		0.098	0.012	0.0010	0.274	0.111	0.016		
0.1 to 0	0.0672	0.0714	0.070		0.071	0.008	0.0010	0.149	0.082	0.010		

Note: Accuracies are valid for measurements following an internal E Series calibration. Averaged numbers assume dithering and averaging of 100 single-channel readings. Measurement accuracies are listed for operational temperatures within ±1 °C of internal calibration temperature and ±10 °C of external or factory-calibration temperature. NI recommends a one-year calibration interval. The Absolute Accuracy at Full Scale calculations were performed for a maximum range input voltage (for example, 10 V for the ±10 V range) after one year, assuming 100 points of averaged data. Go to [ni.com/info](#) and enter info code [rdspac](#) for example calculations.

**Transfer Characteristics**

Relative accuracy .....  $\pm 0.5$  LSB typ dithered,  
 $\pm 1.5$  LSB max undithered

Differential nonlinearity (DNL).....  $\pm 0.75$  LSB typ,  
 $-0.9, +1.5$  LSB max

No missing codes ..... 12 bits, guaranteed

Offset error  
 Pregain error after calibration.....  $\pm 16$   $\mu$ V max  
 Pregain error before calibration.....  $\pm 4$  mV max  
 Postgain error after calibration...  $\pm 1$  mV max  
 Postgain error before calibration.....  $\pm 265$  mV max

Gain error (relative to calibration reference)  
 After calibration (gain = 1).....  $\pm 0.02\%$  of reading max  
 Before calibration .....  $\pm 2.5\%$  of reading max  
 Gain  $\neq 1$  with gain error adjusted to 0 at gain = 1.....  $\pm 0.02\%$  of reading max

**Amplifier Characteristics**

Input impedance  
 Normal powered on ..... 100 G $\Omega$  in parallel with 100 pF  
 Powered off ..... 820  $\Omega$  min  
 Overload ..... 820  $\Omega$  min

Input bias current .....  $\pm 200$  pA

Input offset current.....  $\pm 100$  pA

Common-mode rejection ratio (CMRR), DC to 60 Hz

Range	CMRR
10 to 20 V	85 dB
5 V	95 dB
100 mV to 2 V	100 dB

**Dynamic Characteristics**

Bandwidth  
 Small signal ( $-3$  dB)..... 1.3 MHz  
 Large signal (1% THD)..... 250 kHz

Settling time for full-scale step

Range	Accuracy*		
	$\pm 0.012\%$ ( $\pm 0.5$ LSB)	$\pm 0.024\%$ ( $\pm 1$ LSB)	$\pm 0.098\%$ ( $\pm 4$ LSB)
All	2.5 $\mu$ s typ	2.5 $\mu$ s typ, 4 $\mu$ s max	2 $\mu$ s typ

\* Accuracy values are valid for source impedances  $< 1$  k $\Omega$ . Refer to *Multichannel Scanning Considerations* of the *E Series Help* for more information.

System noise (LSB<sub>rms</sub>, not including quantization)

Range	Dither On	Dither Off
1 to 20 V	0.25	0.6
500 mV	0.4	0.75
200 mV	0.5	0.8
100 mV	0.8	1.0

Crosstalk (DC to 100 kHz)

Adjacent channels .....  $-75$  dB  
 All other channels .....  $-90$  dB

**Stability**

Offset temperature coefficient  
 Pregain .....  $\pm 5$   $\mu$ V/ $^{\circ}$ C  
 Postgain.....  $\pm 240$   $\mu$ V/ $^{\circ}$ C

Gain temperature coefficient .....  $\pm 20$  ppm/ $^{\circ}$ C

**Analog Output**

**Output Characteristics**

Number of channels ..... 2 voltage  
 Resolution..... 12 bits, 1 in 4,096

Max update rate, waveform generation

FIFO Mode		Non-FIFO Mode	
Internally Timed	Externally Timed	1 Channel	2 Channels
850 kS/s	850 kS/s	800 kS/s, system-dependent	400 kS/s, system-dependent

Type of D/A converter (DAC) .....Double-buffered,  
multiplying

FIFO buffer size .....2,048 samples (S)

Data transfers.....Interrupts,  
programmed I/O

### Accuracy Information

Nominal Range (V)		Absolute Accuracy				Absolute Accuracy at Full Scale (mV)	
Positive Full Scale	Negative Full Scale	% of Reading			Offset (mV)		Temp Drift (%/°C)
		24 Hours	90 Days	1 Year			
10	-10	0.0177	0.0197	0.0219	8.37	0.0005	10.568

**Note:** Accuracies are valid for measurements following an internal E Series calibration. Averaged numbers assume dithering and averaging of 100 single-channel readings. Measurement accuracies are listed for operational temperatures within  $\pm 1$  °C of internal calibration temperature and  $\pm 10$  °C of external or factory-calibration temperature. NI recommends a one-year calibration interval. The Absolute Accuracy at Full Scale calculations were performed for a maximum range input voltage (for example, 10 V for the  $\pm 10$  V range) after one year, assuming 100 points of averaged data. Go to [ni.com/info](http://ni.com/info) and enter info code `rdspoc` for example calculations.

### Transfer Characteristics

Relative accuracy, or integral nonlinearity (INL)

After calibration ..... $\pm 0.5$  LSB typ,  
 $\pm 1.0$  LSB max

Before calibration ..... $\pm 4$  LSB max

DNL

After calibration ..... $\pm 0.5$  LSB typ,  
 $\pm 1.0$  LSB max

Before calibration ..... $\pm 3$  LSB max

Monotonicity .....12 bits, guaranteed  
after calibration

Offset error

After calibration ..... $\pm 1.0$  mV max

Before calibration ..... $\pm 200$  mV max

Gain error (relative to internal reference)

After calibration ..... $\pm 0.01\%$  of output max

Before calibration ..... $\pm 0.7\%$  of output max

Gain error  
(relative to external reference) ..... $\pm 0.5\%$  of output max,  
not adjustable

### Voltage Output

Ranges ..... $\pm 10$  V,  $\pm$ AO EXT REF  
(software-selectable)

Output coupling .....DC

Output impedance .....0.1  $\Omega$  max

Current drive ..... $\pm 5$  mA max

Protection .....Short-circuit to ground

Power-on state .....0 V ( $\pm 200$  mV)

External reference input

Range ..... $\pm 11$  V

Overvoltage protection ..... $\pm 25$  V powered on,  
 $\pm 15$  V powered off

Input impedance .....10 k $\Omega$

Bandwidth ( $-3$  dB) .....50 kHz

### Dynamic Characteristics

Settling time for full-scale step .....3.5  $\mu$ s to  $\pm 0.5$  LSB  
accuracy

Slew rate .....10 V/ $\mu$ s

Noise .....200  $\mu$ V<sub>rms</sub>  
DC to 300 kHz

Glitch energy (at midscale transition)  
 Magnitude  
 Reglitching disabled .....  $\pm 80$  mV  
 Reglitching enabled .....  $\pm 30$  mV  
 Duration ..... 3  $\mu$ s

**Stability**

Offset temperature coefficient .....  $\pm 50$   $\mu$ V/ $^{\circ}$ C  
 Gain temperature coefficient  
 Internal reference .....  $\pm 25$  ppm/ $^{\circ}$ C  
 External reference .....  $\pm 25$  ppm/ $^{\circ}$ C

**Digital I/O**

Number of channels ..... 8 input/output  
 Compatibility ..... 5 V/TTL  
 Digital logic levels on P0.<0..7>

Level	Min	Max
Input low voltage	0 V	0.8 V
Input high voltage	2.0 V	5.0 V
Input low current ( $V_{in} = 0$ V)	—	-320 $\mu$ A
Input high current ( $V_{in} = 5$ V)	—	10 $\mu$ A
Output low voltage ( $I_{OL} = 24$ mA)	—	0.4 V
Output high voltage ( $I_{OH} = -13$ mA)	4.35 V	—

Power-on state ..... Input (high-impedance)  
 Data transfers ..... Programmed I/O  
 Max transfer rate ..... 50 kwords/s,  
 system dependent  
 Constant sustainable rate ..... 1 to 10 kwords/s, typ

**Timing I/O**

Number of channels ..... 2 up/down  
 counter/timers,  
 1 frequency scaler  
 Resolution  
 Counter/timers ..... 24 bits  
 Frequency scalars ..... 4 bits  
 Compatibility ..... 5 V TTL/CMOS

Base clocks available  
 Counter/timers ..... 20 MHz, 100 kHz  
 Frequency scalars ..... 10 MHz, 100 kHz  
 Base clock accuracy .....  $\pm 0.01$  %  
 Max source frequency  
 up/down counter/timers ..... 20 MHz  
 Min source pulse duration ..... 10 ns in edge-detection  
 mode  
 Min gate pulse duration ..... 10 ns in edge-detection  
 mode  
 Data transfers ..... Interrupts,  
 programmed I/O

**Triggers**

**Analog Trigger**

Source ..... AI <0..15>,  
 external trigger  
 (PFI 0/AI START TRIG)  
 Purpose  
 Analog input ..... Start, reference,  
 and pause trigger,  
 sample clock  
 Analog output ..... Start and pause trigger,  
 sample clock  
 Counter/timers ..... Source, gate  
 Level  
 Internal .....  $\pm$ Full-scale  
 External .....  $\pm 10$  V  
 Slope ..... Positive or negative  
 (software-selectable)  
 Resolution ..... 8 bits, 1 in 256  
 Hysteresis ..... Programmable  
 Bandwidth (-3 dB)  
 Internal ..... 500 kHz  
 External ..... 2.5 MHz  
 External input (PFI 0/AI START TRIG)  
 Impedance ..... 12 k $\Omega$   
 Coupling ..... DC  
 Protection  
 When configured as  
 a digital signal ..... -0.5 to  $V_{CC}$   
 When configured as an analog  
 trigger signal or disabled .....  $\pm 35$  V  
 Powered off .....  $\pm 35$  V

## Digital Trigger

Purpose	
Analog input	Start, reference, and pause trigger, sample clock
Analog output	Start and pause trigger, sample clock
Counter/timers	Source, gate
External sources	PFI <0..9>
Compatibility	5 V TTL
Response	Rising or falling edge
Pulse width	10 ns min

## Calibration

Recommended warm-up time	30 minutes
Calibration interval	1 year
External calibration reference	>6 and <9.999 V
Onboard calibration reference	
Level	5.000 V ( $\pm 2.5$ mV) (actual value stored in EEPROM)
Temperature coefficient	$\pm 5$ ppm/ $^{\circ}$ C max
Long-term stability	$\pm 15$ ppm/ $\sqrt{1,000}$ h

## Power Requirement (from PCMCIA I/O Channel)

+5 VDC ( $\pm 5\%$ )	340 mA typ, 750 mA max
Power available at I/O connector	+4.65 to +5.25 V at 250 mA



**Note** These power usage figures do not include the power used by external devices that are connected to the fused supply present on the I/O connector.

Under ordinary operation, the DAQCard has a current requirement of 320–350 mA. The current requirements of the DAQCard might increase to 450 mA in any of the following conditions:

- The analog inputs you are sampling are overdriven at high gains.
- The analog inputs are left floating when the DAQCard is not in use.
- The analog outputs are driving high loads.

## Physical

PC card type	Type II
Weight	33 g (1.1 oz)
I/O connector	68-position female VHDCI connector

## Environmental

Operating temperature	0 to 40 $^{\circ}$ C
Maximum device temperature	70 $^{\circ}$ C measured by internal temperature sensor
Case temperature	55 $^{\circ}$ C recommended max
Storage temperature	-20 to 70 $^{\circ}$ C
Relative humidity	10 to 90%, noncondensing
Maximum altitude	2,000 m
Pollution Degree (indoor use only)	2

## Maximum Working Voltage

Maximum working voltage refers to the signal voltage plus the common-mode voltage.

Channel-to-earth	11 V, Installation Category I
Channel-to-channel	11 V, Installation Category I

## Safety

This product is designed to meet the requirements of the following standards of safety for electrical equipment for measurement, control, and laboratory use:

- IEC 60950-1, EN 60950-1
- UL 60950-1
- CAN/CSA-C22.2 No. 60950-1



**Note** For UL and other safety certifications, refer to the product label, or visit [ni.com/certification](http://ni.com/certification), search by model number or product line, and click the appropriate link in the Certification column.

## Electromagnetic Compatibility

Emissions ..... EN 55011 Class A at 10 m  
FCC Part 15A above  
1 GHz

Immunity ..... EN 61326:1997  
A2:2001, Table 1

CE, C-Tick, and FCC Part 15 (Class A) Compliant



**Note** For EMC compliance, operate this device with shielded cabling.

## CE Compliance

This product meets the essential requirements of applicable European Directives, as amended for CE marking, as follows:

Low-Voltage Directive (safety) ..... 73/23/EEC

Electromagnetic Compatibility

Directive (EMC) ..... 89/336/EEC



**Note** Refer to the Declaration of Conformity (DoC) for this product for any additional regulatory compliance information. To obtain the DoC for this product, visit [ni.com/certification](http://ni.com/certification), search by model number or product line, and click the appropriate link in the Certification column.

AI 8	34	68	AI 0
AI 1	33	67	AI GND
AI GND	32	66	AI 9
AI 10	31	65	AI 2
AI 3	30	64	AI GND
AI GND	29	63	AI 11
AI 4	28	62	AI SENSE
AI GND	27	61	AI 12
AI 13	26	60	AI 5
AI 6	25	59	AI GND
AI GND	24	58	AI 14
AI 15	23	57	AI 7
AO 0	22	56	AI GND
AO 1	21	55	AO GND
AO EXT REF	20	54	AO GND
P0.4	19	53	D GND
D GND	18	52	P0.0
P0.1	17	51	P0.5
P0.6	16	50	D GND
D GND	15	49	P0.2
+5 V	14	48	P0.7
D GND	13	47	P0.3
D GND	12	46	AI HOLD COMP
PFI 0/AI START TRIG	11	45	EXT STROBE
PFI 1/AI REF TRIG	10	44	D GND
D GND	9	43	PFI 2/AI CONV CLK
+5 V	8	42	PFI 3/CTR 1 SRC
D GND	7	41	PFI 4/CTR 1 GATE
PFI 5/AO SAMP CLK	6	40	CTR 1 OUT
PFI 6/AO START TRIG	5	39	D GND
D GND	4	38	PFI 7/AI SAMP CLK
PFI 9/CTR 0 GATE	3	37	PFI 8/CTR 0 SRC
CTR 0 OUT	2	36	D GND
FREQ OUT	1	35	D GND

Figure 1. NI DAQCard-6062E Pinout

National Instruments, NI, ni.com, and LabVIEW are trademarks of National Instruments Corporation. Refer to the *Terms of Use* section on [ni.com/legal](http://ni.com/legal) for more information about National Instruments trademarks. Other product and company names mentioned herein are trademarks or trade names of their respective companies. For patents covering National Instruments products, refer to the appropriate location: **Help>Patents** in your software, the `patents.txt` file on your CD, or [ni.com/patents](http://ni.com/patents).

© 2003–2005 National Instruments Corporation. All rights reserved.

370724C-01

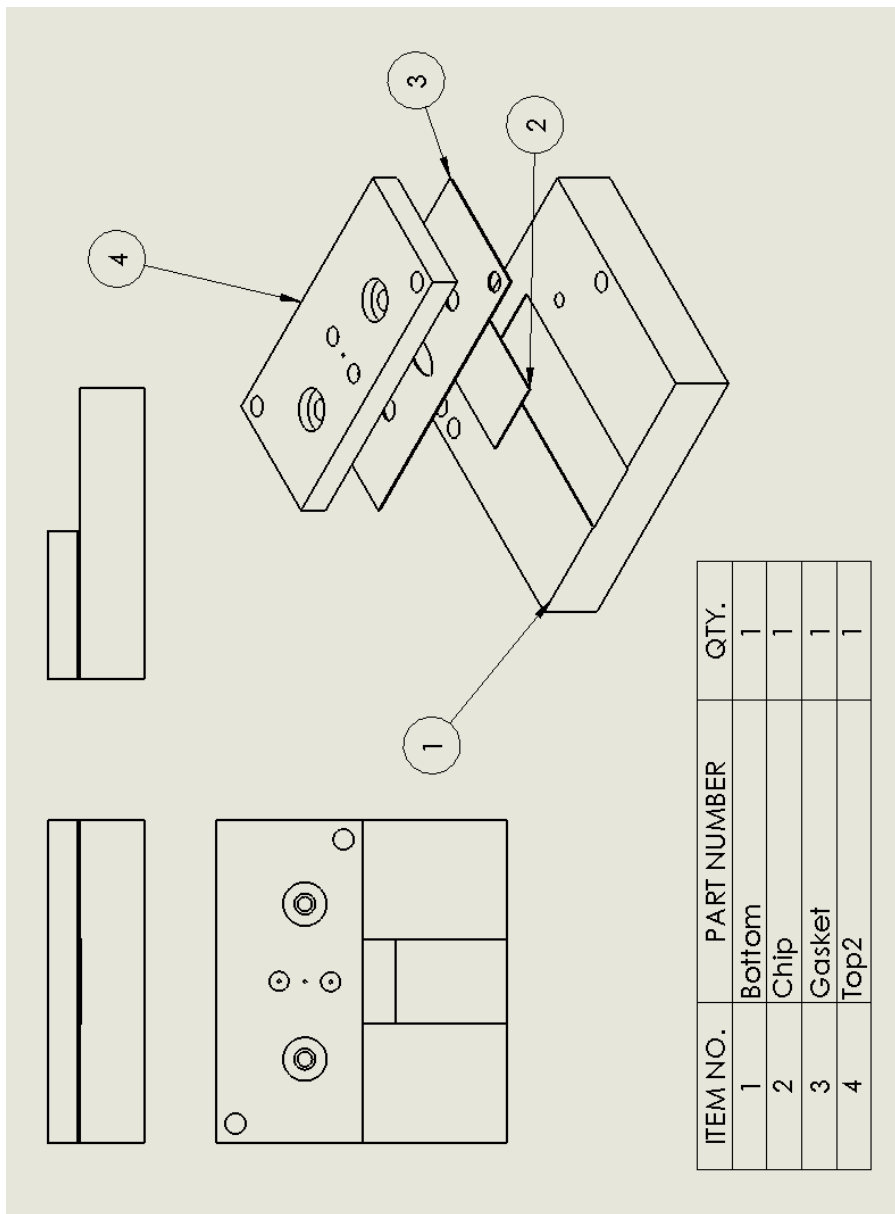
Dec05



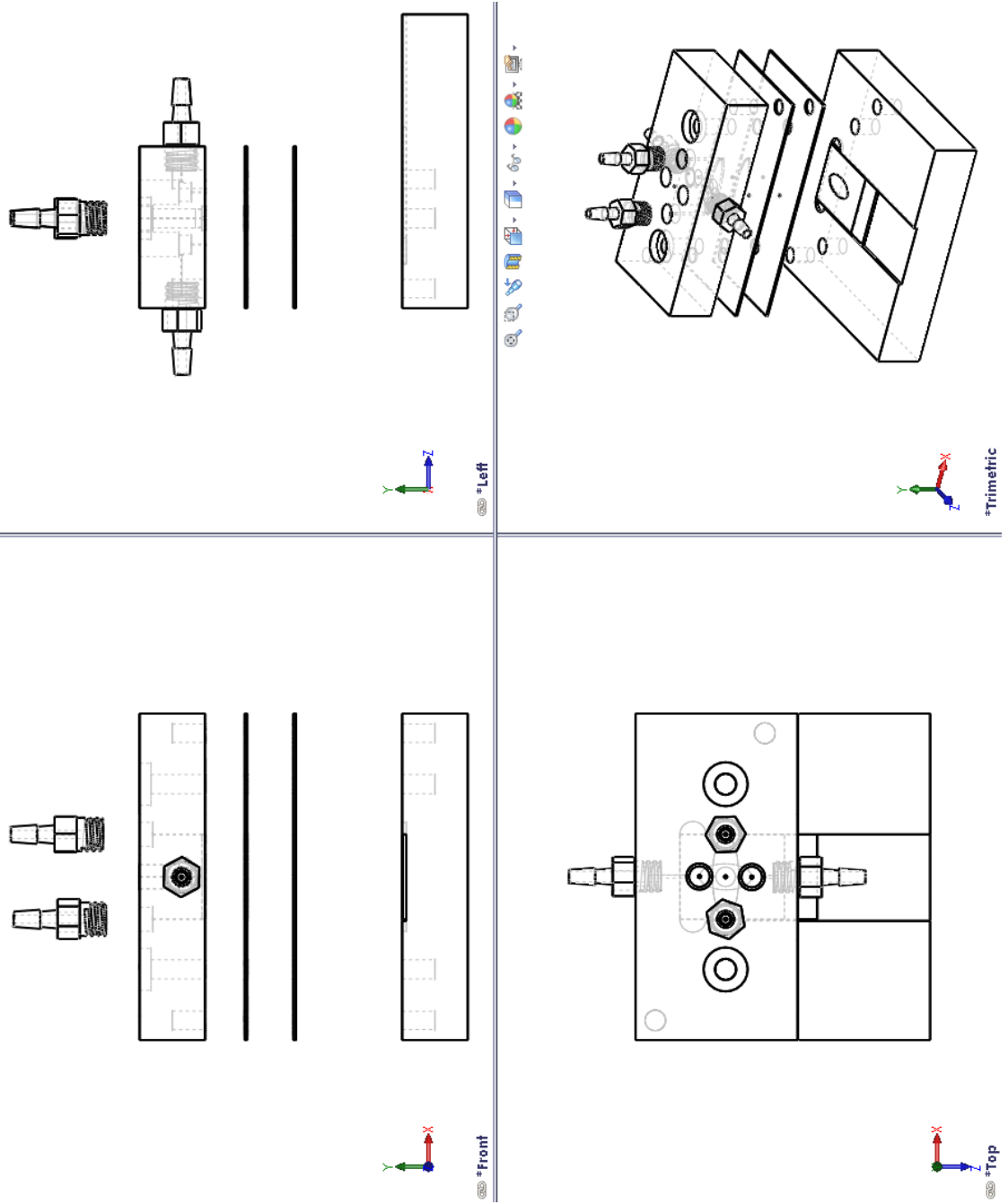
# Appendix D

## Flow Cell Designs

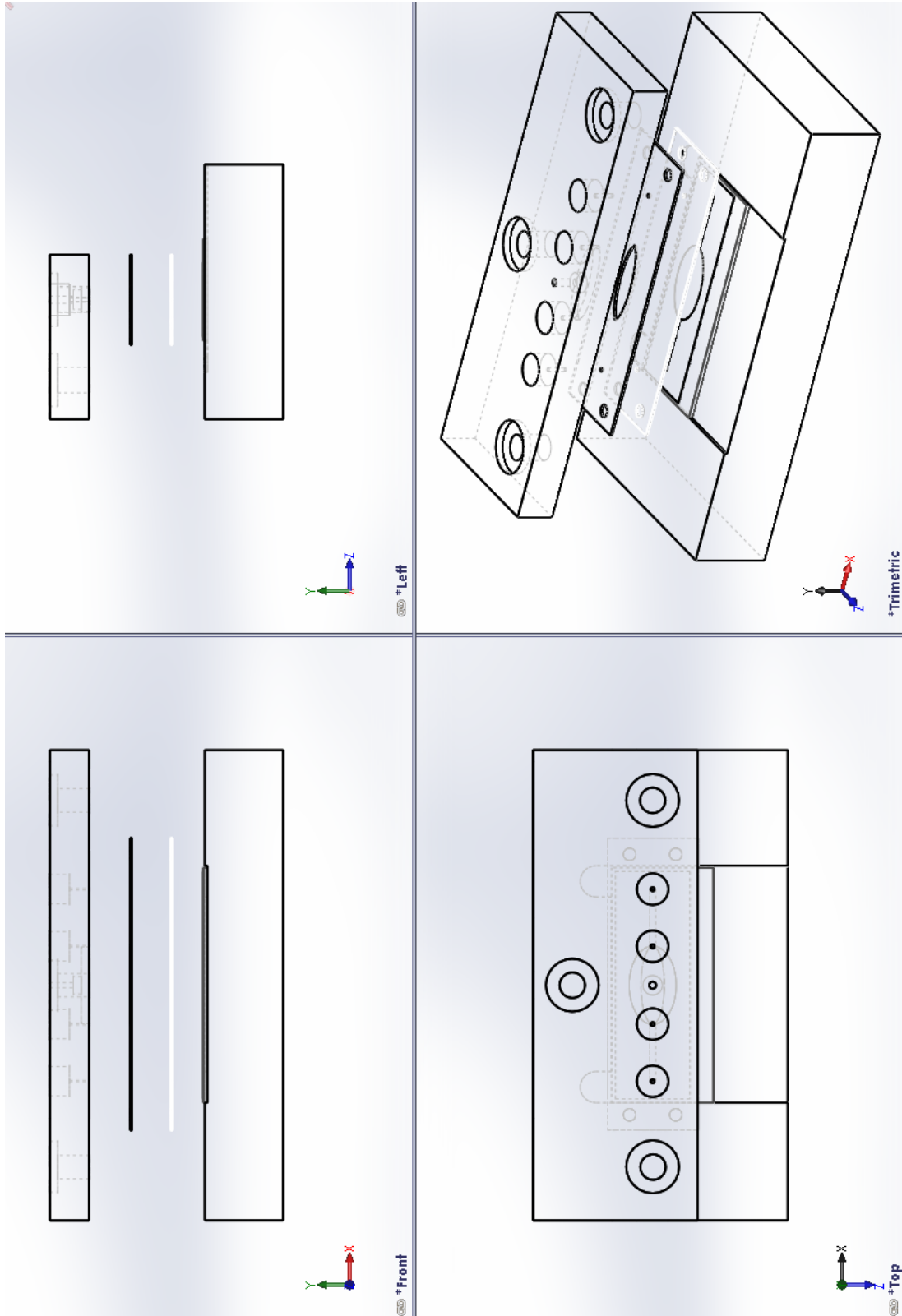
Version 1 A



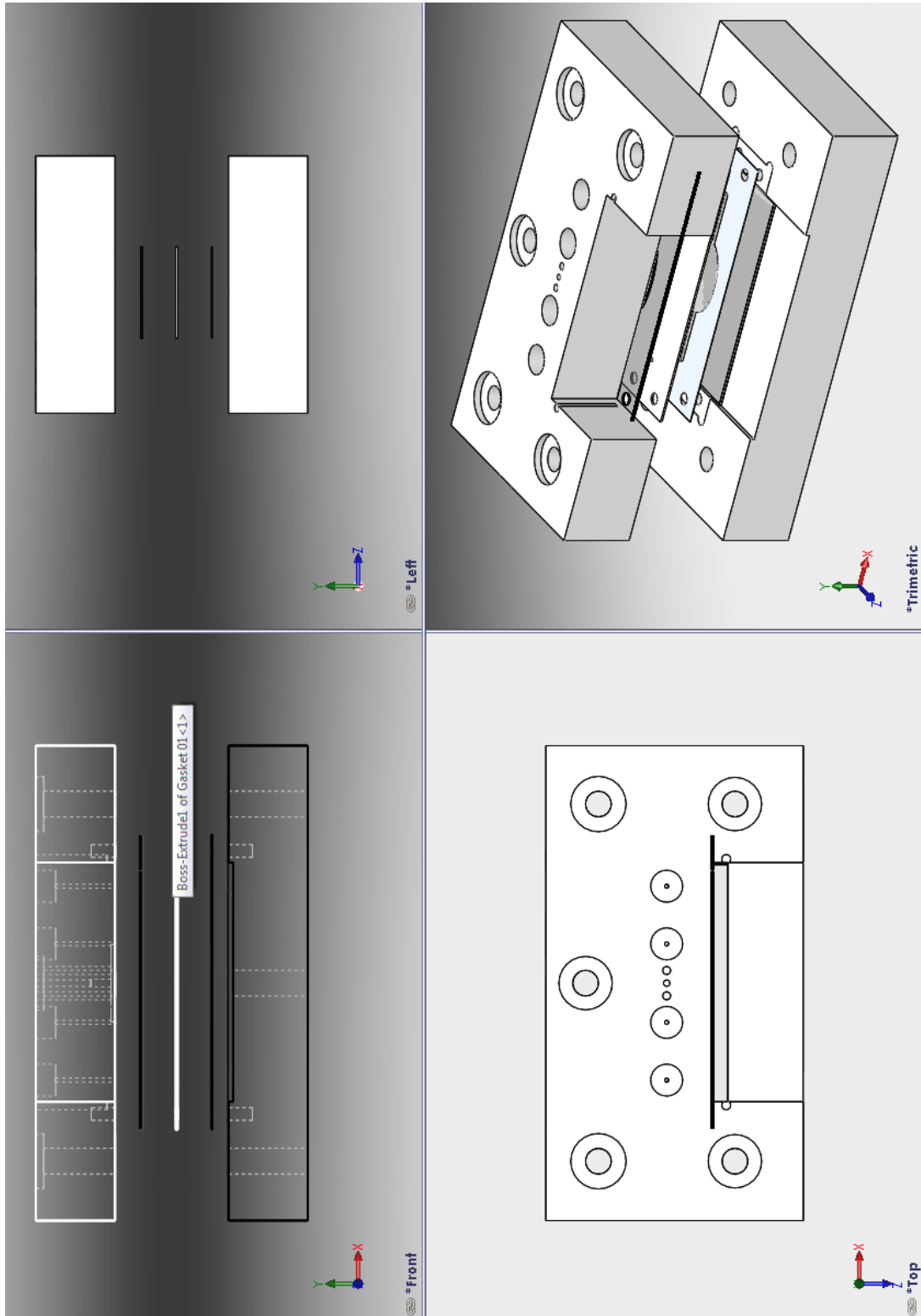
Version 1 B



Version 2A



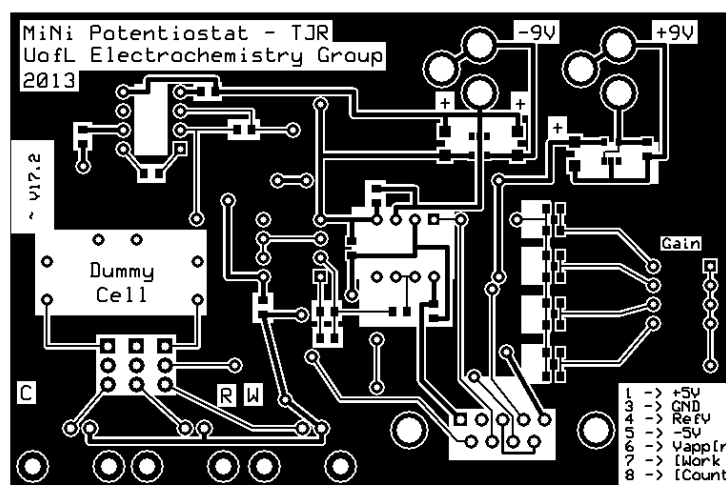
Version 2B



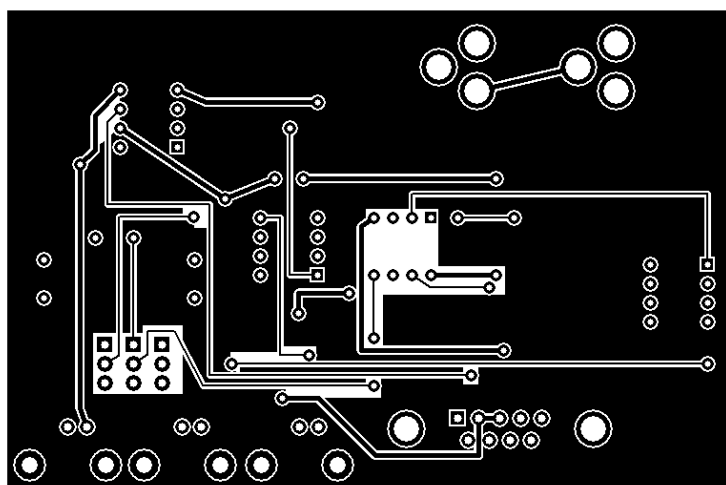
## Appendix E

### Printed Circuit Board Layout

Top Layer



Bottom Layer



## CURRICULUM VITA

THOMAS J. ROUSSEL, JR.

Research Engineer/Scientist

Speed School of Engineering

University of Louisville

Louisville, KY 40292

(w) 502.852.3971

(h) 502.451.8613

[thomas.rousseau@louisville.edu](mailto:thomas.rousseau@louisville.edu)

### **PERSONAL**

#### **Education**

1/08 – 4/2014

#### **Ph.D - Mechanical Engineering**

GPA 3.812 (4.00)

University of Louisville, Louisville, KY

Dissertation topic: Development and Evaluation of a Calibration Free Exhaustive Coulometric Detection System for Remote Sensing

- Concentration – Analytical Chemistry Instrumentation, Microtechnology/Micro-Electro-Mechanical Systems (MEMS), BioMEMS, Microfluidics, Finite Element Analysis, Circuit Theory, Analog Circuit Design.

6/97 – 11/03

#### **Master of Science in Biomedical Engineering**

GPA 3.75 (4.00)

Louisiana Tech University, Ruston, Louisiana

Thesis topic: Comparative Computational and Experimental Flow Studies in a Microfabricated Capillary Electrophoresis Device

- Concentration – Microtechnology/Micro-Electro-Mechanical Systems (MEMS), BioMEMS, and Microfluidics

8/94 - 5/97

**Bachelor of Science Biomedical Engineering**

GPA 3.89 (4.00)

Louisiana Tech University, Ruston, Louisiana

- Senior Design Project: Design and Fabrication of a Fetal Heart Sound Monitor

1987 – 1992

**Bachelor of Arts in Chemistry** GPA 2.69 (4.00)

University of New Orleans, New Orleans, Louisiana

**Experience**

4/14 – present

**University of Louisville, Louisville, Kentucky,** Department of Bioengineering (BE), *Term Faculty*.

10/99 – present

**University of Louisville, Louisville, Kentucky,** Department of Bioengineering (BE), *Research Engineer/Scientist*.

7/06 – 12/13

**Ultra Trace Detection, LLC, Louisville, Kentucky,** Co-founder

5/03 – present

**Assenti, LLC, Louisville, Kentucky,** Co-founder

6/96 - 6/99

**Institute for Micromanufacturing, Louisiana Tech University, Ruston, Louisiana,** *Graduate Assistant*.

8/95 - 9/96

**Intrepid Computer Consultants, Ruston, Louisiana,** Owner/Operator

**Affiliations**

Louisiana State Board of Registration for Professional Engineers and Land Surveyors – Registered EIT

Alpha Epsilon Delta

Alpha Eta Mu Beta

American Society of Mechanical Engineers

ASME

IEEE

IEEE-EMBS

## **Awards**

Biomedical Engineering Society (BMES)  
Tau Beta Pi Engineering Honor Society  
Tau Kappa Epsilon International Fraternity  
Dean's Citation, 2014  
Cenzig Topakoglu Scholarship - Outstanding Biomedical  
Engr Undergraduate, 1996  
Louisiana Tech University Dean's List  
Ben Bogard Memorial Scholarship, 1995-1996  
Outstanding Senior of Biomedical Engineering, 1996-1997  
Outstanding Junior of Biomedical Engineering, 1995-1996  
University of New Orleans Distinguished Leadership  
Award, 1992  
Tau Kappa Epsilon Fraternity National Scholar, 1991

## **SCHOLARSHIP OF DISCOVERY, INTEGRATION, AND APPLICATION**

### **Professional Skills and Research Specialties**

*Engineering Principles:* Instrumentation, Data Acquisition, Heat Transfer, Thermodynamics, Control System Theory, Circuit Design and Analysis, Metrology, Lithography, Fundamentals of Micro- Pressure and Flow Sensors, Finite Element Analysis

*Programming Experience:* Fortran, Visual Basic, C, C++, LabVIEW, Matlab

*Operating Systems:* Windows, Mac OSX, Unix, Linux

*Software:* LabVIEW, AutoCAD, Coventorware®, L-Edit, Silvaco, MathCAD, Matlab, Microsoft Office Suite, ORCAD, Adobe Suite, SolidWorks, Eagle, Multisim, Ultiboard

### **Publications**

#### **Book Chapters**

1. **Roussel, Jr., T.J.**, Jackson, D.J., Baldwin, R.P., and Keynton, R.S., "Amperometric Techniques," Encyclopedia of Microfluidics and Nanofluidics, Ed. Dongqing Li, Springer-Verlag New York Inc., 2008, ISBN: 978-0-387-32468-5.
2. £Crain, M.M., Keynton, R.S., Walsh, K.M., **Roussel, Jr., T.J.**, Baldwin, R.P., Naber, J.F. and Jackson, D.J., "Fabrication of a Glass CE Microchip with



Integrated Electrodes" Microchip Capillary Electrophoresis: Methods and Protocols, Ed. Charles S. Henry, Chapter 2, pp. 13-26, Humana Press, Inc. 2006.

### Refereed Publications

1. Mohamed M. Marei, **Thomas J. Roussel**, Robert S. Keynton, Richard P. Baldwin, "Electrochemical and Microfabrication Strategies for Remotely Operated Smart Chemical Sensors: Application of Anodic Stripping Coulometry to Calibration-free Measurements of Copper and Mercury," *Analytica Chimica Acta*, Vol. 803, Nov 25, 2013, pp 47-55, DOI 10.1016/j.aca.2013.06.047.
2. Mai-Dung Nguyen, Joseph P. Tinney, Fangping Yuan, **Thomas J. Roussel**, Ayman El-Baz, Guruprasad Giridharan, Bradley B. Keller, and Palaniappan Sethu, "Cardiac Cell Culture Model As a Left Ventricle Mimic for Cardiac Tissue Generation", *Anal. Chem.*, 2013, 85 (18), pp 8773–8779.
3. Rosendo Estrada, Guruprasad A. Giridharan, Mai-Dung Nguyen, **Thomas J. Roussel**, Mostafa Shakeri, Vahidreza Parichehreh, Sumanth D. Prabhu and Palaniappan Sethu, "Endothelial Cell Culture Model (ECCM) for Replication of Physiological Profiles of Pressure, Flow, Strain and Shear Stress In-Vitro", *Anal Chem.* 2011 Apr 15;83(8):3170-7.
4. R. Dorairaj, T. J. Roussel, Jr., M. M. Crain, D. J. Jackson, D. Franco, K. M. Walsh, R. P. Baldwin, J. F. Naber, and R. S. Keynton, "Multi-Channel Capillary Electrophoresis Device with Simultaneous, Integrated Electrochemical Detection of a Single Sample," Submitted 9/13/2013, Springer Open Journal.
5. S.M. Berry, **T.J. Roussel, Jr.**, S.D. Cambron, R.W. Cohn and R.S. Keynton, "Fabrication of Suspended Electrokinetic Microchannels from Directly-Written Sacrificial Polymer Fibers," Published On-line 4/10/2012, *Microfluidics & Nanofluidics*, DOI: 10.1007/s10404-012-0973-z.
6. Estrada R, Giridharan GA, Nguyen MD, **Roussel TJ**, Shakeri M, Parichehreh V, Prabhu SD, Sethu P., "Endothelial cell culture model for replication of physiological profiles of pressure, flow, stretch, and shear stress in vitro," *Analytical Chemistry*, 2011 Apr 15;83(8):3170-7. Epub 2011 Mar 17.
7. S. Carroll, M. Marei, **T.J. Roussel**, R.S. Keynton and R.P. Baldwin, "Microfabricated Electrochemical Sensors for Exhaustive Coulometry Applications," *Sensors and Actuators B: Chemical*, Vol. 160, Iss. 1, 318-326, DOI:10.1016/j.snb.2011.07.055.
8. M. Martin, **T. Roussel**, S. Cambron, J. Aebersold, D. Jackson, K. Walsh, J.-T. Lin, M. O'Toole, and R. Keynton, "Performance of Stacked, Flow-through Micropreconcentrators for Portable Trace Detection," *International Journal for Ion Mobility Spectrometry*, 2010, vol. 13, issue 3, pp. 109. DOI:10.1007/s12127-010-0048-3.
9. R.S. Pai, K.M. Walsh, M.M. Crain, **T.J. Roussel, Jr.**, D.J. Jackson, R.P. Baldwin, R.S. Keynton, and J.F. Naber, "Fully integrated three dimensional electrodes for electrochemical detection in microchips: fabrication, characterization and

- applications,” *Analytical Chemistry*, 2009, vol. 81, no. 12, pp 4762-4769, DOI:10.1021/ac9002529.
10. £Keynton, R.S., **Roussel, T.J.**, Crain, M.M., Jackson, D.J., Franco, D.B., Naber, J.F., Walsh, K.M., and Baldwin, R.P., "Design and development of microfabricated capillary electrophoresis devices with electrochemical detection," *Analytica Chimica Acta*, vol. 507, no. 1, pp. 95-105, April 2004. . DOI: 10.1016/j.aca.2003.12.042
  11. £Jackson, D., Naber, J., **Roussel, Jr., T.J.**, Crain, M.M., Walsh, K.M., Keynton, R.S., and Baldwin, R.P., "Portable High Voltage Power Supply and Electrochemical Detection Circuits for Microchip Capillary Electrophoresis," *Anal. Chem.*, 75(14), 3311-17, 2003
  12. £Baldwin, R., **Roussel, T.J.**, Crain, M.M., Bathlagunda, V., Jackson, D.J., Gullapalli, J., Conklin, J.A., Pai, R., Naber, J.F., Walsh, K.M., and Keynton, R.S., "Fully-Integrated On-Chip Electrochemical Detection for Capillary Electrophoresis in a Microfabricated Device," *Analytical Chemistry*, vol. 74, no. 15, pp. 3690-3697, 2002.

#### Refereed Publications – In Preparation

13. T. Burkhead, B. King, **T. Roussel**, R. Keynton and B. Panchapakesan, “Carbon Nanotube Sensor Platforms for Detecting Radiation Dosed Cells: An Exploration into Different Sensing Architectures,” 2013, *Nanotechnology*
14. **T.J. Roussel, Jr.**, S. Carroll, M. Marei, R.S. Keynton, and R.P. Baldwin, “A Calibration-Free Coulometric Detection System for Remote Monitoring,” 2014, *Lab-on-a-Chip*
15. R. Dorairaj, **T.J. Roussel**, G. Sumanasekera, P. Sethu, C.M. Klinge and R.S. Keynton, “Carbon Nanotube Meshes for Separating Proteins Electrophoretically,” 2013, *RSC LOC*.
16. R. Dorairaj, **T.J. Roussel, Jr.**, G. Sumanasekera and R.S. Keynton, “Design, Fabrication and Characterization of Carbon Nanotube Meshes in Microchannels for Electrophoresis,” 2013, *RSC Lab-on-a-Chip (LOC)*.
17. D.M. Brey, W.D. Ehringer, J.S. Alexander, X. Yang, **T.J. Roussel**, W. Sumanasekera, C.M. Klinge, and R.S. Keynton, "Shear stress regulation of occludin expression in human umbilical vein endothelial cells," *Microcirculation*.
18. Yang, X., McGuyer, J.C., Friedrich, C.R., **Roussel, T.J.**, Morley, A.T., Price, L., Barnett, E., Young, A.M., Volz, J., and Keynton, R.S., "Production of Miniaturized Acoustical Lenses using Micromanufacturing Techniques," *Institute of Physics: J. Micromechanics & Microengineering*.

## Full-Length Peer-Reviewed Conference Papers

1. M.M. Marei, **T.J. Roussel**, R.S. Keynton, R.P. Baldwin, “Electrochemical and Microfabrication Strategies for Remotely Operated Smart Chemical Sensors: The Dual Challenges of Sample Preparation and Calibration-less Measurements”, September 8-12, 2013, 246th ACS National Meeting, Indianapolis, IN, USA
2. R.P. Baldwin, S. Carroll, M.Marei, **T.J. Roussel** and R.S. Keynton, “A Calibration-Free Coulometric Detection System for Remote Sensing Applications,” Proceedings of the International Society of Electrochemistry, Turku, Finland, May 8-11, 2011.
3. **T.J. Roussel**, S. Carroll, M. Marei, R.S. Keynton and R.P. Baldwin, “A Calibration Free Coulometric Detection System for Remote Monitoring,” Proceedings of the IEEE Sensor 2010 Conference, Waikoloa, HI, Nov. 1-4, 2010.
4. H. Dong, D. Jackson, **T. Roussel**, D. Dosal, R. Ideker, J. Naber, S. Koenig and R. Keynton, “Design and Characterization of Thin-film Microelectrode Arrays and Signal Conditioning Microchips for High Spatial Resolution Surface Laplacian Measurements,” Proceeding of the IEEE Sensor 2010 Conference, Waikoloa, HI, Nov. 1-4, 2010.
5. H. Dong, D. Jackson, **T. Roussel**, D. Dosal, R. Ideker, J. Naber, S. Koenig and R. Keynton, “Design and Characterization of a Signal Conditioning Microchip and Thin-Film Microelectrode Array for High Spatial Resolution Cardiac Mapping,” Proceedings of the 6th World Congress on Biomechanics, Singapore, August 1-6, 2010.
6. M. Martin, **T. Roussel**, M. O’Toole, J. Aebersold, S. Cambron, D. Jackson, R. Keynton and K. Walsh, , “Working In-line Stacked Preconcentrator (WISP) for Portable IMS,” Proc. of the 19th Annual Conf. of the International Society for Ion Mobility Spectrometry, Albuquerque, NM, July 18-23, 2010.
7. M. O’Toole, S. Cambron, M. Martin, **T. Roussel**, J. Aebersold, D. Jackson, K. Walsh, and R. Keynton, “Dual-stage High Volume Sampling for IMS Detection of Trace Substances,” Proc. of the 19th Annual Conf. of the International Society for Ion Mobility Spectrometry, Albuquerque, NM, July 18-23, 2010.
8. M. Martin, **T. Roussel**, J. Aebersold, S. Cambron, R. Hageman, D. Jackson, J. Naber, K. Walsh, and R. Keynton, “Characterization of a Cascaded Micro-Preconcentrator Sampler for IMS,” Proc. of the 18th Annual Conf. of the International Society for Ion Mobility Spectrometry, Thun, Switzerland, July 25-31, 2009.
9. Scott M. Berry, Scott D. Cambron, **Thomas J. Roussel, Jr.**, Robert W. Cohn and Robert S. Keynton, “Electrokinetic Transport in Suspended Microchannels Fabricated from Sacrificial Polymer Fibers,” Proc. of the 5th Microtechnologies in Medicine & Biology (MMB), Quebec, Canada, April 1-3, 2009.
10. Michael Martin, **Thomas Roussel**, Julia Aebersold, Scott Cambron, Rick Hageman, Douglas Jackson, Ji-Tzuoh Lin, Robert McGill, John Naber, Jennifer

- Stepnowski, Stan Stepnowski, Kevin Walsh, and Robert Keynton, "Investigation of a Microfabricated Flow-Through Preconcentrator using a Custom Explosives Vapor Generator and Calibrated Ion Mobility Spectrometer," Proceedings of the 2008 International Symposium on Spectral Sensing Research, Hoboken, NJ.
11. Rathish Dorairaj, **Thomas J. Roussel, Jr.**, Gamini Sumanasekera, Palaniappan Sethu, Carolyn M. Klinge and Robert S. Keynton, "Effect of Carbon Nanotube Membrane Length on Electrophoretic Flow," Proceedings of the 13th Solid State Sensors, Actuators and Microsystems Workshop 2008, #0125, Hilton Head Island, SC, Jun 1-5, 2008.
  12. Scott M. Berry, **Thomas J. Roussel**, Scott D. Cambron, Robert W. Cohn, and Robert S. Keynton, "Fabrication of suspended electroosmotic microchannels from sacrificial polymer fibers," 2007 Micro Total Analytical Systems ( $\mu$ TAS) Proceedings, Paris, France, Oct. 7-11, 2007.
  13. Scott M. Berry, **Thomas J. Roussel**, Scott D. Cambron, Robert W. Cohn, and Robert S. Keynton, "Fabrication of suspended electroosmotic microchannels from sacrificial polymer fibers," 2007  $\mu$ TAS Proceedings, Paris, France, Oct. 7-11, 2007.
  14. £ Scott M. Berry, **Thomas J. Roussel, Jr.**, Scott D. Cambron, Robert W. Cohn and Robert S. Keynton, "Fabrication and Electroosmotic Flow Analysis of Freely-Suspended, Three-Dimensional Microchannels," 2007 SEM Annual Conference & Expo, Springfield, MA.
  15. **Thomas J. Roussel, Jr.**, Rekha Pai, Mark Crain, Douglas Jackson, Lukasz Sztaberek, Kevin Walsh, John F. Naber, Richard P. Baldwin, and Robert S. Keynton, "3D Microelectrodes for Coulometric Screening in Microfabricated Lab-on-a-Chip Devices," *Proceeding of the 4<sup>th</sup> Microtechnology in Medicine and Biology 2006*, Okinawa, Japan, May 9-12, 2006.
  16. Scott M. Berry, **Thomas J. Roussel, Jr.**, Scott D. Cambron, Robert W. Cohn and Robert S. Keynton, "Fabrication of Freely-Suspended, Three-Dimensional Microchannels from Sacrificial Polymer Fibers," *Proceeding of the 4<sup>th</sup> Microtechnology in Medicine and Biology 2006*, Okinawa, Japan, May 9-12, 2006.
  17. Scott M. Berry, **Thomas J. Roussel, Jr.**, Scott D. Cambron, Robert W. Cohn and Robert S. Keynton, "Micromanipulator Controlled Fabrication of Micro- and Nanoscale Polymer Fibers and Application as Sacrificial Structures in the Production of Microchannels," *Proceedings of the 12<sup>th</sup> Solid State Sensors, Actuators and Microsystems Workshop 2006*, Hilton Head Island, SC, Jun 4-8, 2006. (40% Acceptance rate)
  18. Rathish Dorairaj, **Thomas J. Roussel, Jr.**, Mark M. Crain, Douglas J. Jackson, Danielle Franco, Kevin M. Walsh, Richard P. Baldwin, John F. Naber, and Robert S. Keynton, "Dual Capillary Electrophoresis Devices with Electrochemical Detection on a Single Platform," *Proceeding of the 3<sup>rd</sup> International IEEE EMBS Special Topics Conference on Microtechnologies in Medicine and Biology, Oahu, Hawaii, May 2005*

19. Rekha S. Pai, Mark M. Crain, **Thomas J. Roussel, Jr.**, Douglas J. Jackson, Richard P. Baldwin, Robert S. Keynton, John F. Naber, and Kevin M. Walsh, "Lab-on-a-Chip Systems with Three-Dimensional Microelectrodes," *Proceeding of the 3<sup>rd</sup> International IEEE EMBS Special Topics Conference on Microtechnologies in Medicine and Biology, Oahu, Hawaii, May 2005*.
20. R.S. Pai, M.M. Crain, **T.J. Roussel, Jr.**, D.J. Jackson, R.P. Baldwin, R.S. Keynton, J.F. Naber and K.M. Walsh, "Fabrication and Characterization of a Novel Three Dimensional Microelectrode for Lab on a chip Systems", *11<sup>th</sup> Solid State Sensors, Actuators and Microsystems Workshop 2004*, Hilton Head Island, SC, Jun 6-10, 2004.
21. Yang, X., **Roussel, Jr., T.J.**, Crain, M.M., Morley, A., Conklin, J.A., Price, L., Barnett, E., McGuyer, J.C., Walsh, K.M. and Keynton, R.S., "Fabrication of a High Frequency *In Vivo* Ultrasonic Doppler Wall Shear Rate Measuring Device Using Micromolding Techniques," *2<sup>nd</sup> Annual International IEEE EMBS Special Topic Conference on Microtechnologies in Medicine and Biology*, pp. 84-87, 2002.
22. **Roussel, T.J.**, Crain, M.M., Bathlagundu, V., Jackson, D.J., Gullapalli, J., Conklin, J.A., Pai, R., Baldwin, R.P., Naber, J.F., Walsh, K.M., and Keynton, R.S., "Integration of "On-Chip" Electrochemical Detection in a Microfabricated Capillary Electrophoresis Device," *Proceedings of the 10<sup>th</sup> Solid-State Sensor, Actuator, and Microsystems Workshop, Hilton Head 2002*, 38% acceptance rate.
23. **Roussel, T.J.**, Crain, M.M., Jackson, D.J., Walsh, K.M., Naber, J.F., Baldwin, R.P., and Keynton, R.S., "A Capillary Electrophoresis Platform with "On-Chip" Electrochemical Detection: Experimental and Computational Flow Studies," *Proceedings of the 2001 International Mechanical Engineering Congress and Exposition, Microelectromechanical Systems Sub-Division, New York, NY, 2001*.
24. Conklin, J.A., Crain, M.M., Pai, R.S., Martin, M., Pitts, K., **Roussel, T.J.**, Jackson, D.J., Baldwin, R.P., Keynton, R.S., Naber, J.F., and Walsh, K.M., "Alternative Fabrication Methods for Capillary Electrophoretic Device Manufacturing," *Proceedings of the 14th Biennial University/Government/Industry Microelectronics Symposium*, pp. 83-85, 2001.
25. Bathlagundu, V., Jackson, D., Naber, J., Baldwin, R., Walsh, K., Keynton, R., Crain, M., **Roussel, T.**, and Diaconu, M., "A Portable Battery Powered Electrochemical Detection Circuit with a 1000 Volt CE Power Supply for Microchip Capillaries," *Proc. of the 14th Biennial University/Government/Industry Microelectronics Symposium*, pp. 197-200, 2001.
26. Pai, R.S., **Roussel, T.J.**, Crain, M.M, Jackson, D.J., Conklin, J.A., Baldwin, R.P., Keynton, R.S., Walsh, K.M. and Naber, J.F., "Integrated Electrochemical Detection for Lab-on-a-Chip Analytical Microsystems," *Proceedings of the Fourteenth Biennial University/Government/ Industry Microelectronics Symposium*, pp. 167-170, 2001.

## Abstracts Published in Proceedings and Invited Presentations

1. Marei, M.M., **Roussel, T.J.**, Keynton, R.S., and Baldwin, R.P. "Electrochemical Determination of As(III) by Subtractive Anodic Stripping Coulometry in a Micro-fabricated Platform," *Accepted to the 2014 Pittcon Conference*, Chicago, IL March 2-6, 2014.
2. M.M. Marei, **T.J. Roussel**, R.S. Keynton, R.P. Baldwin, "Calibration-free Micro-fabricated Electrochemical Sensor for Heavy Metal Determination", , March 19-23, 2013, PITTCON Conference & Expo, Philadelphia, PA USA
3. R.P. Baldwin, M.M. Marei, **T.J. Roussel**, R.S. Keynton, "Calibration-free Microfabricated Electrochemical Sensor Based on Coulometry", December 11-14, 2012, 20th Annual Research and Development Conference 2012, Melbourne, Australia.
4. T. Burkhead, **T. Roussel**, R. Keynton and B. Panchapakesan, "Development of a Carbon Nanotube Biosensor for the Detection of Radiation Damage in Human Blood," 1st Annual ISS Research and Development Conference, Denver, CO June 26-28, 2012.
5. J. Lake, K. Walsh, S. McNamara, R. Keynton, M. Crain, **T. Roussel**, A. Kieswetter, C. McKenna, "The Kentucky NanoNet", *18th Biennial University / Government / Industry Micro-Nano (UGIM) Symposium*. West Lafayette, IN. pp. 170-172, 6/28 – 7/1/2010.
6. S. Carroll, **T.J. Roussel**, R.S. Keynton, and R.P. Baldwin, "Towards a Smart Sensing Platform for Water Quality Determination," *Proc of the Pittcon Conference*, Orlando, FL, Feb. 28-Mar 5, 2010.
7. R. Dorairaj, **T.J. Roussel, Jr.**, G. Sumanasekera, W. Sumanasekera, P. Sethu, C.M. Klinge and R.S. Keynton, "Carbon Nanotube Membrane-based Electrokinetic Separation of Proteins," *Proceedings of the BMES 2009 Annual Fall Meeting*, Pittsburgh, PA, Oct. 7-10, 2009.
8. Rathish Dorairaj, **Thomas J. Roussel**, Gamini Sumanasekera, Palaniappan Sethu, Carolyn M. Klinge, and Robert S. Keynton, "Electrophoretic Separations of Large Proteins Using Carbon Nanotube Membranes," *Proceedings of the 2009 Pittcon Conference*, Chicago, IL, March 8-13, 2009.
9. Lukasz Sztaberek, Michael Martin, **Tommy Roussel, Jr.**, Kevin M. Walsh, John F. Naber, Robert S. Keynton, Richard Baldwin, "Microfabrication Electrochemical Sensor for Water Monitoring System," *Proceedings of the 2008 IEEE-EDS University/Government/Industry Microsystems Conference*, Louisville, KY, July 13-16, 2008.
10. Julia Aebersold, Michael Martin, **Tommy Roussel**, Robert S. Keynton, Kevin Walsh, "Microfabrication Process and Characteristic Testing of a MEMS-based Preconcentrator," *Proceedings of the 2008 IEEE-EDS University/Government/Industry Microsystems Conference*, Louisville, KY, July 13-16, 2008.

11. J. Aebersold, D. Jackson, M. Crain, J. Naber, **T. Roussel, Jr.**, R. Keynton, K. Walsh, P. Van der Pol, G. Tezel, and H. Kaplan, "Development of an implantable, RFID-based intraocular pressure sensing system for glaucoma patients," *Proceedings of the ARVO 2008*, Fort Lauderdale, FL, April 27 – May 1, 2008.
12. Rathish Dorairaj, **Thomas J. Roussel**, Gamini Sumanasekera, Palaniappan Sethu, Carolyn M. Klinge, and Robert S. Keynton, "Carbon Nanotube Membranes for Size-based Electrophoretic Separation of Proteins," *Proceedings of the 2008 IEEE-EDS UGIM Conference*, Louisville, KY, July 13-16, 2008.
13. L. Sztaberek, M.D. Martin, **T. Roussel, Jr.**, J. Naber, K. Walsh, R. Keynton and R.P. Baldwin, "Microfabrication techniques for the development of a miniaturized Hg-free ASV sensor for drinking water," *Proceedings of the ACS 235th National Meeting & Exposition*, New Orleans, LA, April 6 – 10, 2008.
14. M.D. Martin, L. Sztaberek, R. Baldwin, **T. Roussel, Jr.**, R. Keynton, K. Walsh, J. Naber, B. Vaughn, and D. Jackson, "Application of microfabrication techniques for the development of a miniaturized Hg-free ASV system," *Proc. of the American Chemical Society 234th National Meeting & Exposition*, Boston, MA, August 19 – 23, 2007.
15. J. Naber, P. Van der Pol, D. Jackson, K. Walsh, R. Keynton, H. Kaplan, G. Tezel, M. Crain, and T. Roussel, "A Real-Time IOP Monitoring System for the Management of Glaucoma. Venture Forum Conference, San Francisco, CA, p. 80, 2007.
16. **T. Roussel, Jr.**, M. Martin, R. Hageman, D. Jackson, J. Aebersold, S. Cambron, J.F. Naber, S. Alexander, J. Stepnowski, S. Stepnowski, A. McGill, K.M. Walsh, and R.S. Keynton, "Development of an HVAC-Integrated Explosives Vapor Detection System for Public Facility/Infrastructure Protection," *Proceedings from the 2007 Pittsburgh Conference (PITTCON) on Analytical Chemistry and Applied Spectroscopy, Chicago, IL*.
17. M. Martin, **T. Roussel, Jr.**, J. Aebersold, J. Stepnowski, S. Stepnowski, A. McGill, K.M. Walsh, and R.S. Keynton, "Progress with the CASPAR Preconcentrator for Trace Detection of Explosives," *Proceedings from the 2007 Pittsburgh Conference (PITTCON) on Analytical Chemistry and Applied Spectroscopy, Chicago, IL*.
18. L. Sztaberek, **T. Roussel, Jr.**, M. Martin, D. Jackson, J.F. Naber, K.M. Walsh, R.S. Keynton and R.P. Baldwin, "Application of Microfabricated Techniques for the Development of a Miniaturized ASV System," *Proceedings of the 2007 Pittsburgh Conference (PITTCON) on Analytical Chemistry and Applied Spectroscopy, Chicago, IL*.
19. Richard Baldwin, Danielle Franco, **Thomas J. Roussel, Jr.**, Jayadeep Gullapalli, Mark M. Crain, Douglas J. Jackson, Robert S. Keynton, Kevin M. Walsh, and John F. Naber, "Microfabricated Multi-electrode Arrays for

- Electrochemical Detection in Lab-on-a-Chip Devices," *International Symp. on Sensor Science*, Nanjing, China, May 29-June 3, 2004.
20. Franco, D.B., Baldwin, R.P., **Roussel, Jr., T.J.**, Gullapalli, J., Crain, M.M., Jackson, D.J., Keynton, R.S., Walsh, K.M., and Naber, J.F., "Microfabricated Multi-electrode Arrays for Electrochemical Detection in Lab-on-a-Chip Devices," *2004 Pittsburgh Conference (PITTCON) on Analytical Chemistry and Applied Spectroscopy*, Chicago, IL.
  21. Pai, R.S., **Roussel, Jr., T.J.**, Crain, M.M., Jackson, D.J., Baldwin, R.P., Keynton, R.S., Naber, J.F. and Walsh, K.M., "Electroplating for Three Dimensional Lab-on-a-Chip Electrodes and Microstructures," Kentucky Nano Materials Workshop, Louisville, KY, Sept. 25-26, 2003.
  22. Tang, L., Cambron, S.D., **Roussel, T.J.**, Keynton, R.S. and Kang, K.A., "Multi-biosensor Development for Simultaneous Multi-Factor Detection," *2003 Biomedical Engineering Society Meeting*, Nashville, TN, 2003.
  23. Richard P. Baldwin, **Thomas J. Roussel, Jr.**, Mark M. Crain, Danielle Franco, Jayadeep Gullapalli, Douglas J. Jackson, Robert S. Keynton, John F. Naber, and Kevin M. Walsh, "Integrated On-Chip Electrochemical Detection on Microfabricated Capillary Electrophoresis Platforms," *Proceedings of the 2002 American Inst. for Chem Engr. Conference*, Indianapolis, IN, 2002.
  24. D. M. Brey, W. D. Ehringer, J. S. Alexander, Y. Xu, **T. J. Roussel, Jr.**, and R. S. Keynton, "Wall Shear Stress Regulation of Occludin Expression in Human Umbilical Vein Endothelial Cells," *Proceedings of the 2002 Joint Institute for Electrical and Electronic Engineers (IEEE) – Engineering in Medicine and Biology (EMBS)/Biomedical Engineering Society (BMES) Conference*, Houston, TX, 2002, pp. 316-317.
  25. **T. J. Roussel, Jr.**, M. M. Crain, V. Bathlagundu, D. J. Jackson, J. A. Conklin, R. Pai, J. F. Naber, K. M. Walsh, J. Gullapalli, R. P. Baldwin, and R. S. Keynton, "Integration of 'On-Chip' Electrochemical Detection in a Microfabricated Capillary Electrophoresis Device," *Proceedings of the 2002 Joint IEEE-EMBS/BMES Conference*, Houston, TX, 2002, pp. 1640-1641.
  26. Rekha S. Pai, **Thomas J. Roussel, Jr.**, Mark M. Crain, Douglas J. Jackson, Richard P. Baldwin, Robert S. Keynton, John F. Naber, and Kevin M. Walsh, "Electroplating for Three Dimensional Lab-on-a-Chip Electrodes and Microstructures," *Proceedings of the 2002 Joint IEEE – EMB/BMES Conference*, Houston, TX, 2002, pp. 1663-1664.
  27. Morley, A.T., Rock, A., Volz, J., **Roussel, Jr., T.J.**, McGuyer, J.C., and Keynton, R.S., "Fabrication of Miniaturized Acoustical Lenses for High-Frequency Ultrasound Transducers," *Book of Abstr.: 2001 Research Louisville! Conf.*, Louisville, KY, 2001. Brey, D.M., Yang, X., **Roussel, Jr., T.J.**, Ehringer, W.D., Alexander, J.S., and Keynton, R.S., "Effects of Wall Shear Stress on the Expression of Occludin in Human Umbilical Vein Endothelial Cells," *Book of Abstr.: 2001 Research Louisville! Conf.*, Louisville, KY, 2001.



28. **Roussel, Jr., T.J.**, Crain, M.M., Jackson, D.J., Pai, R.S., Bathlagundu, V., Conklin, J.A., Walsh, K.M., Baldwin, R.P., Naber, J.F., and Keynton, R.S., "A Fully-Integrated Capillary Electrophoresis System with On-Chip Electrochemical Detection," *Book of Abstr.: 2001 Research Louisville! Conf., Louisville, KY, 2001*.
29. **Roussel, T.J.**, Keynton, R.S., Walsh, K.M., Crain, M.M., Naber, J.F., Jackson, D.J., and Baldwin, R.P., "A Capillary Electrophoresis Platform with "On-Chip" Electrochemical Detection: Experimental and Computational Flow Studies," *Proceedings of the 2001 International Mechanical Engineering Congress and Exposition (IMECE) MEMS sub-Division, Abstract #23911, 2001*.
30. Brey, D.M., Ehringer, W.D., Alexander, J.S., Yang, X., **Roussel, T.J.**, and Keynton, R.S., "Role of Wall Shear Stress on Occludin Expression within Human Umbilical Vein Endothelial Cells," *Proceedings of the 2001 IMECE Bioengineering Division, Abstract # 23010, pp. 1-2, 2001*.
31. Morley, A.T., Price, L.E., Barnett, E.M., Young, A.M., Volz, J., **Roussel, T.J.**, Friedrich, C.R., McGuyer, J.C., and Keynton, R.S., "Development and Fabrication of Miniaturized Acoustical Lenses using Micro Molds," *Proceedings of the 2001 IMECE Bioengineering Division, Abstract # 23004, pp. 1-2, 2001*.
32. **Roussel, Jr., T.J.**, Crain, M.M., Jackson, D.J., Pai, R.S., Bathlagundu, V., Conklin, J.A., Walsh, K.M., Baldwin, R.P., Naber, J.F., and Keynton, R.S., "Capillary Electrophoresis Device with "On-Chip" Electrochemical Detection," Gordon Research Conference, The Physics and Chemistry of Microfluidics, 2001, *Invited Poster*.
33. McGuyer, J.C., Friedrich, C.R., **Roussel, T.J.**, Morley, A.T., Price, L., Barnett, E., and Keynton, R.S., "Production of Miniaturized Acoustical Lenses using a Micromanufactured Stamp and Molding Technique," *Proceedings of the 19<sup>th</sup> Annual Houston Conference on Biomedical Engineering Research*, p. 136, 2001.
34. **Roussel, T.J.**, Jackson, D., Crain, M.M., Baldwin, R.P., Naber, J.F., Walsh, K.M. and Keynton, R.S., "Accuracy of Computational Models for Predicting Flows in Microfabricated Capillary Electrophoresis Devices," *Proceedings of the 19<sup>th</sup> Annual Houston Conference on Biomedical Engineering Research*, p. 137, 2001.
35. McGuyer, J.C., Friedrich, C.R., **Roussel, T.J.**, Morley, D., and Keynton, R.S., "Microfabrication of Miniaturized Acoustical Lenses," *Proceedings of the 20<sup>th</sup> Annual Southern Biomedical Engineering Conference*, p. 39, 2001.
36. **Roussel, T.**, Keynton, R., Walsh, K., Crain, M., Jackson, D., Naber, J., and Baldwin, R., "Computer Simulation of Separation and Flow within Microfabricated Capillaries," *Pittsburgh Conference on Analytical Chemistry and Applied Spectroscopy (PITTCON 2001)*, #114, 2001.

37. Baldwin, R., Crain, M., Walsh, K., Keynton, R., Naber, J., **Roussel, T.**, and Jackson, D., "Integrated Electrochemical Detection for Lab-on-a-Chip Analysis Systems," *Pittsburgh Conference (PITTCON) on Analytical Chemistry and Applied Spectroscopy*, #115, 2001.
38. Jackson, D., Naber, J., Baldwin, R., Walsh, K., Keynton, R., Crain, M., **Roussel, T.** and Diaconu, M., "A Compact Battery Powered High Voltage Power Supply for Capillary Electrophoresis Using Microchip Capillaries," *PITTCON 2001*, #116, 2001.
39. Jackson, D., Naber, J., Baldwin, R., Walsh, K., Keynton, R., Crain, M., **Roussel, T.** and Diaconu, M., "A Portable Battery Powered Electrochemical Detection Circuit," *Pittsburgh Conference (PITTCON) on Analytical Chemistry and Applied Spectroscopy*, #1345, 2001.

#### Patents Issued

1. D.J. Jackson, **T.J. Roussel**, M.M. Crain, R.P. Baldwin, R.S. Keynton, J.F. Naber, K.M. Walsh, J.G. Edelen, "Capillary electrophoresis-electrochemical detection device and supporting circuits," International App. No. PCT/US03/04047, filed Feb. 10, 2003; U.S. Patent No. 7,344,628 B2, issued Mar. 18, 2008.
2. R. Dorairaj, R.S. Keynton, **T.J. Roussel, Jr.**, M.M. Crain, D.J. Jackson, K.M. Walsh, R.P. Baldwin, J.F. Naber, and D. Franco, "Capillary Electrophoresis Systems and Methods," U.S. Patent No. 7,988,839 B2, issued August 2, 2011.
3. S. Cambron, **T.J. Roussel**, R.S. Keynton, M.D. Martin, D.J. Jackson, K.M. Walsh, J.F. Naber, "Interchangeable preconcentrator connector assembly," U.S. Patent No. 8,178,045 B2, issued May 15, 2012.
4. R. Dorairaj, R. Keynton, **T. Roussel, Jr.**, C. Klinge, G. Sumanasekera; W. Sumanasekera, "Microfluidic devices and methods of using same," U.S. Patent No. 8,298,392, issued October 30, 2012
5. S. Cambron, **T. Roussel, Jr.**, R. Keynton, "Preconcentrator for analysis instruments," U.S. Patent No. 8,569,691, issued October 29, 2013

#### Patent Disclosures and Provisional Patents

1. S. Cambron, R. Keynton, **T. Roussel**, J. Franco, K. Walsh, M. Crain, "Microtack," ULRF Disclosure No. 05014, submitted Sep. 10, 2004.
2. M. Martin, R.S. Keynton, **T.J. Roussel**, S.D. Cambron, K.M. Walsh, D.J. Jackson, J. Aebersold, and R. Hageman, "Large volume analyte preconcentrator," ULRF Disclosure No. 08005, submitted Jul. 17, 2007; International App. No. PCT/US2009/52483, filed July 31, 2009; U.S. Patent App. Serial No. 13/056,091, filed Jan. 26, 2011.

3. J. Naber, D. Jackson, H. Kaplan, J. Aebersold, K. Walsh, R. Keynton, **T. Roussel**, and P. van der Pol, "A method and system for monitoring a condition of an eye," US Patent Application #12/174,458, 7/16/08.
4. S.D. Cambron, **T.J. Roussel**, R.S. Keynton, "Module for increasing the sensitivity of chemical detectors," ULRF Disclosure No. 09042, U.S. Provisional App. No. 61/264,047, filed Nov. 24, 2009; U.S. Patent App. Serial No. 12/953,108, filed Nov. 24, 2010.
5. **T.J. Roussel**, R.S. Keynton, S.D. Cambron, M.D. Martin, K.M. Walsh, "Auto-triggering technique for initiating coordinated desorption into vapor/particle detector," ULRF Disclosure No. 09043, submitted Dec. 12, 2008.
6. M. Martin, K. Walsh, **T. Roussel**, R.S. Keynton, S. Cambron, "Surface desorber and sample collector for chemical analysis," ULRF Disclosure No. 10014, subm. Sep. 8, 2009.
7. M. Martin, K. Walsh, **T. Roussel**, R.S. Keynton, D. Jackson, S. Cambron, M. O'Toole, "Trace sampler as an add-on for baggage x-ray scanners," ULRF Disclosure No. 10057, submitted Jan. 19, 2010.
8. S. Cambron, M. Martin, **T. Roussel**, R.S. Keynton, "Mechanically actuated low-power large volume high flow rate preconcentrator for chemical detection," ULRF Disclosure No. 11003, submitted July 19, 2010.

## Grants and Contracts

### Externally Funded Proposals – Co-Principal Investigator

"Development and Field Testing of a Shopping Mall and Public Facility HVAC Explosives Monitoring System," Department of Homeland Security, R. Keynton (PI/PD), Co-PIs – K. Walsh, J. Naber, S. Alexander, M. Martin and **T. Roussel**, \$1,205,000, 7/1/05-3/31/09.

"A Statewide Micro/Nano Network for Collaborative Research, Education, and Outreach" Principal Investigator – Kevin Walsh, Co-PIs – R. Keynton, S. McNamara, M. Crain, J. Lake, **T. Roussel**, 7/1/08-6/30/13, 20%, NSF-EPSCoR, \$887,661.

"An Implantable System to Monitor Eye Pressure for Glaucoma," J. Naber (PI), Co-PIs – D. Jackson, H. Kaplan, R. Keynton, K. Walsh, M. Crain, and **T. Roussel**, Kentucky Science & Technology Corporation, KSTC-02-DCI-024, \$375,000, 1/1/08 – 12/31/09.

"A Real-Time Monitoring System to Measure IOP in Glaucoma," D. Jackson (PI), Co-PIs – J. Naber, H. Kaplan, R. Keynton, K. Walsh, M. Crain, and **T. Roussel**, NIH NEI Phase II SBIR, \$750,000, 10/1/05 – 9/30/07.

"Development of Microfabricated Chemical Agents and Explosives Preconcentrators for Building Monitoring," NRL, 6/1/04 – 03/1/05, K. M. Walsh (PI), Co-PIs – R. S. Keynton, M. Martin, M. Crain, **T. Roussel**, \$262,883.

## **TEACHING AND SCHOLARSHIP OF TEACHING**

### **Courses Taught**

#### Undergraduate Level Courses

Circuits and Sensors for Bioengineers (BE 322)

Computational Methodologies in Bioengineering (BE340)

Bioengineering Measurements (BE423)

Biomedical Device Design (BE480) - Mentor

Bioengineering Senior Project Design (BE 497) – Group/Project Mentor

#### Graduate Level Courses

Bioinstrumentation (BE621)

Rehabilitation Engineering and Assistive Technology (BE 658) – Mentor

Biomedical Rotation (BE691) - Mentor

Micro-Electrical-Systems (MEMS) Design (ME 660)

Introduction to Microfabrication and MEMS (ECE 543) – Invited Lecturer

LabVIEW for Electrical Engineers (ECE 526) – Invited Lecturer

### **Curriculum Development**

Currently developing an integrated link between all courses involving circuit theory and analysis, measurements systems and techniques, data acquisition, sensors, and instrumentation technologies for the Bioengineering Curriculum (Aligning BE322, BE423, and BE621)/

## **SERVICE**

### **University Committees**

#### Departmental

Bioengineering Department Continuous Improvement Committee

Responsible for the Bioinstrumentation and Biomeasurements teaching laboratory

### **Professional Activities**

#### Reviewer of Manuscripts

Analytica Chimica Acta

2000 – present